

# **Near-infrared spectroscopy as an analytical tool for the biorefinery**

**Majed Almuqhim**

Doctor of Philosophy

University of York

Chemistry

June 2022

## Abstract

Transforming from fossil fuel to renewable resources is essential to reduce carbon dioxide emissions into the atmosphere. Biorefineries produce fuel and chemicals from biomass resources and use biowaste as a resource. It plays a significant role in this transformation. Some processes in the biorefineries need to be controlled in a greener way rather than using conventional analysis such as High-Performance Liquid Chromatography (HPLC), Gas Chromatography (GC) and Nuclear Magnetic Resonance (NMR) spectroscopy. Although they provide accurate results, they employ solvents, produce waste, and require highly qualified labour and time.

In this project, Near-infrared spectroscopy (NIRS) with a fibre-optics probe was used to analyse the conversion in chemical reactions in real-time, detect chemicals in mixtures in different ratios, identify particle size for solid sucrose samples, and measure the moisture contents in sawdust. NIRS provides instant results during the chemical conversion process offering a greener approach to the current standard analytical techniques. A fibre-optics probe controlled the real-time conversion of Levoglucosenone (LGO) to its triol form in an aqueous solution. The results were consistent with NMR, Mid-Infrared (MIR) and Ultraviolet-visible (UV-Vis) spectroscopic techniques. Investigation of OH 1<sup>st</sup> overtone of an aqueous solution of LGO has revealed that LGO has a negligible effect on the water self-association below 60 °C. Above this temperature, the enthalpy change ( $\Delta H$ ) increased to more than double the value.

During this investigation, it was found that Monohydroxy Cyrene (MHC) is produced from LGO in high yield, resulting in 98 % purity after purification using column chromatography. The MHC was characterised by NMR, IR, UV-Vis, CHN, GC, Mass Spectrometry (MS), Simultaneous Thermal Analysis (STA) and Differential Scanning Calorimetry (DSC) analytical methods. All these analytical results fit together to provide an accurate product picture.

## List of contents

Abstract.....	2
List of contents.....	3
List of figures.....	7
List of schemes .....	11
List of tables.....	13
Acknowledgement .....	15
Declaration.....	17
Chapter 1: Introduction to NIRS in biorefineries .....	19
1.1 Introduction.....	19
1.2 REACH.....	20
1.3 Biomass and the biorefinery .....	21
1.3.1 Biomass conversion:.....	22
1.3.2 Microwave (MW) .....	23
1.3.3 Water presence in biorefinery and biomass .....	25
1.4 IR spectroscopy.....	27
1.4.1 (background).....	27
1.4.2 The simple harmonic oscillator.....	28
1.4.3 The anharmonic oscillator .....	30
1.4.4 Absorption and emission spectra .....	32
1.5 Near-Infrared Spectroscopy (NIRS) .....	34
1.5.1 History of NIRS .....	34
1.5.2 The Importance of NIRS.....	34
1.5.3 Vibration bands in NIRS.....	39
1.5.3.1 NIR spectra of Carbon-hydrogen overtone bands .....	40
1.5.3.2 NIR spectra of Oxygen-hydrogen overtone bands .....	41
1.5.3.3 NIR spectra of carbon-hydrogen combination bands .....	41
1.5.3.4 NIR spectra of Oxygen-hydrogen combination bands .....	42
1.6 Hydrogen bonding .....	42
1.6.1 Hydrogen bonding in IR .....	42
1.6.2 Hydrogen bonding in NMR spectroscopy: .....	43
1.6.3 The importance of using chemometric analysis in NIRS .....	44
1.6.4 The reason behind not using advanced chemometric methods in this thesis.....	45

1.7 Biomass converted compounds .....	45
1.7.1 Saccharides:.....	45
1.8 Conclusion.....	49
Chapter 2: Materials and methods.....	51
2.1 Materials.....	51
2.2 Analysis and instrument .....	53
2.2.1 MIR spectroscopy.....	53
2.2.2 NIR spectroscopy .....	53
2.2.2.1 Bruker Matrix-F .....	53
2.2.2.2 Bruker Equinox55 NIRS .....	54
2.2.2.3 Metrohm .....	54
2.2.2.4 UV-Vis spectroscopy .....	54
2.2.2.5 NMR spectroscopy .....	54
2.2.3 Simultaneous Thermal Analysis (STA) .....	55
2.2.4 CHN.....	55
2.2.5 HPLC.....	55
2.2.6 GC .....	55
Chapter 3: NIR Spectroscopy analysis of sugars and their derivatives.....	57
3.1 Introduction .....	57
3.2 Individual substances .....	59
3.2.1 fructose .....	59
3.2.2 Glucose at very low concentrations.....	62
3.2.3 1 <sup>st</sup> Overtone region for sugars .....	64
3.2.4 Combination region for sugars .....	66
3.2.5 1 <sup>st</sup> Overtone region for anhydrosugars, LA and HMF .....	67
3.2.6 Combination region for anhydrosugars, LA and HMF .....	68
3.3 Mixtures.....	70
3.4 Comparison between NIRS vs HPLC .....	75
3.4.1 Individual samples.....	75
3.4.2 Mixtures.....	80
3.5 Real-time analysis of (Cyrene : LGO) in different ratios.....	84
3.6 The effect of temperature on water detected by NIRS .....	87
3.7 O-H 1 <sup>st</sup> overtone of water and sugar .....	89

3.8 Conclusion .....	92
Chapter 4: NIR Spectroscopy for solid samples .....	93
4.1 Introduction.....	93
4.2 Measuring particle size using NIRS .....	95
4.2.1 Particle size for pure sugar.....	95
4.2.2 Particle size for sawdust in water .....	96
4.3 The Hydrogen bonding for solid samples.....	97
4.3.1 Sucrose.....	99
4.3.2 Glucose .....	101
4.3.3 Lactose Monohydrate .....	103
4.3.3.1 Investigation of water in lactose monohydrate .....	104
4.3.3.2 Hydrogen bonding investigation in dry lactose sample.....	109
4.4 Moisture content in sawdust .....	113
4.5 Conclusion .....	120
Chapter 5: H <sub>2</sub> O/LGO interaction (temperature-dependant) by investigating H <sub>2</sub> O overtones vibration .....	121
5.1 Introduction.....	121
5.2 The effect of temperature on water and LGO.....	122
5.2.1 Water.....	122
5.2.1.1 general.....	122
5.2.1.2 Deconvolution of the band.....	127
5.2.2 LGO .....	131
5.2.3 Cyrene.....	134
5.2.4 Methyl Ethyl Ketone MEK.....	135
5.2.5 NMR spectroscopy for LGO in water (temperature-dependent) .....	136
5.3 H <sub>2</sub> O/LGO interaction (time-dependent) .....	139
5.3.1 IR spectroscopy – fundamental vibration .....	139
5.3.2 Near-infrared spectroscopy (NIRS) – 1 <sup>st</sup> overtone vibration.....	142
5.3.3 UV-Vis for LGO .....	145
5.3.4 Reichardt's dye .....	147
5.3.5 NMR spectroscopy for LGO.....	152
5.3.6 LGO:water interaction time-dependant using NMR spectroscopy.....	155
5.4 Conclusion .....	164

Chapter 6: The production of Monohydroxy Cyrene (MHC) .....	165
6.1 Introduction .....	165
6.2 MHC production methods .....	166
6.2.1 First method of extraction .....	166
6.2.2 Second method of extraction .....	167
6.3 Analytical techniques used for the MHC .....	169
6.3.1 NMR spectroscopy .....	169
6.3.2 IR spectroscopy .....	173
6.3.3 Gas Chromatography (GC) .....	174
6.3.4 CHN analysis.....	176
6.3.5 MS spectrometry and the difference between MHC prepared from H <sub>2</sub> O and D <sub>2</sub> O .....	177
6.4 The effect of the temperature on the MHC production .....	181
6.5 Protons on C3 of MHC.....	184
6.6 LGO - H <sub>2</sub> O interaction using microwave/raman spectroscopy.....	189
6.7 Monohydroxy Cyrene properties.....	193
6.7.1 The polarity of MHC.....	193
6.7.2 Solubility .....	195
6.7.3 Dissolving MHC in water.....	196
6.7.4 Thermal analysis.....	202
6.8 Conclusion.....	205
Chapter 7: Conclusion and future work .....	207
7.1 Conclusion.....	207
7.2 Future work .....	208
Appendix .....	211
Abbreviations and symbols .....	249
References .....	251

## List of figures

Figure 1.1 Circular vs. linear economy system .....	19
Figure 1.2 Converting biomass to chemicals in a greener way .....	24
Figure 1.3 The difference between MW and conventional biorefinery.....	25
Figure 1.4 Vibration of a diatomic molecule .....	28
Figure 1.5 The vibrational energy levels .....	29
Figure 1.6 IR Radiation absorbed by a sample .....	33
Figure 1.7 MIR and NIR spectroscopy regions .....	35
Figure 1.8 The use of (NIRS) in the literature .....	39
Figure 3.1 IR spectra for pure (powder) sugars and LGA .....	58
Figure 3.2 NIR spectra of diluted fructose samples.....	59
Figure 3.3 NIR spectra of H <sub>2</sub> O and diluted fructose samples.....	60
Figure 3.4 NIR spectroscopy for fructose samples.....	60
Figure 3.5 Subtracted method for NIR spectra of diluted fructose.....	61
Figure 3.6 NIR spectroscopy for fructose samples with subtraction method.....	62
Figure 3.7 NIR spectra of diluted fructose samples with subtraction method.....	63
Figure 3.8 NIR spectra of diluted LGA samples .....	63
Figure 3.9 NIR spectra of fructose, sucrose and glucose 1 <sup>st</sup> overtone.....	64
Figure 3.10 NIR spectra of fructose, sucrose, and glucose combination region .....	66
Figure 3.11 1 <sup>st</sup> overtone region of different diluted samples .....	67
Figure 3.12 Combination region of different diluted samples.....	68
Figure 3.13 NIR spectra of mixtures at the combination region with the subtraction method .....	70
Figure 3.14 NIR spectra of mixtures at the 1 <sup>st</sup> overtone region with subtraction method...	71
Figure 3.15 NIR spectra of biomass hydrolysates .....	72
Figure 3.16 NIR spectra of biomass hydrolysates of O-H 1 <sup>st</sup> overtone region at 21°C.....	73
Figure 3.17 HMF quantitative analysis.....	75
Figure 3.18 LA quantitative analysis.....	77
Figure 3.19 LGO quantitative analysis .....	78
Figure 3.20 HMF : LA quantitative analysis .....	80
Figure 3.21 HMF : LGO quantitative analysis .....	81

Figure 3.22 LA : LGO quantitative analysis .....	82
Figure 3.23 CH vibration of LGO and Cyrene.....	84
Figure 3.24 The 1 <sup>st</sup> overtone vibration of LGO and Cyrene mixtures .....	85
Figure 3.25 The 2 <sup>nd</sup> derivative spectra of LGO and Cyrene mixtures .....	86
Figure 3.26 NIR spectra of water in variable temperature .....	87
Figure 3.27 Subtraction and 2 <sup>nd</sup> derivative methods for water spectra in variable temperature.....	88
Figure 3.28 NIR spectra of (sample BM5) in variable temperature.....	88
Figure 3.29 NIR spectra of neat solid samples using (DRIFT) technique .....	90
Figure 3.30 NIR spectra of diluted sucrose (water spectrum was subtracted).....	90
Figure 3.31 NIR spectra of sugars using subtraction method .....	91
Figure 3.32 The potential work which can apply variable temperature using NIRS .....	92
Figure 4.1 NIR spectra of sucrose in different particle size .....	96
Figure 4.2 NIR spectra of sawdust in water in different particle size .....	97
Figure 4.3 N- and M-IR spectra of sucrose, glucose, fructose and LGA.....	98
Figure 4.4 NIR spectra of sucrose at variable temperatures.....	99
Figure 4.5 STA analysis for sucrose .....	101
Figure 4.6 NIR spectra of glucose at variable temperatures .....	101
Figure 4.7 STA analysis for glucose with three heating cycles .....	102
Figure 4.8 NIR spectra for lactose monohydrate during drying process.....	104
Figure 4.9 the intensity of the band at 5170 cm <sup>-1</sup> during heating process.....	105
Figure 4.10 STA analysis of lactose monohydrate in three cycles .....	106
Figure 4.11 STA analysis for lactose monohydrate with two hours heating .....	107
Figure 4.12 NIR spectrum of lactose monohydrate .....	108
Figure 4.13 NIR spectra of lactose after 24 minuets of drying at 160 °C .....	109
Figure 4.14 Shifting band position with temperature.....	111
Figure 4.15 NIR spectra for lactose monohydrate before and after drying in different temperatures .....	111
Figure 4.16 NIR spectrum for sawdust 250-500 μm in different moisture contents.....	113
Figure 4.17 NIR spectra of water band in sawdust samples .....	114
Figure 4.18 STA analysis for sawdust.....	115
Figure 4.19 NIR spectra of water band in sawdust samples .....	117



Figure 4.20 STA for wet sawdust of the sample dried at 40C.....	117
Figure 4.21 Deconvolution of the OH combination band of sawdust sample.....	118
Figure 4.22 Deconvoluted band for wet sawdust, dried and exposed to air in different times .....	118
Figure 5.1 NIR spectra of water in variable temperature .....	124
Figure 5.2 NIR spectra of water in variable temperature .....	126
Figure 5.3 NIR spectra of H <sub>2</sub> O in variable temperatures (5 – 95 °C).....	128
Figure 5.4 Deconvoluted 1 <sup>st</sup> overtone band of water OH at (5 & 95 °C).....	129
Figure 5.5 Band area of water OH at (5 - 95 °C).....	129
Figure 5.6 Deconvoluted 1 <sup>st</sup> overtone band of 0.4 m LGO at (5 & 95 °C) .....	131
Figure 5.7 (A) Band area of deconvoluted OH band of 0.4 m LGO at (5 - 95 °C).....	132
Figure 5.8 STA for (A) 0.4 m LGO in H <sub>2</sub> O and (B) its 1 <sup>st</sup> derivative.....	133
Figure 5.9 <sup>13</sup> C NMR stacked spectra of 4 wt% LGO in D <sub>2</sub> O in variable temperatures ....	136
Figure 5.10 <sup>1</sup> H NMR spectroscopy integration results for LGO conversion by temperature change .....	138
Figure 5.11 MIR spectra of 10 wt% LGO in H <sub>2</sub> O .....	141
Figure 5.12 NIR spectra of diluted LGO (10 wt%) in H <sub>2</sub> O in different days.....	143
Figure 5.13 UV-Vis spectra of (A) 0.001 % and (B) 0.1 % LGO in H <sub>2</sub> O in different days .....	145
Figure 5.14 Reichardt's dye dissolved in 1 % LGO in different days.....	149
Figure 5.15 $\lambda_{\max}$ of the Reichardt's dye dissolved in 1% LGO in different days, 1% Cyrene and water.....	150
Figure 5.16 <sup>1</sup> H NMR spectrum for LGO 99.11% dissolved in CDCl <sub>3</sub> .....	152
Figure 5.17 <sup>13</sup> C NMR spectrum for LGO 99.11% dissolved in CDCl <sub>3</sub> .....	154
Figure 5.18 <sup>13</sup> C NMR spectrum for LGO dissolved in D <sub>2</sub> O a. freshly mixed and b. after few days .....	155
Figure 5.19 <sup>1</sup> H NMR spectrum of LGO in D <sub>2</sub> O when it is fully reacted with water forming triol.....	157
Figure 5.20 <sup>13</sup> C NMR spectrum of LGO in D <sub>2</sub> O when it is fully reacted with water forming triol. A small amount of MHC is present in the solution as indicated by the green arrows .....	158
Figure 5.21 <sup>13</sup> C NMR antiphase spectra (DEPT-135) for LGO in D <sub>2</sub> O after 4 months. Negative bands show the CH <sub>2</sub> species.....	160
Figure 5.22 The conversion of LGO to triol-LGO by time .....	161

Figure 5.23 The MIR spectra of ketone absorbance of (from left) 10 wt% LGO in D <sub>2</sub> O freshly mixed and after 7 days, pure LGO and diol, triol-LGO .....	162
Figure 5.24 The MIR spectra of CH stretching of pure LGO and the expected two forms (diol, triol-LGO) in the range (from left) 3300 – 2600 cm <sup>-1</sup> and 1850 – 1400 cm <sup>-1</sup> .....	163
Figure 6.1 MHC. Two steps from biomass .....	165
Figure 6.2 EtOAc extraction method .....	167
Figure 6.3 <sup>13</sup> C NMR spectra of MHC .....	169
Figure 6.4 <sup>1</sup> H NMR spectroscopy for MHC.....	170
Figure 6.5 IR spectra of LGO and MHC .....	173
Figure 6.6 MS fragments of MHC .....	177
Figure 6.7 Spectra of MHC in different water sources and production methods.....	180
Figure 6.8 IR spectra for MHC prepared in different temperatures .....	181
Figure 6.9 NMR spectra of MHC production in different temperatures.....	183
Figure 6.10 The difference between <sup>1</sup> H NMR spectra of MHC prepared from H <sub>2</sub> O and D <sub>2</sub> O .....	185
Figure 6.11 Protons coupling on C3.....	187
Figure 6.12 The polarizability effect on H <sub>2</sub> O and CO <sub>2</sub> molecules .....	189
Figure 6.13 Raman spectra of LGO in water under MW heating from freshly mixed (0 to 24) hours.....	190
Figure 6.14 IR and Raman spectra of the LGO in different process.....	192
Figure 6.15 (Left). MHC produced in different temperatures 90, 60 and 40 °C and (right). MHC 40 °C after purification.....	193
Figure 6.16 UV-Vis spectra of 1% aqueous solutions of: LGO (green), Cyrene (blue), MHC (red) and H <sub>2</sub> O (black). All samples showing the effect of the solution on Reichardt's dye .....	194
Figure 6.17 UV-Vis spectrum of pure MHC with Reichardt's dye (deconvoluted bands) 194	
Figure 6.18 Solubility of (A) Cyrene and (B) MHC in different solvents .....	196
Figure 6.19 IR spectrum of 10% MHC in D <sub>2</sub> O shows no vibration band for the ketone .	197
Figure 6.20 shows no difference between the produced oils in comparison with the original Cyrene sample .....	201
Figure 6.21 shows that the MHC has higher boiling point than both Cyrene and LGO...	202
Figure 6.22 DSC for MHC .....	203
Figure 6.23 shows 3D modelling using COSMO to identify the intramolecular H-bonding for MHC, Cyrene and LGO in different electronic configurations .....	204

## List of schemes

Scheme 1.1 Cellulose is converted to different molecules .....	49
Scheme 4.1 Glucose unit of amylose.....	95
Scheme 4.2 The different structure of amylopectin and amylose.....	119
Scheme 5.1 H <sub>2</sub> O : LGO interaction .....	140
Scheme 5.2 the effect of conjugation.....	146
Scheme 5.3 the Reichardt's dye structure.....	147
Scheme 6.1 The production of MHC in two different methods .....	166
Scheme 6.2 LGO interaction with H <sub>2</sub> O and D <sub>2</sub> O .....	179
Scheme 6.3 The difference between conventional and MW heating on the equilibrium..	191
Scheme 6.4 Solvent effect on Reichardt's dye absorbency .....	195
Scheme 6.5 The difference between LGO and MHC in water .....	197
Scheme 6.6 The reaction of ketone in water forming geminal diol.....	197
Scheme 6.7 the ketone angel affects the equilibrium .....	199
Scheme 6.8 the interaction between LGO and water producing geminal diol then MHC	199
Scheme 6.9 the interaction between Cyrene and water producing geminal diol then Cyrene .....	200



## List of tables

Table 1.1 Infrared regions.....	39
Table 2.1 Materials used in this thesis.....	51
Table 2.2 GC set up for method 1.....	56
Table 2.3 GC set up for the first method 2 .....	56
Table 3.1 Biomass samples for MW hydrolysis.....	74
Table 3.2 Chemical assignments of CH stretching for LGO and Cyrene.....	85
Table 4.1 Shifting band position with temperature.....	110
Table 5.1 <sup>1</sup> H NMR spectroscopy assessment of LGO in CDCl <sub>3</sub> .....	153
Table 5.2 <sup>13</sup> C NMR spectroscopy assessment of LGO in CDCl <sub>3</sub> .....	154
Table 5.3 <sup>1</sup> H NMR spectroscopy assessment of triol in D <sub>2</sub> O .....	157
Table 5.4 <sup>13</sup> C NMR spectroscopy assessment of triol in D <sub>2</sub> O .....	158
Table 6.1 <sup>13</sup> C NMR spectroscopy assessment of MHC in CDCl <sub>3</sub> .....	170
Table 6.2 <sup>1</sup> H NMR spectroscopy assessment of MHC.....	171
Table 6.3 <sup>1</sup> H COSY NMR spectroscopy assessment of MHC. It shows protons coupling .....	172
Table 6.4 MHC production from the literature.....	172
Table 6.5 GC results of the new compound, LGO and Cyrene using the first method.....	175
Table 6.6 GC results of the new compound, LGO and Cyrene using the modified method .....	176
Table 6.7 MS fragments for MHC.....	178
Table 6.8 Samples of MHC .....	180
Table 6.9 the calculated integration for LGO in the new product MHC .....	184
Table 6.10 The integration of each peak for Figure 6.10 of MHC prepared from H <sub>2</sub> O ....	185
Table 6.11 The integration of each peak for figure (5.30) of MHC prepared from D <sub>2</sub> O ..	186
Table 6.12 Equilibrium constant for some compounds containing ketone when interacting with water forming geminal diol* .....	198



## **Acknowledgement**

Firstly, I would like to express my gratitude to Professor James Clark for accepting me as a PhD student in the first place, for supervising me for the previous four years, and for his excellent thoughts and suggestions which influenced my entire project to the best. In addition, Doctor Alice Fan and Doctor Vitaliy Budarin have significantly affected this study, supervising and guiding me for the better.

I am thankful to the technical team in the Green Chemistry Centre of Excellence laboratories for their support, assistance and detailed analytical equipment experience. Paul Elliott, Doctor Tabitha Peachy, Doctor Richard Gammon, Doctor Surajana Bose and Doctor Hannah Briers have spent their time and effort setting up devices and teaching me laboratory techniques.

I would also like to express my gratitude to Doctor Rob McElroy for his daily assistance during this project. Doctor James Sherwood for his assistance with NMR spectroscopy, COSMO modelling programme and for supplying the solvometry testing. I am also thankful for the rest of our group, who have supported me with their effort.

Additionally, I extend my thanks to Bruker for providing (Bruker Matrix-F) Near-infrared spectroscopy with IN236E Transmission fibre-optics probe and IN271X-2 a transflection fibre-optics probe for a trial.

I am also thankful to my sponsor, the Government of Saudi Arabia, for providing me with the chance to complete my PhD with full financial support and the assistance of the Saudi cultural bureau – London team, who have contributed to my work.

I owe much to my entire family. To my parents, Modhi and Saleh, I hope my study is a credit to them, to my beloved wife, Norah, who has supported me from all aspects and especially for being patient throughout my whole period of study and constantly pushing me to my best, and to our two beautiful children, Abdulaziz and Reema, have enriched our lives.

This project has received funding from the Bio-Based Industries Joint Undertaking (BBI-JU) under grant agreement No 887674. The JU receives support from the European Union's Horizon 2020 Research and Innovation Programme and the Bio-Based Industries Consortium.

Finally, many thanks to all of the students I have met at York during my studies. It has been enjoyable to learn, discuss, and chat with you.





## **Declaration**

I declare that this thesis is a presentation of original work and I am the sole author. This work has not previously been presented for an award at this, or any other, University. All sources are acknowledged as References.



# Chapter 1: Introduction to NIRS in biorefineries

## 1.1 Introduction

Sustainable (renewable) alternatives to fossil fuels are vital, especially after the consequences of environmental change caused by the industrial revolution.<sup>1</sup> Environmental changes include rising average temperature, melting ice and rising sea level, extreme weather and rising risks for human health and wildlife. Governments are becoming increasingly concerned with environmentally friendly practices and increasingly use legislation to progress this. Governments, organisations, and individuals are more committed to sustainability than ever before. This behaviour motivates industries to seek out and support better environmentally friendly systems.<sup>2-5</sup>

According to the most recent research on carbon dioxide emissions, figures and graphs demonstrate that efforts toward green chemistry and sustainability have improved significantly over the previous several years.<sup>2, 6, 7</sup> CO<sub>2</sub> emissions in the United Kingdom decreased by 2.7 percent in 2017 compared to the previous year and by 42.1 percent compared to 1990<sup>6</sup> although some of this reduction can be explained by out-sourcing of more polluting processes such as steel manufacture.

Chemists have substantial responsibility for developing more environmentally friendly chemicals and systems.<sup>3, 7-11</sup> There are several phases involved in the conversion of biomass to desired compounds. Although considerable work has been done in this area, more effort is needed to develop greener approaches that boost green effect, carbon efficiency, and waste reduction. As chemists, we may contribute to the creation of new industrial systems that will move the economy toward a circular economy rather than the linear economy that resulted from the industrial revolution.<sup>1, 3, 10, 12-14</sup>

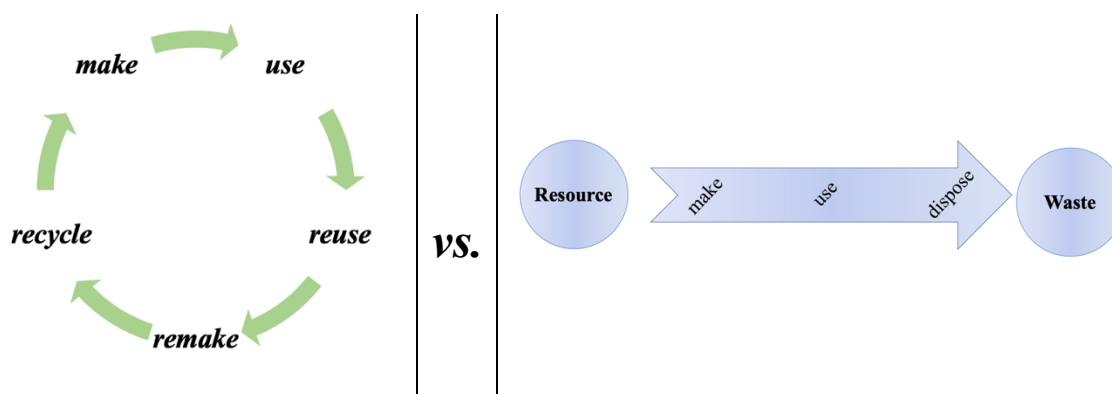


Figure 1.1 Circular vs. linear economy system

This thesis aims to establish a framework for improved biomass conversion process analysis. Conversion of bioresources includes utilising food supply chain wastes and other kinds of biomass to improve selectivity to the target product(s), carbon efficiency, and waste reduction. Real-time monitoring of the thermochemical conversion of bioresources to valuable compounds is investigated in this research. NIRS approaches will be developed, in particular to enable process control in applications such as low-temperature microwave (MW) biomass hydrolysis. This effort will enable biomass conversion to desired molecules in a more environmentally friendly manner, in less time, and at a lower cost.

With the growth of the population and industrial activities, annual oil consumption is a clear reflection of the severe energy requirements of many activities. By consuming fossil fuels in the same manner, our and future generations may face the calamity of oil becoming depleted or extinct. In addition, the main element that is used in life is carbon, and the leading resource, for now, is fossil fuels.<sup>1, 15, 16</sup> On the other hand, the emissions of CO<sub>2</sub> and other greenhouse gases associated with fossil fuels represent another big calamity. The recent UK emission of greenhouse gases, mainly caused by fossil fuel, was estimated to be 460.2 million tonnes of CO<sub>2</sub> equivalent (MtCO<sub>2</sub>e).<sup>6</sup> This increasing usage of crude oil has effects on geopolitics and the environment. Human activity has impacted the environment, mainly due to CO<sub>2</sub> emissions.<sup>2</sup> The public's attitude toward sustainability, plays a crucial role in influencing manufacturing production systems toward greener technologies.

Authorities should examine alternatives to fossil fuels derived from sustainable sources to keep duties and legislation under control. Not just for future global energy needs but also for chemical suppliers.<sup>17, 18</sup> Numerous compounds, including solvents, reagents, and other chemicals, are derived from crude oil. Governments should consider a realistic and robust strategy to increase this transition.

## 1.2 REACH

REACH (Registration, Evaluation, Authorisation and restriction of Chemicals) is a European Union regulation which came into force on the 1<sup>st</sup> June 2007. It seek to mitigate the risks of chemicals to human health and the environment by managing their risk and promoting the use of alternative methods.<sup>19</sup> There is no other option than to seek alternatives. There is some effort and collaboration in both industry and academic sectors to discover the quickest and most efficient path to greener solutions.

According to the linear economic model developed in the twentieth century, waste is growing and resources are depleting. This model was accelerated by the industrial revolution and expanded in synch with the expansion of the same economic model's industrial activity. This concept was based on "mine – process – consume – dispose" as Clark<sup>1</sup> described the "throwaway society" in his paper. In this kind of society, an object which was valuable one day becomes disposed of very quickly.<sup>1</sup> Eventually, these items will end up in a landfill (seas or rivers) which are not designed to be. This behaviour results in increased cost and scarcity of resources. With this attitude, it is essential for the transition from a linear to a circular economic model.<sup>1, 3, 14</sup> Attitudes of individuals and industrial product design governed by regulation (e.g. REACH) should result in a greener transformation.

### **1.3 Biomass and the biorefinery**

Biomass is one of the renewable energy sources that may be used as an alternative to fossil fuels. It is renewable and sustainable. It is used to generate heat and electricity and chemicals and liquid fuel.<sup>17, 20</sup> As carbon is the key element necessary in life and fossil fuels remain the primary source of carbon, scientists and researchers should place greater attention on biomass for carbon production while avoiding the use of resources that are edible. Accordingly, bio-waste is an optimal feedstock for carbon resources. This will contribute to developing a greener method of dealing with waste and obtaining renewable resources. As a result, research, industry, and government have shifted their focus to biomass waste resources.<sup>1, 21, 22</sup>

The conversion of bio-resources, including food supply chain wastes and other forms of biomass, is an increasingly well-studied area and represents an essential part of the growing move towards a circular bio-economy. It is critical that the associated conversion processes make biomass more efficient and easier to monitor. So, there are several papers on biomass conversion for use as biofuels and or producing chemicals. Budarin *et al.*<sup>17</sup>, for example, turned wheat straw into biofuel. Additionally, they have synthesised and manufactured compounds from bio-waste.<sup>23</sup> Clark *et al.*<sup>24</sup> at the Green Chemistry Centre of Excellence GCCE reported an unexpected opportunity to get LGO from unconverted saccharides in waste lignin, a new perspective in bio-refining.

As Jet A-1 aviation kerosene contributes 2% of anthropogenic CO<sub>2</sub> emissions, Chuck and Donnelly<sup>25</sup> alternatively examined nine potential biofuels produced by renewable resources.

They concluded that n-hexanol and n-butanol are great alternatives for aviation kerosene. And butyl butyrate shows a distillation profile more comparable to Jet A-1, which has a higher boiling point than the alcohols and is thus more volatile. On the other hand, Yeasts, especially *Saccharomyces cerevisiae*, were investigated and found that it plays a significant role in transport fuel development, helping in bioresources to fuel conversion.<sup>26</sup> Recently, integrated Subcritical Water Extraction (SWE) method was used in a biorefinery to produce useful chemicals and materials from coffee waste.<sup>27</sup>

Global attitudes toward how the public and organisations manage resources and waste are improving. Biomass has got attention as a global concern during the last decade. For instance, lignocellulosic biomass is gaining popularity in biomass refineries.<sup>22</sup> Huang *et al.*<sup>28</sup> from National Taiwan University discussed the sustainability of primary biomass resources such as agriculture and forestry waste, crops, and wood (lignocellulosic biomass) for the production of green materials and bioenergy.

Biomass is a significant part of a sustainable future energy system; it has been studied extensively worldwide and is a critical issue for this generation. Denmark<sup>29</sup>, USA, UK<sup>17, 23, 24</sup>, Taiwan<sup>28</sup> and many other countries have intensified their research attention on renewable energy and chemicals. Nowadays, scientists are experimenting with cutting-edge solutions for reducing CO<sub>2</sub> emissions. They make an effort to convert greenhouse gases into something valuable and reduce the emissions.<sup>30, 31</sup> One experiment was presented at the Goldschmidt conference in Boston,<sup>32</sup> where scientists discovered a faster technique to produce magnesite, which captures CO<sub>2</sub>. This project will contribute to reducing CO<sub>2</sub> from the atmosphere and the slowing of global warming.

### **1.3.1 Biomass conversion:**

There are two main processes used for biomass conversion, thermochemical and biochemical processes.<sup>17, 33</sup> They are used for biomass conversion into fuels and chemicals. Currently, the thermochemical process is more suitable for energy infrastructure. Medium temperature pyrolysis is used to produce mixtures of organic compounds from biomass. In fuel applications, pyrolysis is not a proper technique to convert biomass since it causes undesirable properties of the fuel use like high water content, high acidity and alkali metal content which makes it difficult to be exploited as a fuel.<sup>17, 34</sup>

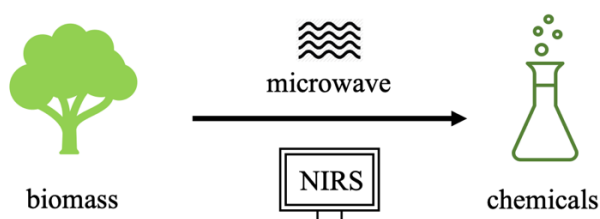
A recent investigation into the use of MW shows that using MW is a clean and efficient method of biomass conversion, especially in terms of carbon potential exploitation.<sup>17</sup> Miura *et al.*<sup>35</sup> have used MW successfully in producing levoglucosan (LGA) from wood pyrolysis with a yield of LGA was more significant than that obtained from conventional pyrolysis. As mentioned in their article, yields of 2.6, 6 and 12% LGA were obtained from larch log, used papers and filter papers, respectively, when applying MW pyrolysis. Budarin *et al.*<sup>17</sup> successfully produced LGA from wheat straw using MW pyrolysis at low temperature. The GC-MS results suggested that the amount of LGA were high in all cases of the produced oil with some additives. Based on peak area in GC, the results were in a mass balance (%) of LGA of 27.87, 20.64, 35.46 and 46.44, respectively, from wheat straw pellets without additives, with the additive of HCl, H<sub>2</sub>SO<sub>4</sub> and NH<sub>3</sub>. The latter additive increased the yield dramatically. In addition, a MW have been used in waste treatment.<sup>36</sup>

Most research in this field has been carried out at temperatures above 350 °C.<sup>17, 37</sup> Budarin *et al.*<sup>17</sup> obtained novel results by wheat straw pyrolysis at low temperatures. They produced bio-oil with desirable properties such as decreased acidity, sulphur content, and alkali metal concentration and energy efficiency. These properties make them suitable for fuel applications. They concluded that simple HCl adds could result in a minor increase in oil output compared with no additives resulting in 28% and 36%, respectively of LGA, whereas NH<sub>3</sub> additives result in a significantly greater amount of 46% LGA in the mixture.<sup>17</sup>

### 1.3.2 Microwave (MW)

Recent research has demonstrated that MW heating for biomass is suitable technique for producing molecules with a high degree of functionality.<sup>23</sup> Compared to traditional heating, MW can quickly activate a broad range of biomass. For example, both hemicellulose and cellulose decompose to char at substantially lower temperatures in the MW condition compared to traditional heating, giving the greatest calorific values achieved at temperatures much lower (150 and 100 °C, respectively) than when convection heating is utilised. Additionally, the hemicellulose char produced by microwave-assisted pyrolysis contains more hydrogen than char produced by traditional pyrolysis. It is a more environmentally friendly method of utilising energy. It has several benefits over conventional heating methods; it can efficiently produce compounds at substantially lower temperatures<sup>23</sup>, improved energy transfer (not heat transfer, therefore no-touch heating), increased heating

rate, material selectivity, increased safety level, and rapid and easy start-up and shutdown.<sup>28</sup> Additionally, MW can produce molecules with a high degree of functionality. By comparison, conventional heating creates mostly lower-value gases.<sup>23</sup> On the other hand, it is hard to separate the acidic aqueous fraction from the organic one when using conventional pyrolysis without additional steps. Pyrolysis using the MW, in contrast, can allow the separate of biomass products *in situ*.<sup>23</sup>



*Greener resource, greener heating method, greener analysis, and greener compounds*

*Figure 1.2 Converting biomass to chemicals in a greener way*

A beneficial chemical conversion process should maximise value while spending the fewest costs possible while producing such compounds from bioresources. However, there are other approaches to obtaining the appropriate chemicals from biomass. A depolymerisation method of lignocellulosic materials has been successfully achieved using hydrothermal MW depolymerisation at 220° C, producing significant quantities of sugars without additives such as acid/alkaline. It is a greener way of production as lower energy is needed, there is no enzymatic treatment and higher yield with less process units.<sup>38, 39</sup> MW have been used successfully to produce glucose from waste office paper. It was noticed that the MW technique produced more than 60 times more glucose than conventional approaches.<sup>40</sup>



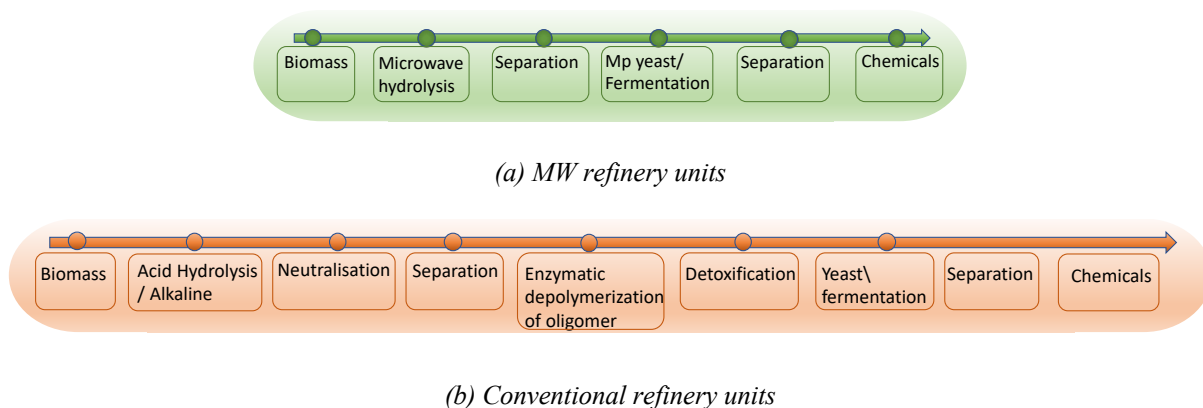


Figure 1.3 The difference between MW and conventional biorefinery

This figure was reproduced with permission from Fan et al.<sup>38</sup>

### 1.3.3 Water presence in biorefinery and biomass

Water is the most abundant liquid on the planet and acts as the main solvent.<sup>41, 42</sup> However, when water is used as a solvent, some hydrogen bonds between water molecules are disrupted. After that, the dipole-dipole (electrostatic) or ion-dipole interaction are established.<sup>41</sup> Several forces, such as dispersion forces, dipole-dipole forces, hydrogen bonding, and ion-dipole interactions, can impact the formation of solutions in solids and liquids.<sup>43, 44</sup> If the solvent-solute interaction is weaker than the solvent-solvent and solute-solute interactions, the solution cannot be formed.<sup>43</sup> However, when predicting solubility, it is always true that like dissolves like. Water, for example, tends to dissolve a broad range of polar and ionic solutes.

Water is an ubiquitous part of biomass feedstock and the biorefinery process.<sup>45-47</sup> For example, biomass has a low bulk density and a relatively high-water content (up to 90% for grass); it is significantly more expensive to transport in its raw condition than natural gas or petroleum.<sup>48</sup> Water-soluble carbohydrates cellulose and hemicellulose, pectin, and d-limonene are substantial components of wet orange peel. In some cases, water is a concern, such as in thermochemical conversion processes whereby much of the energy is spent in heating the water. Biomass may include a large amount of water, which must frequently be removed prior to thermochemical treatment. As a result, biomass is frequently crushed, dried, and ground prior to thermochemical processing. Without drying, biomass is transformed directly into products via liquefaction operations (a thermochemical conversion

process in which liquid fuels are created from biomass). This is essential since drying is an energy-intensive process. The yields and composition of the produced bio-oil and char vary depending on whether the process is catalytic or direct liquefaction. Generally, there is no requirement to dry the biomass before liquefaction; however, pyrolysis frequently needs a pre-drying process.<sup>48</sup>

Biorefineries convert biomass into various products such as energy, chemicals, and materials<sup>48</sup>. Biomass is often split into a fibre-rich press cake and a nutrient-rich green juice due to its high-water content. Green juice includes a variety of beneficial compounds, including amino acids, organic acids, and dyes. The press cake can be used as a feed or for energy production, insulating materials, building panels, and biocomposites, among other things.<sup>48</sup>

Water present in biomass conversion is critical for LGO production since it affects the quantity of LGO produced from LGA conversion. Huang *et al.*<sup>49</sup> investigated the conversion of LGA to LGO in various concentrations of water and Dimethyl sulfoxide DMSO. Accordingly, while the addition of water had a minimal effect on glucose production, it increased the yield of LGO through the use of in-situ water removal. The authors found that the lack of water reduced glucose and 5-Hydroxymethyl-furfural (HMF) synthesis by preventing LGA hydrolysis and HMF isomerisation.<sup>49</sup> The direction of the chemical reaction is determined by controlling the water concentration in this type of production.

To allow a sound analytical approach for a biorefinery control, it is essential to study the conversion of these chemicals in an aqueous solution. Therefore, most of our work was in water solutions. On the other hand, water has a massive absorbency in NIR spectroscopy reflected by very intense bands of OH vibration compared with the other vibrations such as CH although it is not as relatively strong as in the mid- or normal IR due to hydrogen bond enhancement of the bands. This high vibration absorbency affects and overlaps with the other desired chemicals' absorbency causing difficulties in interpreting the desired solution's spectrum. One solution for this issue is chemometric analysis to detect any change in the NIRS bands.

## 1.4 IR spectroscopy

### 1.4.1 (background)

The principle of IR spectroscopy underlies the interaction between electromagnetic radiation and matter (molecule or atoms).<sup>41, 43, 50-53</sup> When IR incident radiation is subjected to a sample, absorption occurs in molecular bonds. Depending on the amount of energy (specific wavenumber) absorbed by the molecule, it is easy to decide which molecule is responsible for this reaction. Molecules are different in chemical bonding and have other functional groups. Each bond has a different energy to join two atoms together depending on which atom is joined. (Hydrogen-carbon) bond is stronger than (carbon-oxygen) bond. Therefore, the C-H stretching absorption band occurs at a higher wavenumber than C-O. Depending on this energy, molecules are different in energy absorption. This absorption happens as a vibrational motion (IR, sometimes referred to as vibrational spectroscopy). Bonds vibrate when absorbing discrete frequencies corresponding to the well-known amount of energy (specific wavenumber). Based on this principle, it is possible to calculate the energy absorbed and decide which bond or functional group is present in the sample.<sup>41, 43, 50-53</sup>

A simple way to describe a molecule's vibration is to illustrate the most fundamental characteristic of a diatomic molecule. The vibration in a single bond between two atoms occurs by absorbing IR radiation is stretching/compression. It is called the oscillation of the bond.<sup>41</sup> The molecule is never static; it is constantly vibrating. At 0 K, H<sub>2</sub> still vibrates and produces energy called *zero-point energy*. This energy corresponds to *the vibrational ground state*. By subjecting the molecule to energy (IR), a transition to a *higher vibrational level* may occur. The strength of molecule vibration increases when rising the vibrational level (increasing energy) until it reaches a point where dissociation of the molecule may occur.<sup>41</sup> To simplify this activity, it is always imagined as two balls (atoms) connected by a spring (bond). As shown in figure (2), when the bond absorbs energy, it stretches and contracts in an equilibrium position corresponding to the bond length ( $r_0$ ).<sup>50</sup>

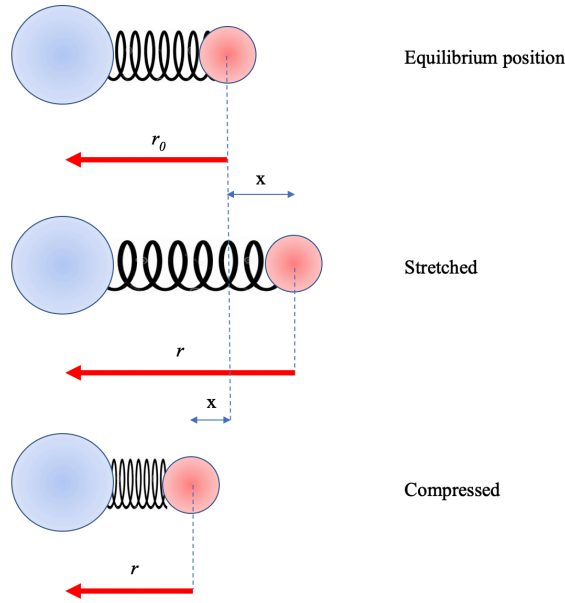


Figure 1.4 Vibration of a diatomic molecule

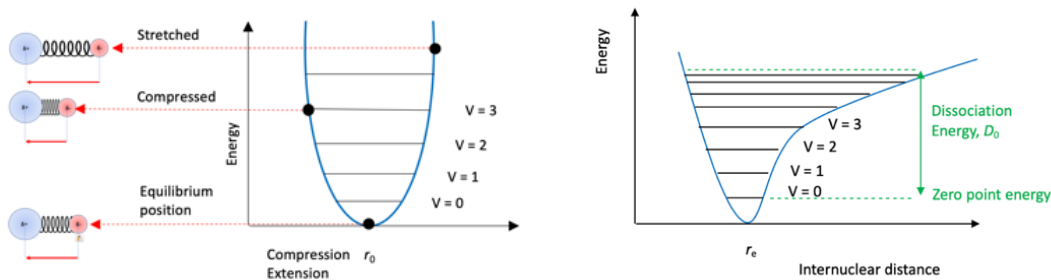
Two factors influence the frequency of vibration of the bond. First is the masses of atoms. The greater the masses of the atoms, the slower vibration of the spring (the chemical bond) and vice versa. The second factor is the hardness of the spring. The stiffer spring is less easy to deform and vibrate more quickly. However, restoring force can control the spring when it is displaced from the equilibrium position. When the spring is stretched or compressed, the restoring force pulls or pushes the spring back to the equilibrium position respectively.<sup>50</sup>

### 1.4.2 The simple harmonic oscillator

When this vibration force happens, another force is applied to counter this vibration and bring this spring back to the previous state (ground state). It is called restoring force,<sup>50</sup> which depends on the oscillation magnitude and the spring property, called *force constant*,  $k$  (see equation 1.1).

Restoring force = - ( $k$  x displacement of particle (m) in equilibrium position) equation 1.1

The energy curve is shown in Figure 1.5 (A) describes the motion of a simple harmonic oscillator. When the spring is in the equilibrium position (length)  $r_0$ , the kinetic energy is at its maximum. In contrast, at the extremes of the vibration (fully stretched or fully compressed), the kinetic energy is zero. So, the potential energy is controlled by the extension  $x$ .<sup>50</sup> equation 1.2 is the vibrational energy levels for harmonic oscillation.



(A) the vibrational energy levels for harmonic oscillation

(B) the vibrational energy levels for anharmonic oscillation

Figure 1.5 The vibrational energy levels

$$E_v = \left(v + \frac{1}{2}\right) h\nu \quad (E_v \text{ in J}) \quad \text{equation 1.2}$$

Where  $v$  is the vibrational quantum number

$h$  Plank constant

$\nu$  Frequency of vibration

To apply  $E = 0,1,2,3\dots$  in equation 1.2, it gives values of

$$E_v = \left(\frac{1}{2}\right) h\nu, \left(\frac{3}{2}\right) h\nu, \left(\frac{5}{2}\right) h\nu, \left(\frac{7}{2}\right) h\nu \dots$$

The spaces between  $v$  levels are equal, as shown in Figure 1.5 (A). When the diatomic molecule undergoes a simple harmonic oscillator, it never dissociates. In reality, it is not valid. A diatomic molecule will disassociate when enough energy is applied. So, an anharmonic oscillator must be studied.<sup>50</sup>

### 1.4.3 The anharmonic oscillator

The diatomic molecule as seen in Figure 1.5 (B) is undergoing an anharmonic oscillation. An anharmonic oscillator curve is asymmetric, and the spaces between energy levels are not equal as in a harmonic oscillation curve.<sup>50</sup> It can be calculated by equation 1.3.

$$E_v = \left(v + \frac{1}{2}\right) h\nu - \left(v + \frac{1}{2}\right)^2 h\nu x_e \quad (E_v \text{ in J}) \quad \text{equation 1.3}$$

Where

- $v$  is the vibrational quantum number
- $h$  Plank constant
- $\nu$  Frequency of vibration
- $x_e$  Anharmonicity constant

By substituting  $E = 0, 1, 2, 3, \dots$  in equation 1.3, various spaces between levels are obtained. As the  $E$  level increases, the gaps decrease, bringing them closer together until they converge. According to Figure 1.5,  $v = 0$  is the molecule's zero-point energy. The molecule's dissociation energy is the difference between its zero-point and convergence energy levels.<sup>41, 50</sup>

The value of the force constant ( $k$ ) and the two masses ( $m_1$  and  $m_2$ ) of the molecule play a significant role in controlling the frequency of the vibration of a diatomic molecule. The stronger of the bond, the larger the ( $k$ ) value. The smaller mass will move more easily than the larger one during the spring's oscillation. The *reduced mass*,  $\mu$ , is the quantity of the

mass when it reflects the relative masses of the nuclei.<sup>41</sup> Equation 1.4 is applied to obtain the reduced mass for two nuclei of masses  $m_1$  and  $m_2$

$$\frac{1}{\mu} = \frac{1}{m_1} + \frac{1}{m_2} \quad \text{or} \quad \mu = \frac{m_1 m_2}{m_1 + m_2} \quad \text{equation 1.4}$$

**Fundamental absorption**, which is described as a vibrational transition from the ground state to the first excited state, can be calculated by equation 1.5.

$$\nu = \frac{1}{2\pi} \sqrt{\frac{k}{\mu}} \quad \text{equation 1.5}$$

Equation 1.5 is used to calculate the vibrational frequency in (Hz), while the IR spectroscopy usually is expressed in wavenumber ( $\nu'$ ). By applying the equation 1.6

$$\nu' = \frac{\nu}{c} \quad \text{equation 1.6}$$

Where  $\nu'$ : wavenumber,  $\nu$ : frequency and  $c$ : speed of light

The frequency is converted to wavenumber as illustrated in equation 1.7.

$$\nu' = \frac{1}{2\pi \times c} \sqrt{\frac{k}{\mu}} \quad \text{equation 1.7}$$

Where  $c$ : is speed of light

Knowing the IR molecule absorption wavenumber makes it easy to calculate the force constant or reduced mass and know which molecule is responsible for this absorption. There are, however, two selection rules to consider<sup>52, 53</sup>; first is that the transition is limited as  $\Delta v = \pm 1$  where the transition may occur. The second selection rule is that the molecule should be *infrared active*. That means the molecule must give rise to change in its dipole moment. During the vibration, the molecule must change in the dipole moment to give rise to a band in the spectrum. All homonuclear diatomic molecule does not gain a dipole moment. For example: (O<sub>2</sub>, Br<sub>2</sub>, N<sub>2</sub> and H<sub>2</sub>) are all IR inactive.

The most important transitions in IR spectroscopy are:<sup>51</sup>

$$v = 0 \rightarrow v = 1 \quad \Delta = + 1 \quad \Delta E = hv (1 - 2x)$$

$$v = 0 \rightarrow v = 2 \quad \Delta = + 2 \quad \Delta E = 2hv (1 - 3x)$$

$$v = 0 \rightarrow v = 3 \quad \Delta = + 3 \quad \Delta E = 3hv (1 - 4x)$$

Therefore, the line near  $v$  is called fundamental absorption, known in the mid-infrared region.<sup>51</sup> The lines near  $2v$  and  $3v$  appear in the NIR region and are called first and second overtones, respectively. Combined bands can occur when two or more different vibrations interact to raise a band with frequencies that are their fundamental sums. It is most likely no more than two vibrations involving bonds of common atoms or multiple bonds.<sup>51</sup>

#### 1.4.4 Absorption and emission spectra

The spectrum can be displayed in two different ways. The *Absorption spectrum* displays the amount of absorbed radiation against the energy (wavenumber  $\text{cm}^{-1}$ ). Alternatively, the *transmission spectrum*, measures the proportion of energy transmitted through the sample.<sup>50</sup>



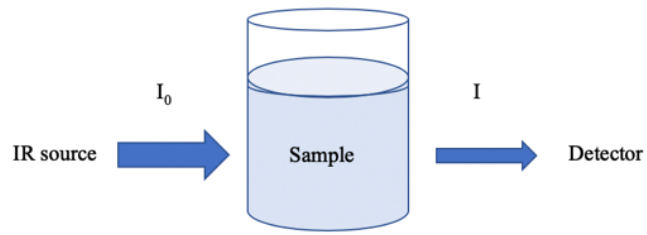


Figure 1.6 IR Radiation absorbed by a sample

$$T = \frac{I}{I_0} \quad \text{equation 1.8}$$

$$A = -\log T \quad \text{equation 1.9}$$

$$A = \varepsilon c l \quad \text{equation 1.10}$$

Where	$T$	Is the transmittance
	$I$	Transmitted radiation reduced in intensity due to absorption
	$I_0$	Incident radiation
	$A$	Absorbance
	$\varepsilon$	Molar absorption coefficient
	$c$	Concentration
	$l$	Path length

## 1.5 Near-Infrared Spectroscopy (NIRS)

### 1.5.1 History of NIRS

The importance of NIRS became apparent after the Second World War and after sensitive detector availability in 1954 when the first commercial NIR spectrophotometer was produced. Since then, NIR experiments have become extensively studied.<sup>51</sup> According to Pasquini<sup>54</sup>, who has published a review on NIRS, the decade of the 1980s was characterised by the technique's "boom." Between 1930 and 1980, the use of NIRS was very rare, while the following decade witnessed a number exceeding 1000 papers with more appropriate names were published, such as "Near-Infrared Spectroscopy – The Giant is Running Strong"<sup>55</sup> published in 1994 and "The history of near-infrared spectroscopy analysis: Past, Present, and Future – From sleeping method to the morning star of spectroscopy"<sup>56</sup> published in 1989. Regardless of the Covid-19 crisis, the total number of publications on the NIR method is undoubtedly larger than 300,000 publications in 2016, reflecting its widespread popularity and indicating that it is a good subject for development. This activity level resulted in the establishment of the Journal of Near Infrared Spectroscopy in 1993, the first periodical devoted explicitly to this area. Karl Norris emerges as the most famous name in the history of NIR spectroscopy.<sup>54</sup> He began his work with NIRS by investigating novel ways of detecting the moisture content of agricultural products, initially by extracting the water in methanol and then by suspending ground seeds in CCl<sub>4</sub>. The initial results using this technique were published in 1965 and were reissued in 1996 as part of a special edition of the Journal of Near Infrared Spectroscopy dedicated to Karl Norris.<sup>54</sup>

### 1.5.2 The Importance of NIRS

NIRS is a unique method for a region where the combination and different order-overtone bands occur. This range is from MIR to Visible parts of the spectrum. The intensity, therefore, varies between the two ends of the spectrum.<sup>57</sup> The NIR spectrum intensity decreases dramatically in the direction from MIR to the visible region. The variable path length cell, in contrast, covers this kind of issue. The observed spectrum is enhanced by increasing the path length cell from 0.4 mm in the combination area (4000–5000 cm<sup>-1</sup>) to 10 mm for the higher-order overtone near the visible region (above 9000 cm<sup>-1</sup>). This unique property of NIRS enables it to analyse a sample in more detail.<sup>57</sup>

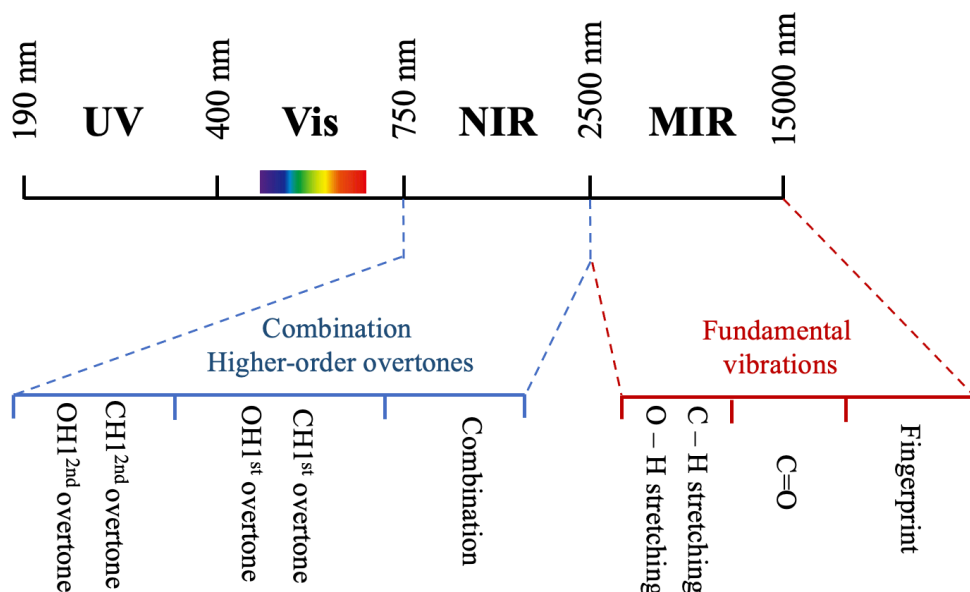


Figure 1.7 MIR and NIR spectroscopy regions

NIRS is used mainly for C-H, O-H and N-H functionalities, while Raman spectroscopy is used for homonuclear functionalities (S-S, C-C, C=C) and MIR for more polar groups such as (C=O, C-O-C, C-F). This phenomenon can be explained as NIRS needs a large anharmonicity of vibration in addition to the dipole moment change.<sup>57</sup> Combination and overtones vibration bands of OH and CH cover the whole NIRS range, whereas other functionalities which are characteristics in MIR do not appear. The main reason is that most of the fundamental bands of MIR functionalities appear under  $2000\text{ cm}^{-1}$ , which makes it harder to appear in the NIRS region for their higher-order overtones. For example, the 1<sup>st</sup> overtone bands of (C=O, C-O-C, C-F) groups can be studied and utilized in the MIR region. The intensity decreases from fundamental to overtone band by 10-100 from one step to the next. This means that by the time the overtone band of these functional groups reaches the NIRS region, the intensity of the vibrational band becomes negligible. That makes it rare for some functional groups to appear in the NIRS region.

### NIRS is a Greener Analytical Method:

The use of solvents and other toxic chemicals became a critical issue in green chemistry. Therefore, both industrial and governmental organisations look forward to using greener methods in analytical chemistry. Choosing NIR spectroscopy for monitoring MW hydrolysis among other traditional chemical methods is that NIR is a simple, nondestructive and rapid

method. Using NIRS can lower labour costs as no sample preparation, no reagents, no solvents needed subsequently no waste. So, there is no need for a higher education level as a PhD or MSc to deal with daily use. Physical and chemical properties can be measured using the same instrument. From a safety perspective, NIRS reduces/eliminates the handling of dangerous materials. It has been successfully used in analysing a wide range of applications for food as real-time analysis coupled with a fibre-optic probe.<sup>58</sup> This ability allows NIRS to send signals from the reactor to the detector for tracking in real-time.<sup>19, 59</sup> Thus, using NIR spectroscopy as an analytical method for monitoring biomass hydrolysis in a MW is a greener method. It is a green method because it allows greater chemical products, reduces the cost of both labours and chemicals (reagents and solvents) used, and no destructive or waste is produced.<sup>59</sup>

Wolfrum and Sluiter<sup>60</sup> have mentioned that NIRS is a suitable method when adequately used for biomass compositional analysis. They have recommended improving the calibration set by expanding the number of samples for future jobs. It can be used for a wide range of materials including food.<sup>58, 59</sup> Yano *et al.*<sup>61</sup> carried another experiment in Hiroshima, Japan, utilising NIRS to determine glucose and citric acid concentrations. They said that NIRS can offer precise and simultaneous readings of the two compounds in an aqueous solution. Currently, this method is carried out using HPLC, which takes a long time (about 20 minutes) for each sample and requires a certified individual due to its complexity. In comparison, NIRS takes seconds and so may be employed in real-time. They stated that it might be feasible to utilise NIRS online to determine the glucose and citric acid concentrations in the blood anticoagulant in future studies.<sup>61</sup>

Maleki *et al.*<sup>62</sup> investigated the soil using NIRS online. They have demonstrated that this methodology is a valid technique for measuring soil. They indicate that NIRS may be used to test multiple materials online, in addition to soil. In some instances, GC-MS is utilised to determine the oil content of wheat straw that has been microwaved at a low temperature. While GC-MS is accurate, it requires time for sample preparation and analysis by professionals, which requires time and the use of solvents.<sup>17</sup>

FT-NIR has been developed to be used as a rapid analysis method for analysing the chemical composition of biomass feedstock under renewable energy. They have used a broad-based model hypothesis to study a wide range of feedstock. The concentrations of some compounds have been checked in corn stover and switchgrass. The result of this method is promising for future biomass prediction, and also it is potential for wheat straw.<sup>63</sup>

Dispersive NIRS has been studied for biomass feedstock. It showed visibility of the NIRS method for chemical composition analysis, but it can only scan one single frequency at a time.<sup>63</sup> FT-NIR, in comparison, has many advantages over dispersive NIRS. It can provide all frequencies simultaneously at the same time as well as perform a more accurate spectrum by averaging more scans. FT-IR can provide higher resolution basically because there is no degradation for the optical throughput without using a signal-to-noise ratio.<sup>63</sup> FT-NIR has the capability of wavelength calibration by using the laser's constant wavelength, which allows for better repeatability.<sup>63</sup> There are studies on switchgrass as feedstock in the biofuel industry and the use of NIRS for investigation. However, there is a lack of studying NIR spectroscopy to investigate some feedstock species.<sup>63</sup> Some studies have been done on analysing biomass feedstock including animal feeds, legumes, wood, pulpwood, eucalyptus and Norway spruce. Most of this work has been done on individual species rather than on mixtures.<sup>63</sup>

Sanderson *et al.*<sup>64</sup> have previously investigated the chemical composition of biomass feedstocks using a diverse variety of feedstocks (woody and herbaceous species). Although this study demonstrated the feasibility of employing NIRS, the researchers recommended calibrating restricted populations, one woody, one herbaceous, or even one single species at a time, to increase accuracy. Santana *et al.*<sup>65</sup> used NIRS to identify soil organic matter in Brazil. The task was completed utilising Vis-NIR spectroscopy and Principle Component Analysis (PCA) for data processing.

Generally, analytical techniques such as NMR spectroscopy, MS, and chromatography are employed behind the closed doors of laboratories. They are handled by or under the guidance of more educated technicians. These devices are not extensively utilised to monitor chemical production on a routine basis. The manufacturing environment is built on rapid and straightforward processes that can be performed 24 hours a day and do not require a PhD level of knowledge, such as pH, moisture content, melting point, and viscosity. Chemical analysis procedures that are more instructive, such as IR, GC, and HPLC, have become relatively regular in recent years. Following manufacturing, a sample will be taken and analysed at an offline chemical laboratory while the batch is on hold. This process will take an hour or more until a decision is made. Second, the operator is often exposed to the contents of the reactor, which may include dangerous elements.<sup>19</sup>

On the other hand, the online or in-line monitoring approach is critical for overall efficiency improvement. It conserves time and energy, which results in reduced waste. Fibre-optics are

capable of transmitting signals from the reactor to the detector for monitoring the process.<sup>19</sup> Thus, employing NIR spectroscopy as an analytical tool for measuring MW hydrolysis for biomass is a significantly more environmentally friendly technology. Another advantage of in- or online monitoring, when combined with an in-process control approach, is that it enables automated corrections, such as temperature control or reagent addition.<sup>19</sup>

NIR spectroscopy may be used to determine a variety of parameters.<sup>57</sup> Particle size<sup>66, 67</sup> may be determined using DRIFT sampling technique or a fibre-optics reflectance probe for more mobility and instant testing. The latter probe was extensively utilised for portable and rapid tests on various sample types. Arthit *et al.*<sup>68</sup> examined the cane sugars in growing cane stalks using a portable Visible / Near-Infrared (Vis/NIR) spectroscopy device. The same group used a portable Vis/NIR device to conduct a similar experiment to detect the sugarcane stalks directly, with fibre content.<sup>69</sup> Arshadi *et al.*<sup>70</sup> applied portable Vis-NIR spectroscopy to assess the moisture and acid content of sawdust biomass. Biomass drying to 40, 8 and 2% moisture content prior to gasification increases the efficiency of the produced biomethane to 55.2% LHV<sub>50%</sub>, 70.3% LHV<sub>50%</sub> and 72.2% LHV<sub>50%</sub>, respectively.<sup>71</sup>

NIR spectroscopy has garnered attention for the last two decades, particularly when combined with a fibre-optics probe for real-time detection. Figure 1.8 demonstrates how extensively the NIRS has been referenced in the literature. Since around 1995, there has been a remarkable growth in the use of NIRS. Additionally, it has been employed for highly delicate and significant works. Recently, the National Aeronautics and Space Administration (NASA) has been developing a UV/NIR spectrometer probe for upper atmospheric chemical monitoring and another probe for mass spectrometer and laser spectrometer techniques.<sup>72</sup> This probe will be attached to one of two potential missions to research the Venusian atmosphere. DAVINCI+ (Deep Atmosphere of Venus Investigation of Noble Gases, Chemistry, and Imaging, Plus) is the name of this expedition.<sup>72</sup> This highlights the significance of NIRS as a successful instrument applicable to various scientific applications.

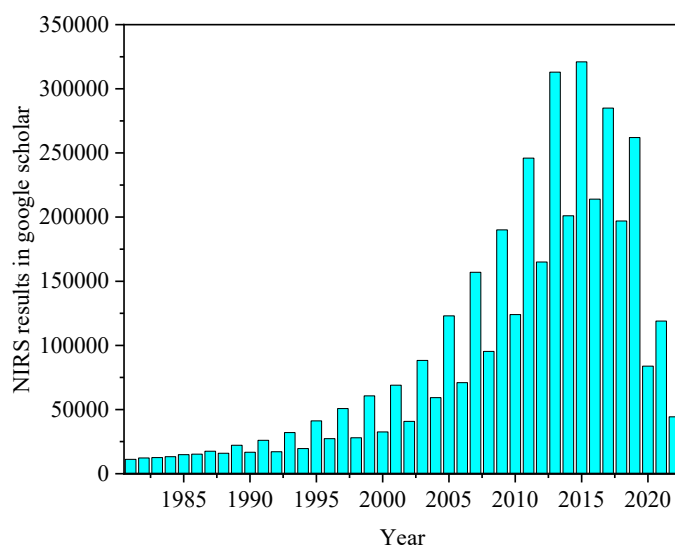


Figure 1.8 The use of (NIRS) in the literature

Table 1.1 Infrared regions

<b>Region</b>	<b>Action</b>	<b>Wavenumber range (<math>cm^{-1}</math>)</b>	<b>Wavelength range (<math>nm</math>)</b>
<b>Middle infrared (IR or MIR)</b>	Fundamental vibrations	4,000 – 200	2,500 – $5 \times 10^4$
<b>Near infrared (NIR)</b>	Overtones/ combinations	14,300 – 4,000	700 – 2,500
<b>Far infrared</b>	Rotations	200 – 10	$5 \times 10^4$ – $10^6$

\* This table was inspired by Introduction to Organic Chemistry textbook<sup>51</sup>

### 1.5.3 Vibration bands in NIRS

If the sample (molecule) is exposed to electromagnetic wave radiation, a transition from a ground state to the first excited state (fundamental) may occur. This absorption can be measured characteristically accordingly to what the sample includes. A characteristic measurement can be identical to the amount of energy consumed. According to the energy

needed, chemical bonding can absorb the energy at different wavenumber. However, differences in energy absorbed allow bands to appear in different positions (as a fingerprint) in the spectrum.<sup>19, 50</sup>

However, the mid-infrared region MIR is located at (400 – 4000  $\text{cm}^{-1}$ ), where the fundamental transitions occurs, and the NIR (4000 – 12820  $\text{cm}^{-1}$ ) region. NIRS includes overtones and combination bands where the second or third...etc. excited state may occur, and two or more overtones transitions may co-occur.<sup>19</sup>

Absorptions in the NIRS region correspond to overtones and combinations of fundamental vibrations. Although structural studies of NIRS are limited, it is used successfully for quantitative analysis. There are, however, some reasons behind that. Availability of sensitive solid-state detectors, high energy throughput, low stray radiation result and an emission maximum of the source is close to the region of interest are all advantages of using NIRS.<sup>51</sup>

### 1.5.3.1 NIR spectra of Carbon-hydrogen overtone bands

The C-H bond is the fundamental bond in organic compounds. Its fundamental stretching occurs between 2972 – 2843  $\text{cm}^{-1}$ , 3010 – 3095  $\text{cm}^{-1}$  and 3310 – 3320  $\text{cm}^{-1}$ , respectively, for alkanes, alkenes, aromatic, and alkynes systems. Osborne and Fearn's<sup>51</sup> includes several spectra of different compounds as shown in their book. When the following formula is used, the NIRS absorption position of the 1<sup>st</sup> overtone band is expected to be:

$$2\nu \text{ cm}^{-1} \quad \text{or} \quad 10^7/2\nu \text{ nm} = 1700 \text{ nm} \quad \text{equation 1.11}$$

More accurately,

$$\nu = n \nu_0 (1 - nx) \quad \text{equation 1.12}$$



Where  $\nu$  wavenumber of the overtone band (or  $1/\nu$  is the wavelength).  $x$  is the anharmonicity constant and  $n$  is an integer (same value as  $\Delta\nu$ ) (i.e. 2 for the 1<sup>st</sup> overtone). Using equation 1.12, Osborne and Fearn<sup>51</sup> have made a table of constructed predicted wavelength. However, the 1<sup>st</sup> overtone band for C-H vibration usually appears in as few bands between  $5917\text{ cm}^{-1} - 5650\text{ cm}^{-1}$ . The 2<sup>nd</sup> overtone band, which is weaker than the 1<sup>st</sup> overtone, is expected to be around ( $1150\text{ nm} = 8696\text{ cm}^{-1}$ ) with maximum differences between species  $460\text{ cm}^{-1}$  wavenumber. The 3<sup>rd</sup> overtone is extremely weak absorption in the region ( $880\text{ nm} = 11364\text{ cm}^{-1}$ ).

### 1.5.3.2 NIR spectra of Oxygen-hydrogen overtone bands

1<sup>st</sup>, 2<sup>nd</sup>, and 3<sup>rd</sup> O-H stretch overtone bands occur at  $6896$ ,  $10309$  and  $13158\text{ cm}^{-1}$  respectively.<sup>51, 73</sup> An important thing that should be considered is that the position of O-H bands is affected by temperature and the hydrogen bonding environment. For example, the position of O-H 1<sup>st</sup> overtone of water bound to protein is not the same as that in alcohol and phenol.<sup>51</sup> The effect of hydrogen bonding is different depending on the O-H bond type and in which the sample is contained. The free O-H group in carbohydrates is different from intra or intermolecularly hydrogen bond group.<sup>51</sup> Band position, to some extent, is a key to distinguishing between the different types of hydrogen bonding and free OH.

### 1.5.3.3 NIR spectra of carbon-hydrogen combination bands

The most crucial combination with the CH group is stretching and different deformation modes. They usually occur in the range between ( $4000\text{-}5000\text{ cm}^{-1}$ ). Some weaker bands appear in the two regions ( $6897\text{-}7692\text{ cm}^{-1}$ ) and ( $9091\text{-}10000\text{ cm}^{-1}$ ). Some chemical compounds have been investigated using NIRS, such as wheat gluten, wheat starch, wheat lipid, polyethylene, nylon, etc. Each has different bands in different positions with no significant difference.<sup>51</sup> However, the maximum differences in band positions in wavenumber are about  $100\text{ cm}^{-1}$ , more or less of each band. These bands arise from =CH or CH<sub>2</sub> and C=C vibration. For instance, the two fundamental absorptions (in MIR) of CH stretch and C=C stretch at  $3020\text{ cm}^{-1}$  and  $1660\text{ cm}^{-1}$ , respectively, will give a combination band (in NIRS) at  $4679\text{ cm}^{-1}$ .<sup>51</sup>

### 1.5.3.4 NIR spectra of Oxygen-hydrogen combination bands

O-H combination band has been studied with different results depending on the water-bound in the sample and the hydroxyl compounds present. For example, liquid water and water bound to a protein have bands at  $5155\text{ cm}^{-1}$  and  $5141\text{ cm}^{-1}$ , respectively. It is a combination band of fundamental O-H stretch at  $3500\text{ cm}^{-1}$  and O-H deformation at  $1645\text{ cm}^{-1}$ . A combination of the fundamental O-H stretch at  $3500\text{ cm}^{-1}$  and O-H deformation at  $1300\text{ cm}^{-1}$  may occur for all hydroxyl compounds. In addition, the overtone bands may affect how the combination bands to be shifted with hydrogen bonding. Moreover, the combination bands may also occur between O-H stretching and C-O or C-C stretching.<sup>51</sup> At  $2150\text{ cm}^{-1}$ , there is a relatively small broad band of a combination of  $\nu_2$  binding and liberation band.<sup>74, 75</sup>

## 1.6 Hydrogen bonding

A hydrogen bond is an electrostatic attraction between an atom that is covalently bonded to another atom and a hydrogen atom due to the partial positive charge on the hydrogen atom.<sup>76</sup> In this scenario, the hydrogen bond is a weaker intermolecular link than the covalent bond. This section presents both IR and NMR spectroscopy analyses of hydrogen bonding.

### 1.6.1 Hydrogen bonding in IR

The water 1<sup>st</sup> overtone band in the NIRS is centred at  $\sim 6897\text{ cm}^{-1}$ . This band is broad and represents several hydrogen-bonded (H-bonded) species.<sup>57</sup> Different hydrogen bonding species, intra and intermolecular, cause a shift in the band position influenced by force constants of (X-H) bonds. Additionally, the O-H band can dramatically change the band position and intensity by changing temperature, as discussed in detail in this chapter. The water band contains multiple overlapped bands. Each band changes its position and intensity depending on the sample type causing a difference in the broad band position.<sup>57</sup> However, hydrogen bonding is responsible for the most significant change in the NIRS region. When applying temperature change, heating and cooling, the combination band at  $5181\text{ cm}^{-1}$  shifts in position for moisture samples. This is caused by reforming hydrogen bonding in the sample, either forming or/and breaking.<sup>57</sup> The shift of the OH band to a lower wavenumber is due to inter- or intramolecular hydrogen bonding formation and, in some cases broadening of the band. Increasing the non-hydrogen bonding of a sample, on the other hand, causes

narrowing and shifting of the band to a higher wavenumber.<sup>57</sup> The maximum shift due to this phenomenon is  $120\text{ cm}^{-1}$ . That means that NIRS is very sensitive to even slight differences in ionic changes; temperature or stereochemistry can cause massive differences in the spectrum reading of a sample. Consequently, these conditions should be carefully considered, and extra care must be applied when using the NIR spectroscopy.

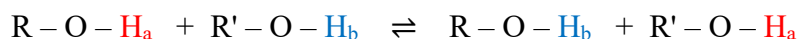
### 1.6.2 Hydrogen bonding in NMR spectroscopy:

O-H and N-H give relatively broad peaks in  $^1\text{H}$  NMR spectroscopy. This is caused by the fact that they undergo a relatively long exchange process compared with the NMR spectroscopic timescale.<sup>41</sup> Temperature, concentration and solvent affect the hydrogen bonding by changing the shift value<sup>52</sup>. Temperature, for example, has a considerable influence on the hydrogen bonded proton. Increasing temperature causes the breaking down of hydrogen bonds, and lowers the band position to a lower frequency.

Concentration also influences the NIRS shift value for hydrogen bonding. A phenol solution in  $\text{CCl}_4$  is an excellent example of this phenomenon. At a low phenol concentration, the hydroxyl group will be surrounded by  $\text{CCl}_4$ , not allowing any intermolecular hydrogen bonding to occur. By increasing the phenol concentration, the hydrogen atom will undergo hydrogen bonding with the oxygen atom on the hydroxyl group of the other phenol molecule.<sup>52, 77</sup> The solvent also plays a significant role in NMR spectroscopy, especially hydrogen bonding effects. NMR spectroscopy signals shift due to the formation/breaking down of the hydrogen bonding when the sample is diluted. Ethanol, for example, has a signal at  $\delta+5.4$  assigned for (OH), but it is lower when ethanol is diluted due to a reduction in hydrogen bonding which causes a change in electron density.<sup>41</sup> Another example of concentration dependency of the NMR spectroscopy shift is a carboxylic acid. In solution, the carboxylic acid is associated by hydrogen bonding (dimers), appearing in the 11 – 14 ppm region. However, when it is diluted, the value will shift to a much lower frequency.<sup>77</sup>

So, changing temperature, sample purity and/or solvent can play a significant role in NMR spectroscopy. This change leads to changing the rate of exchange of the proton on a compound (i.e. alcohol) and the other proton in another molecule or with a proton of the solvent.<sup>78</sup> Therefore, the peak shape and the value shift will change accordingly. As previously mentioned, the timescale of the NMR spectroscopy sometimes goes slower than

these kinds of exchanges can happen. So, the result is to find a relatively broad peak with less information.



Lowering temperature can lower the rate of exchange. Therefore, the NMR spectroscopy has more chance to catch this change within its timescale.<sup>78</sup> The result will be a better spectrum. At room temperature, NMR spectroscopy needs  $10^{-2}$  to  $10^{-3}$  seconds to measure a sample (scan and record), while intermolecular proton exchange occurs at  $10^5$  proton per second<sup>78</sup>. That means  $10^{-5}$  seconds is the average residence time of a proton to be held on an oxygen atom of alcohol. This is considered a significantly shorter time than the NMR spectroscopy can record. The spectrum will be changed dramatically by slowing down the rate of exchange to the point where the NMR spectrometer can detect. For example, the NMR spectrum of methanol sample at room temperature consists of two singlets peaks for ( $-OH$ ) proton and ( $-CH_3$ ) protons. When the temperature is lowered to  $-33$  °C for the same sample, the bands associated with ( $-OH$ ) and ( $-CH_3$ ) become quartet and doublet, respectively. In this case, the exchange rate became slower than the NMR spectroscopy timescale.<sup>78</sup> So, the spectrum is enhanced, and the coupling of the hydroxyl group was observed.

### 1.6.3 The importance of using chemometric analysis in NIRS

The following chapters demonstrate that the NIR spectra of diluted substances, particularly in aqueous solutions, are remarkably similar and sometimes impossible to differentiate. A similar difficulty occurs with solid samples belonging to the same category, such as sawdust from several types of wood. Consequently, several terms have been written utilising the chemometric analysis to simplify the spectral interpretation process, resulting in more accurate findings and time savings. For this reason, many works have been carried out using chemometric analysis to simplify the spectra interpretation giving more accurate results and saving time. A recent study by De Freitas Homem de Faria *et al.*<sup>79</sup> used NIR spectroscopy to estimate changes to biomass properties during storage. They emphasise the necessity of using chemometric methods to extract spectral information. They have used waste feedstock

such as sugarcane bagasse, coffee husk, eucalyptus, and pine. NIR spectra of the results were applied to a series of chemometric methods such as Partial Least Squares for Discriminant Analysis (PLS-DA) and Partial Least Squares Regression (PLSR). Table (A.1.2) illustrates other NIRS experiments with the use of chemometric analysis.

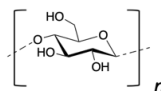
#### 1.6.4 The reason behind not using advanced chemometric methods in this thesis

The academic level of study should include the basic principles behind any chemistry when using analytical techniques. The simplest example is when individual samples undergo band shifting or transformation from one band to another as a result of a chemical interaction, this information is not always required when applying chemometric analyses. They distinguish between a large number of samples by grouping them according to their spectral differences, which are often difficult to see with the human eye. However, it is advantageous to use chemometric analysis at the industrial stage after a thorough knowledge of the fundamental principle underlying this chemical shift. This research gave a complete explanation of the spectra given and discussed the chemical changes that occurred as a result of each spectrum.

### 1.7 Biomass converted compounds

Our study will focus on a few sugars and anhydrosugars and a few additional platform compounds. These compounds include glucose, fructose, sucrose, LGO, Cyrene, HMF, and levulinic acid (LA). This chapter will provide background information on each of these samples, analysed in the following chapters.

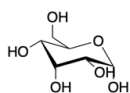
#### 1.7.1 Saccharides:



**Cellulose** is an essential compound that occurs naturally in plants as a structural element. It is produced in massive quantities ( $10^{15}$  kg) annually.<sup>80</sup> Cellulose is a glucose polymer that has been joined together ( $\beta$ -linked)<sup>16, 81</sup> to form a unique arrangement through the anomeric bond (C1) and the other end of the next monomer (C4) and so on. The cellulose rigidity property is due to the extra hydrogen bond linkage in linear order as the anomeric bonds are

all equatorial. Furthermore, cellulose polymer is coiled, which increases the stability of the

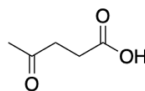
plant.<sup>80</sup>



**Glucose** is considered one of the most important organic compounds and one of the most abundant carbohydrates.<sup>81</sup> Glucose is an example of a monosaccharide and has a formula  $C_6H_{12}O_6$ . It is found naturally in honey and many varieties of fruits. In the human body, glucose plays a significant role in cell function as a source of energy. Starches are large molecules consisting of glucose monomers linked together by  $\alpha$ -linked.  $\alpha(1 - 4)$  and  $\alpha(1 - 6)$  linkages form a linear (amylose) and branch (amylopectin) structure of starch, respectively.<sup>81</sup> More than 99% of glucose is in a cyclic form in solution, while less than 1% is in the open-chain form.<sup>80</sup> About 64 % of glucose contains (equatorial OH), and 35 % is (axial OH). Both are in equilibrium with each other.

Glucose dissolves very rapidly in water-based solutions such as blood. So, it is dissolved in water easily. Usually, organic compounds which consist of only hydrogen and carbon do not dissolve in water, whereas organic compounds which include nitrogen and oxygen in their structure increase the water solubility. Glucose has six (O) atoms which increase its solubility in water. Five oxygen atoms are in the form of alcohol group which forms hydrogen bonds with water molecule.<sup>81</sup> This is the reason behind the solubility of glucose in water.

**Sucrose**, commonly known as sugar or table sugar, is a cheap natural compound isolated from sugar cane or sugar beet with white solid crystals<sup>80, 82</sup>. The sucrose molecule combines glucose and fructose, by linking them together via glycosidic bond, losing a water molecule. The two reducing ends of fructose and glucose linked together making non-reducing sucrose with a limited chemical activity.<sup>82</sup> It has a molecular formula of  $C_{12}H_{22}O_{11}$ , containing eight hydroxyl groups,<sup>82</sup> where hydrogen bonds help forming the molecules in crystal lattice.<sup>83</sup> The hydroxyl groups in the sucrose make it soluble in water. Nowadays, it is used in food chemistry as a sweetener in bakery, cooked, non-cooked food and drinks. It is isolated in an enormous scale with annual product of billion metric tonnes in 2011/2012 worldwide, making it the most abundant compound produced.<sup>80, 82</sup>

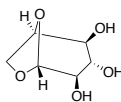


Levulinic acid

**Levulinic Acid (LA):**

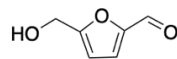
United States Department of Energy have classified LA as one of the best building blocks, and it is an excellent organic synthesis intermediate for a wide range of chemical compounds. It can be used as an intermediate for many applications such as fuel and oil additives, pharmaceuticals, fragrances and plasticisers.<sup>84, 85</sup> LA has ketone and carboxylic acid as functional groups in its molecule, which play an essential role in producing several chemicals. For producing LA from biomass, hydrolysis of cellulose takes place to form glucose. The next step is the dehydration of glucose into HMF. The main product obtained is furfural. When sugars are dehydrated, pentose and hexose yield furfural and HMF, respectively. Through the hydrolysis of HMF, LA is produced under acidic conditions. As a low-value chemical, formic acid is the by-product of this process and can be used to make rubber, pharmaceuticals, formaldehyde, plasticisers and textiles.<sup>84, 85</sup>

Hydrogenolysis is another process for converting biomass into desired chemicals, including LA. It results in breaking down C-C and C-O bonds by hydrogen. In the presence of mineral acids, LA can be produced from biomass and saccharides such as cellulose and glucose. This can happen in the presence of both solid catalysts and liquid mineral acids. Nevertheless, it is not a green method as the mineral acids cause environmental pollution and equipment corrosion. As LA has a significant role as a value-added chemical in industries obtained from biomass, it has been studied intensively for the last decades.<sup>84</sup> A greener way to produce LA is to use beneficial solid catalysts (hydrogenation system) to increase the final yield by using a solid heterogeneous catalyst rather than a homogenous catalyst.

**Levoglucosan (LGA)**

LGA is an anhydro sugar with a molecular formula of  $C_6H_{10}O_5$ , containing three hydroxyl groups. It has more rigid ring structure than glucose molecule, allowing for more selective chemistry on the free hydroxy groups.<sup>15</sup> So, it has been recognised as a crucial renewable platform molecule due to its properties, which makes it a desirable feedstock for the fermentation sector, both directly and indirectly. Using *Aspergillus niger* CBX-209, citric acid may be fermented from LGA generated by pyrolysis of cellulose.<sup>15, 86</sup> LGA can be used as a starting material for stereoregular polysaccharides synthesis, for biological activities,

such as anti-human immunodeficiency virus and blood anticoagulants.<sup>15</sup> LGA can be hydrolysed to produce glucose with the presence of water. Using DMSO and amberlyst70, LGA can be dehydrated to produce LGO.<sup>49</sup>



HMF

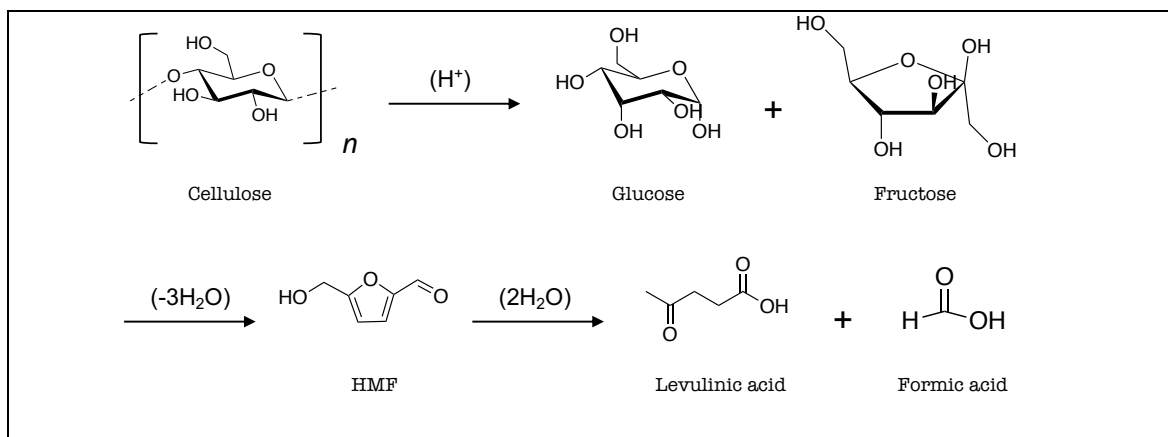
**5-Hydroxymethyl-furfural (HMF):**

also known as 5-(Hydroxymethyl)-2-furancarboxaldehyde and 5-(Hydroxymethyl)-2-furaldehyde. HMF is a solid chemical at room temperature, and it has a melting point in the range between 28 and 34 °C.<sup>85</sup> It boils at 114 – 116 °C at 1 mbar pressure.

HMF plays a significant role in the bio-based economy due to its production of biomass-derived intermediates. This is why it is referred to as a 'sleeping giant'. As HMF has several functionalities such as hydroxyl, aldehyde groups, and furan ring, it is one of the chemicals that attract researchers to study in detail. It can produce several chemicals which are used in different applications. HMF can be used to make formic acid, ethoxy methyl furfural, furfuryl alcohol, 2-methylfuran, 2,5-diformylfuran (DFF) and many other chemicals which used in chemicals, textiles, road salt, catalysts, fuel cells, biofuels, resins, solvents and pharmaceuticals.<sup>48</sup>

HMF production is an acid catalysed reaction see, *scheme 1.1*: hexose materials lose three water molecules. As a side reaction, HMF is re-hydrated to LA and formic acid.<sup>85</sup> From the first generation derivative HMF, many monomers can be produced, such as 2,5-FCDA, 2,5-FDCA, 2,5-FDCC and isopropylidene bis-(2,5-furandiylmethlene)diisocyanate. For condensation polymerisation, these monomers are suitable for producing polyesters, polyamides and polyurethanes.<sup>48</sup> A recent study by Pereira *et al.*<sup>87</sup> produced HMF from microalgae and waste coffee in an integrated biorefinery.





*Scheme 1.1 Cellulose is converted to different molecules*

## 1.8 Conclusion

This chapter summarised critical academic and practical uses of NIRS in biomass, highlighting its value in real-time analysis. The modern industrial economy is mainly based on a linear system based on petroleum-derived chemical feedstock.<sup>48</sup> There is a strong need for biomass as a critical resource for chemicals and energy. This advancement will depend not only on the biomass used as a feedstock or the conversion processes applied but also on the process control using an appropriate analytical methodology with appropriate real-time monitoring technology. This investigation may be achievable due to NIRS's ability to link to a fibre-optics probe. This approach must be capable of addressing specific challenges, such as water and NIRS is extremely moisture-sensitive. Water's vibration bands are intense and temperature-dependent. These factors contribute to NIRS's potential effectiveness in monitoring biorefinery operations in real-time.

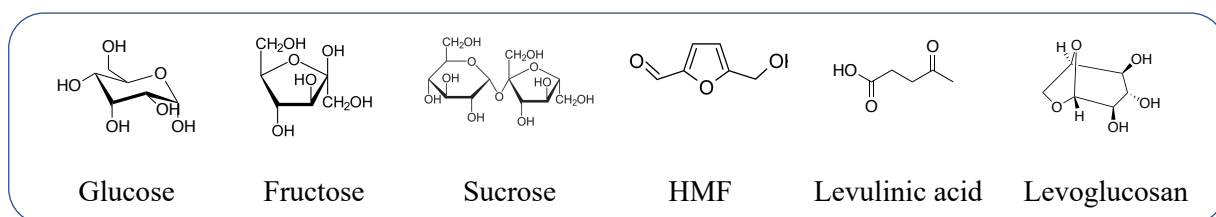
In this thesis, real-time NIRS is to determine the concentrations of sugars and anhydrosugars in aqueous solutions, the water content of biomass, particle size measurements and chemical conversions. By employing the NIRS technology, an analytical methodology that is more environmentally friendly than the present approaches is utilised. NIRS can save sample preparation, reagents, and solvents are not required, resulting in no waste. This technique has applications in the biorefinery, the food industry, and the pharmaceutical sector. Utilizing NIRS can benefit personnel in quality control of an industry or at many steps where analysis is required. This approach is appropriate for identifying biomass moisture content prior to feeding it into the biorefinery reactor, investigating hydrogen bonding, investigating the temperature change of the water system, and measuring particle size.



## Chapter 2: Materials and methods

### 2.1 Materials

Samples were prepared in two main phases; solids and liquids dissolved in deionized (DI) water. All samples were prepared in room temperature. Different concentrations for each sample were prepared for quantitative analysis. Concentrations are given in weight %.



*Scheme 2.1 Some of the materials used*

Solvents were purchased from Merck or Alfa Aesar, with a typical purity of  $\geq 99\%$

The main chemicals, LGA and Cyrene, used in this study were kindly provided by Circa Group. Deionised DI water was provided in-house by the lab using an ELGA CENTRA<sup>®</sup> system.

*Table 2.1 Materials used in this thesis*

Chemical	Purity (%)	Supplier
Acetonitrile	99.8	ThermoFisher Scientific
Cellulose	–	Sigma Aldrich
Cyrene	99.48	Circa
Cyrene	99.71	Circa
D – (–) – Fructose	99	Sigma Aldrich
D – (+) – Maltose monohydrate		Sigma Aldrich
D – Lactose monohydrate		Sigma Aldrich
Deuterium oxide	99.9 atom D	Sigma Aldrich

Ethyl acetate	99.8	ThermoFisher Scientific
Heptane	99	Sigma Aldrich
HMF		AVA Biochem
Levoglucosenone	90.67	Circa
Levoglucosenone	99.11	Circa
Levulinic acid LA	98	Alfa Aesar
Reichardt's dye	90	Sigma Aldrich
Sucrose	99	Alfa Aesar
Tetrahydrofuran	99.5	ThermoFisher Scientific
Toluene	99.8	ThermoFisher Scientific

Glucose, fructose, sucrose, LGA, LGO, LA and HMF have been prepared in different concentrations (0.5, 1.0, 1.5, 2, 4,6 ,8, 10 and 25 %) dissolved in deionized water. In addition, extra glucose and LGA samples have been prepared in lower concentrations (0.01, 0.03, 0.05 and 0.1 molal) to check the instrument sensitivity.

The current investigation included sugars and other chemicals samples. These samples have been chosen carefully as standard compounds for future work as results of biomass conversion using low temperature MW hydrolysis. Biomass conversion produces chemicals such as different types of sugars i.e. glucose, fructose and sucrose in addition to other chemicals such as Levulinic Acid (LA), LGA, 5-Hydroxymethylfurfural (HMF) and more other compounds. Each sample has been dissolved in DI water in different concentrations to study the behaviour of spectra. DI water was used as a solvent for all samples to simulate MW hydrolysis for biomass unless otherwise stated.

## 2.2 Analysis and instrument

### 2.2.1 MIR spectroscopy

PerkinElmer Spectrum 400 ATR-FTIR Spectrometer with absorbance bands in the range 4000 – 450  $\text{cm}^{-1}$  region at room temperature, with resolution 4  $\text{cm}^{-1}$  and (16 scans). For each experiment, a blank background subtraction (of ambient air, 16 scans) was done. Sampling technique was Attenuated Total Reflectance (ATR). The obtained data was analysed using the OriginPro 2020b software.

### 2.2.2 NIR spectroscopy

There are several techniques used for the NIRS depending on the experiment. Liquid samples were analysed using:

#### 2.2.2.1 Bruker Matrix-F

(Bruker Matrix-F) Near-infrared spectroscopy was used for liquid samples. IN236E Transmission fibre-optics probe was connected to be used for standard samples. IN271X-2 A transfection fibre-optics probe was used with samples which contained liquid and solid particles such biomass hydrolysate to allow the instrument to detect both liquid and solid by combining transmittance and reflectance methods simultaneously on one probe. The resolution was 8  $\text{cm}^{-1}$  with 64 scans for samples and background. The data were collected in the region from 12,000 to 4000  $\text{cm}^{-1}$ .

#### *Sampling techniques*

IN236E Transmission fibre-optics probe was connected to be used for standard samples. IN271X-2 A transfection fibre-optics probe was used with samples which contained liquid and solid particles such as biomass hydrolysate to allow the instrument to detect both liquid and solid by combining transmittance and reflectance methods simultaneously in one probe. Samples were obtained in pure phase and examined in DRIFT cup for powders



*NIRS Fibre-optics probe*

### **2.2.2.2 Bruker Equinox55 NIRS**

Bruker Equinox55 Near-infrared spectroscopy was used and set for solid samples in DRIFT sampling technique fitted with a ZnSe window and MCT detector (liquid N<sub>2</sub> cooled) and a ground KBr used as a background. Air background spectrum of 256 scans and a sample spectrum of 128 scans were collected. However, the instrument was limited in the range between 4000 – 8000 cm<sup>-1</sup> for DRIFT, and between 5000 – 10000 cm<sup>-1</sup> for transmittance. So, it was set as MIR in order to collect data at the range between 4000 – 5000 cm<sup>-1</sup>. Therefore, to collect a spectrum of one sample in NIRS region, it must use a different set up for the instrument in two times. This is one of the limitations of this instrument. Another limitation is that the range 8000 – 12000 cm<sup>-1</sup> was not clear to obtain. It is so noisy which limits the spectra to combination and 1<sup>st</sup> overtone regions.

### **2.2.2.3 Metrohm**

NIRS XDS Process Analyzer (Metrohm) with fibre-optic connected to reflectance or transmittance probe. Vision Software<sup>®</sup> is used for the analysis but the data were collected and the results were presented using the OriginPro 2020b software. The analyser temperature was set to set to 38.0, ± 0.4 °C. The Data Collection Method (DCM) selection range is extended InGaAs detector: 800-2200 nm with 0.5 nm Data Interval. 50 Watt Tungsten Halogen Reflector Lamp was applied.

### **2.2.2.4 UV-Vis spectroscopy**

A Jasco V-550 UV-vis spectrometer at a range of 190 – 900 nm with scanning speed of 1000 nm/min and a band width of 1.0 nm. The path length of the cell is 1 cm. The data was analysed using Spectra Manager software and the data were collected and presented using the OriginPro 2020b software.

### **2.2.2.5 NMR spectroscopy**

Three different instruments were used: 300, 400 and 500 MHz spectrometer. All spectra shown in the thesis was obtained from the 400 MHz unless otherwise stated. The 500 MHz was used for the different temperature experiments. The data was analysed using Mnova  
The 300 and 500 MHz instruments were provided as a service by the chemistry department. Thus, the sample was submitted to the service provider, the result will be collected from the local data.

### **2.2.3 Simultaneous Thermal Analysis (STA)**

STA was conducted using a PL Thermal Sciences STA 625. It is consisted of heating samples between 8 – 12 mg, using open aluminium cup run in flowing air (ca. 50 mL min<sup>-1</sup>) typically from ca. 21 – 625 °C at a rate of 10°C/min unless otherwise stated. The data were collected and presented using the OriginPro 2020b software.

### **2.2.4 CHN**

The CHN analysis using a CE-440 Analyser (Exeter Analytical Inc.) coupled with a Sartorius S2 analytical balance and involved combusting samples at 975 °C followed by subsequent analysis of the resulting products via thermal conductivity detection. This technique was provided as a service by the chemistry department. Thus, the sample was submitted to the service provider, who then emailed the results.

### **2.2.5 HPLC**

HPLC: Sugars, LGA, LA and HMF analysis were separated using an Agilent Hi-Plex H+ column (300 × 7.7 mm, 8 µm particle size) operated at 60 °C with a 0.005 M H<sub>2</sub>SO<sub>4</sub> as a mobile phase at flow rate of 0.6 ml/min. An injection volume of 5 µL, a refractive index detector at 55°C and a total run time of 55 minutes. This technique was provided as a service by the GCCE and the samples were submitted to the service provider, who then emailed the results.

### **2.2.6 GC**

Gas chromatographic measurements were made with an Agilent Technologies HP 6890 gas chromatograph (Or Agilent Technologies 7890B gas chromatograph), with a flame ionisation detector (GC-FID), fitted with a Rxi-5HT capillary column (30 m 250 mm x 0.25 mm nominal, max temperature 400°C). Helium was used as the carrier gas at a flow rate of 2 mL/min with a split ratio of 30:1 and a 5 µl injection. There are two methods of set up were used:

**Method 1***Table 2.2 GC set up for method 1*

Oven	Rate (°C/min)	Value (°C)	Hold time (min)	Run time (min)
initial		70	1	1
Ramp 1	10	140	1	9
Ramp 2	30	260	5	18

**Method 2***Table 2.3 GC set up for the first method 2*

Oven	Rate (°C/min)	Value (°C)	Hold time (min)	Run time (min)
initial		70	1	1
Ramp 1	10	140	1	9
Ramp 2	5	200	5	26
Ramp 3	5	260	5	43



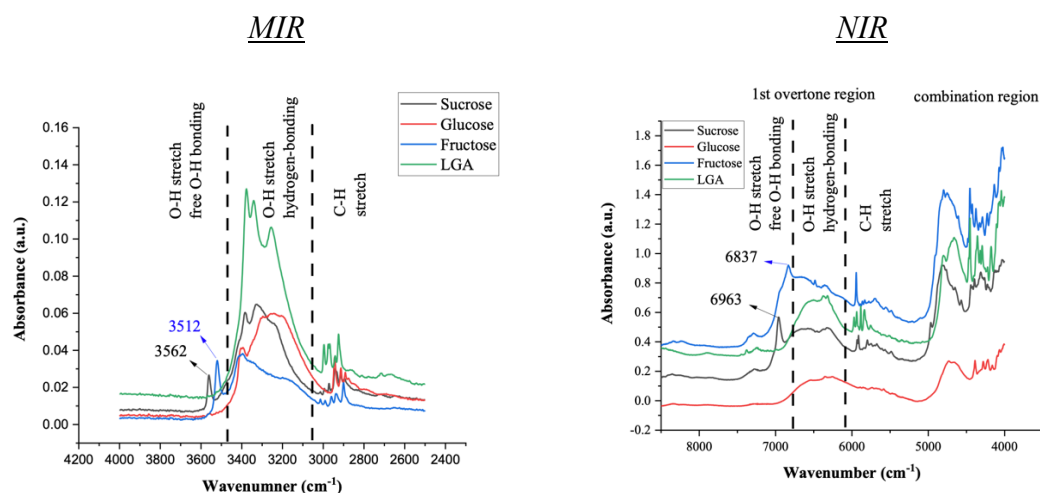
## **Chapter 3: NIR Spectroscopy analysis of sugars and their derivatives**

### **3.1 Introduction**

It is necessary to study and apply the NIRS method and compare it with other analytical methods. In our case, the interesting area is to identify the intermediate or converted chemicals from the biomass. In other words, NIRS was used for some fundamental qualitative and quantitative analyses for some sugars, LGA, LGO, LA, HMF and Cyrene. The aim is to identify whether the NIRS can analyse the chemicals individually and in mixtures. NIRS as a real-time instrument can be carried out whenever this step is proven.

As a result of biomass thermal conversion using a MW as a heat source, it is expected to find sugars and anhydrosugars that are mixed in different ratios for the hydrolysis process, where the water will be dominant in the mixture. So, it is important to test those pure chemicals individually and dilute them in different concentrations in water. Different concentrations of some sugars and anhydrosugars have been investigated in more detail.

To detect and locate the 1<sup>st</sup> overtone bands for each diluted sample, it is necessary to identify the fundamental bands for each pure substance. Figure 3.1 illustrates the fundamental (MIR) combination with the 1<sup>st</sup> overtone bands (NIRS) for some pure samples run as powders. The figure shows sucrose, glucose, fructose and LGA as solid samples using DRIFT sampling technique. The figure demonstrates fundamental stretching bands for MIR, CH and OH. In NIRS, the different regions represent different absorption. Combination bands, CH and OH 1<sup>st</sup> overtone stretching bands appear in different regions. Despite the similarities of the sample's functional groups, IR spectra show significant differences in their vibrations. One such case is the free hydroxyl group for the sucrose, which is a unique band at  $3562\text{ cm}^{-1}$  in the MIR. This is reflected in the NIRS for the 1<sup>st</sup> overtone of the same absorption at  $6963\text{ cm}^{-1}$ . Similarly, the multiple CH fundamental stretching band of LGA can also be seen in the NIRS. Through this process, it is possible to identify the specific features in the spectrum of each sample, compare the MIR with NIR and then analyse the relevant region.



*NIR spectra for pure (powder) sucrose, glucose, fructose and LGA crystals in both N- and M-IR regions*

*Figure 3.1 IR spectra for pure (powder) sugars and LGA*

This chapter discusses NIRS to analyse liquid samples such as diluted sugars and anhydrosugars in aqueous solutions. The primary concern here is water absorption. As a consequence, various techniques were used to improve the outcome. The chapter begins with a discussion of specific chemicals. A single case of diluted sugar, fructose, that was analysed using NIRS to start with. The spectrum was then enhanced using the subtraction approach. The subsequent task investigated a very low glucose concentration to demonstrate the NIRS's sensitivity. The sugars' 1<sup>st</sup> overtone region was studied, followed by the combination region. Likewise, anhydrosugars were investigated. The following section discusses sample mixtures in aqueous solutions. The next section includes a comparison of NIRS and HPLC. The final section applies NIRS to water at variable temperatures, which opens the way to two more chapters in this thesis.

## 3.2 Individual substances

### 3.2.1 fructose

The first example was diluted fructose which was dissolved in water in different concentrations.

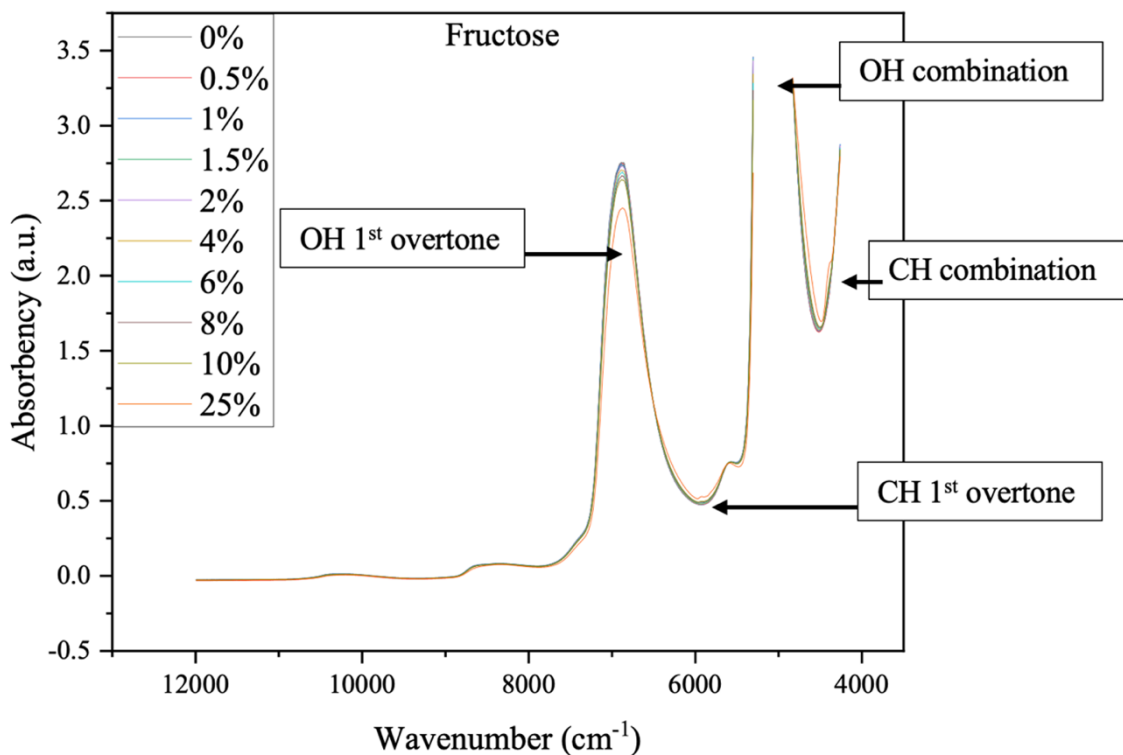


Figure 3.2 NIR spectra of diluted fructose samples

Generally, water absorption dominates the spectra of the diluted samples. The fructose sample at different concentrations illustrates this issue, as shown in Figure 3.2. Two primary absorbances at about  $5000\text{ cm}^{-1}$  and  $6880\text{ cm}^{-1}$  are due to water absorbency. The band at  $5000\text{ cm}^{-1}$  is due to a combination of fundamental stretching and deformation bands for O-H. The band at  $6880\text{ cm}^{-1}$  is due to a fundamental stretching 1<sup>st</sup> overtone for O-H. The region around  $5000\text{ cm}^{-1}$  was cut as the absorption of this vibration is very high, causing noise at the top of this peak. The high absorbency can be controlled by the path length of the cell. The higher the path length, the higher the absorbency and the higher-order overtones observed.<sup>57</sup> So, to reduce the band intensity at  $5000\text{ cm}^{-1}$ , a smaller path length is needed. Due to the high water absorption in NIRS, the solute components cannot be seen clearly in the spectra. However, NIRS spectrum analysis can give more detail of what the spectrum contains.

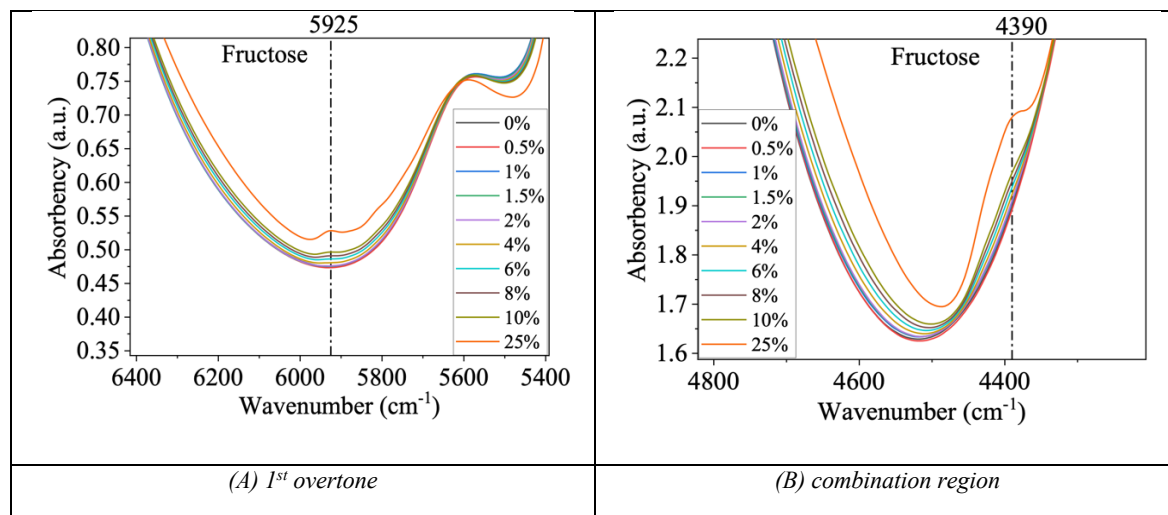


Figure 3.3 NIR spectra of H<sub>2</sub>O and diluted fructose samples

The spectra of diluted fructose samples have two prominent bands in NIR spectroscopy, as demonstrated in Figure 3.3. The first band is centred at 4390 cm<sup>-1</sup>, representing a combination band of C-C and O-H stretching as illustrated in Figure 3.3 (B). The second band centred at 5925 cm<sup>-1</sup> corresponds to the CH 1<sup>st</sup> overtone as shown in Figure 3.3 (A). Note that this band is broad, indicating other overlapped bands. This will be demonstrated using the subtraction method in the next step.

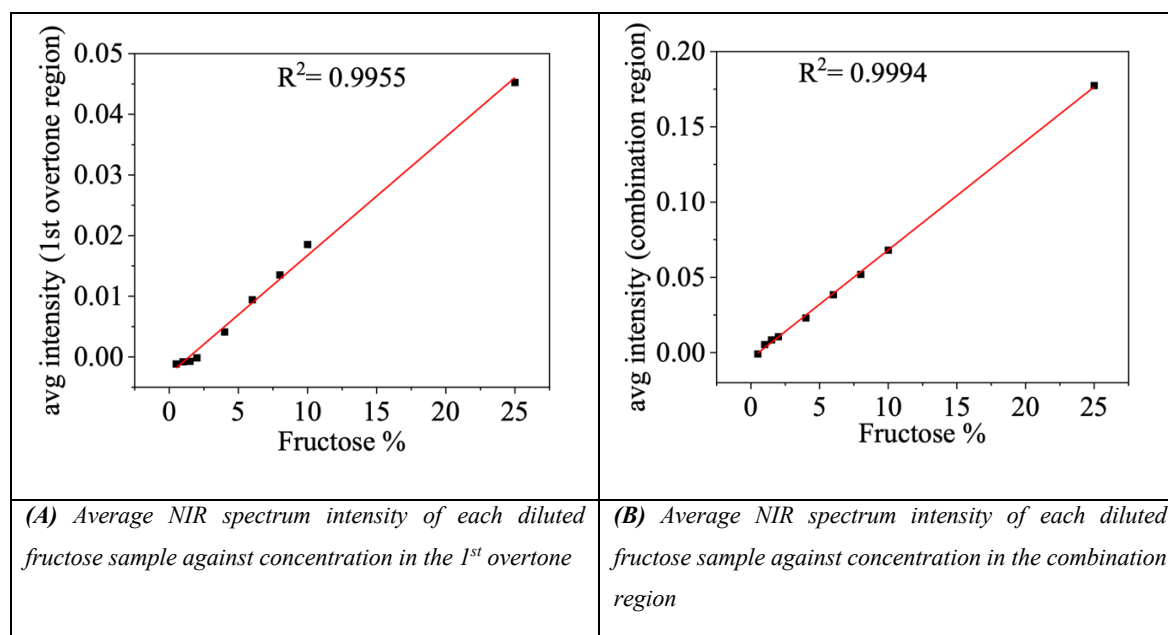


Figure 3.4 NIR spectroscopy for fructose samples

The CH combination vibration corresponds to the concentration of the solution, as illustrated in Figure 3.4 (B). The 1<sup>st</sup> overtone region of fructose, on the other hand, shows similar behaviour, as demonstrated in Figure 3.4 (A). However, at lower than 2% concentration, the 1<sup>st</sup> overtone vibration is less effective than the combination band. One potential reason behind the efficiency is the high absorbency of water 1<sup>st</sup> overtone, so subtraction of the water spectrum should enhance the sugar spectra. This mathematical method has the potential to obtain the pure spectrum of the sugar in aqueous solutions. These findings can make NIRS a successful instrument for the quantitative analysis of sugars in aqueous solutions.

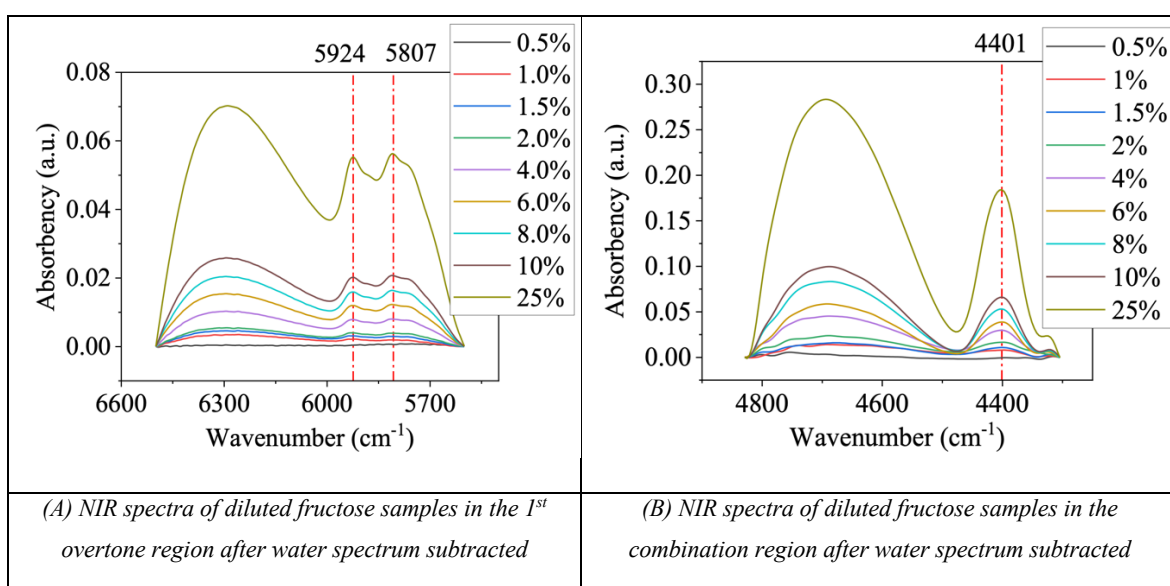
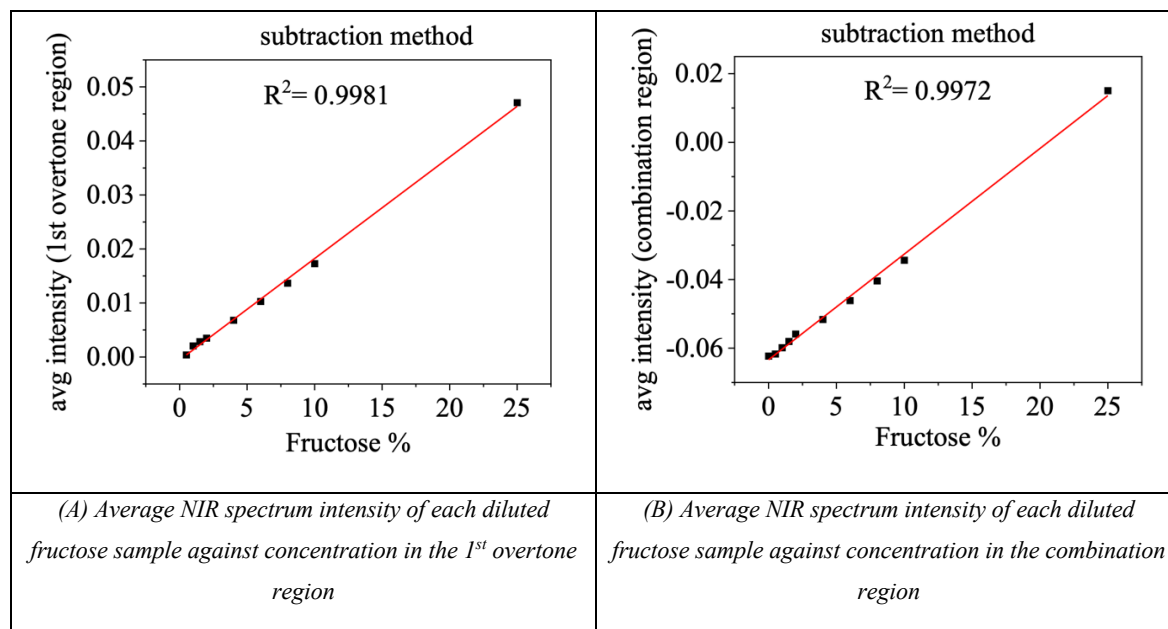


Figure 3.5 Subtracted method for NIR spectra of diluted fructose

In Figure 3.5, the water absorbency was subtracted from each solution spectrum to show the pure fructose absorption in the combination region between 4300 – 4830  $\text{cm}^{-1}$ . Figure 3.5 (B) shows two different bands, one sharp band at 4390  $\text{cm}^{-1}$  representing a combination band. The second band was broader and centred at 4700  $\text{cm}^{-1}$ . To compare these subtracted spectra with the original spectra in Figure 3.3 (B), it is found that the band at 4390  $\text{cm}^{-1}$  can appear at the original spectra while the band centred at 4700  $\text{cm}^{-1}$  cannot be recognised before the subtraction as it is located within the very high absorbance band of O-H (probably due to water and sugar). Therefore, a water-subtracted spectrum gives promising detailed information that can help us to apply a quantitative analysis method. For more analysis, the combination band (4331 – 4466  $\text{cm}^{-1}$ ) has been cut and baselined. Consequently, a negative spectrum developed where there was no CH band. A calibration curve in Figure 3.6 proved

to be a successful approach. To compare spectra of the 1<sup>st</sup> overtone region in Figure 3.4 (A) with subtracted spectra in Figure 3.6 (A) subtraction gave more detailed information about the sugar.



*Figure 3.6 NIR spectroscopy for fructose samples with subtraction method*

As shown in Figure 3.6, there is a linear regression between fructose concentration and its band intensity at both combination and 1<sup>st</sup> overtone regions. This was proof of the success of the subtraction method. This is an excellent tool for using NIR spectroscopy as a greener method in many applications to analyse sugar concentration.

### 3.2.2 Glucose at very low concentrations

Similarly, lower concentrations, down to 0.01 m, of glucose in water were tested to check the instrument sensitivity. Note that 0.01 m is equivalent to 0.162 wt % of glucose in water. It is hard to identify any differences in band intensities in the original spectra without using the subtraction method. By using the subtraction technique, NIRS, with its high sensitivity, was able to identify the differences even at low concentrations of glucose. There is a linear regression at the 1<sup>st</sup> overtone region of glucose's CH vibration, as illustrated in Figure 3.7.

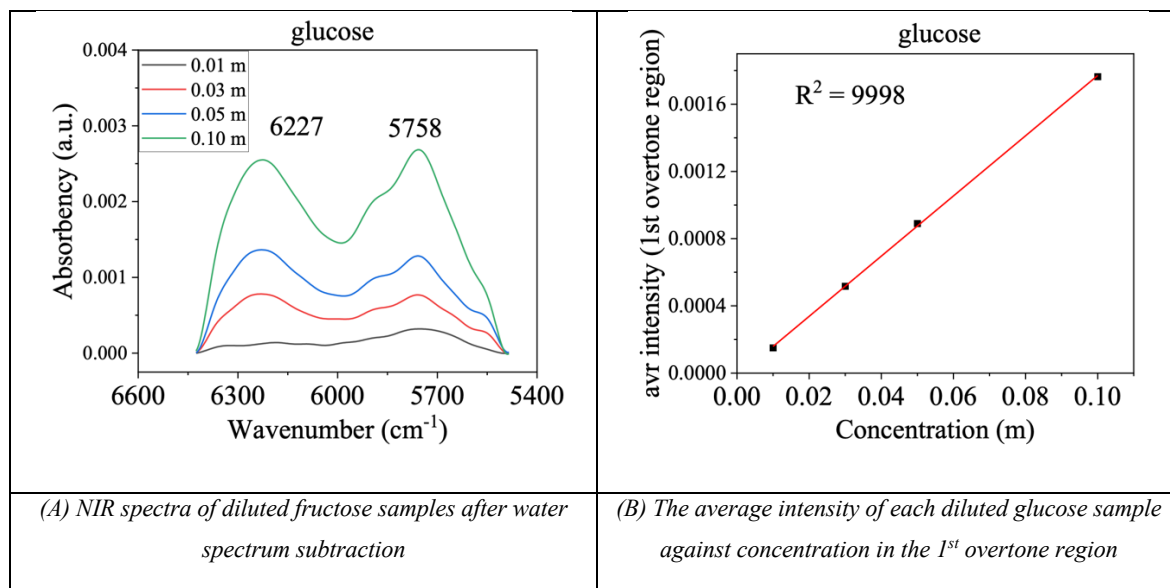


Figure 3.7 NIR spectra of diluted fructose samples with subtraction method

Another example, LGA, was tested at low concentrations down to 0.01 m, as shown in Figure 3.8. Again, a linear regression exists between LGA concentration and its band intensity. Even without water subtraction, the results were taken, proving the instrument's sensitivity. This method can be used as a quantitative tool to measure LGA concentration in aqueous solutions.

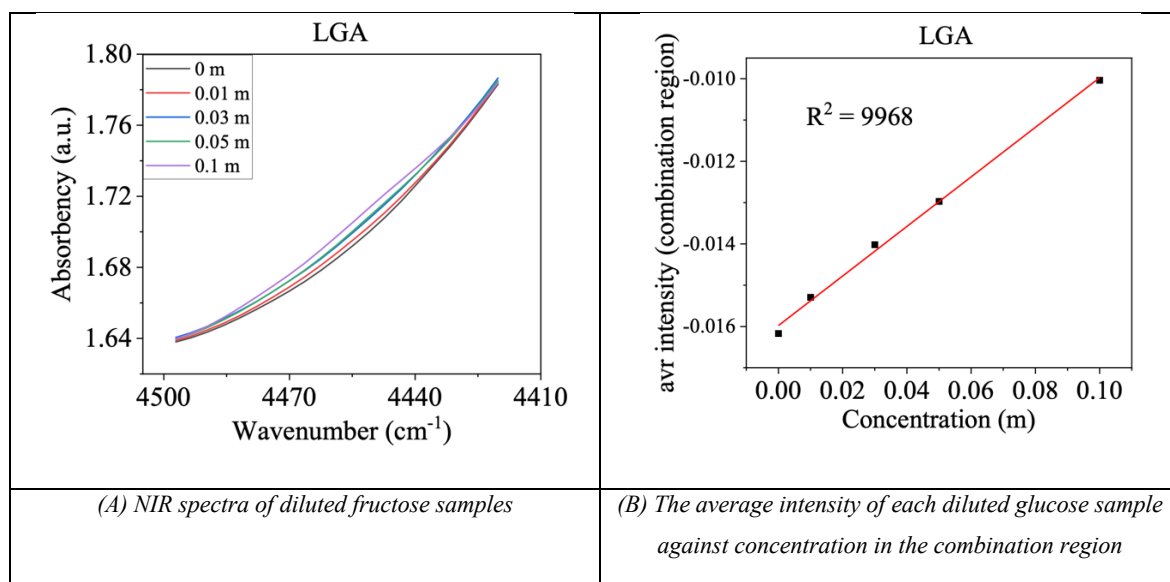


Figure 3.8 NIR spectra of diluted LGA samples

After showing that the NIR spectroscopy with the fibre-optics probe is very sensitive to glucose and LGA, a detailed study for sucrose, glucose, fructose, LGA, LGO, LA and HMF samples took place in both the 1<sup>st</sup> overtone and combination region of CH vibration as presented below.

### 3.2.3 1<sup>st</sup> Overtone region for sugars

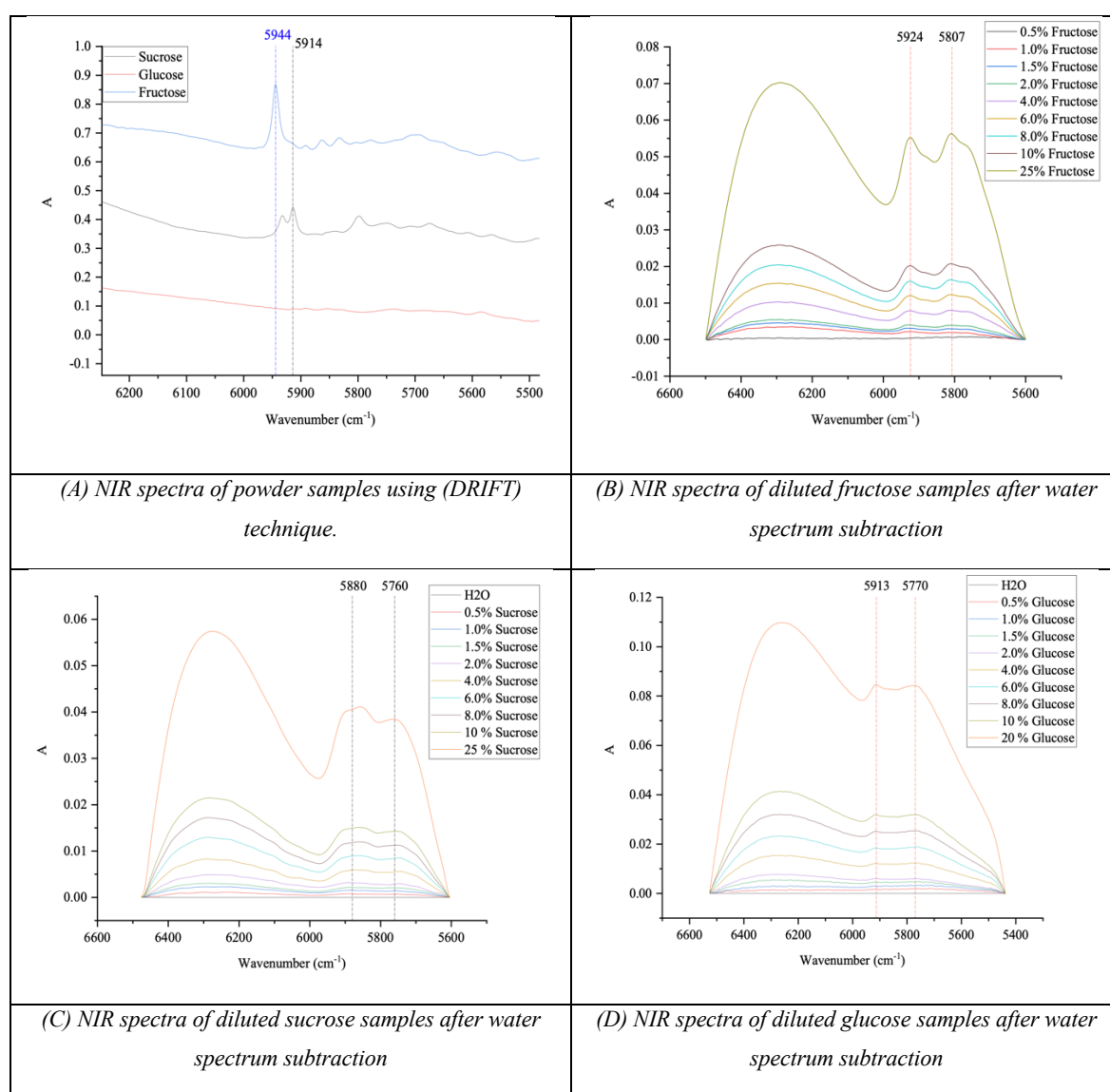


Figure 3.9 NIR spectra of fructose, sucrose and glucose 1<sup>st</sup> overtone

The NIR spectrum of solid fructose using DRIFT technique shows the 1<sup>st</sup> overtone band of C-H at  $5944\text{ cm}^{-1}$  while the same band for sucrose appeared at lower wavenumber ( $5914\text{ cm}^{-1}$ )



<sup>1</sup>). This is illustrated in Figure 3.9 (A) the glucose spectrum shows almost no vibration in this region because it was run as a fine powder causing no diffuse reflection. However, the MIR spectroscopy using the ATR sampling technique reveals the glucose's fundamental CH vibration. Meanwhile, the 1<sup>st</sup> overtone can be seen when using the transmittance sampling technique to analyse the diluted sample.

Using the subtraction method mentioned earlier for the spectra of different fructose concentrations reveals two main bands for the CH 1<sup>st</sup> overtone vibration, as shown in Figure 3.9 (B). It is challenging to locate those two bands on the original spectra, as illustrated in Figure 3.2, without using the subtraction technique. The band at 5924 cm<sup>-1</sup>, which appeared in the diluted spectra, is the same band spotted for the solid sample, with some neglectable shifting in band position due to the different machines and sampling techniques used. Those bands are difficult to be seen without subtracting the water spectrum.

In Figure 3.9 (C) shows NIR spectra for sucrose display bands for the CH 1<sup>st</sup> overtone vibration at lower wavenumbers than those for fructose. The reason behind that is that sucrose contains more CH<sub>2</sub> than those in fructose. This result is consistent with the pure samples illustrated earlier in Figure 3.9 (A). Glucose spectra show very low band intensity compared with sucrose and fructose in this region. The very low intensity of this band in Figure 3.9 (D) is due to its solid state - Figure 3.9 (A), with almost no band at this position. Comparing a diluted glucose spectrum in liquid and solid-state, shows that the solid glucose has no apparent band of C-H 1<sup>st</sup> overtone. Diluted samples proved that glucose still shows the C-H 1<sup>st</sup> overtone as expected.

### 3.2.4 Combination region for sugars

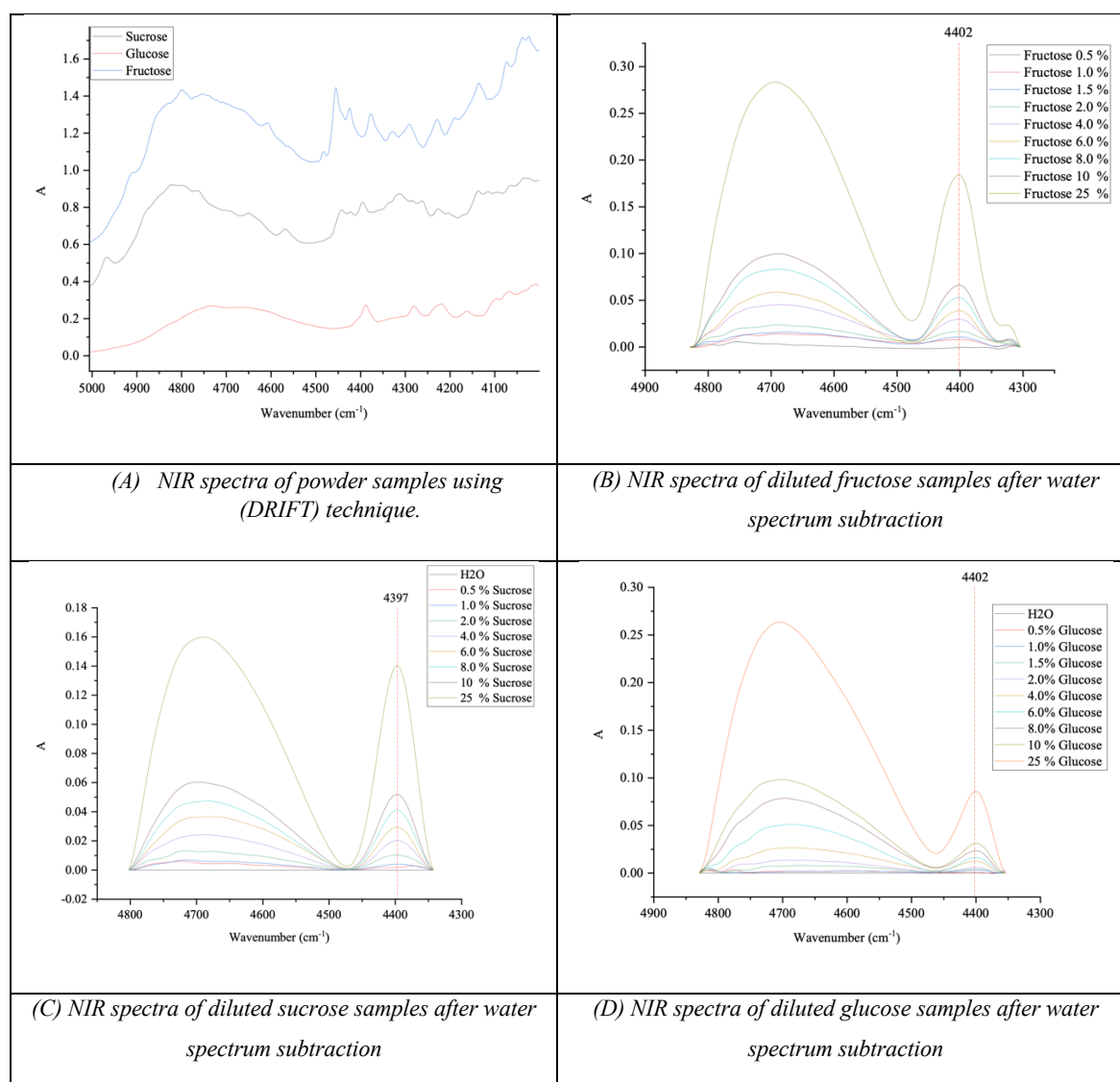


Figure 3.10 NIR spectra of fructose, sucrose, and glucose combination region

The remarkable band in the combination region for sugars is the region (4350 – 4450 cm<sup>-1</sup>) which represents a combination of fundamental bands of C-C and C-O stretch. As shown in Figure 3.10, (A) all sugars have relatively sharp small bands in this region. Fructose shows this band at a relatively higher wavenumber compared to sucrose. However, spectra of the the three sugars are rather similar.

The band at 4808 cm<sup>-1</sup> is broad, and it is due to a combination of O-H stretch and deformation. In its diluted aqueous phase, fructose shows an expected band at 4402 cm<sup>-1</sup> as a combination band of fundamental C-C and C-O stretching, as shown in Figure 3.10 (B). This band could not be easily found without subtraction of the water spectrum. The band at

4397  $\text{cm}^{-1}$  of sucrose indicates the difference in band position between sucrose and fructose and the difference in their intensity of the same band at the same concentration. Sucrose has lower band intensity as compared to fructose. The very low intensity of the glucose band at 4402  $\text{cm}^{-1}$  compared with the other sugars was a notable factor for glucose due to the less combinations of common carbon atoms HO – C – H compared to other sugars.

### 3.2.5 1<sup>st</sup> Overtone region for anhydrosugars, LA and HMF

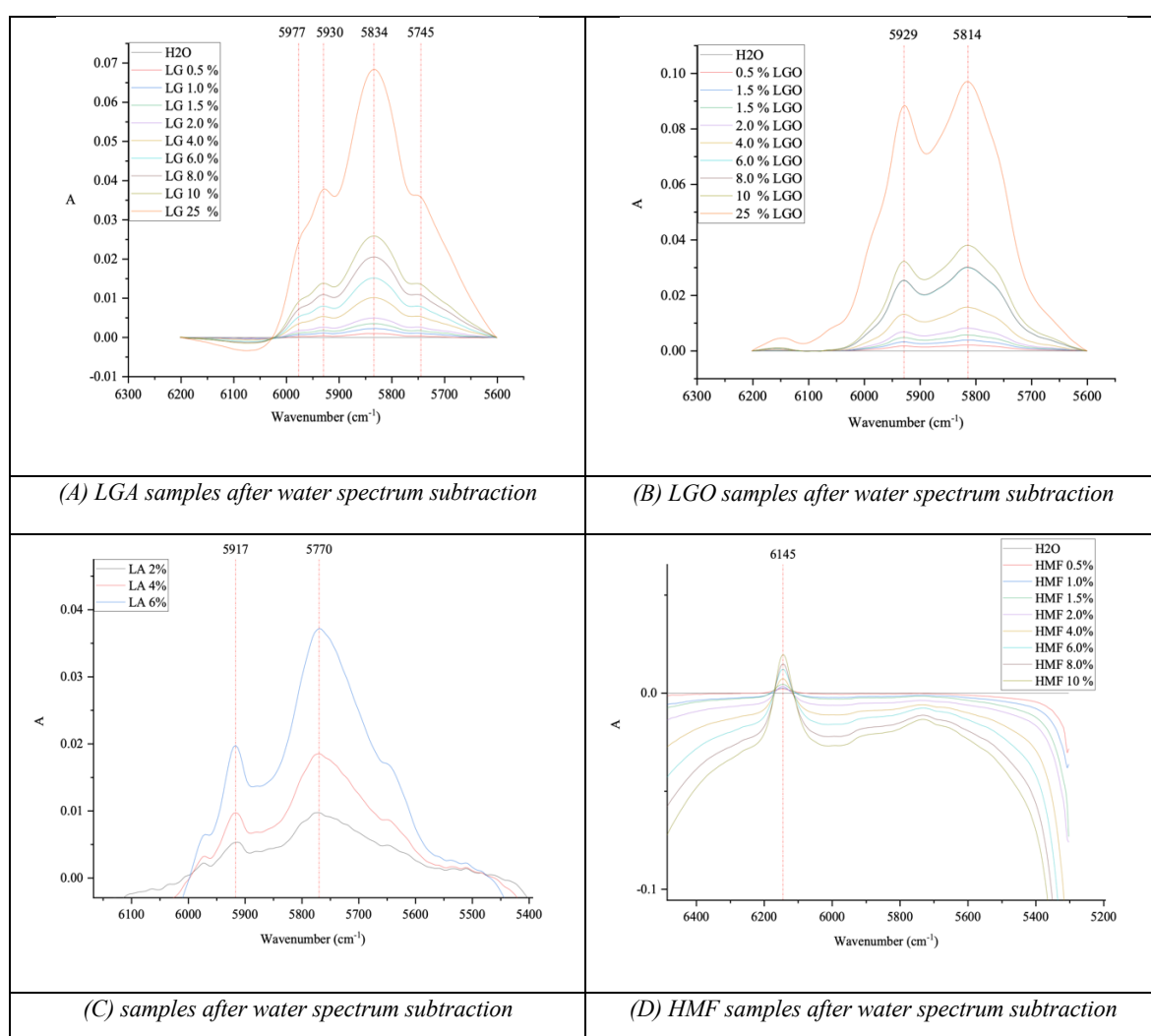


Figure 3.11 1<sup>st</sup> overtone region of different diluted samples

Spectra of LGA diluted samples gave four bands near each other; the intense one centred at 5834  $\text{cm}^{-1}$ , as shown in Figure 3.11 (A). These bands represent the different types of C-H 1<sup>st</sup>

overtone stretching vibrations of LGA. This is similar to the spectrum of solid-state LGA when using DRIFT, as stated in Figure 3.29.

Although LGO has a similar chemical structure to LGA, it has different vibrational due to C-H 1<sup>st</sup> overtone, C=C and C=O in NIRS. They are, however, more similar in the combination region. LA's 1<sup>st</sup> overtone region gave two bands at 5770 and 5917 cm<sup>-1</sup> due to CH<sub>3</sub> and CH<sub>2</sub> stretch 1<sup>st</sup> overtone, respectively. There is a notable band of HMF located at 6145 cm<sup>-1</sup> due to the C-H 1<sup>st</sup> overtone. This band is significant for distinguishing HMF in a mixture.

### 3.2.6 Combination region for anhydrosugars, LA and HMF

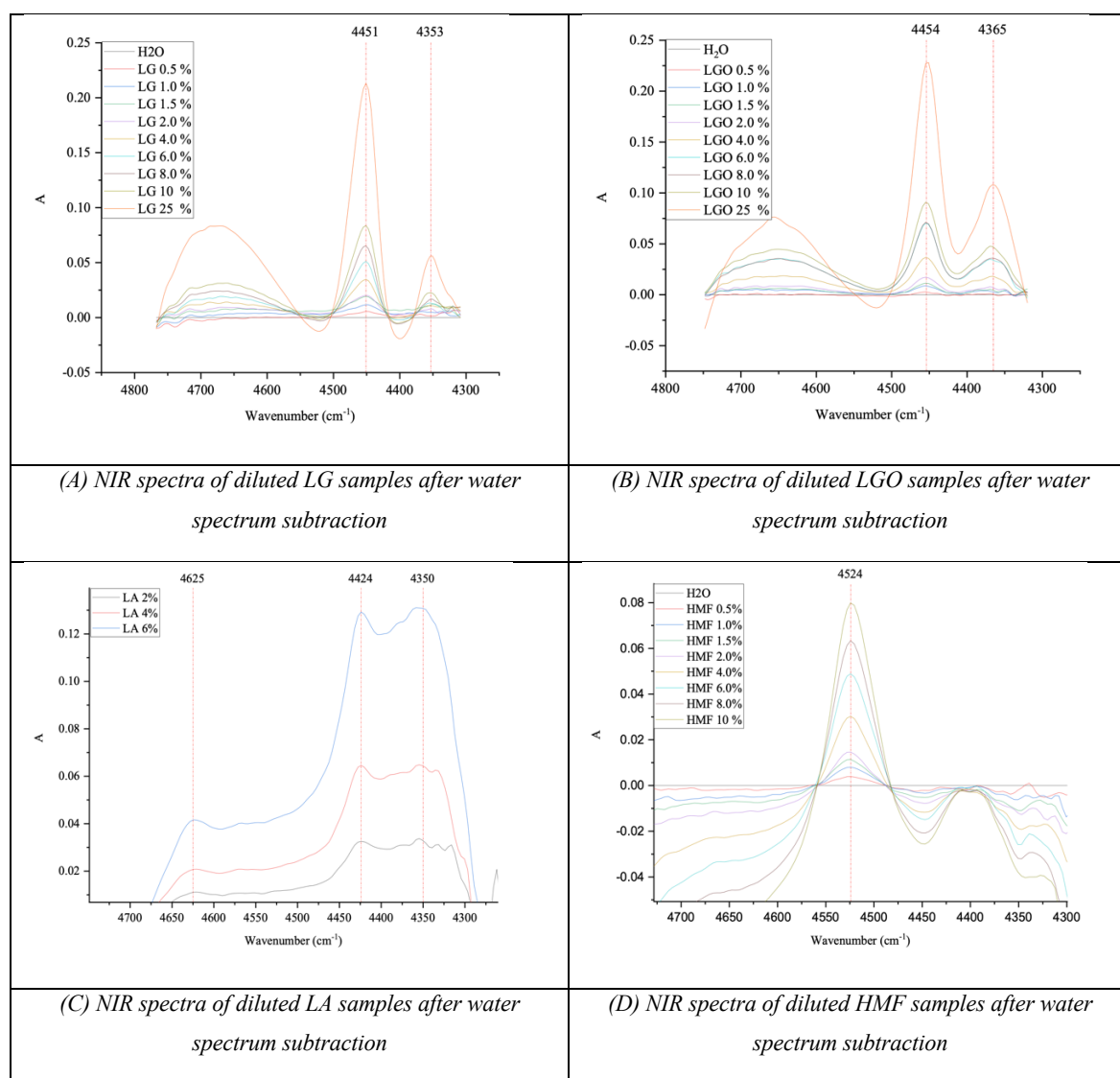


Figure 3.12 Combination region of different diluted samples

As illustrated in Figure 3.12, LGA shows two main bands at 4353 and 4451  $\text{cm}^{-1}$  due to a combination of C-H stretch and deformation and a combination of O-H stretch and deformation, respectively. LGO shows a similar band position with little difference regarding the intensity of the band at 4365  $\text{cm}^{-1}$ , which is higher in its intensity compared to the band at 4353  $\text{cm}^{-1}$  for LGA. Generally, the combination region is not suitable for distinguishing between the two samples due to the similarities between them in this region. So, the 1<sup>st</sup> overtone region was a better region to discriminate between them, as seen in Figure 3.11.

LA shows some bands at 4350, 4424 and 4625  $\text{cm}^{-1}$ , as demonstrated in Figure 3.12 (C). The first two bands correspond to the combination of fundamental C-H stretching and deformation. The third band at 4625  $\text{cm}^{-1}$  shows the combination of O-H and C-H stretch bands. However, the combination region of LA was different from that of LGA and LGO, making it distinguishable for LA. The remarkable sharp band of HMF at 4524  $\text{cm}^{-1}$  is due to combination bands of fundamental C-H stretching and C=O stretch. The other smaller band at 4400  $\text{cm}^{-1}$  is due to O-H and C-C stretching combination bands.

### 3.3 Mixtures

Based on the results from the previous section, NIR spectral data library has been collected and studied. Although mixtures are very complicated in the NIR spectrum, there is a potential success in detecting some compounds. So, a mixture of sugars, anhydrosugars, and other biomass derivative compounds was analysed. To simplify this test, 4 wt% glucose was tested first. Then 4 wt% sucrose was added, followed by 4 wt% diluted solution of fructose, LGA, LGO, LA, and HMF. Each time a chemical is added to the mixture, a test is performed. Each compound was diluted in an aqueous solution with a concentration of 4 wt %. This experiment allows us to see the difference in the spectrum when adding a compound.

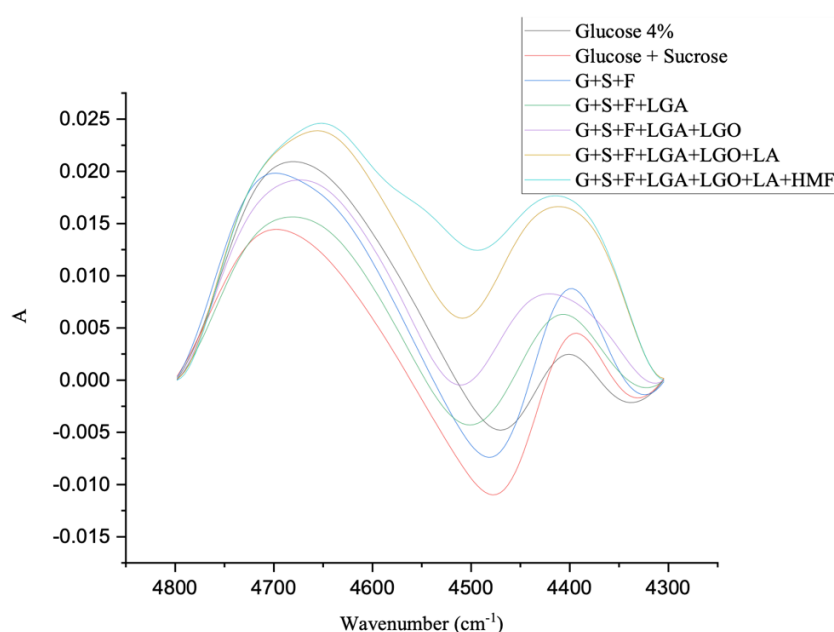


Figure 3.13 NIR spectra of mixtures at the combination region with the subtraction method

*G: glucose, S: sucrose, F: fructose,*

As shown in Figure 3.13, the spectra of the mixtures in the combination region are similar. They all have two main bands located around 4400 and 4700  $\text{cm}^{-1}$ . However, LA and HMF show significant changes when added to the mixture. The band at 4400  $\text{cm}^{-1}$ , in LA and HMF increased in intensity compared to the other components in the mixture. Glucose shifted the band to lower wavenumbers, and fructose increased the band frequency and made it sharper. LGA and LGO shifted the band to a higher wavenumber and made it broader.

On the other hand, there is no helpful information that can be obtained from the band at around  $4700\text{ cm}^{-1}$ . However, there is a shoulder at  $4524\text{ cm}^{-1}$  when HMF was added to the mixture. This shoulder is notable for predicting the existence of HMF in a mixture in the combination region, but it is too weak to be useful for this detection. Hence, the combination region was not a better option for this analysis.

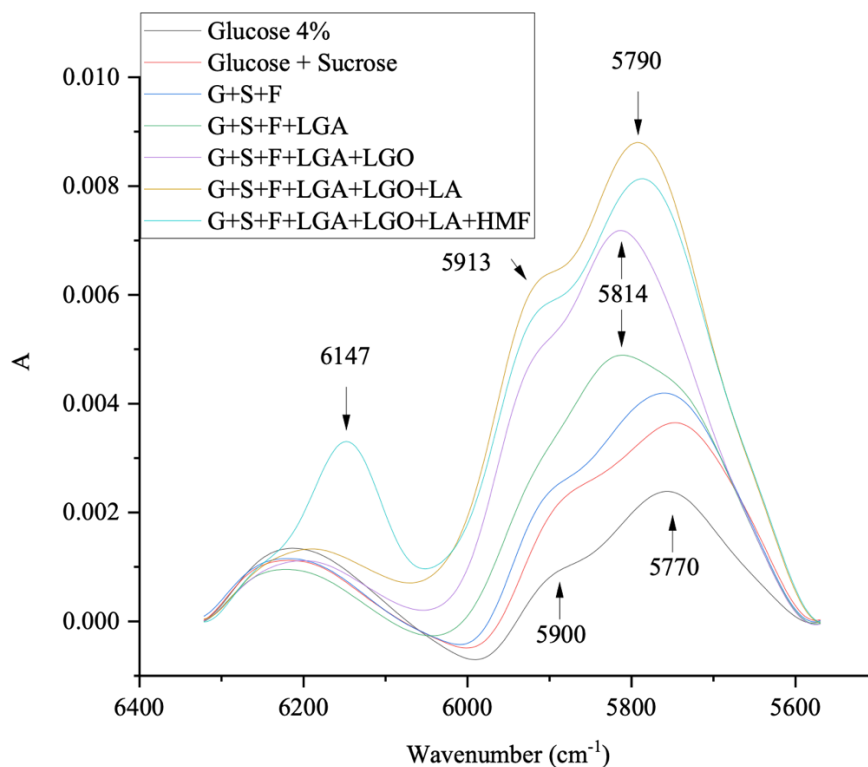


Figure 3.14 NIR spectra of mixtures at the 1<sup>st</sup> overtone region with subtraction method

G: glucose, S: sucrose, F: fructose,

Although the 1<sup>st</sup> overtone region illustrated in Figure 3.14 seems complicated, it is rich in useful information. Generally, there are two main groups in terms of spectra similarities. The first group is the three sugars, as they behave similarly as the two bands at  $5770\text{ cm}^{-1}$  and  $5900\text{ cm}^{-1}$ . The second group is LGA and LGO, as they had a unique band at  $5814\text{ cm}^{-1}$ . Then LA showed a higher frequency band at  $5790\text{ cm}^{-1}$  while HMF showed a unique band at  $6147\text{ cm}^{-1}$ .

For more specific discrimination between species, it is shown that sucrose and glucose are similar for the two bands at  $5770\text{ cm}^{-1}$  in their location, with higher intensity of sucrose

bands. Fructose is slightly different as its band was shifted to a higher wavenumber. LGO gives a shoulder at  $5913\text{ cm}^{-1}$  in comparison with LGA. Therefore, the contents of a mixture which contains no more than two or three different components can be predicted. The spectrum becomes more complicated as the compounds are added to the mixture due to overlapping bands. However, it is possible to detect a compound in a mixture like the one used in the previous experiment using the 1<sup>st</sup> overtone region.

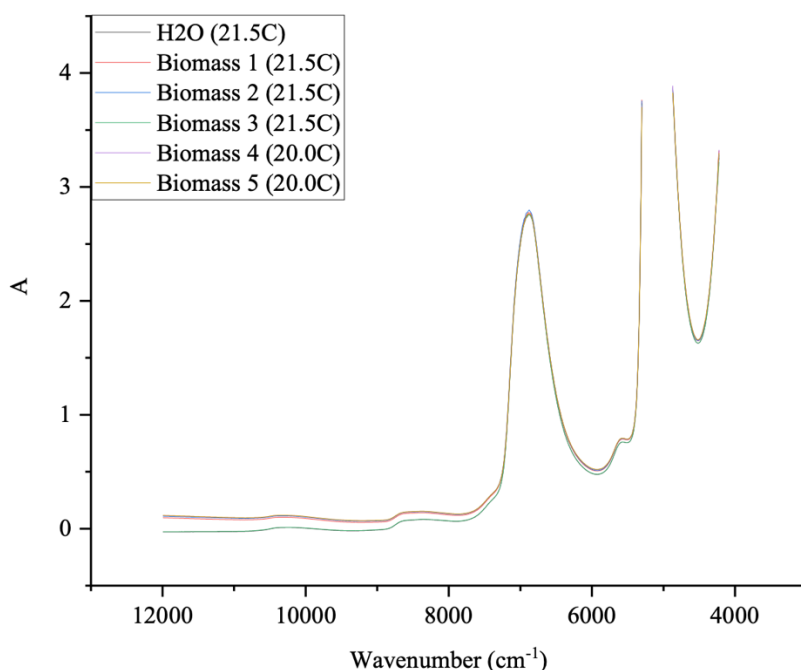


*Figure 3.15 NIR spectra of biomass hydrolysates*

As biomass hydrolysates contain a relatively large amount of water. It is expected to see similar spectra as demonstrated in Figure 3.15. Although the spectra seem similar, some information can be obtained. The variable intensity of the baseline gives an idea of which sample contains particles or if the sample looks cloudy. Water and cellulose spectra showed zero baseline intensity at  $12,000\text{ cm}^{-1}$ , while other samples (wheat straw) hydrolysates gave baseline at a higher intensity. The band centred at about  $6880\text{ cm}^{-1}$ , with high intensity due to O-H stretching 1<sup>st</sup> overtone band represents the high water content. C-H combination and 1<sup>st</sup> overtone regions did not show any apparent differences without the use of chemometrics. To study the baseline in more detail, it is essential to have different samples with different particle sizes or different scales of cloudiness levels. This can be obtained by using sawdust



particles in various particle sizes mixed in water or using coloured samples in different concentrations such as HMF or LGO. This can be carried out using a transfection probe. Also, it is possible to check particle size using solid samples after being sieved, such as sucrose, using the DRIFT sampling method. Later in this report, particle size will be discussed in more detail.

The O-H band at  $6880\text{ cm}^{-1}$  is one of the most important bands in NIR spectroscopy. It represents the highest 1<sup>st</sup> overtone band of aqueous samples in the NIR region. The intensity of this band represents the amount of O-H present in the sample. Therefore, it is easy to predict the amount of each chemical in your sample compared with the H<sub>2</sub>O sample. Figure 3.16 shows the different intensity levels of different samples for the 1<sup>st</sup> overtone band of O-H.

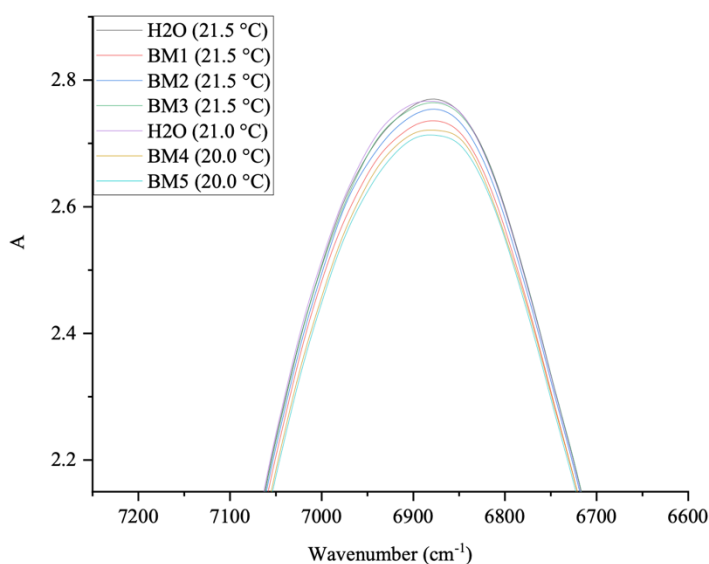


Figure 3.16 NIR spectra of biomass hydrolysates of O-H 1<sup>st</sup> overtone region at 21°C

The band at about  $6900\text{ cm}^{-1}$  corresponds to the water O-H 1<sup>st</sup> overtone band. The decrease in intensity of this band indicates the water contents in the sample. Figure 3.16 illustrates the difference between the OH vibration of biomass hydrolysate. As (Biomass 5) sample was treated longer than other samples (half an hour holding time in the MW at  $190\text{ °C}$ ), it showed the lowest band intensity. The longer the time hydrolysis is applied, the more chemical conversion occurs. Biomass 4 was slightly higher intensity as the holding time was 15 minutes. Biomass 1 and 2 have no holding time, so the difference in intensity is due to the

ratio of the wheat straw pellets and the water. Biomass 1 and 2 have a ratio of 1:10 and 1:20, respectively, making biomass 2 higher in water content presented in the band. Biomass 3 was the highest sample but slightly lower than H<sub>2</sub>O as it contains cellulose only.

*Table 3.1 Biomass samples for MW hydrolysis*

<b>Sample name</b>	<b>Sample contents</b>	<b>holding time (minutes) in MW at ... °C</b>	<b>Biomass to water ratio</b>
<b>Biomass 1 (BM1)</b>	Wheat straw	0 @ 190° C	1:10
<b>Biomass 2 (BM2)</b>	Wheat straw	0 @ 190° C	1:20
<b>Biomass 3 (BM3)</b>	cellulose	0 @ 220° C	1:10
<b>Biomass 4 (BM4)</b>	Wheat straw	15 @ 190° C	1:10
<b>Biomass 5 (BM5)</b>	Wheat straw	30 @ 190° C	1:10

### 3.4 Comparison between NIRS vs HPLC

#### 3.4.1 Individual samples

NIRS is a quantitative technique and can be used at real-time using fibre-optics. So, it is beneficial to check this ability and compare it with a more conventional method such as HPLC, as the latter technique is suitable for analysing aqueous solutions. HMF, LA and LGO were diluted in different concentrations of 0, 1, 3, 5, 7, 9 and 10 wt % in aqueous solutions. They were analysed using NIRS and the results compared with HPLC.

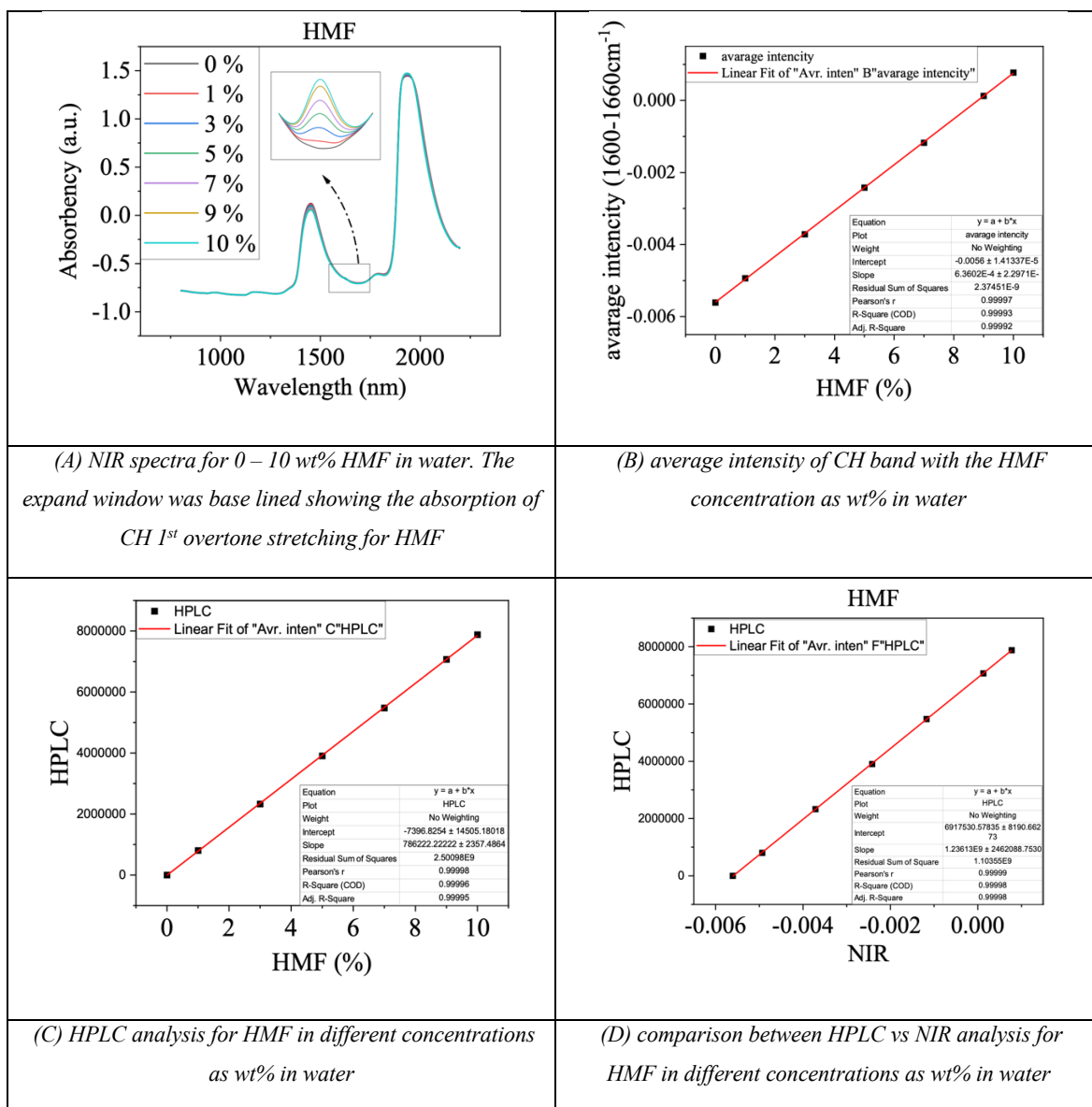


Figure 3.17 HMF quantitative analysis

HMF has a unique CH 1<sup>st</sup> overtone stretching band at 1622 nm, representing the slightly lower wavelength for alkene =C–H– band compared with alkane CH stretching. This is demonstrated in Figure 3.17 (A). This band is very useful for distinguishing the existence of the alkene. The CH 1<sup>st</sup> overtone band is located between the two big bands of OH combination and 1<sup>st</sup> overtone of the water. Therefore, it is not easy to quantitatively calculate the absorbency of the CH band of the HMF. However, it is possible when using the 2<sup>nd</sup> derivative or band deconvolution to eliminate the effect of those two bands of the water and isolate the CH band of the HMF.

In this case, the 2<sup>nd</sup> derivative was applied to correct the baseline and isolate the CH band. As the minima in the 2<sup>nd</sup> derivative represent a peak in the spectra, a negative sign was applied to the value to make it acceptable with calculations. This is shown in the expansion in Figure 3.17 (A).

There is an accurate linear regression between the HMF concentration and CH absorbency with an R<sup>2</sup> of 0.99993, as shown in Figure 3.17 (B). This makes NIRS a very suitable technique for concentration monitoring. On the other hand, HPLC is a beneficial and accurate method for this kind of analysis. But there are some issues with HPLC, such as time, solvents, cost, and many others. In our experiment, HPLC was used as a comparison technique.

The same samples were analysed using HPLC. An apparent separation was seen for the HMF samples in water. The area under the desired band was calculated for each sample. The results demonstrate a linear regression between the area under the band and the HMF concentration, as shown in Figure 3.17 (C). It is very accurate, as expected from this machine with an R<sup>2</sup> of 0.99996, similar to that obtained using NIRS. That makes NIRS a very robust technique for quantitative analysis. As demonstrated in Figure 3.17 (D), the accuracy of both techniques is very similar. When plotting results from HPLC against NIRS, a good linear relationship with an R<sup>2</sup> of 0.99998 was obtained.

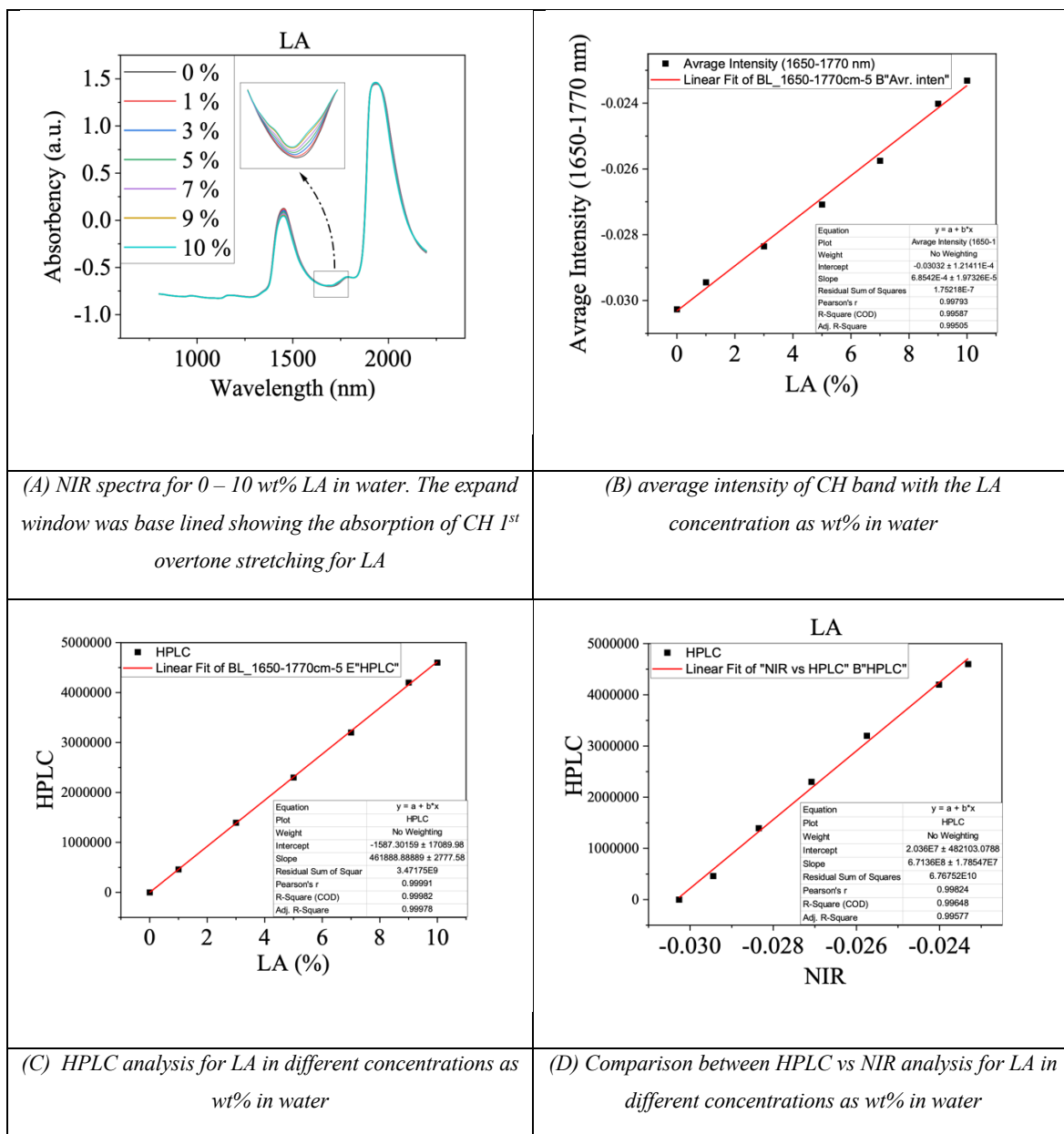


Figure 3.18 LA quantitative analysis

LA has no alkene, making its CH stretching band higher in wavelength than HMF. As demonstrated in Figure 3.18, the 1<sup>st</sup> overtone CH band if LA is detected at two positions. One is at 1688 nm, and the second is a smaller and broader band at 1732 nm. Those two bands represent two different CH absorptions for CH<sub>2</sub> and CH<sub>3</sub>, respectively. To compare this absorption with HMF is an easy way to distinguish between the two chemicals.

Baseline correction was applied to this experiment with LA to eliminate the mentioned issues of the water's high absorbency. There was no need for a 2<sup>nd</sup> derivative, but the whole range of CH bands intensity at (1650 – 1770 nm) was calculated. The average intensity of

each sample in this range was plotted against the concentration of LA. Figure 3.18 (B) demonstrates a linear regression with an  $R^2$  of 0.99587. That means the accuracy value of the results is similar to that obtained from the HMF experiment.

The samples were run in HPLC as well for comparison. LA was successfully separated in HPLC, and the area under the expected band was calculated quantitatively. The linear regression showed  $R^2$  of 0.99982 as expected from the HPLC technique. As shown in Figure 3.18 (D), the accuracy of HPLC vs NIRS is very similar. When plotting the results of the two methods, they show a linear regression with an  $R^2$  of 0.99648, representing a similarity between the two methods.

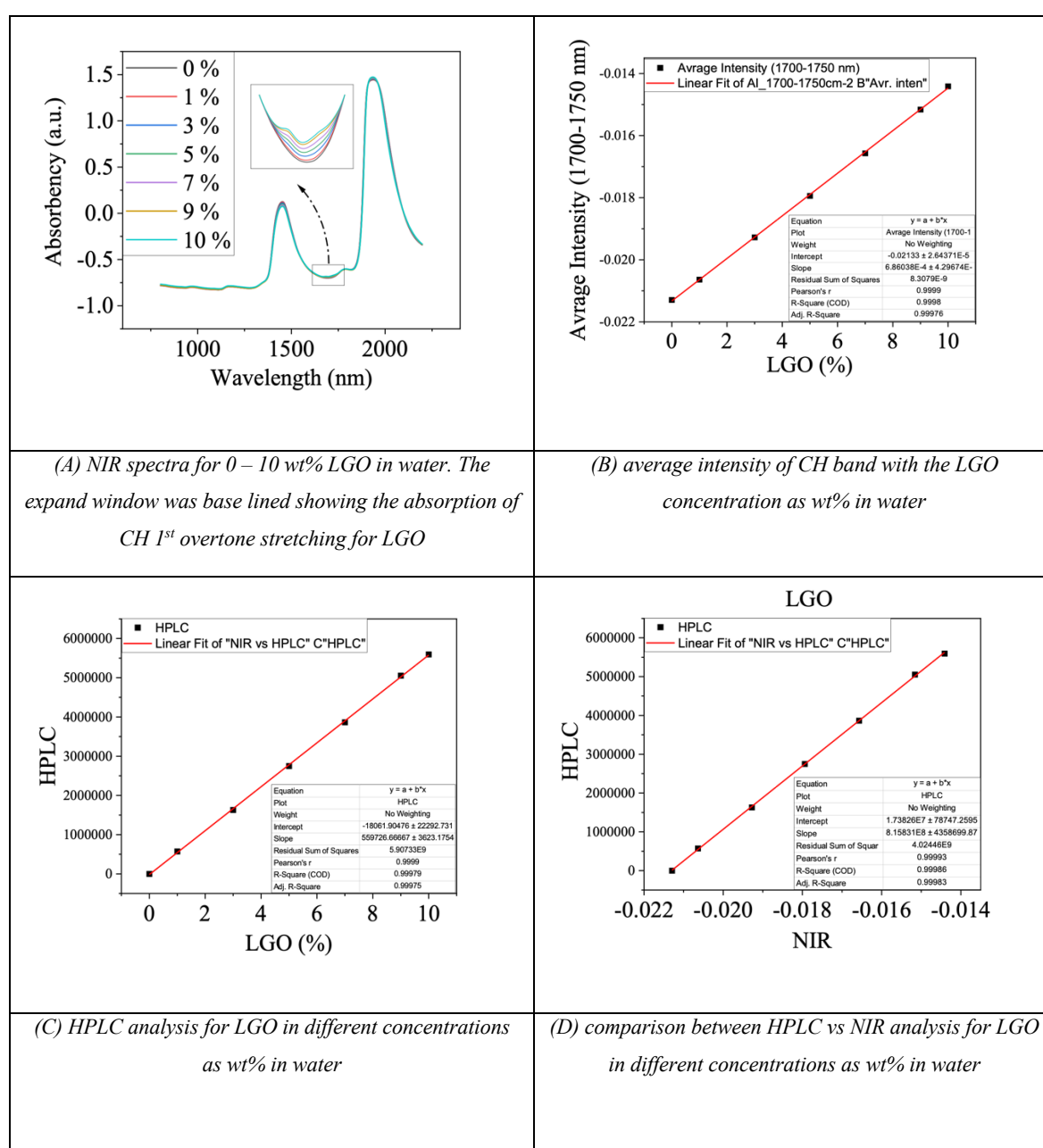


Figure 3.19 LGO quantitative analysis

It is expected that LGO will interfere with HMF in absorbency as both contain alkene functional groups. This is no longer the case. LGO contains alkene but not when dissolved in water. When the LGO is dissolved in water, the alkene bonds forms an hydroxyl groups on one side and a CH<sub>2</sub> on the other side of the (original) alkene. No longer lower wavelength band is observed. (This is presented in more detail in chapter 5). The 1600 – 1750 nm range was baselined, and an average intensity was calculated. The average intensity of the CH band was plotted against LGO concentration wt% in water. Similar to the previous experiments, very accurate linear regression was observed with an R<sup>2</sup> of 0.9998, as displayed in Figure 3.19.

On the other hand, HPLC successfully separated the LGO from water and the area of bands was calculated quantitatively. The linear regression with R<sup>2</sup> of 0.99979 for the calibration curve of HPLC results. To compare the two methods, it is illustrated in Figure 3.19 (D) that the accuracy of HPLC vs NIRS is very similar, with a very accurate linear relationship of R<sup>2</sup> 0.99986 representing the robustness of the two methods.

Based on the previous experiments on different concentrations of HMF, LA and LGO. NIR spectroscopy is an ideal method to be used online for quantitative measurements and can obtain similar accuracy as HPLC but in a greener way.

### 3.4.2 Mixtures

In this section, two compounds in different ratios were mixed and tested by NIRS. This experiment aims to identify whether NIRS can detect these different ratios quantitatively. The focus will be on the CH 1<sup>st</sup> overtone vibration range due to the high absorbency of the water OH bands mentioned earlier. It is expected to identify the different CH bands in the same solution in mixtures. It is easier to separate the alkene or alkyne CH from alkane CH within the same spectra. The CH stretching band moves towards a lower wavelength with a higher degree of unsaturated carbon in the compound.<sup>50, 77</sup> Based on this method, different ratios of two chemicals were experimented. Mixtures of HMF & LA, HMF & LGO and LA & LGO were prepared in different ratios of % (0 : 0), (0 : 10), (1 : 9), (3 : 7), (5 : 5), (7 : 3), (9 : 1) and (10 : 0). All samples were dissolved in water. For example, (0 : 0) was a sample of the water only, and HMF & LA (3 : 7) is an aqueous solution of 3 wt % of HMF mixed with 7 wt% of LA and so on.

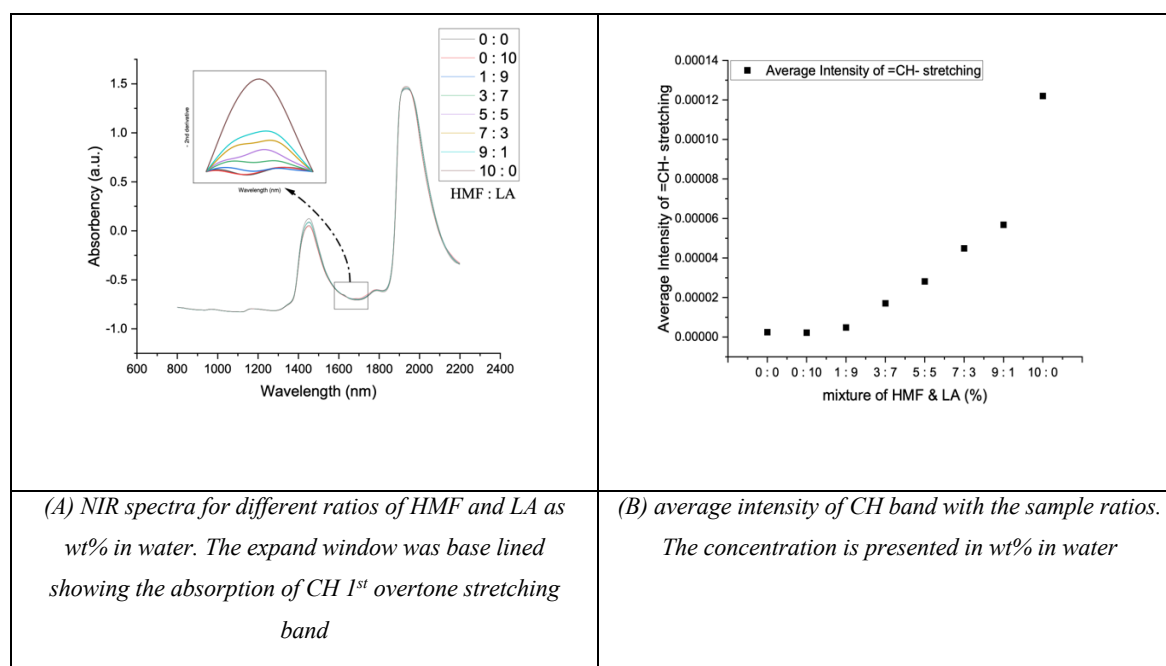


Figure 3.20 HMF : LA quantitative analysis

Mixtures of HMF and LA in different ratios were analysed using NIR spectroscopy. As the two chemicals have different CH bonds and HMF absorption is unique due to the alkene =C–H– band, it is expected that the CH band in this region to be calculated as an indicator of HMF. It is shown in Figure 3.20 (A) that the band at 1622 nm increases with increasing



HMF ratio in the mixture. The second derivative with a negative sign was applied to this region to correct the baseline and have positive values. The average intensity of this region was plotted against the different ratios of the two chemicals, as shown Figure 3.20 (B). It is shown clearly that the first two points with no absorbency in this region coincide to when no HMF is present in the sample. Then starting from the 3<sup>rd</sup> point at a 1 : 9 ratio, there is a linear regression up to the ratio of 9 : 1. Unexpectedly, the 10 : 0 ratio jumped to a higher intensity than was expected. This phenomenon happened when the LA was absent. In other words, the presence of LA lowers the intensity of the alkene =C–H– band. The LA may form hydrogen bonds with the water, increasing the pH and making the two big bands of OH combination and 1<sup>st</sup> overtone wider than the sample with only HMF. This will affect the absorbency of the small CH band in between OH bands, especially when applying baseline correction.

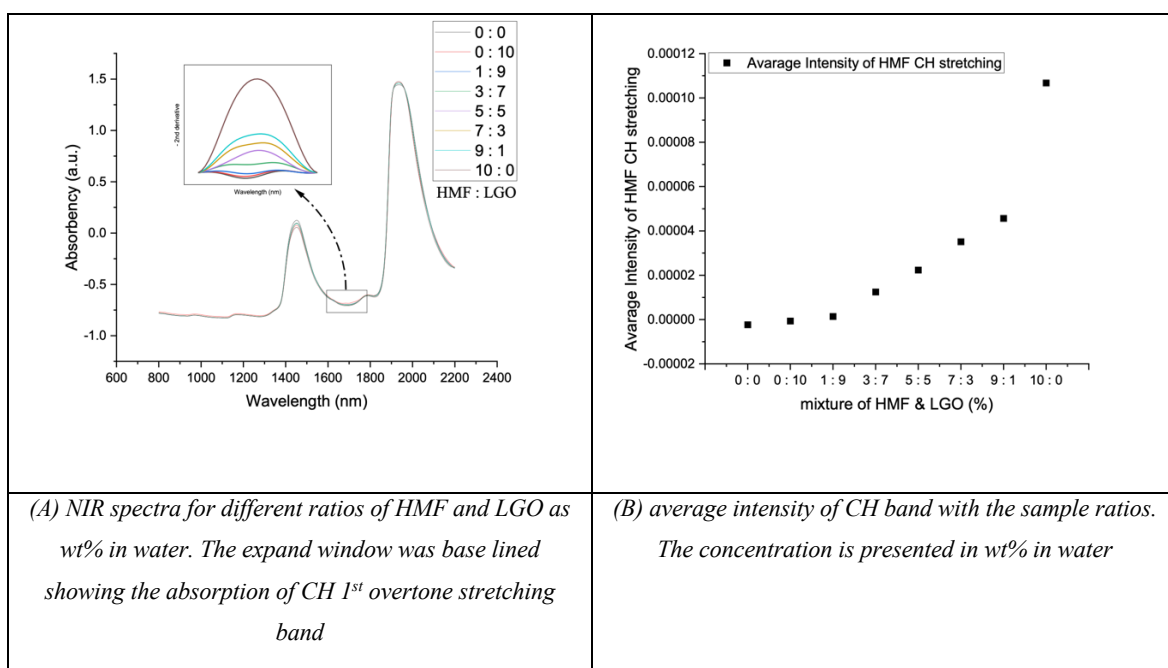


Figure 3.21 HMF : LGO quantitative analysis

Similar process to the previous experiment of HMF:LA, mixtures of HMF and LGO in different ratios were analysed using NIR spectroscopy. As HMF is present in this mixture, the unique alkene =C–H– the band will be used to monitor the change in the ratio of those two compounds in the mixture. When HMF was added to the mixture (1 : 9), its band

intensity rose, as shown in Figure 3.21 (A). Linear regression was started from (1 : 9) to (9 : 1) but the (10 : 0) ratio sample again jumped to higher intensity.

To compare this mixture with HMF and LA, a similar phenomenon happened when using HMF and LGO. As it is now known that the LGO forms hydrogen bonds with the water and converts to the Cyrene triol, it is now acceptable to see the 10 : 0 ratio get to higher intensity than expected. That is due to more OH bands making the bands wider. This affects the CH band of HMF when mixed with LGO. This sensitivity for NIRS towards hydrogen bonding gives a potential success to this method to be used in this field with an ability for online monitoring.

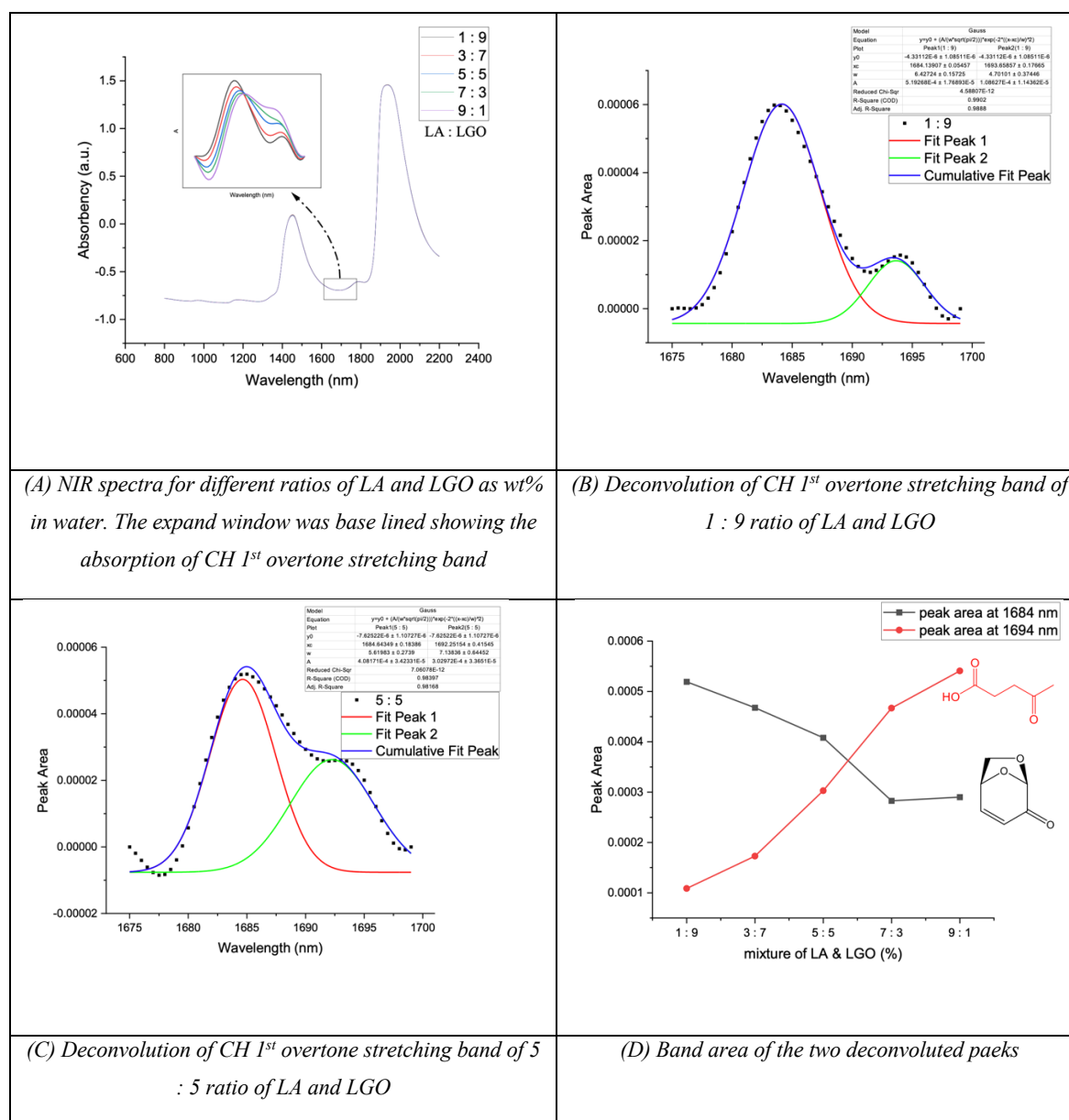


Figure 3.22 LA : LGO quantitative analysis

In this experiment, mixtures of LA and LGO were analysed using NIRS in different ratios (1 : 9) to (9 : 1). As LGO converts to triol when mixed with water, no alkene CH is observed. Therefore, the two compounds show closer bands of CH to each other (1694 and 1684 nm) for LA and LGO, respectively. In this case, the 2<sup>nd</sup> derivative is no longer helpful. Instead, deconvolution of overlapped bands was applied successfully to discriminate between the two compounds. Figure 3.22 (A) demonstrates the two different ratios of LA and LGO with deconvolution of their spectra. The area under each deconvoluted band was plotted against the various ratios in Figure 3.22 (D). This figure shows how the different CH band intensity increases/decreases with the concentration change.

### 3.5 Real-time analysis of (Cyrene : LGO) in different ratios

Cyrene and LGO have similar chemical structures. The only difference is that the LGO contains an alkene group while Cyrene does not. That leads to a significant difference in terms of IR vibrations of these two molecules. By focussing on the CH stretching range in IR spectroscopy, it is clear that alkene shows a band at a higher wavenumber than alkane. Figure 3.23 shows the difference between Cyrene and LGO in the fundamental and 1<sup>st</sup> overtone vibrations of CH stretching.

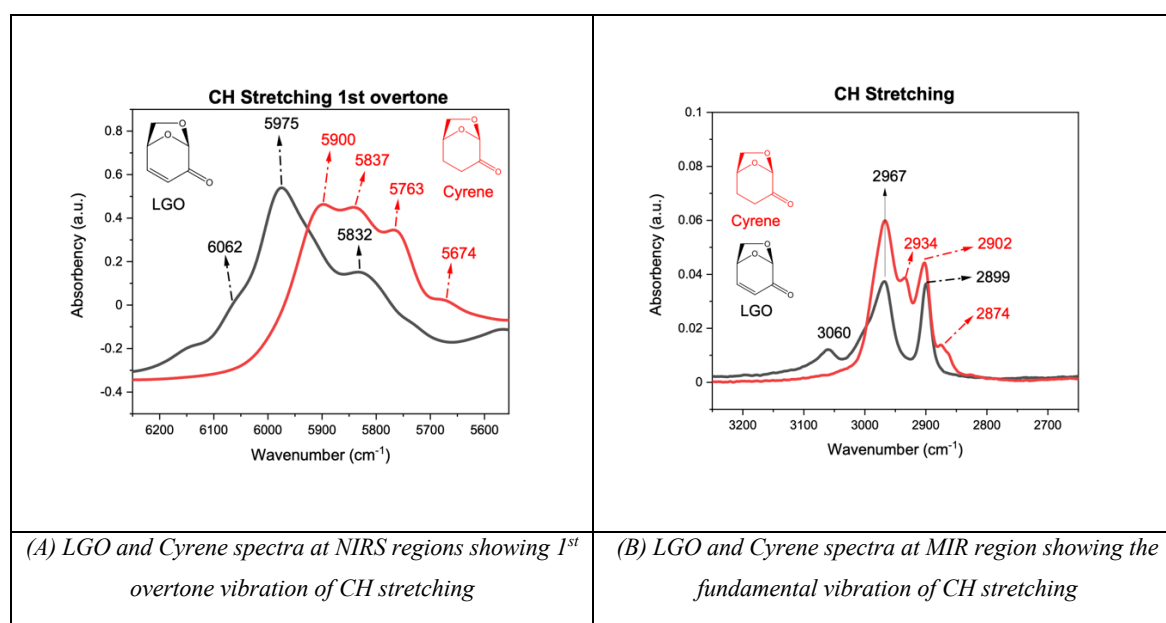


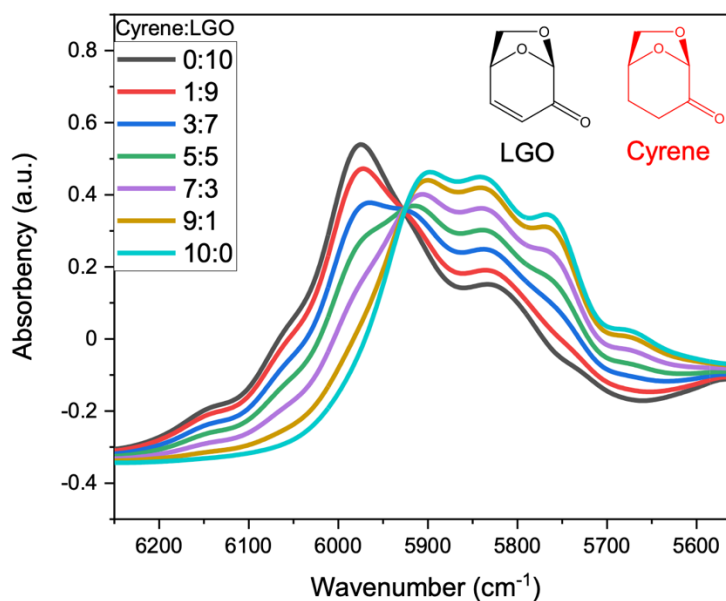
Figure 3.23 CH vibration of LGO and Cyrene

Cyrene contains about four different bands at 2967, 2934, 2902 and 2874 cm<sup>-1</sup> for different CH species in the molecule. LGO, on the other hand, shows about three different bands at 3060, 2967 and 2899 cm<sup>-1</sup>. It is clear that the band at 3060 cm<sup>-1</sup> corresponds to the alkene vibration and shares a similar band positions to Cyrene.

The 1<sup>st</sup> overtone region reveals more information in compare with the fundamental vibration. NIR spectra of Cyrene and LGO show a higher intensity and a broader range of bands compared with MIR. That makes it easier to separate between CH species in each molecule in mixtures. Figure 3.23 (A) shows Cyrene and LGO spectra within NIR spectroscopy at the 1<sup>st</sup> overtone region. Table 3.2 shows the fundamental and the 1<sup>st</sup> overtone CH stretching for Cyrene and LGO.

Table 3.2 Chemical assignments of CH stretching for LGO and Cyrene

Sample	band	Vibration of ( $\text{cm}^{-1}$ )				
		=CH-C	CH	CH <sub>2</sub>	CH	CH <sub>2</sub>
Cyrene	fundamental		2967	2934	2902	2874
	1 <sup>st</sup> overtone		5900	5837	5763	5674
LGO	fundamental	3060	2967		2899	
	1 <sup>st</sup> overtone	6062	5975		5832	

Figure 3.24 The 1<sup>st</sup> overtone vibration of LGO and Cyrene mixtures

The CH 1<sup>st</sup> overtone region is the best region in NIRS to discriminate between Cyrene and LGO. As shown in Figure 3.24, there is an apparent transformation between LGO bands to Cyrene bands as the ratios change towards one another. By comparing Figure 3.23 (A) with Figure 3.24, one can observe that the same bands appear in different ratios depending on the concentration of each component. Bands are overlapped, so either deconvolution or 2<sup>nd</sup>

derivative may help to reveal more details of each band and its abundance. Note that the 2<sup>nd</sup> derivative minima correspond to bands in the original spectrum.

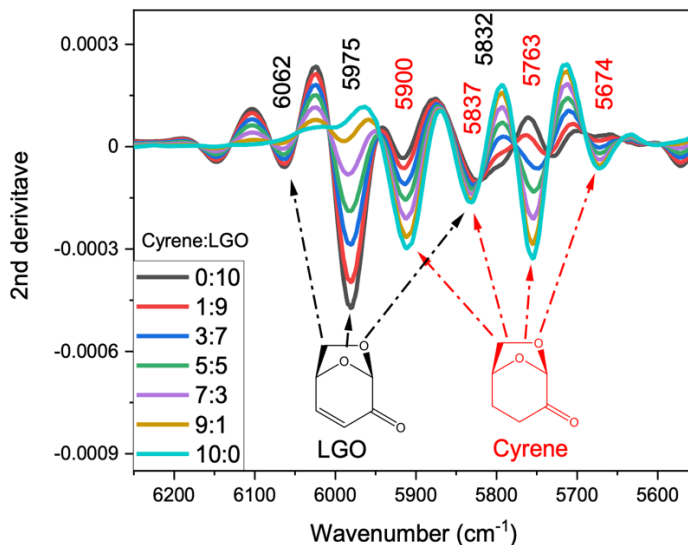


Figure 3.25 The 2<sup>nd</sup> derivative spectra of LGO and Cyrene mixtures

It is helpful to apply the second derivative, as shown in Figure 3.25. The LGO corresponds to 3 minima while four minima are shown by Cyrene. They are at the same position as illustrated in Figure 3.24 but the 2<sup>nd</sup> derivative reveals more differences.

### 3.6 The effect of temperature on water detected by NIRS

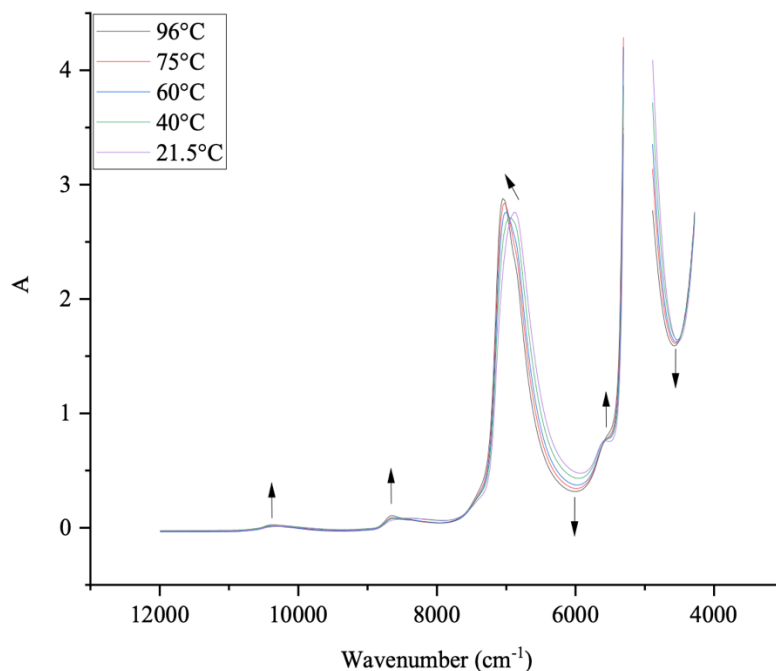


Figure 3.26 NIR spectra of water in variable temperature

The spectrum of water is very susceptible to temperature when using NIRS. The spectra of water at variable temperatures show significant differences, as shown in Figure 3.26. The arrow's direction indicates the change in band intensity with increasing temperature. The most significant change is the band of the O-H stretch 1<sup>st</sup> overtone at about 7000 cm<sup>-1</sup>. This is a dramatic change in the water spectrum.

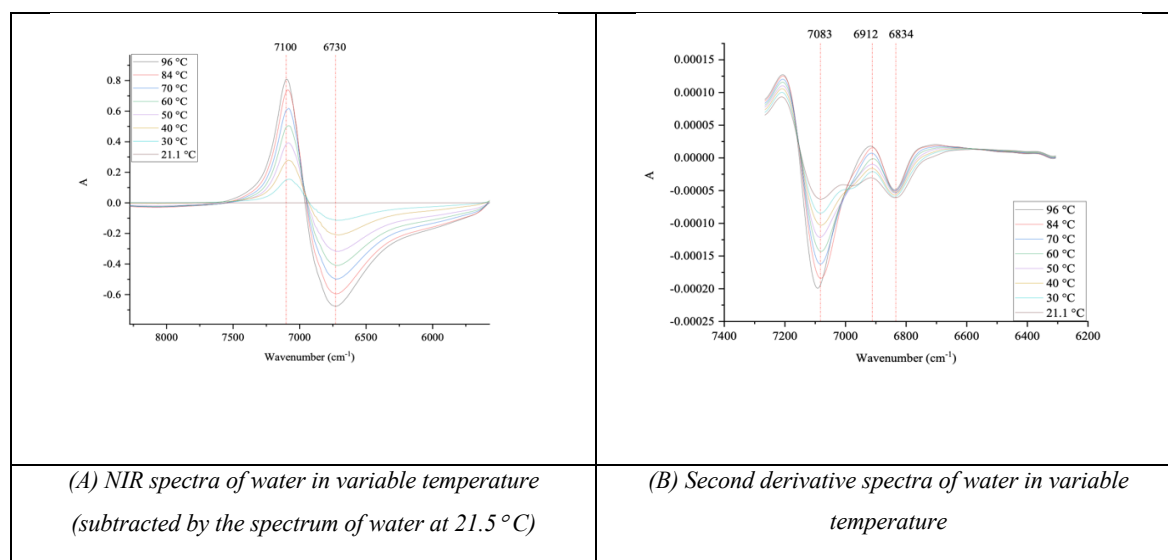


Figure 3.27 Subtraction and 2<sup>nd</sup> derivative methods for water spectra in variable temperature

Figure 3.27 (A), illustrates the water spectra at variable temperatures after subtraction. The spectrum at 21.5 °C was taken as a reference spectrum. The reason for applying the subtraction method is that it is very effective in helping to detect tiny differences or changes in spectra. There is indeed a trend in spectra with changing temperature, as displayed in Figure 3.27 (A). As the temperature rises, there is a decrease in band intensity at 6730 cm<sup>-1</sup> and an increase in band intensity at 7100 cm<sup>-1</sup>. Figure 3.27 (B) reveals more differences in terms of the O-H band. The differences in bands at 7083 and 6834 cm<sup>-1</sup> represent the behaviour of these two bands at 21 – 96 °C. At higher temperatures, the band at higher wavenumber increases more sharply. In comparison, the band at 6834 cm<sup>-1</sup> only shows a slight decrease.

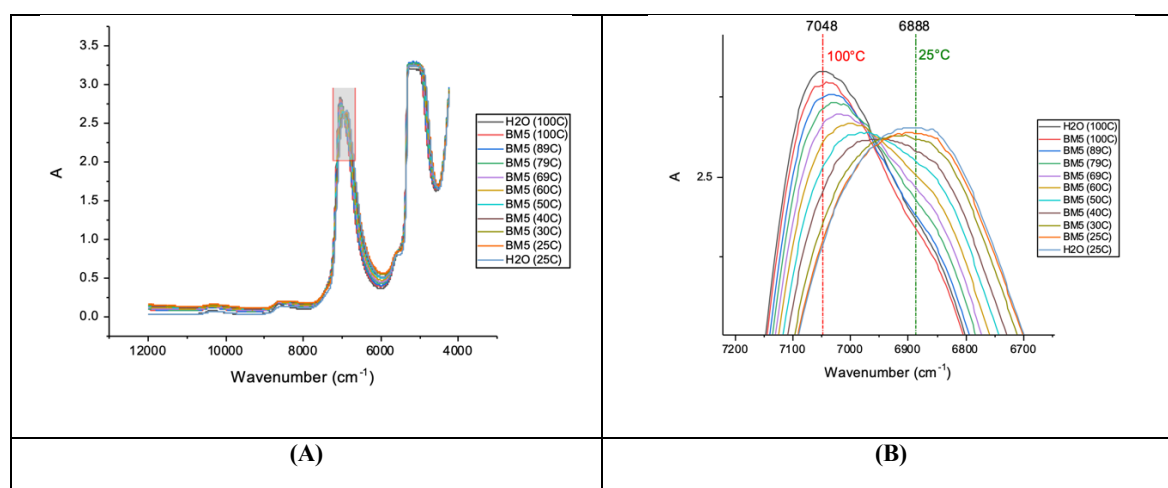


Figure 3.28 NIR spectra of (sample BM5) in variable temperature



Two observations can be made from Figure 3.28. Firstly, the vibration band of O-H 1<sup>st</sup> overtone is very sensitive to temperature. The band was shifted 160 wavenumbers from 6888 cm<sup>-1</sup> to 7048 cm<sup>-1</sup> between 25 – 100 °C. Secondly, the band at lower temperatures seemed to be one broad, strong band, while at higher temperatures, a second band at higher wavenumber is apparent in addition to the first band. As the temperature rises, the second band becomes stronger than the first band. That is due to the effect of the water hydrogen bonding. As the temperature increases, the more free OH are dominant, increasing the band at higher wavenumber. Simultaneously, the hydrogen bonds become less dominant decreasing the band at the lower wavenumber. This is discussed in more detail in chapter 5.

### **3.7 O-H 1<sup>st</sup> overtone of water and sugar**

The water spectrum shows a strong band centred at 6896 cm<sup>-1</sup> due to the O-H stretch 1<sup>st</sup> overtone. The spectra of neat sugars have relatively low intensity and broad bands almost in the same region (6000 – 7000 cm<sup>-1</sup>), as shown in Figure 3.29. Sucrose, in particular, has a distinct sharp band at 6960 cm<sup>-1</sup> compared with other sugars. This band is due to the free OH hydrogen bonds. It appears at higher wavenumber than OH hydrogen bonds. The free OH band for the sucrose spectrum is sharp because it does not participate with other hydrogen bonding to other neighbouring molecules<sup>88</sup> and it is assigned to the C4 hydroxyl group.<sup>89</sup>

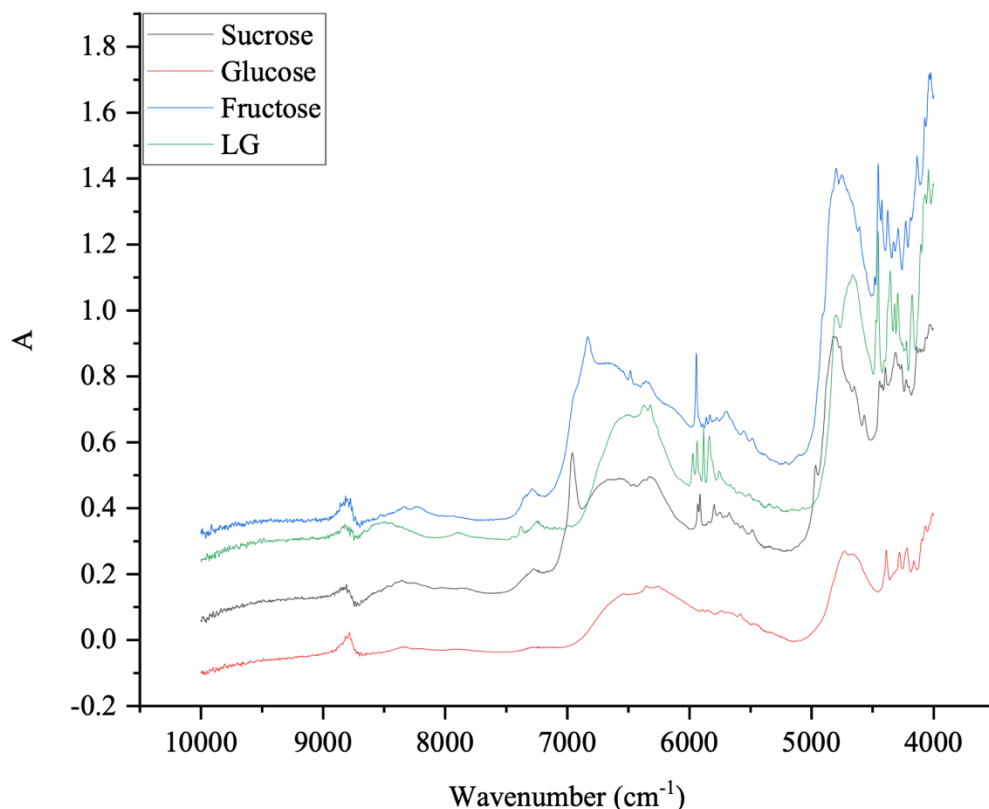


Figure 3.29 NIR spectra of neat solid samples using (DRIFT) technique

In general, the O-H 1<sup>st</sup> overtone band of sugars dissolved in water is not easy to see due to the overlapping high-intensity band of water O-H, including the sharp band of sucrose at 6950 cm<sup>-1</sup> for free O-H band.<sup>90</sup> However, subtraction of the water spectrum may make a significant difference.

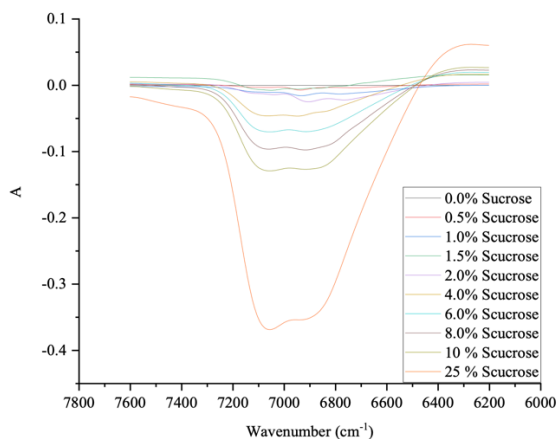


Figure 3.30 NIR spectra of diluted sucrose (water spectrum was subtracted)

It is expected to see a negative band (minima) when subtracting the water spectrum. The water band has a higher intensity than that of diluted sugars. Therefore, 1.0 % sucrose has more water than 8.0 % sucrose. The latter shows a stronger negative band when applying the spectral subtraction method. Figure 3.30 shows the region (6200 – 7600  $\text{cm}^{-1}$ ) after subtraction using the water spectrum as a reference. At low concentrations, it is not easy to study the behaviour of the band due to the potential change in properties of water O-H after dissolving sugar. In other words, the water O-H has changed after dissolving a sugar. So, it was decided to use the concentration of 2 % as a reference for subtraction instead of the water spectrum. Testing the sample at different temperatures may help find the small sharp band of sucrose by shifting the water O-H band.

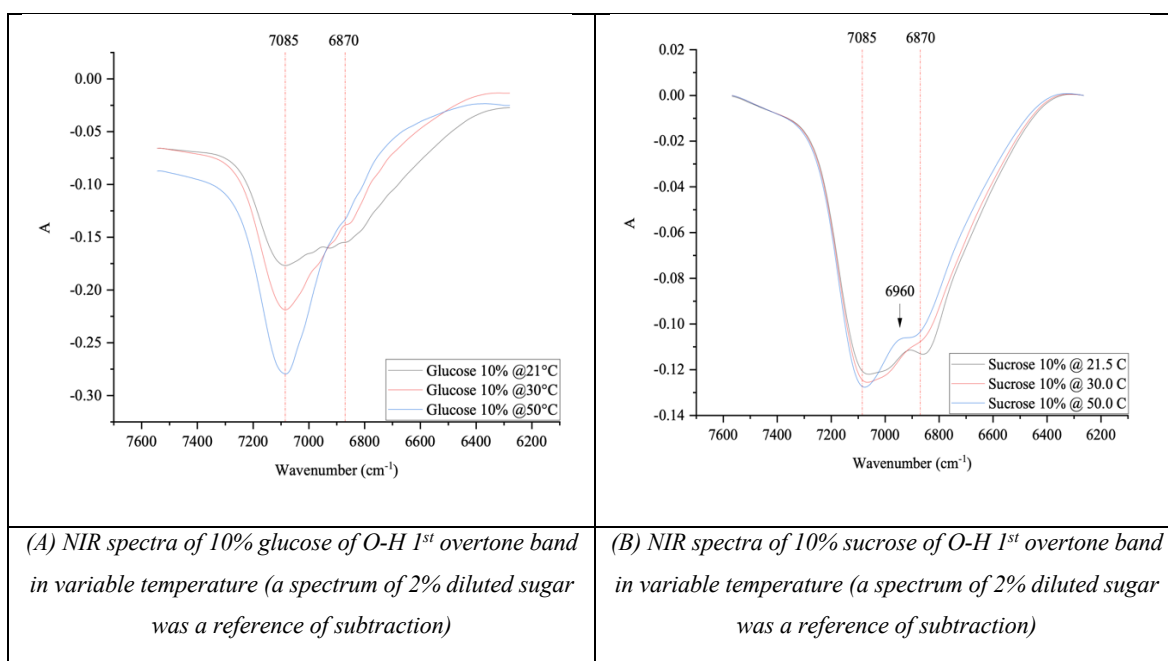


Figure 3.31 NIR spectra of sugars using subtraction method

As expected, the subtraction method successfully detects the O-H 1<sup>st</sup> overtone band of sucrose, as illustrated in Figure 3.31 (A). So, the band of solid sucrose at 6960  $\text{cm}^{-1}$  was observed in its water solution. The glucose, in contrast, does not have the same sharp band of free OH as shown in Figure 3.31 (B).

### 3.8 Conclusion

The extremely high absorption of the water vibration affects the NIR spectra of diluted samples of sugars and anhydrosugars. However, information about the compounds, such as the CH 1<sup>st</sup> overtone and CH combination vibration, may still be obtained. The sample's spectrum was improved, revealing more prominent bands of the CH 1<sup>st</sup> overtone vibration by employing an appropriate spectral subtraction approach. As a result, it was demonstrated improved discrimination between the CH vibrations of sugars.

Accurate quantitative measurements were obtained for some sugars and their derivatives using NIR spectroscopy. The figures suggested a linear regression between NIR spectroscopy and HPLC which reflects the accuracy of NIRS. Results show  $R^2$  in the range of (0.99998 – 0.996480), demonstrating how NIRS can be trusted as a reliable real-time quantitative technique. It can obtain similar accuracy to HPLC but in a “greener” way.

NIRS is a good technique for tracking the conversion of LGO to Cyrene in real-time. Although the real solution does not contain pure LGO or Cyrene, it is helpful to analyse the purest components first and then investigate the real solution. Additionally, pure compounds will be ideal for use as a standard for the last phase of a process or industrial quality control.

The variable temperature experiment of water reveals potential discrimination of the different OH species. This method can be applied to liquid and solid samples to detect water content, hydrogen bonding and enthalpy change  $\Delta H$ . In the following two chapters, variable temperature will be applied using NIRS.

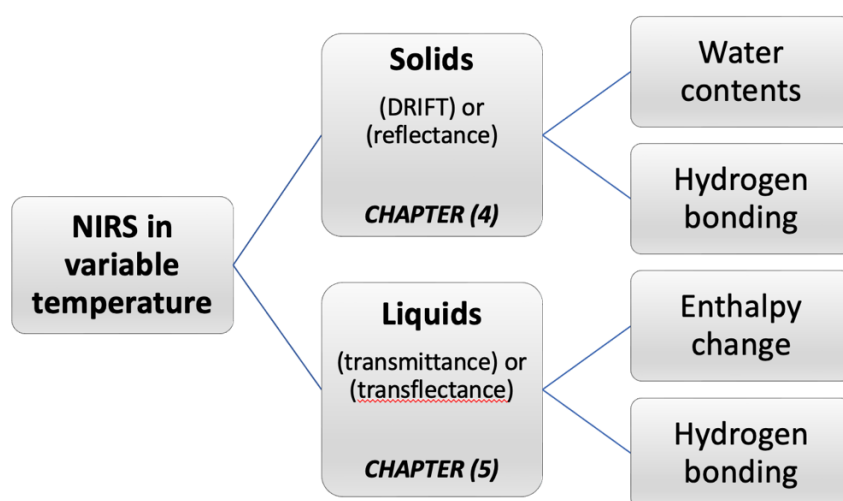


Figure 3.32 The potential work which can apply variable temperature using NIRS

## Chapter 4: NIR Spectroscopy for solid samples

### 4.1 Introduction

One of the advantages of using NIRS is the ability to study several parameters simultaneously. For example, from one spectrum, it is possible to obtain information on the physical and chemical composition of a sample: particle size,<sup>67, 91-93</sup> chemical characterisation of a sample and moisture content.<sup>54</sup> This chapter reports particle size and moisture contents measurements of biomass, pure sugars, and anhydrosugars. It is essential to investigate the water contents of the biomass whenever it is used or stored. Several factors affect the chemical change in sawdust, including particle size and moisture contents especially in outdoor storage. For instance, there is a real need to monitor the chemical change (the degree of maturity) in the pellet storage using a rapid and non-destructive method.<sup>70</sup> NIRS shows potential in replacing more conventional GC/MS. Arshadi *et al.*<sup>70</sup> carried out a study of determining how pine and spruce sawdust's chemical and physical properties are affected during outdoor storage. They have concluded that NIRS showed how changes in moisture content of the sawdust is important for monitoring sawdust's maturity and some other parameters.

Measuring moisture contents in biomass is essential for biorefinery processes. It significantly impacts the net calorific value of the given fuels. Currently, the standard method involves drying the biomass in an oven at 105 °C for one day.<sup>94, 95</sup> With many loads of biomass, it is expected that it is not stored in a suitable place before feeding it to the boiler where they may be subject to water vapour from the surrounding air. That makes it difficult to accurately predict the moisture contents, resulting in inefficient combustion. So, there is a need to use a fast and accurate method to predict the biomass moisture contents easily before processing. Some researchers are developing a new method for moisture contents measurements, including electric meters using capacitance technology<sup>96, 97</sup> and Metro MR moisture analyser using nuclear magnetic resonance.<sup>94</sup> Although both techniques work well and fast, they need a lab, and the sample will be brought to the lab.

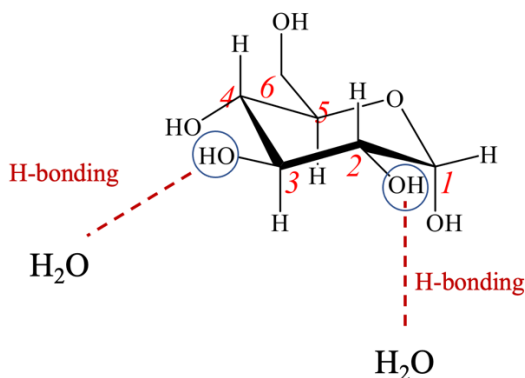
Another example of the importance of measuring the moisture content adsorption in starch-based materials has been recognised and reported in the literature.<sup>70, 98-100</sup> The adsorption of water in ethanol production plays a significant role in energy consumption. An alternative route for this process was recognised to reduce energy consumption. To produce alcohol using the distillation process consumes a lot of energy. Ladisch and Dyck<sup>98</sup> have found an

alternative route by preferential water adsorption using cellulosic and starchy materials. NIRS was successfully used to distinguish between the adsorption performance on the surface of different carbohydrate materials.<sup>100</sup>

On the other hand, it is essential to discuss the ability of carbohydrate to adsorb water molecules. The desiccant properties of the carbohydrate materials are due to the free hydroxyl group bonded to the water molecules by the hydrogen bonding. Rebar *et al.*<sup>99</sup> found that branched glucose units in the amylopectin increase the ability to absorb water more than the linear glucose units in the amylose.<sup>99</sup> The branch structure of amylopectin enables the overlapping of OH – groups which then attract the water molecules where they will be trapped. Cellulose, in contrast, has very low water adsorption due to the flat sheet formation of the glucose unit chains, which lie on top of one another, held firmly by hydrogen bonding.

This finding was also observed by Christy<sup>100</sup> who has used NIRS for the same materials. The two sets of results are consistent, suggesting that the NIRS, with its ability to detect these differences in real-time, could add value to the greener analytical chemistry. Christy<sup>100</sup> investigated the water adsorption for some carbohydrate polymers such as amylose, amylopectin, cellulose, and other chemicals in the region 5000 – 5300  $\text{cm}^{-1}$ . This region shows a combination of OH groups from water connected by a hydrogen bond to the hydroxyl group of carbohydrate molecules and some other sites of the polymer.<sup>100</sup> In this region, however, carbohydrates do not show any absorbance, making this region ideal for detecting any water contents in the polymers. It is found that the different polarities of OH groups play a significant role in water adsorption in which the OH group of water is connected to the C2, C3 and C6-OH group of the glucose unit of the polymer. The band at (5100 – 5300  $\text{cm}^{-1}$ ) increases over time of adsorption monitored by NIRS.

Christy found that bands at 5190, 5246, 5210 and 5165  $\text{cm}^{-1}$  represent the adsorption of water molecules on hydroxyl group at C6, C2+C3, C4 and C1-OH groups, respectively. He also found that the rate of adsorption of C2-OH + C3-OH is higher than that of C6-OH and C1-OH groups of glucose units of amylose as illustrated in figure 4 in his article. Interestingly, the C2- and C3-OH groups of the glucose unit of the polymer have a higher chance of water adsorption than other carbon positions. It describes how the location of the hydroxyl group inside the molecule influences the creation of hydrogen bonds.



*Scheme 4.1 Glucose unit of amylose*

Another experiment was done by the same author studying the adsorption of water on silica gel surfaces.<sup>101</sup> They found that the adsorption of water molecules on silica gel materials takes place instantly on silanol groups with hydrogen bonding. So many other solid samples have been analysed using NIRS and are well reported in the literature; examples include wheat flour, Aspirin tablets, sugar cane and grains.<sup>54</sup>

This chapter used the NIRS approach to study biomass analysis, including carbohydrates and sawdust. The instrument detected different parameters such as particle size, hydrogen bonding and moisture contents.

## 4.2 Measuring particle size using NIRS

This experiment was carried out to determine how NIRS can predict particle size. Two different sampling methods were used. The first sampling method was DRIFT on sucrose powder with various particle sizes. The second sampling method was a transfection fibre-optics probe for liquids, including particles.

### 4.2.1 Particle size for pure sugar

In this experiment, a sample of sucrose with different particle sizes were analysed. Samples of 75 – 125 , 125 – 180 , 180 – 250 , 250 – 500 and above 500  $\mu\text{m}$  (area of sphere 31400, 73024.6, 145146.5, 441562 and 1766250  $\mu\text{m}^3$  respectively) were sieved and analysed using NIRS. Samples were placed in DRIFT sampling cells.

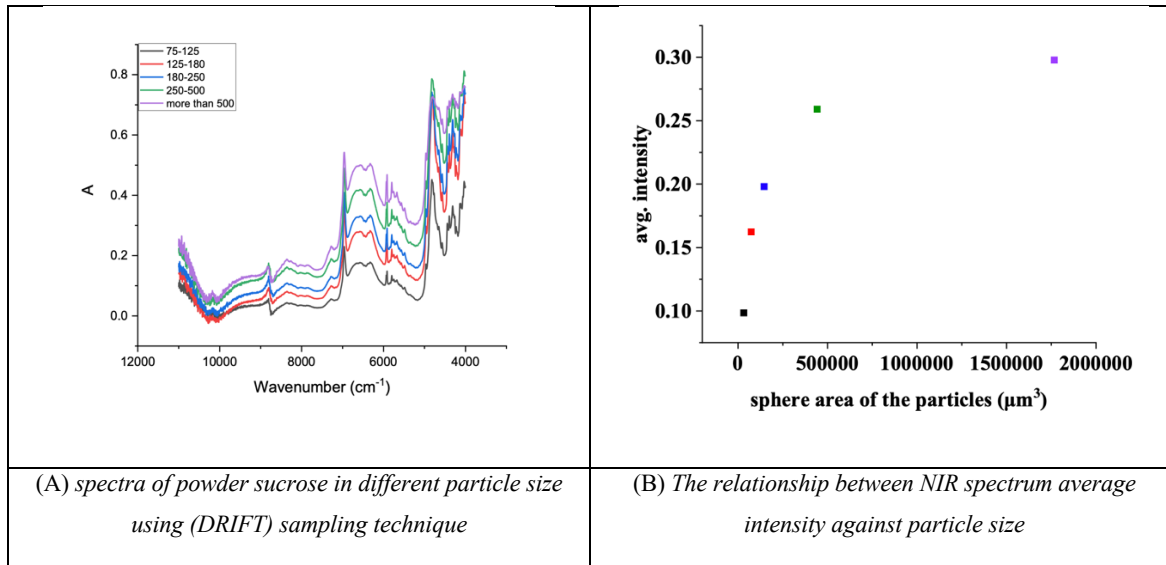


Figure 4.1 NIR spectra of sucrose in different particle size

As illustrated in Figure 4.1, sucrose spectra with different intensity levels show a dependence on particle size. The intensity of the spectrum increases with the particle size. The average intensity of each spectrum was taken, and they were plotted against the average size of the particles. It was found that there is a linear regression between particle size and the average intensity of the spectrum of the same sample. However, to succeed with more accurate results, narrowing down the particle size scale should be done and different species need to be studied.

This approach can be used with a specific online fibre-optics probe to check moisture content in biomass before processing in a biorefinery. In addition, at some stages of a biorefinery, a mixture of liquid and solid may be included in the process. The transfection technique will be efficient for solids in liquids samples such as a slurry. The following section describes results from some solids in liquid.

#### 4.2.2 Particle size for sawdust in water

This experiment was conducted using water and four different known sizes of beech and unknown size of wheat straw pellets mixed with water to study this approach.



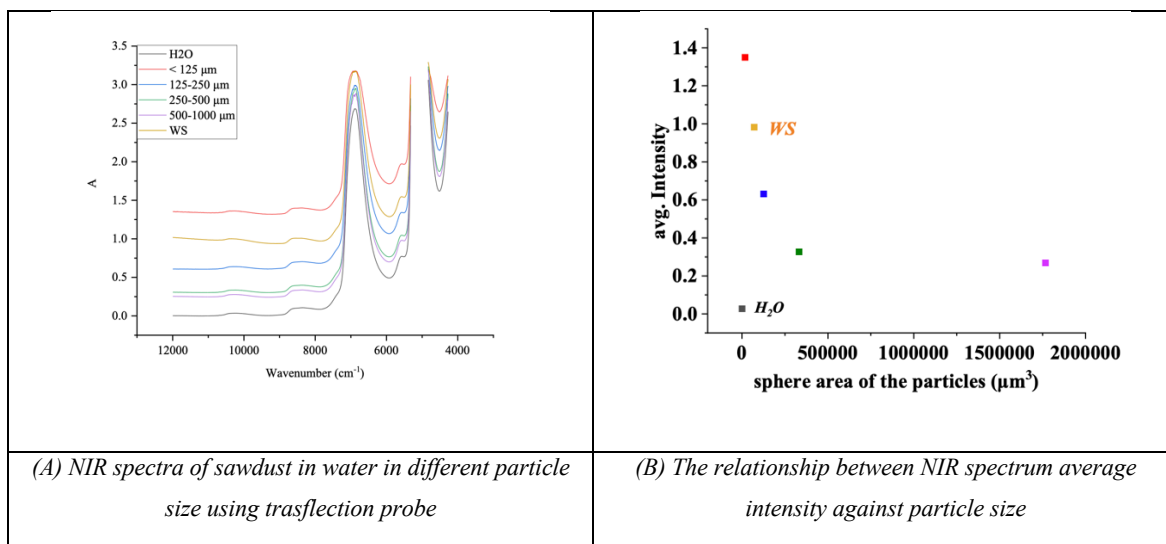


Figure 4.2 NIR spectra of sawdust in water in different particle size

Sawdust (beech) was sieved in different particle sizes. < 125, 125 – 500, 250 – 500, and 500 – 1000 μm (area of sphere 17662.5, 125600, 331662.5 and 1766250 μm<sup>3</sup> respectively) each was mixed with DI water in 1:10 ratio. A transfectance probe was used to examine the sample in a beaker with a stirrer bar to be analysed by NIRS fibre-optics probe.

The transfectance probe provided spectra with different baseline intensity levels, like the previous experiment using DRIFT, as illustrated in Figure 4.2. It was found that the baseline intensity of the spectrum increases with decreasing particle size. There is a linear regression between particle size and baseline. For particles above 500 μm, it seems that the particles cannot go through the probe cavity as the path length of the cell is 2 mm. However, the unknown size of wheat straw (WS) pellets was plotted within the particle size 125 – 250 μm (70650 μm<sup>3</sup>), where it is supposed to be as shown in Figure 4.2.

This technique can be helpful, as an online monitor, during thermal biomass conversion using MW (hydrolyses or pyrolysis) treatment. It can be used as an online monitoring detection technique inside the MW to control the process and selectively choose the best condition. NIRS was successfully used for some physical parameters. The following section studies the hydrogen bonding and its changes with changing temperatures.

### 4.3 The Hydrogen bonding for solid samples

The 1<sup>st</sup> overtone region for the OH stretching band is broad and occurs between 6211 – 7092 cm<sup>-1</sup>. According to Seyer *et al.*<sup>88</sup>, the absorbance of sucrose in the NIRS region is distributed

over  $700\text{ cm}^{-1}$ . The majority corresponds to the hydrogen bonding absorbance. They have worked out an assignment of eight OH vibrational bands for sucrose. The vibrational bands at  $6300$ ,  $6560$ ,  $6610$ ,  $6700$ ,  $6760$ ,  $6820$ ,  $6880$  and  $6980\text{ cm}^{-1}$  were respectively associated with intermolecular, 2 intramolecular, 4 intermolecular and non-bonding groups. Similar work was done for the MIR region with the same eight fundamental bands, which agreed with Seyer *et al.*<sup>102</sup>

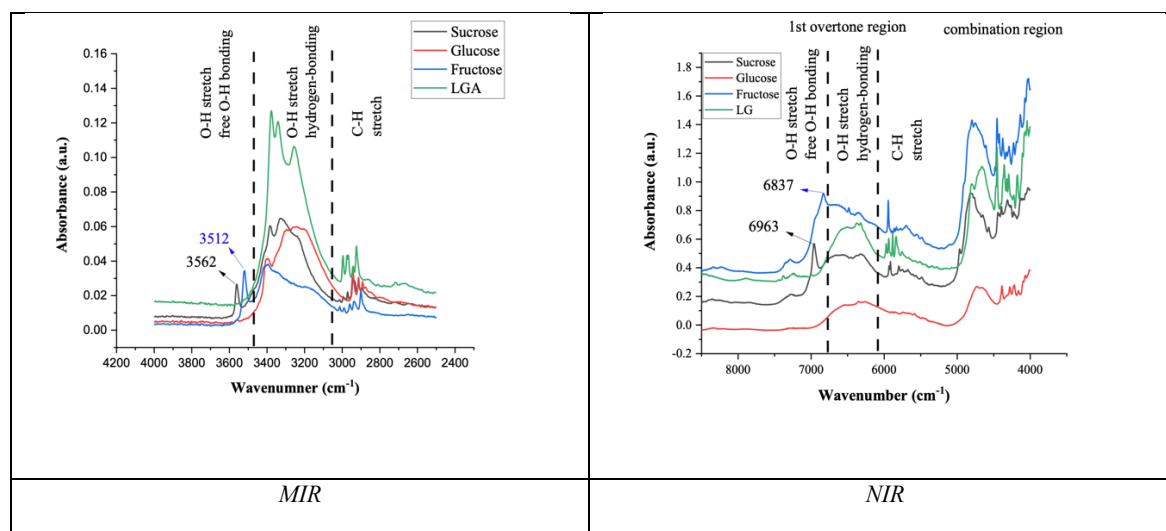


Figure 4.3 N- and M-IR spectra of sucrose, glucose, fructose and LGA

Figure 4.3 shows NIR spectra for sucrose, glucose, fructose and LGA in the near- and mid-infrared regions. Both regions show that the hydrogen bonding bands were broader than free OH and shifted to lower wavenumbers. Each graph has been divided into three main areas: CH stretching, hydrogen- and nonH-bonding areas. Generally, all regions have some similarities in terms of band behaviour. NIRS shows pronounced bands for the free OH group more than hydrogen bonding bands and vice versa. MIRS shows less pronounced bands for free OH bands. Additionally, the area of the OH band in NIRS is broader than the similar area in MIRS, which gives NIRS more advantage over MIRS. This feature allows us to obtain more information about the OH 1<sup>st</sup> overtone overlapping bands. On the other hand, the sharp band at  $6963\text{ cm}^{-1}$  for sucrose corresponds to the free OH group. A similar band, but overlapped, was obtained in the fructose spectrum at  $6837\text{ cm}^{-1}$ .

These results are consistent with the results of Seyer *et al.*<sup>88</sup> mentioned earlier. They noted that the free OH band is sharp for the sucrose spectrum because it does not participate in hydrogen bonding to other neighbouring molecules.<sup>88</sup> According to them, this band does not

appear in the spectrum of amorphous sucrose due to its random distribution.<sup>88</sup> On the other hand, the broad band at  $6305\text{ cm}^{-1}$  is broad because “it is pulled by strongest hydrogen bond”, as Seyer *et al.*<sup>88</sup> mentioned in their article.

NIRS was used to investigate sucrose, fructose, glucose, lactose monohydrate and LGA in our experiment. Samples were prepared as powders using the DRIFT sampling technique. This technique includes water flow and  $\text{N}_2$  environment to control the temperature and to prevent the sample from interacting with external  $\text{O}_2$  respectively. All samples were heated below their melting point and cooled to room temperature in three cycles, and the samples were scanned during heating and cooling. This condition was done to ensure no water molecules in the tested sample affect the hydrogen bonding. If there are any water molecules, they will evaporate from the first heating cycle and can be compared with the third cooling sample to see if there is any decrease in any OH bands.

### 4.3.1 Sucrose

The sucrose with its distinguishable free OH band may help reveal the differentiations in the hydrogen bonds spectrum of the NIRS region. That is due to the broadness of the hydrogen bond band, containing several species. Figure 4.4 shows spectra of sucrose sample heated from room temperature to  $145\text{ }^\circ\text{C}$  which does not show a significant difference between the lowest and highest temperature.

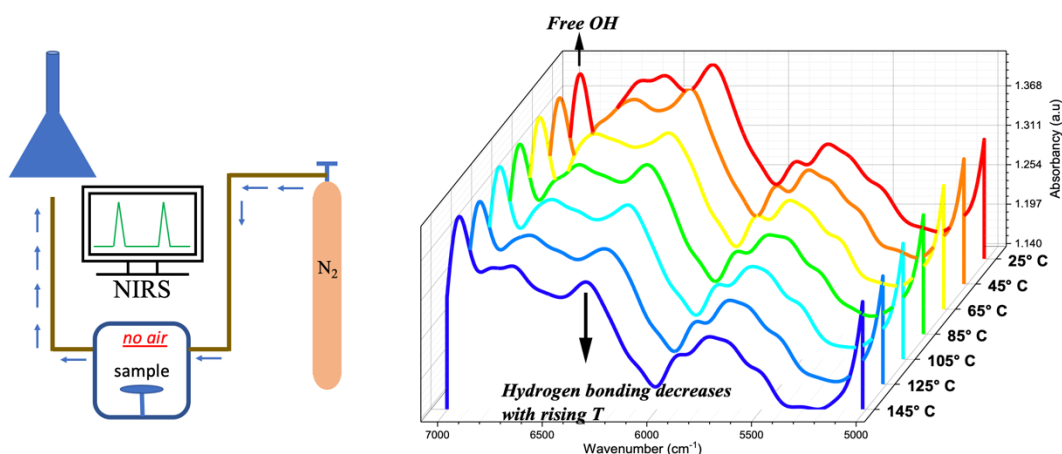


Figure 4.4 NIR spectra of sucrose at variable temperatures

There is a decrease of the band in the range ( $6300 - 6800 \text{ cm}^{-1}$ ), which means a breaking down of hydrogen bonding. In addition, the lower wavenumber of the hydrogen bonding species in the same region was more affected than those at higher wavenumber. To ensure that this change in the spectra was not caused by the moisture being evaporated from the sugar sample, STA analysis was carried out.

Figure 4.5 shows that the weight did not change during the three cycles. The average weight of the sucrose sample at  $25 \text{ }^\circ\text{C}$  in the last cycle was subtracted from the average weight of the first cycle at the same temperature. It suggested that the total weight loss was  $0.01707 \text{ mg}$  or  $0.16403 \%$  of total mass ( $10.4 \text{ mg}$ ). Another STA sample was taken and heated up to  $160 \text{ }^\circ\text{C}$  and held for 2 hours, then cooled down to room temperature. Figure 4.5 shows that the difference in weight before and after the heating process was  $0.6 \%$  which is also negligible and agrees with the three cycles mentioned earlier.

Conventional heating using a furnace for a larger amount of sucrose was carried out to support the previous result.  $20.77 \text{ g}$  of sucrose was placed in a beaker and put in a furnace at  $160 \text{ }^\circ\text{C}$  for 25 minutes to evaporate any moisture in the sample. The sample is then placed in a desiccator to cool it down, and filled with  $\text{N}_2$  to ensure that the sugar does not adsorb any water vapour. The sample had lost  $0.002 \text{ g}$  which means  $0.01 \%$  of the total weight. Then the sample was left in the furnace overnight at  $110 \text{ }^\circ\text{C}$ , and no more weight loss was recorded in the next day.

The three cycles experiment of STA for sucrose, with the loss of  $0.6\%$  and below, shows that the sucrose sample was dry and the amount of water detected is negligible. The results suggest that the change in the spectra of sucrose was caused by the temperature affecting the hydrogen bonding of the sucrose, not caused by evaporating the water. In other words, there are not enough water molecules adsorbed in the sugar that may affect the spectrum of the hydrogen bonds. The sucrose sample did not contain water molecules to affect the NIR spectrum. That means NIRS successfully investigated the hydrogen bonding in sucrose.

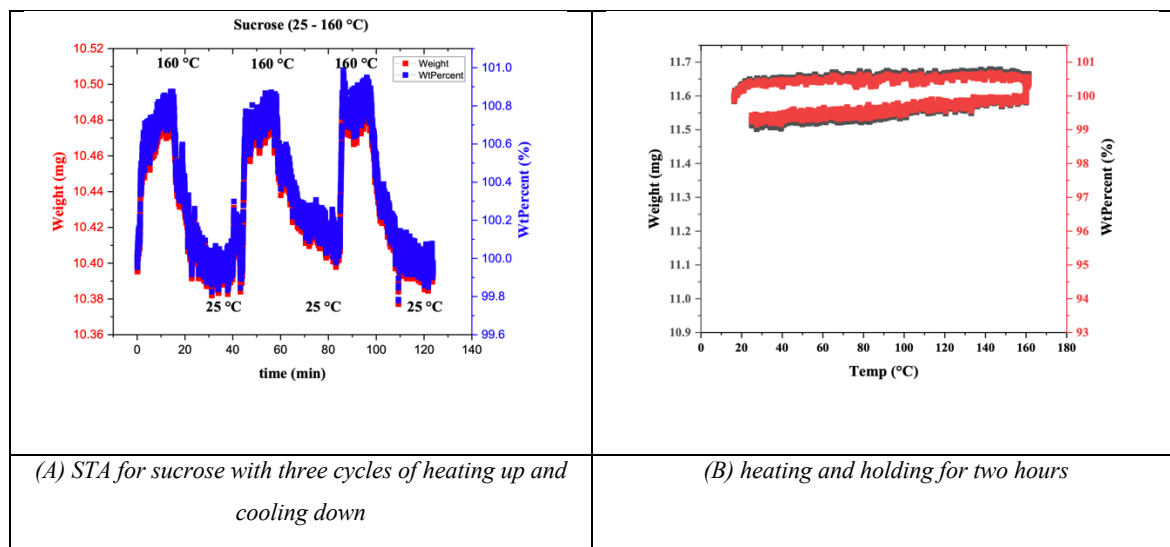


Figure 4.5 STA analysis for sucrose

### 4.3.2 Glucose

Glucose sample was tested using the same method with NIRS. Spectra of glucose show transformation of the band at  $6260\text{ cm}^{-1}$  to that at  $6340\text{ cm}^{-1}$  with a temperature rise to  $105\text{ }^{\circ}\text{C}$ . Although glucose hydrogen bond bands are narrower than sucrose, glucose spectra show an apparent breaking down in some hydrogen bonding species, as shown in Figure 4.6.

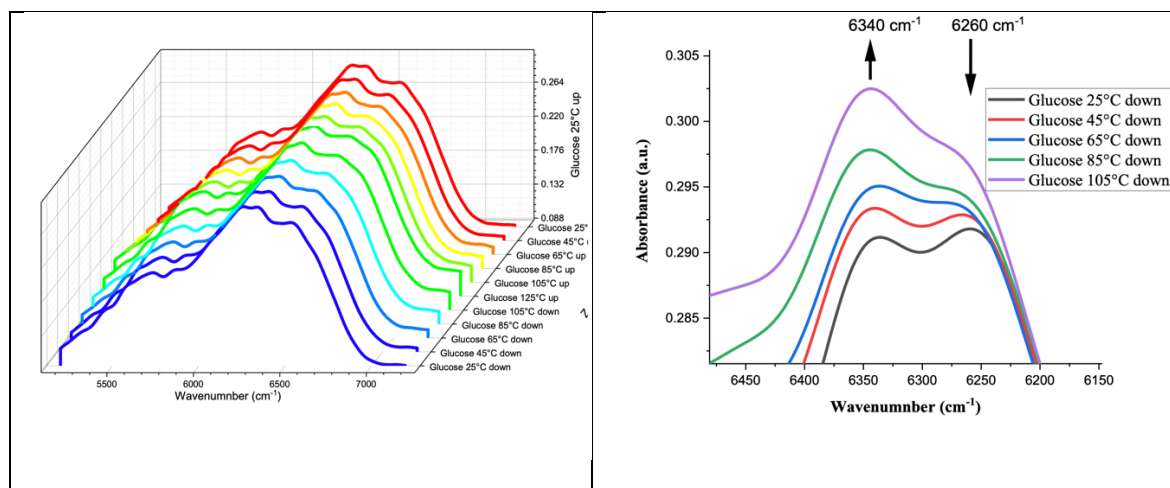


Figure 4.6 NIR spectra of glucose at variable temperatures

The transformation of the two bands ( $6340$  and  $6260\text{ cm}^{-1}$ ) was scanned during the cooling process to ensure that this change was not caused by water being evaporated. Figure 4.6 demonstrates an apparent change in the slope of the two bands indicating the loss of some

hydrogen bonding species and the formation of others. To ensure that the evaporation of water did not cause this shift in the spectra from the sugar sample, STA analysis was performed.

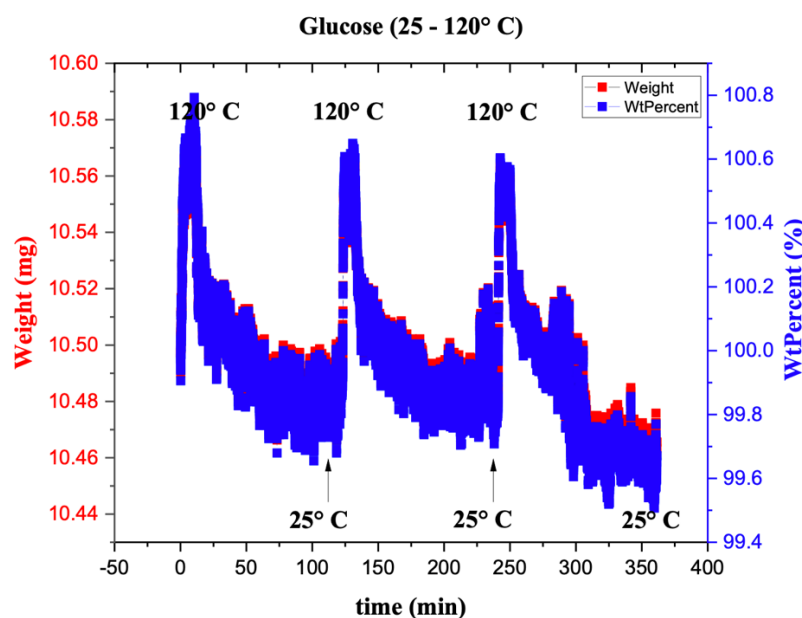


Figure 4.7 STA analysis for glucose with three heating cycles

As shown in Figure 4.7, the STA result shows that glucose was subjected to three heating cycles from room temperature to 120 °C. There is no significant difference in the glucose weight, suggesting that the glucose sample was dry. Therefore, the change in band intensity at (6340 and 6260  $\text{cm}^{-1}$ ) of glucose spectra in different temperatures was caused by breaking down and reforming other hydrogen bonding species of the sugar. The free OH group in glucose, in contrast, is not as pronounced as those in sucrose which was shown by its unique sharp band at 6963  $\text{cm}^{-1}$ , as shown in Figure 4.3.

Fructose and LGA have similar NIR spectral phenomena to glucose, with less pronounced changes in hydrogen bonding over temperature change. NIR spectra of the rest of the carbohydrates and the related STA results are illustrated in the appendix. Fructose sample seems to have some moisture as the STA result suggested. The NIR spectra of fructose in the hydrogen bonding region may interfere with the water OH vibration. Having said that, the spectra show similar effect to the other samples. All results indicate that there are some effects on the hydrogen bonding at different temperature using NIRS. This is a new approach

for investigating hydrogen bonding in sugars which shows potential success for NIR spectroscopy in this area.

The previous work was carried out with dried sugars. If the sample contains moisture, it is expected that the spectra of variable temperature will be affected during heating. Lactose monohydrate is a type of sugar bonded to water and is a good example to illustrate how the water may affect the spectra of the hydrogen bonding.

### 4.3.3 Lactose Monohydrate

It is essential to compare the previous results with sugar that contains water within the sugar crystals, such as lactose monohydrate. This is crucial to determine the difference between water OH and the sugar's hydroxyl groups in terms of infrared vibrations. NIRS as a tool to check water contents in biomass is well-known and used in industrial production.<sup>59, 100, 101, 103-106</sup> Arshadi *et al.*<sup>70</sup> used Vis-NIR spectroscopy for detecting moistures and fatty- and resin acid contents in sawdust biomass to monitor maturity as mentioned earlier.

This experiment aims to determine how the water evaporates and adsorbs in the sugar's molecules in solid-state and to study the change in hydrogen bonding within the sugar molecules.

In our experiment, a sample of lactose monohydrate was analysed to investigate the water content in the sugar and the change in hydrogen bonding. The sample was scanned by NIR spectroscopy and subjected to heat under a nitrogen environment and water flow to control the temperature in the sample cup. The temperature reached 140 °C after 22 minutes and was held for 12 minutes, then increased to 160 °C and held until all the water contents were evaporated after about 44 minutes. The sample was scanned every 2 minutes by NIR spectroscopy using the DRIFT sampling method. The same experiment was done for the second time but reached the temperature directly to 160 °C and held for 22 minutes. The second experiment was carried out to investigate the effect of different temperatures (140 and 160 °C) on the drying time.

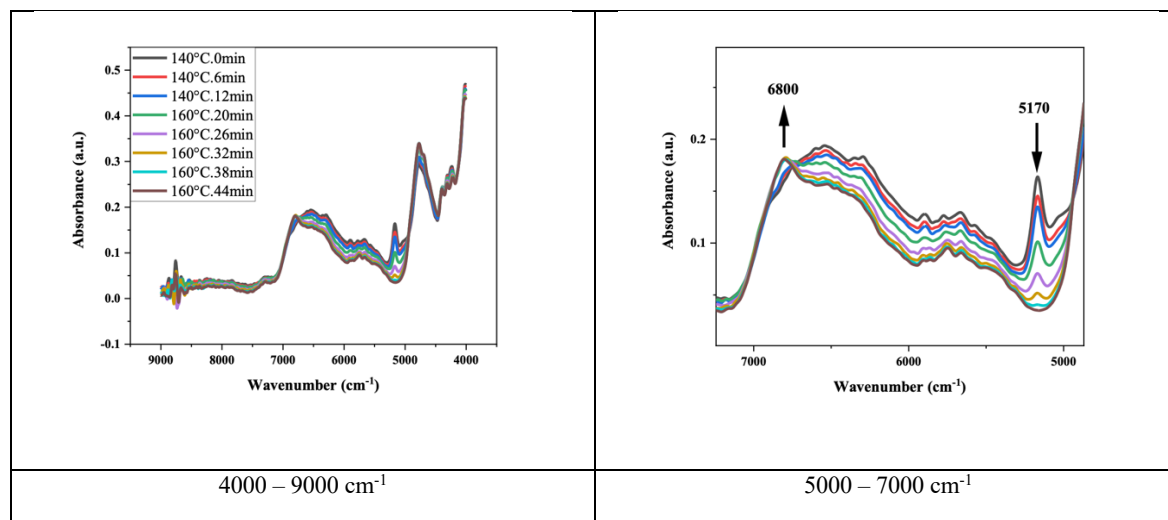


Figure 4.8 NIR spectra for lactose monohydrate during drying process

Figure 4.8 illustrates a general change in band intensity with temperature. Although there is a rise in peak-to-baseline amplitude with rising temperature, there are significant changes in specific features in the lactose monohydrate sample. Two main findings will be demonstrated in the lactose sample. Firstly, the water contents in the combination region; secondly, the effect of the temperature on the hydrogen bonding in the sugar crystal investigating the 1<sup>st</sup> overtone region of OH vibration. The two findings are discussed in the following section.

#### 4.3.3.1 Investigation of water in lactose monohydrate

As the sample of lactose monohydrate contains water, it is expected to detect the combination band of OH above 5000  $\text{cm}^{-1}$ . Figure 4.8 shows a band at 5170  $\text{cm}^{-1}$  for water molecules. This band, however, decreased with time when the sample was exposed to a temperature above 120 °C. This agrees with Christy's results<sup>100</sup> except for the little shoulder  $\sim 5040 \text{ cm}^{-1}$ , which he did not include in his work. This overlapped band decreased with temperature faster than the band at 5170  $\text{cm}^{-1}$  and disappeared when the sample was heated at 160 °C for 20 minutes. An average intensity of each spectrum in the range (4950 – 5325  $\text{cm}^{-1}$ ), where the water band takes place, has been plotted against time under the heating condition of 160 °C.

NIR Spectroscopy reveals the loss of water molecules in the lactose monohydrate was indicated by decreasing the band at 5170  $\text{cm}^{-1}$  until it disappears. The time and temperature



played a significant role during the evaporation process. The sample was subjected to the heat of 160 °C for 44 minutes and still changed in the band at 5170  $\text{cm}^{-1}$ . After 44 minutes of heating (140 °C for 16 minutes and 160 °C for the remaining time). And only 22 minutes of constant heating at 160 °C. It seems that heating with a higher temperature increases the evaporating rate faster than if gradual steps in temperature were carried out. That is clearly illustrated in Figure 4.9.

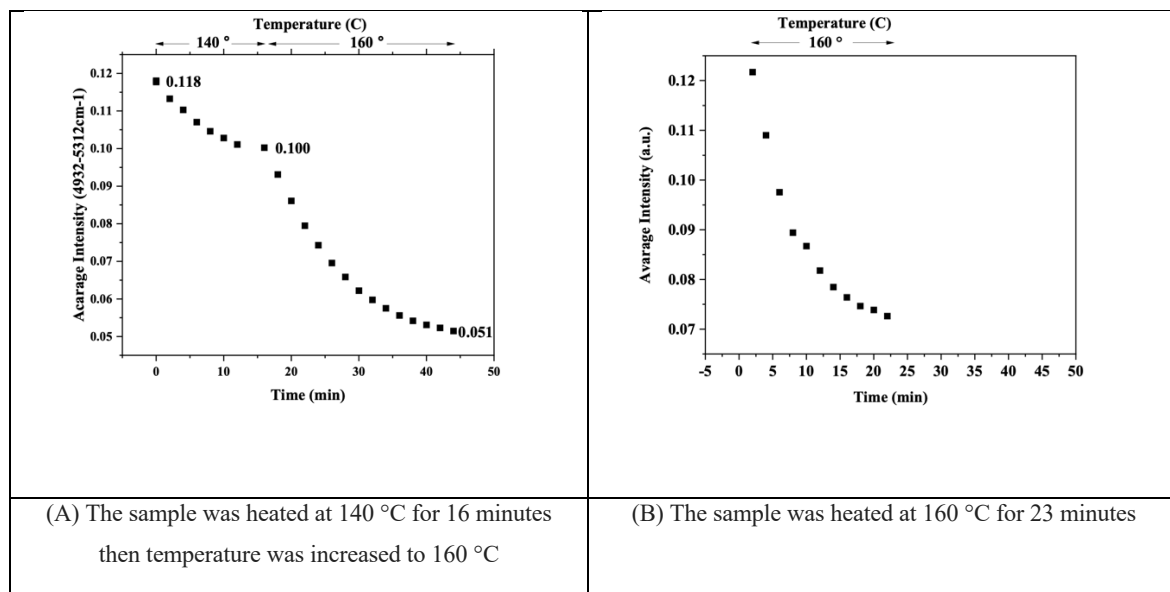


Figure 4.9 the intensity of the band at 5170  $\text{cm}^{-1}$  during heating process

Figure 4.9 shows a rapid and greener quantitative method for detecting water content in polymers which can be used in different applications, including detecting water content in biomass. There is a chance of error caused by the spectra intensity increasing with the temperature. This is a common issue with NIRS when different temperatures are applied.<sup>57, 105</sup> However, this issue can be resolved by subtracting the change in baseline intensity between one spectrum and the next. This issue can be neglectable compared with the previously observed changes, especially with the early evaporating time. Second derivative also can enhance the spectra and solve the baseline shift issue. The next step is to compare NIRS with STA for the same sample to provide a good discrimination between the two methods.

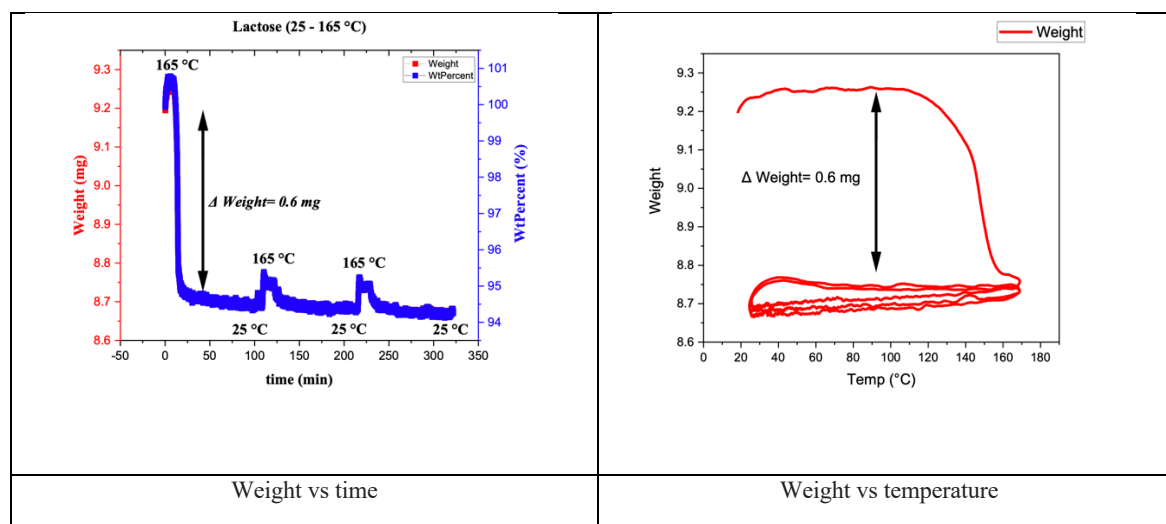


Figure 4.10 STA analysis of lactose monohydrate in three cycles

STA results demonstrate three cycles of heating and cooling, which have been applied to the lactose monohydrate in order to determine the water content. The water was evaporated completely when the sample was subjected to heat during the first cycle. However, the second and the third cycles were identically matched, indicating that no more water loss occurs. The apparent rise in mass around 100 and 225 mins happened when the temperature changed. It is due to chemisorption or strong physisorption. STA results in Figure 4.10 determines that water loss is about 5% of the total mass of the sample. The total molecular weight of lactose monohydrate (water and lactose) is 18 and 342 g/mol, respectively. That gives a ratio of 1:19 or 5% of water in 95% lactose in weight. Figure 4.10 shows a water loss of around 0.6 mg of 10 mg of lactose monohydrate, which is about 6 % of its weight. In other words, almost all water content was evaporated at 160 °C. These results suggest that all water molecules were evaporated.

Another STA sample was taken and heated up to 160 °C and held for 2 hours, then cooled down to room temperature. Figure 4.11 shows that the water loss was 0.6 mg which is similar to what has been done with the three cycles of heating previously mentioned. The amount of water loss during heating above 100 °C seems to take the majority of water losses compared with the holding time for 2 hours at 160 °C, which did not seem to have any noticeable water loss. This result supports our findings with NIRS that the lactose has lost all its water contents during heating process.

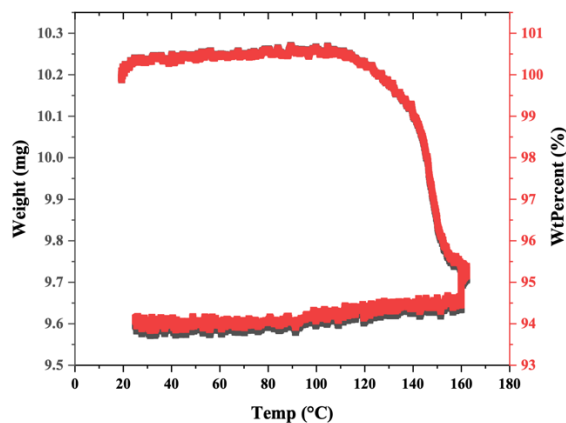


Figure 4.11 STA analysis for lactose monohydrate with two hours heating

Heating the sample with a furnace as a conventional method, a higher amount of lactose monohydrate was examined to support the previous results. 4.2 g of lactose monohydrate was placed in a beaker and put in a furnace at 160 °C for 25 minutes. The sample was then placed in a desiccator to cool down, and it was filled with N<sub>2</sub> to isolate the sample from adsorbing water vapour. The sample had lost an amount of (0.212 g,) which again equals 5 % of the total weight. Then the sample was left in the furnace overnight at 110 °C, and no more weight loss was recorded. In other words, all water molecules were evaporated within the first 25 minutes of placing the sample in the furnace. This finding agrees with all previous methods to support the NIR spectroscopy approach.

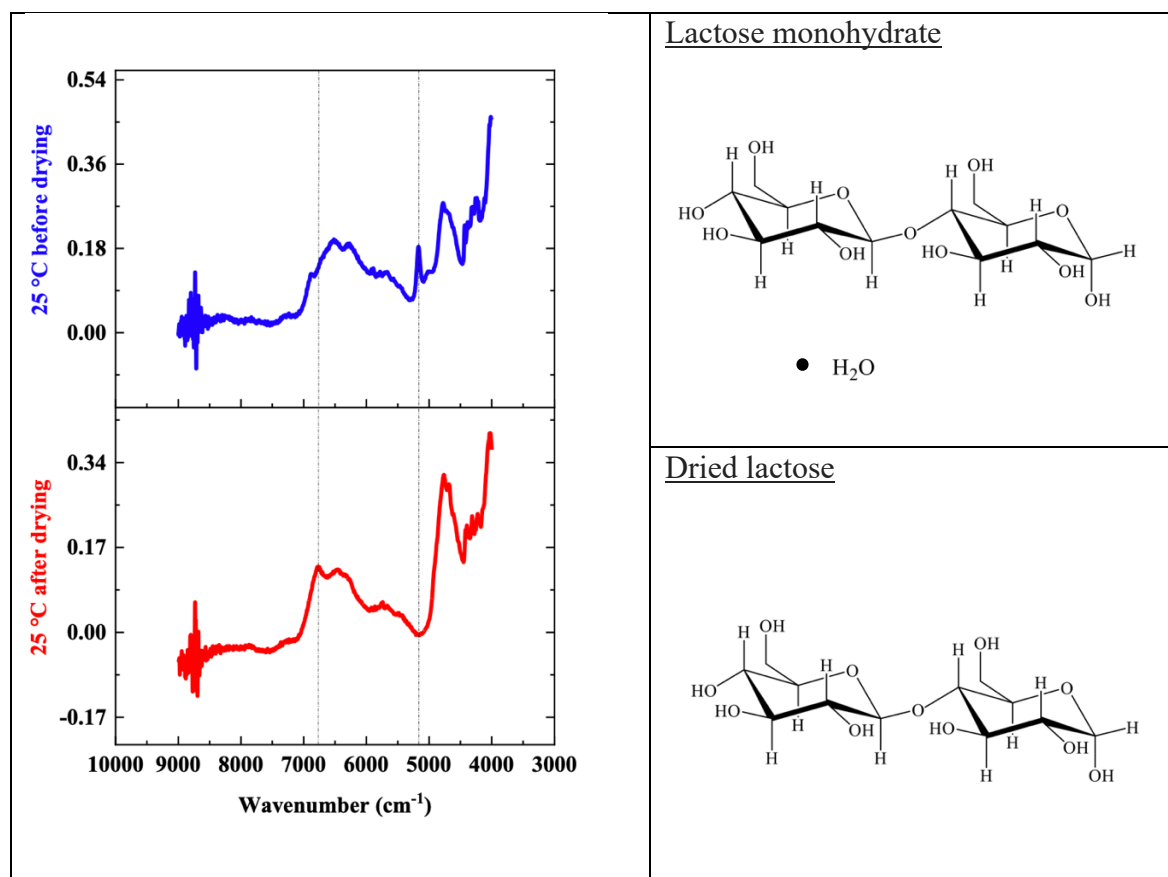


Figure 4.12 NIR spectrum of lactose monohydrate

Finally, the change in spectra of the lactose monohydrate before and after drying was illustrated in Figure 4.12. The spectra were taken at the same temperature (25 °C) to determine how the meagre amount of water (~ 5% of the total sample weight) influences the spectrum of the sugar. As discussed earlier, the band at  $5170\text{ cm}^{-1}$ , a combination band, is a clear indicator of water in the sample. The 1<sup>st</sup> overtone vibration of OH of hydrogen bonding in the range  $6300 - 7000\text{ cm}^{-1}$  varied between the sample before and after drying. In the lactose monohydrate spectrum, most H-bonded species tend to be at lower wavenumber than the dried lactose sample, showing more absorbency in higher wavenumber. This is an evident influence of water absorbance in the NIRS region that needs to be considered.

This approach can be used to calculate the water loss quantitatively and apply it in the food industry as a real-time non-destructive tool. A fibre-optics probe can make this kind of test online to monitor the water level in carbohydrates during the industrial processes. Similarly, this method can be applied in biorefineries processes for biomass conversion to calculate the moisture contents in the early stages.

### 4.3.3.2 Hydrogen bonding investigation in dry lactose sample

The second experiment aimed to investigate the hydrogen bonding changes in the pure sugar crystals at different temperatures. So, the sample was heated directly to 165 °C then the temperature was held until all water was evaporated. The elimination of the band at 5170  $\text{cm}^{-1}$  was an indicator of water being evaporated, and the sugar remained dry. The sample then was cooled to 25 °C. The NIRS scans started during the heating process from room temperature to 165 °C and cooling down to 25 °C with + and - 20°C when heating and cooling, respectively.

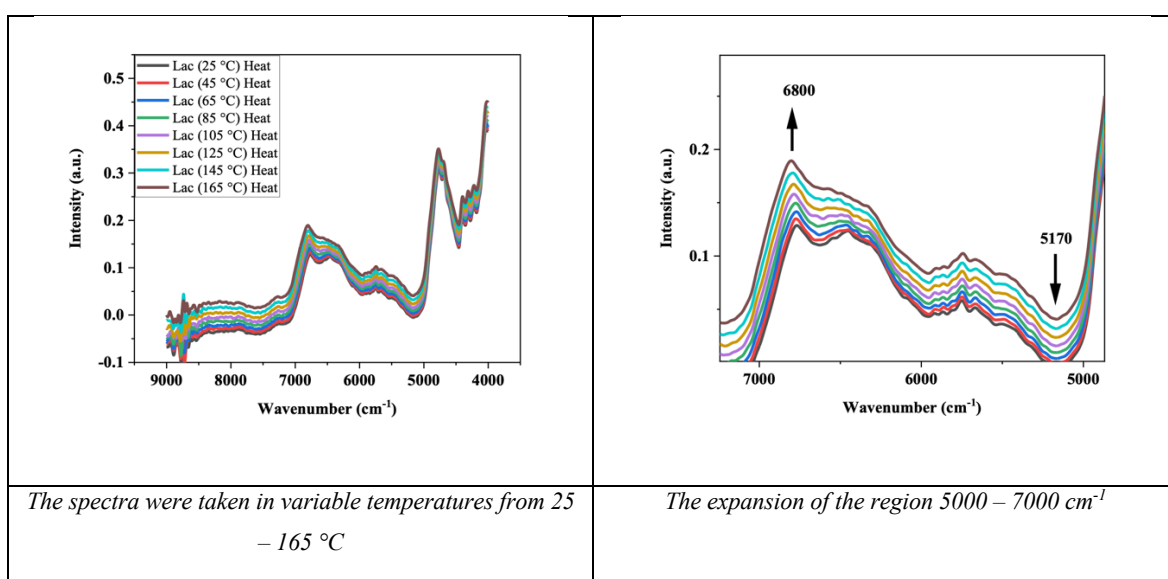


Figure 4.13 NIR spectra of lactose after 24 minutes of drying at 160 °C

When the sample was completely dried, the investigation of hydrogen bonding transformation between species within the sugar molecules had a higher chance of success. Despite increasing the baseline spectra with temperature, a noticeable difference in absorbance in the range 6200 – 6800  $\text{cm}^{-1}$  was found. As the temperature rises, the band at around 6400  $\text{cm}^{-1}$  decreases compared to the band at 6800  $\text{cm}^{-1}$ , as demonstrated in Figure 4.13. There is a transformation from one band to another, breaking down and forming different hydrogen bonding species when the sample is subjected to the temperature. It was hard to calculate the transformation quantitatively as there is no clear point to create a baseline. The whole spectra also show an intensity increase (baseline shift) with temperature, which is a known issue with NIR spectroscopy.<sup>57, 105</sup>

However, this issue can be resolved using a different analytical method: a straight line drawn between the band at  $6800\text{ cm}^{-1}$  and the next one at a lower wavenumber for each spectrum could show a difference, resulting in different slopes in trend with the temperature. At  $5170\text{ cm}^{-1}$ , no band appeared, which indicates that the sample was completely dry. This part of the experiment aims to confirm the change in hydrogen bonding of the sugar itself, which was not interfering with water adsorption. The spectra at each temperature (during the heating and cooling process) remained unchanged. That means no more water loss or any other species that influence the spectra, and all the hydrogen bonding transformation was caused by the sugar crystals only.

The temperature influences the dry lactose sample by shifting the band at  $\sim 6800\text{ cm}^{-1}$ . As shown in Figure 4.14 the band shifts  $34\text{ cm}^{-1}$ , ranging from  $6768$  to  $6802\text{ cm}^{-1}$ , by temperatures at  $25\text{ }^{\circ}\text{C}$  to  $165\text{ }^{\circ}\text{C}$ , respectively. Higher temperature affects the band by shifting the hydrogen bond vibration to a higher wavenumber. These findings are consistent with what Burns<sup>57</sup> stated in his book. That means that some hydrogen bonding species are broken down in the sugar with rising temperature. The band shifts gradually to higher wavenumber with increasing temperature and vice versa. In other words, this band can be used to detect the temperature of lactose during the heating process. Table 4.1 demonstrates a trend of changing in band position with temperature. However, at temperatures  $45$  and  $65\text{ }^{\circ}\text{C}$ , spectra showed no difference in band position.

*Table 4.1 Shifting band position with temperature*

Temp	Wavenumber
( $^{\circ}\text{C}$ )	( $\text{cm}^{-1}$ )
25	6768.0
45	6773.6
65	6773.6
85	6776.0
105	6785.4
125	6789.5
145	6793.7
165	6802.5

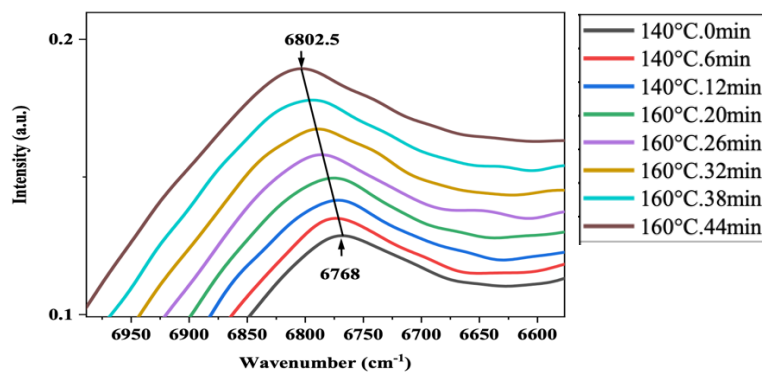


Figure 4.14 Shifting band position with temperature

Similarly, during the heating process of the lactose monohydrate illustrated in Figure 4.8, the band at  $\sim 6770 - 6800 \text{ cm}^{-1}$  was also shifting but with a higher wavenumber for each temperature compared with the dry sample. Because the sample still holds some water molecules, it shifts the same band to a higher wavenumber with rising temperature.

Figure 4.8 suggests that the water molecules have evaporated over time. Some sugars, such as lactose, give a little shoulder at a higher wavenumber than the OH 1<sup>st</sup> overtone band. It is at  $6860 \text{ cm}^{-1}$  for lactose, as illustrated in Figure 4.15. This shoulder, however, appeared clearly when the sample was scanned at room temperature before heating. The shoulder then disappeared gradually with the heating process but never appeared again when the sample was cooled down.

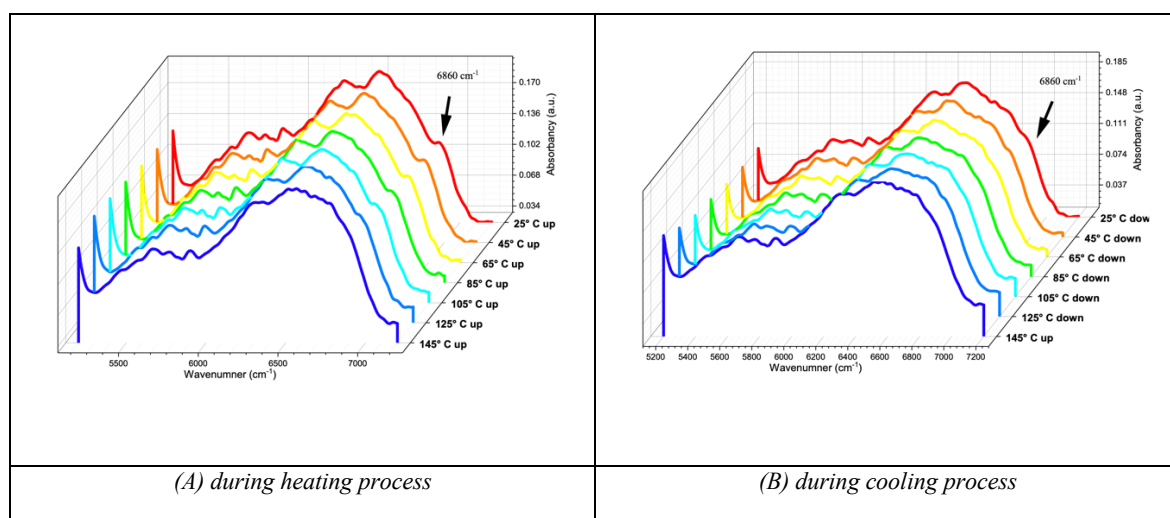


Figure 4.15 NIR spectra for lactose monohydrate before and after drying in different temperatures

It means that the sugar crystals were reformed, and some hydrogen bonds were broken down. It is more likely to be due to water adsorption. As discussed earlier, a sharp band at  $\sim 5170 \text{ cm}^{-1}$  appeared as evidence of water present in lactose molecules. To conclude, the lactose monohydrate was evaporated and monitored carefully by NIRS. On top of that, the dried lactose hydrogen bonding was affected by the temperature, also monitored by NIRS.



#### 4.4 Moisture content in sawdust

This experiment aims to examine the sawdust water contents. That will help to understand the storage conditions for the biomass feedstock and other related parameters for better yields and safety reasons.

Samples of sawdust were prepared in particle sizes of 250 – 500  $\mu\text{m}$ . The sample was tested without any drying, which is called wet in this experiment. Then the sample was dried at 105 °C overnight. A desiccator was used to cool it down in a dry environment followed by NIRS analysis and weight measurement for several times when it was exposed to air, after 1, 2, 3 hours, 1 day and 1, 2 weeks. Spectra are shown in Figure 4.16.

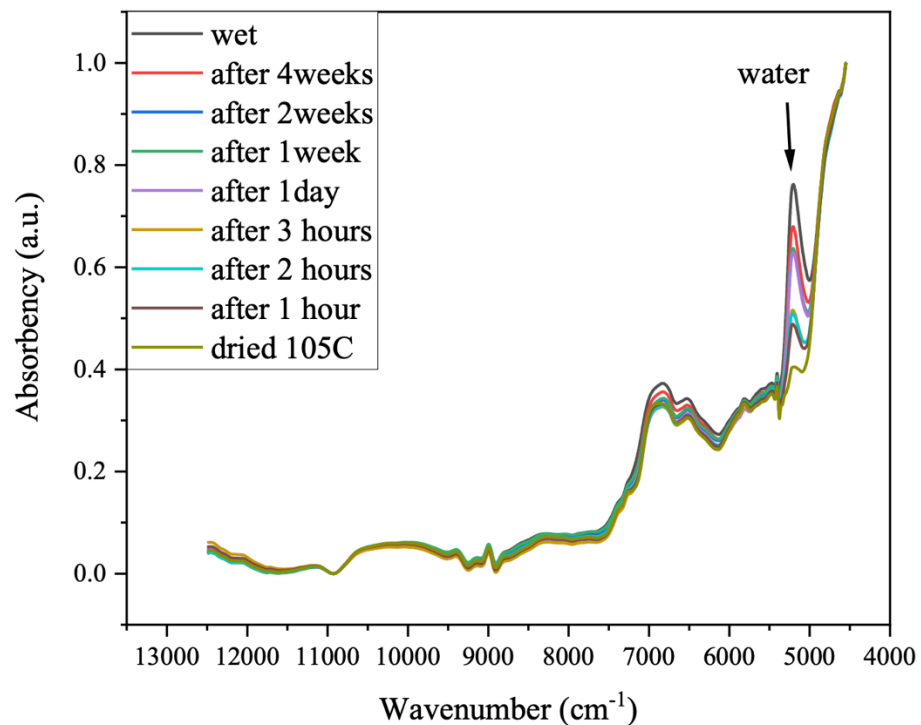


Figure 4.16 NIR spectrum for sawdust 250-500  $\mu\text{m}$  in different moisture contents

Sawdust spectra show some absorptions in different regions of the NIR spectrum. The band at 5217  $\text{cm}^{-1}$  (1917 nm) corresponds to a combination band of water OH fundamental stretching and bending vibrations. C-H 1<sup>st</sup> overtone overlapped bands in the range 5714 – 5465  $\text{cm}^{-1}$  (1750 – 1830 nm). Finally, OH second overtone at about 10000  $\text{cm}^{-1}$  (1000 nm). It is clear that the moisture content can be detected by observing the band at 5217  $\text{cm}^{-1}$  (1917

nm). For more details of water contents, the full absorbency of the band centred at  $5217\text{ cm}^{-1}$  ( $1917\text{ nm}$ ) was cut and investigated in more detail.

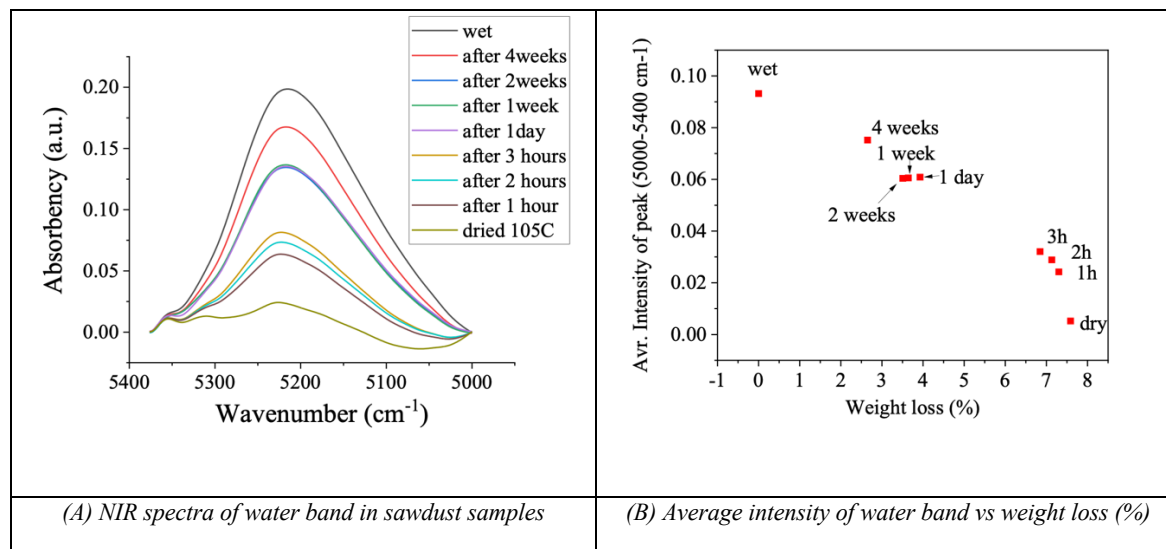


Figure 4.17 NIR spectra of water band in sawdust samples

It is clear that the sawdust gains water very quickly when exposed to air for the first hour after drying. The gains in the second and third hours are less, but it is noticeable. The amount of water gained by the sawdust from the surrounding atmosphere gets less over time. It seems that there is no chance of getting back to the same intensity as before drying. It is expected that it is harder for the water to form hydrogen bonding with the cellulose molecules in the deeper layers. That is precisely what has been found by Rebar *et al.*<sup>99</sup> which also was supported by Christy.<sup>100</sup> They have concluded that the branch structure of the glucose units of the sugar increases its ability to absorb water molecules from the atmosphere, such as the amylopectin, which enables the overlapping of OH – groups which then attract the water molecules where they will be trapped in this structure.

Cellulose, in contrast, has very low water adsorption ability due to the flat sheet formation of the glucose units chains which lie on top of one another, held firmly by hydrogen bonding. It seems that the water molecules in our experiment form hydrogen bonds at the surface of the wood, but it finds it difficult to go to deeper layers.

STA analysis was carried out to support these findings. When the sawdust sample was heated to  $105\text{ }^{\circ}\text{C}$  in the instrument, it seems that the sample lost about 6 % of its moisture contents, as shown in Figure 4.18 a.

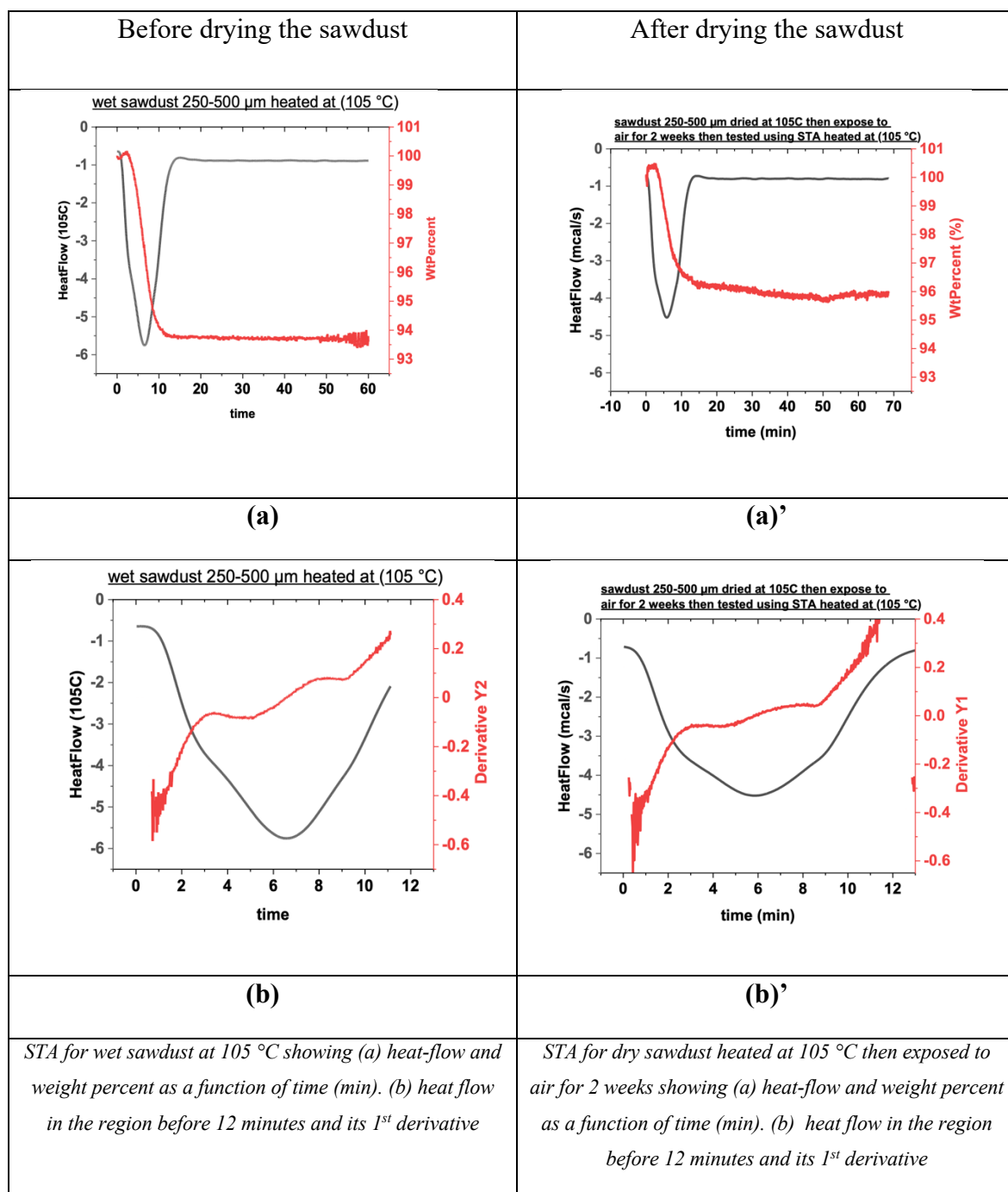


Figure 4.18 STA analysis for sawdust

Another sample of 5.246 g sawdust was dried in an oven at 105  $^{\circ}\text{C}$  overnight and weighed 4.848 g (0.398 g loss) resulted in 7.6 wt% of weight loss. It exposed to air for two weeks to gain moisture from the surrounding atmosphere resulted in 4.1 wt% water gain. The sample then was analysed using STA. Figure 4.18 a' shows 4 wt% of moisture was lost during STA heating, which is in line with the conventional heating. There is an amount of 2 % difference

between the wet sample Figure 4.18 a and the one heated at 105 °C and subjected to air moisture for two weeks Figure 4.18 a'. There is one third of the water lost in the drying process was not gained back to the sawdust from the surrounding atmosphere. These results support the NIRS results showed in the same period using the intensity of the water band. The two methods results are consistent, as well as the conventional weighting using a lab-scale.

The heat flow shows a negative sharp band at the beginning of the sample heating process, especially the first 10 minutes as shown in Figure 4.18 a and a' with a small shoulder hardly seen at about 2-3 minutes. Applying the first derivative for the heat flow shows clear difference in the heat flow behaviour. Figure 4.18 b suggests that the heat flow contains two different waves of changes during the heating process. That means there are two types of water in the sawdust that need different energy to evaporate. However, some of the water removed is going to be from within the sawdust matrix. Once dried, it is going to be hard to re-hydrate presumably within the cellulose and hemicellulose but not the lignin. The difference between b and b' in Figure 4.18 shows that the dry sample could not gain the same amount of water lost during the drying process. The first layer is expected to lose water first, so it is expected to see similar curves for both figures at the beginning of the process until 6 minutes. By then, the system changes to get more water from the inner layers. During this period, the two curves look similar. After 6 minutes, it is clear that the first sample in Figure 4.18 b shows more effect during evaporating the water in the inner layers. In contrast, the second sample in Figure 4.18 b' shows more negligible evaporating effects as it contains less water in the inner layers.

The drying temperature is affecting the results. A similar experiment was conducted but heating the sample at only 40 °C to determine the difference between the high and gentle heating process and its effect on the sawdust moisture content.

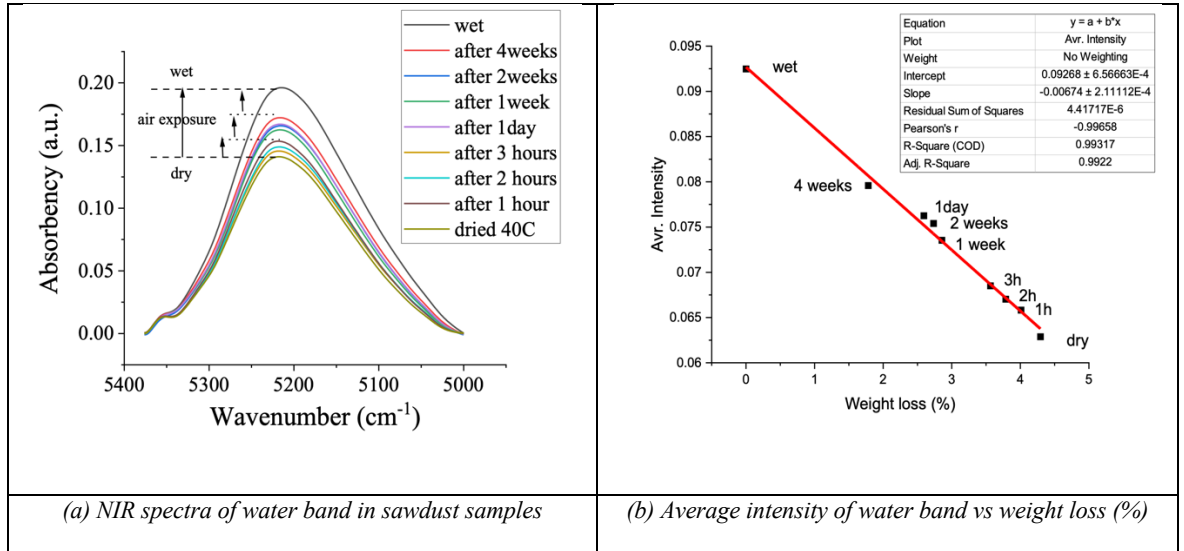


Figure 4.19 NIR spectra of water band in sawdust samples

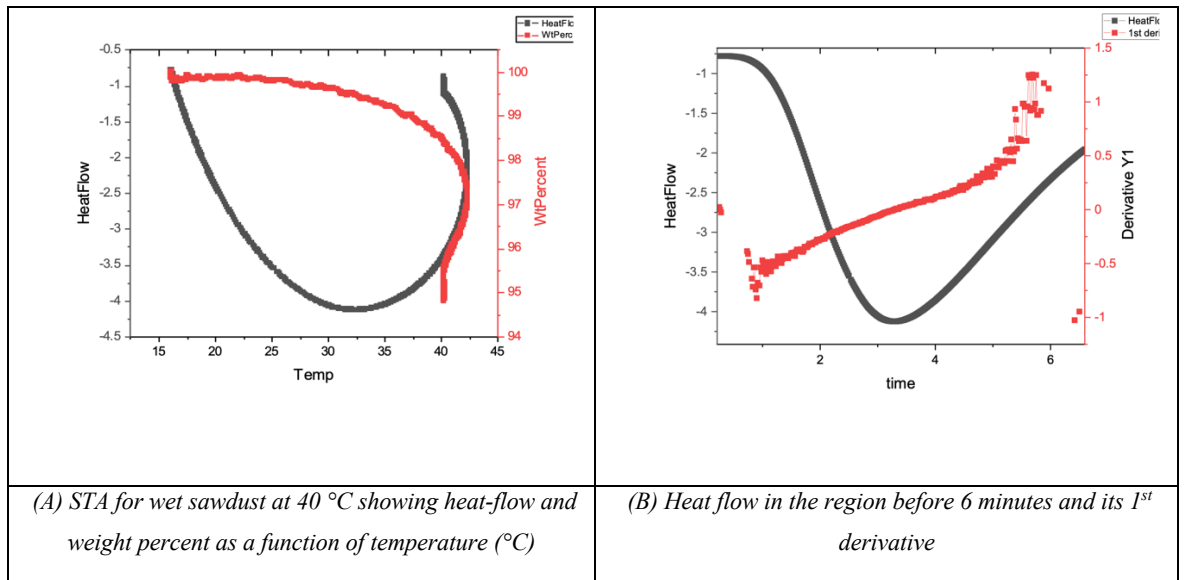


Figure 4.20 STA for wet sawdust of the sample dried at 40C

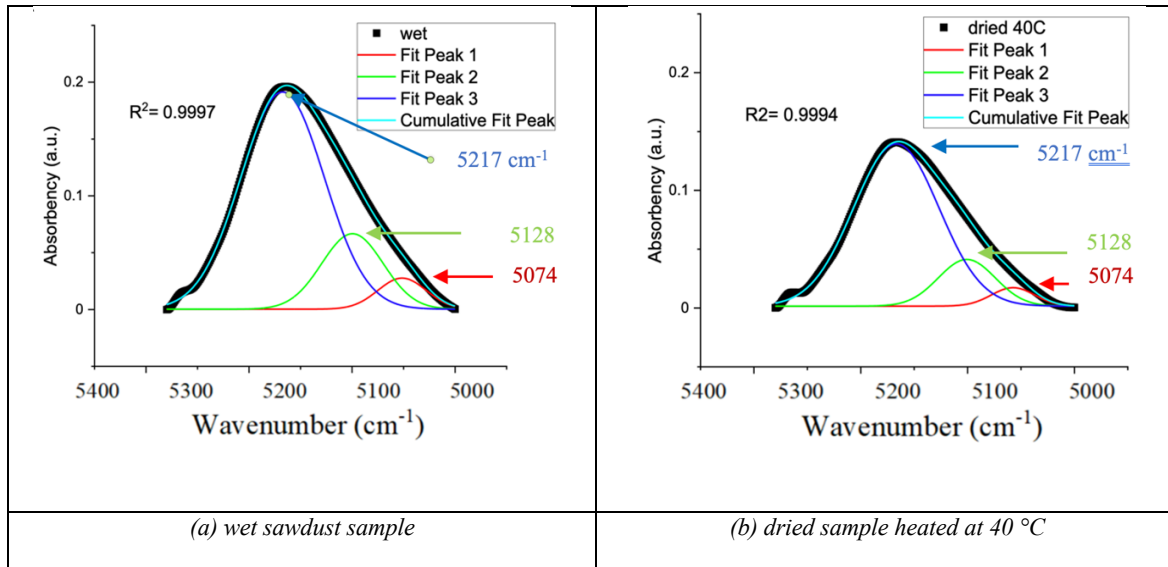


Figure 4.21 Deconvolution of the OH combination band of sawdust sample

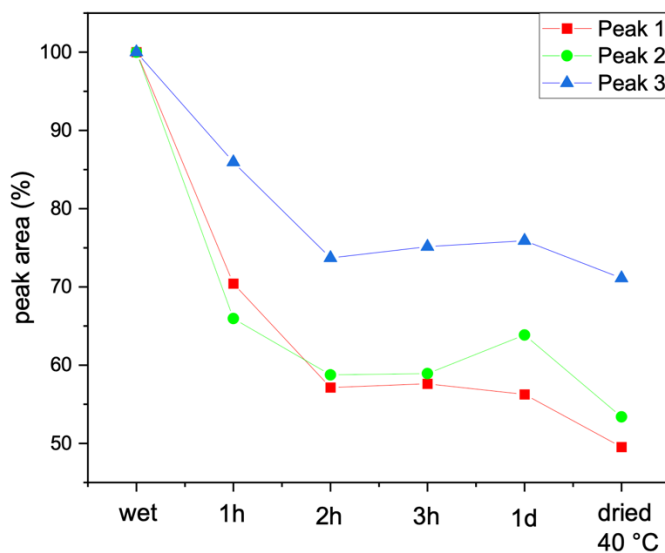
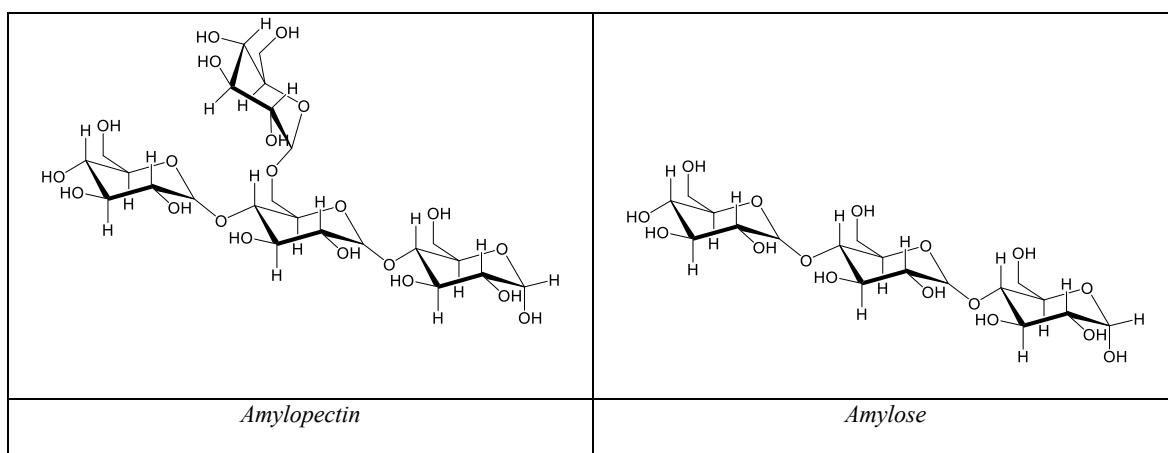


Figure 4.22 Deconvoluted band for wet sawdust, dried and exposed to air in different times

The sample which was dried at only 40 °C seems to have lost quite a noticeable amount of water. But compared with the sample dried at 105 °C, there is a big difference. It is expected that the gentle heating of (40 °C) would not evaporate the water from deeper layers of the sawdust. That was illustrated in Figure 4.20 STA analysis which shows one smooth curve for the heat flow. Compare this figure with the figure in Figure 4.18 b which shows a little shoulder at 2-3 minutes. The first derivative of this curve in Figure 4.20 b reveals that only

water lost during the heating process was on the outer layers of the sawdust. That will be clear by comparing Figure 4.9 b with the figure b on Figure 4.18.

Deconvolution of OH band shows different types of OH groups, which can be seen in Figure 4.21. The deconvolution shows three different bands with different intensities. All three bands have lost intensities during the heating process, as shown in Figure 4.21 b. The deconvolution of the same band at different time of air exposure of 1, 2, 3 hours and one day were calculated in percentage and shown in Figure 4.22.



*Scheme 4.2 The different structure of amylopectin and amylose*

The deconvoluted bands in Figure 4.21 show that band 3 is more intense at a higher wavenumber ( $5217\text{ cm}^{-1}$ ) than bands 1 and 2 ( $5074\text{ cm}^{-1}$  and  $5128\text{ cm}^{-1}$ , respectively). As the bands are in different intensities, and it is not easy to compare one another in different conditions. So, the percentage of each band (lose, gain) was calculated to determine their behaviour in water adsorption. Figure 4.22 shows each convoluted band in percentage plot against sample condition (wet, after 1,2,3 hour of air exposure and dried sample).

Our results are in consistent with Christys.<sup>100</sup> He found that the water-water hydrogen bonding in the combination region is located at a higher wavenumber (lower wavelength) than that of water-sugar hydrogen bonding, which locates at a lower wavenumber depending on which OH group in the sugar is linked to. The structure of carbohydrates also plays a significant role in forming hydrogen bonding with water molecules. Rebar *et al.*<sup>99</sup> suggested that amylopectin is more than amylose in adsorbing water molecules. The branched structure of amylopectin causes that ability to overlap OH groups to H-bonded with water as mentioned earlier. Our results are in consistent with both Christy<sup>100</sup> and Rebar *et al.*<sup>99</sup>

## 4.5 Conclusion

In this chapter NIRS approach was used to study biomass analysis, including carbohydrates and sawdust. The instrument was able to detect different parameters such as particle size, hydrogen bonding and moisture contents of biomass, pure sugars, and anhydrosugars. Two different methods were employed, DRIFT and a transfection fibre-optic probe. The latter was able to be used at real-time.

That means NIRS successfully investigated the hydrogen bonding in sucrose, glucose, lactose monohydrate. It also monitored the evaporation of the lactose monohydrate sample showing that the time and temperature played a significant role during the evaporation process. In addition, dried lactose sample showed variation in hydrogen bonding with changing temperature which indicates the sensitivity of this method. The deconvolution of the combination band reveals that the sawdust sample contains different species of hydrogen bonding. STA results were consistent with NIRS for all the experiments.

It is essential to have a quick method to measure biomass moisture contents whenever stored, used, or even transported. This can be achieved by using NIRS with a fibre-optics probe. Additionally, as an online monitor, this technique can be helpful, during thermal biomass conversion using MW hydrolyses or pyrolysis treatment. It can be used as an online monitoring detection technique inside the MW to control the process and selectively choose the best condition.



## Chapter 5: H<sub>2</sub>O/LGO interaction (temperature-dependent) by investigating H<sub>2</sub>O overtones vibration

### 5.1 Introduction

The use of LGO as a bio-based platform molecule plays a significant role in the transforming fossil fuel dependence to renewable resources. However, LGO is a significant functionalised chiral molecule, which makes it essential to synthesise a wide range of chemicals, including the natural and unnatural compounds, nucleosides, anticancer drugs, building blocks and green solvent.<sup>107-109</sup>

LGO is produced by different methods, mainly from biomass. The primary method used to produce LGO is the pyrolysis of cellulose or cellulosic materials, and/or industrial residuals such as wastepaper are commonly used.<sup>107</sup> A study by Kudo *et al.*<sup>110</sup> successfully produced LGO from cellulose pyrolysis using supported ionic liquid phase. Another method employed by Huang *et al.*<sup>49</sup> involved using LGA to produce LGO with the presence of water and DMSO catalysed by amberlyst 70. Furacell<sup>TM</sup> is another method used for producing LGO on a large scale used by Circa.<sup>111</sup> A very recent experiment was carried out by Chen and Bai<sup>112</sup>, who developed a new method for converting waste containing Polyvinyl chloride (PVC) into desired chemicals. HCl, created from the dehydrochlorination of PVC, was used as an acid catalyst to enhance the conversion of red oak to valuable chemicals, yielding up to 84.1% of liquid products, including 14.4% of LGO. Microwave-assisted pyrolysis has also been used for the first time to produce LGO from cellulose.<sup>113</sup> However, most of the previously mentioned methods in the production of LGO take place in the presence of water.

Water plays a significant role in biomass biorefinery in general. For the LGO production, the presence of water in LGA conversion is a crucial factor, as it influences the amount of LGO produced. Huang *et al.*<sup>49</sup> experimented with LGA conversion to LGO in different concentrations of water and DMSO using amberlyst 70. Without adding water, the yield of LGO was 28.5%-C. [carbon balance % = (total moles of carbon in products / moles of carbon in initial reactants) x 100]. When added 5% water, the yield decreased to 5.5%-C. Furthermore, this water addition influenced glucose yield from a negligible amount to 31.4%-C. By using in-situ water removal, the yield of LGO was increased to 40.4%-C. The authors concluded that the absence of water decreased the production of glucose and HMF by inhibiting the hydrolysis of LGA to glucose and isomerisation of LGO to HMF.<sup>49</sup> The

control of water contents in this kind of productions determines the chemical reaction's direction.

This chapter focuses on the interaction between LGO and water. However, it is divided into two main parts: **temperature-** and **time-**dependent for the LGO in an aqueous solution. Firstly, it is unclear how LGO behaves in water systems. It is temperature-dependent and has completely different behaviour than Cyrene and Methyl ethyl ketone (MEK). Secondly, the interaction between LGO and water takes a long time (days at room temperature) based on our results and has been studied in detail in this chapter. This work was carried out using NIRS as a primary method, and the results were consistent across a range of other appropriate analytical techniques. Starting from water, the only 1<sup>st</sup> overtone vibration of OH was investigated, revealing much information about hydrogen bonding. Adding any amount of a substance, this broad band changes and can be investigated using mathematical computer programmes.

The area of 6000 – 8000 cm<sup>-1</sup> is one of the essential areas to study in more detail as it contains lots of information related to the 1<sup>st</sup> overtone of the O-H vibration. Although this region seems very broad and the O-H water absorbance is very high, there are so many other obscured bands which did not appear due to the complexity of this band. To study this region in more detail, a thorough understanding about what happened to this band of the O-H must be achieved.

## **5.2 The effect of temperature on water and LGO**

### **5.2.1 Water**

#### **5.2.1.1 general**

Water was studied in more detail with different temperatures using the 1<sup>st</sup> overtone of its vibration band as a standard system. It is well known that the OH band associated with hydrogen bonding is broader and shifted towards lower wavenumbers.<sup>53</sup> Therefore, the change in this region indicates the hydrogen bonding involved in the solution. The band shifting with temperature in NIR region is more significant than that in the fundamental region.<sup>114, 115</sup> The free OH band is higher in intensity than the hydrogen bonding band in the overtone region, making the NIR spectroscopy a better choice for studying this phenomenon<sup>114, 115</sup>.

Maeda *et al.*<sup>116</sup> have used temperature-dependent NIRS for water in OH 1<sup>st</sup> overtone band. They found that the system contains five water species of zero, one, two, three and four hydrogen bonds. They came up with the conclusion that hydrogen bonding in water is affected by the change in temperature. Dougherty<sup>117</sup> has applied varied pressure and temperature to investigate hydrogen bonding. He has found that temperature and pressure affected hydrogen bonding strength and length.<sup>117</sup> Collins<sup>118</sup> is one of the earliest scientists who studied the temperature effect on water in the NIR region. He stated that water contains at least two kinds of molecules affected in their quantity by temperature. He failed to calculate the two components quantitatively, as he mentioned in his article, by that time in 1925. He added that there is no method constitutively accurate enough for this kind of quantitative measurements.<sup>118</sup>

Monosmith and Walrafen.<sup>119</sup> used the Raman NIRS region, and they found that the water spectrum contains four components: Two broad bands at ~ 6160 and 6665 cm<sup>-1</sup> were represented as entirely hydrogen bonded molecules. Moreover, the other two components at ~ 6850 and 7030 cm<sup>-1</sup> were respectively related to disrupted H-bonded (at least one of three bonds) and non-hydrogen bonded molecules.<sup>119</sup> On the other hand, Sasic *et al.*<sup>120</sup> came up with the exact approximation that water contains two components based on spectroscopic evidence (NIRS): hydrogen bonding and non-hydrogen bonding species that change with temperature. They calculated  $\Delta H$  of 3.65 kcal/mol (15.3 kJ/mol) for the system.<sup>120</sup> Similarly, Jin *et al.*<sup>115</sup> calculated  $\Delta H$  of 15 kJ/mol for a similar system using NIRS and calculating Van't Hof equation.<sup>115</sup> This band in the range 6500 – 7100 cm<sup>-1</sup> is the 1<sup>st</sup> overtone of water OH deconvoluted into Gaussian components. Each of these components represents a water fraction.

Both Monosmith and Walrafen<sup>119</sup> and Choppin<sup>114</sup> have deconvolution of this band resulting in four bands in which bands at lower wavenumbers represent hydrogen bonding species, and the highest wavenumber band represents free OH of water. However, Choppin's<sup>114</sup> deconvolution resulted in bands centred at 6540, 6860, 7060 and 7370 cm<sup>-1</sup>, while Monosmith and Walrafen's<sup>119</sup> bands tended to be wider and centred at 6160, 6665, 6850 and 7030 cm<sup>-1</sup>. The two papers are quite different in band position, while they are similar in the band deconvolution process. This is due to the broadness of the OH band of the water containing different species.

Another study conducted by Maeda *et al.*<sup>116</sup> suggested that water contains six bands involved with the same range of NIRS. Based on their findings using the second derivative of the water spectrum, the band at  $\sim 7440\text{ cm}^{-1}$  is associated with  $\nu_1 + \nu_2 + \nu$  (rotational mode), which was not included in the hydrogen bonding calculation. They ended up with five bands which are temperature-dependent. However, they did not mention the band position of each of those deconvoluted five bands in their article, possibly because of changing band position with temperature. However, those bands are shown in figure 4 of their article ranging between  $\sim (6450 - 7100\text{ cm}^{-1})$ .<sup>116</sup> A further interesting study from Langford *et al.*<sup>121</sup> used the NIR-visible region, which obtained the 4<sup>th</sup> and 5<sup>th</sup> overtone of OH stretching bands at (604 and 514 nm) or ( $16,666$  and  $19,445\text{ cm}^{-1}$ ). They suggested that the water contains two components. However, at high temperatures, water tends to form a third component.<sup>121</sup>

A recent study by Tan *et al.*<sup>122</sup> suggested that water's 1<sup>st</sup> overtone band contains nine different species, including hydrogen and non-hydrogen bonding species. The water's 1<sup>st</sup> overtone includes lots of information about hydrogen bonding species, which will be investigated.

In this chapter, the region of NIR spectroscopy was analysed where the OH 1<sup>st</sup> overtone vibration takes place, especially for water as well as how this vibration is affected when a solute is added.

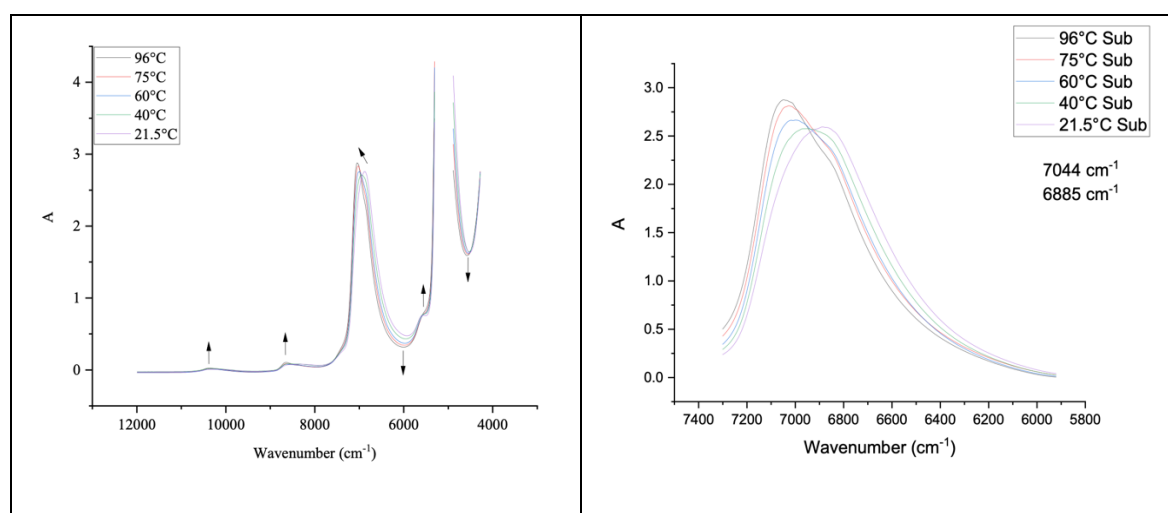


Figure 5.1 NIR spectra of water in variable temperature

Using the NIR spectroscopic technique for water shows very high absorbency at  $6600 - 7200\text{ cm}^{-1}$ . This very high absorbency represents symmetric and asymmetric stretching 1<sup>st</sup> overtone O-H band of water.<sup>101, 105, 119, 123</sup> It is a relatively broad band which indicates a possibility of overlapped bands for different components. See Figure 5.1. In order to study this band in-depth, a water sample was tested with varying temperatures to investigate this

kind of absorbance. An isosbestic point in Figure 5.1 indicates spectral variations showing a transformation from one band to the other, suggesting that the water OH absorption is temperature-dependent. Arrows indicate the change in band intensity with increasing temperature.

As shown in Figure 5.1, it is clear that there are two bands (or two groups of bands) centralised at about 6870 and 7040 cm<sup>-1</sup>. These two bands change oppositely to each other with changing temperature due to the effect of the hydrogen bonding. As the temperature increases, the band at the lower wavenumber decreases and the one at the higher wavenumber increases due to the decrease in water hydrogen bonding and increasing the free OH group.<sup>57, 120</sup> This range indicates at least 2 components of water that change in intensity with temperature. Thus, the NIR spectra of water are temperature-dependent.

For an easy investigation of the temperature-dependent of water band, spectra of water at different temperatures were subtracted using the water spectrum at 21 °C as a reference for subtraction to examine the behaviour of this region. Figure 5.2 displays a clear difference in the two components of the water at ~ 7100 and 6730 cm<sup>-1</sup>, which indicates the temperature-dependency of the water. That means the original spectrum of water in this region consists of at least two overlapped bands. One at ~ 7100 and 6730 cm<sup>-1</sup> increased and decreased respectively with rising temperature, which contains interesting information about hydrogen bonding. The broadness of the two subtracted regions is different, indicating the difference between the two components. Additionally, the nonparallel shape of each feature in subtracted spectra can give evidence of more obscured overlapped bands which exist within each feature. Figure 5.2 (A) demonstrates that both the minima and maxima subtracted spectra show small shoulders for each region. The shoulder of 6730 cm<sup>-1</sup> region is located at lower wavenumber and wider than that located in 7100 cm<sup>-1</sup> region, which is smaller and sharper and located at higher wavenumber.

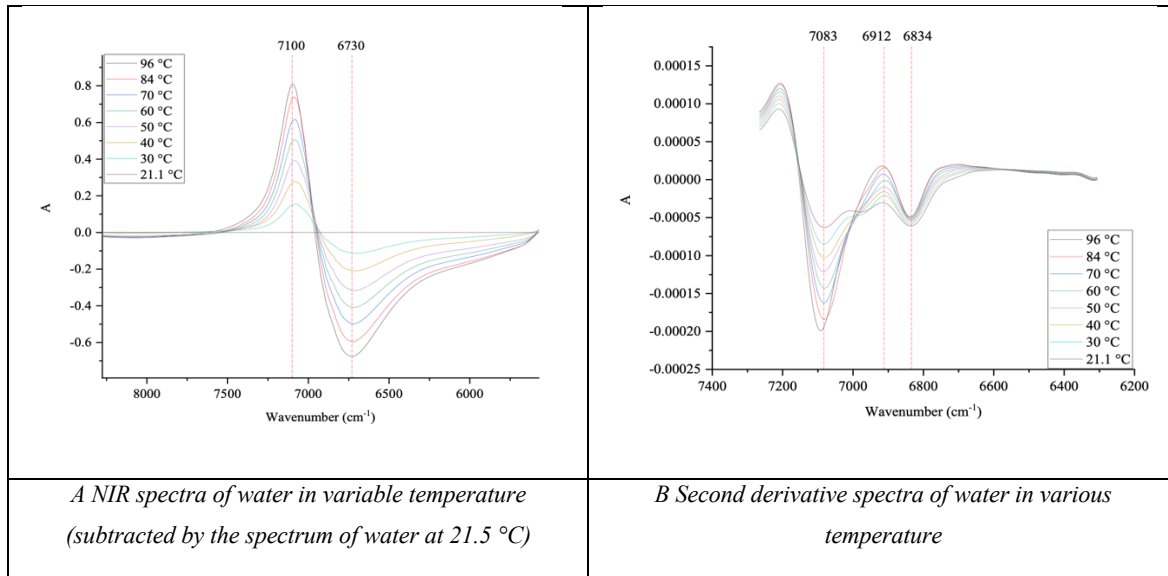


Figure 5.2 NIR spectra of water in variable temperature

However, a second derivative of the same samples was plotted to investigate this behaviour in more detail, as shown in Figure 5.2 B. The second derivative displays more details of these components with changing temperatures. This range contains about four areas which shows differentiation with temperature. It reveals more overlapped bands of at least three or four bands within the same region.

This work has shown that the apparent transformation between the different types of hydrogen vibration moves with the temperature. The second derivative spotted more than three types of vibrations overlapped. One limitation is the high intensity of the water's 1<sup>st</sup> overtone band, reaching 3 (a.u.). In this case, the transmittance of the beam that hit the detector is very low. The probe used in this experiment is fixed at a 2 mm path length cell. In order to reduce the intensity, a smaller path length cell should be used. Therefore, less amount of sample is subjected to the NIRS beam. In the next experiment, a path length cell of 0.4 mm is used. Deconvolution of the band will better illustrate the number of bands present in the water.

### 5.2.1.2 Deconvolution of the band

As discussed earlier, OH 1<sup>st</sup> overtone of water has a very wide absorbency in the NIRS region, characterised by a broad band. This band contains several overlapping bands, which were seen in the second derivative of the previously shown band. The main issue was the relatively high path length cell used, causing the high intensity of the band. In this section, a path length cell of 0.4 mm was used.

A sample of pure H<sub>2</sub>O was analysed using NIR spectroscopy with a path length cell of 0.4 mm. The sample was subjected to varying temperatures from 5 °C to 95 °C with a 5-degree step. A water path was used to heat the sample and placed inside the water path in a beaker. A digital thermometer on a (0 – 300 °C) scale was used to measure the temperature with ± 0.5 °C error. Although the measurement error might appear relatively high, the water path and the hot plate are separate equipment used and controlled by the user. So, it is recommended to use a built-in heating system.

Based on our results in Figure 5.3, it is clear that the 1<sup>st</sup> overtone band of the water moves to higher wavenumbers (a lower wavelength) as the temperature increases. Again, it is well known that hydrogen bonding decreases with the temperature.<sup>53</sup> This vibration band moves to lower wavelength in the IR spectroscopy, where the free OH species are identified. Therefore, the water was established as a standard system and analysed how it is affected when adding other chemicals.

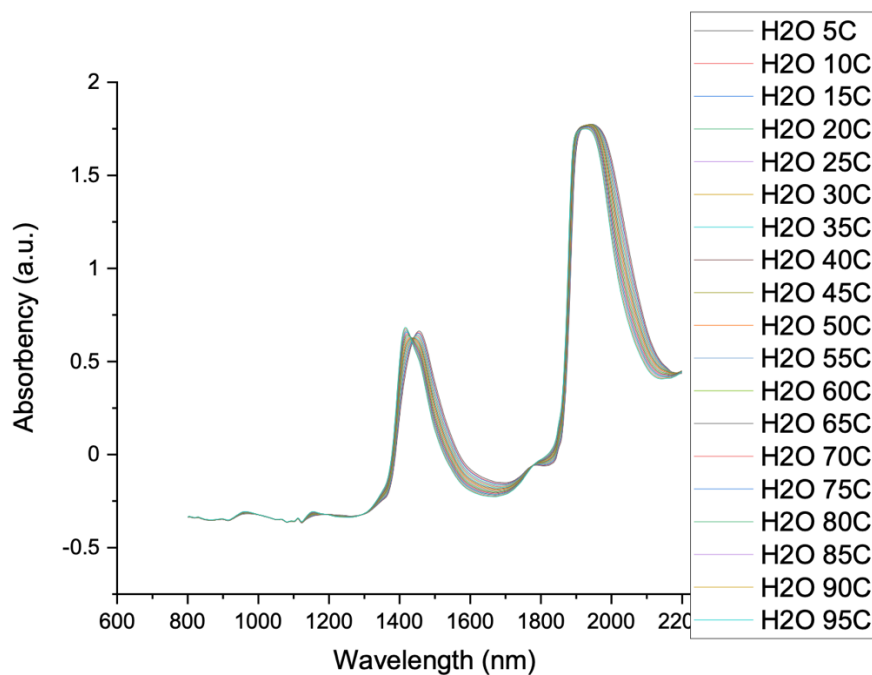


Figure 5.3 NIR spectra of H<sub>2</sub>O in variable temperatures (5 – 95 °C)

Figure 5.3 shows the two major bands at 1950 and 1450 nm, representing the OH vibration of the combination and 1<sup>st</sup> overtone, respectively. With the rising temperature, the 1<sup>st</sup> overtone vibration shifts to a lower wavelength (the left-hand side of the graph). That indicates losing hydrogen bonding and forming free OH species. To see it in more detail, a deconvolution of each band was done, and the area of each deconvoluted band was calculated using Origin.



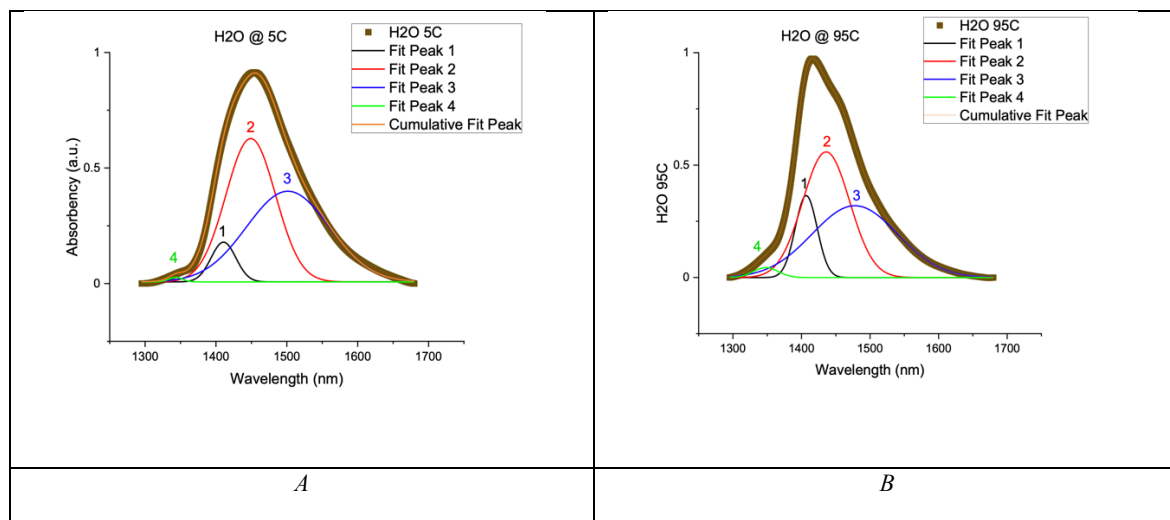
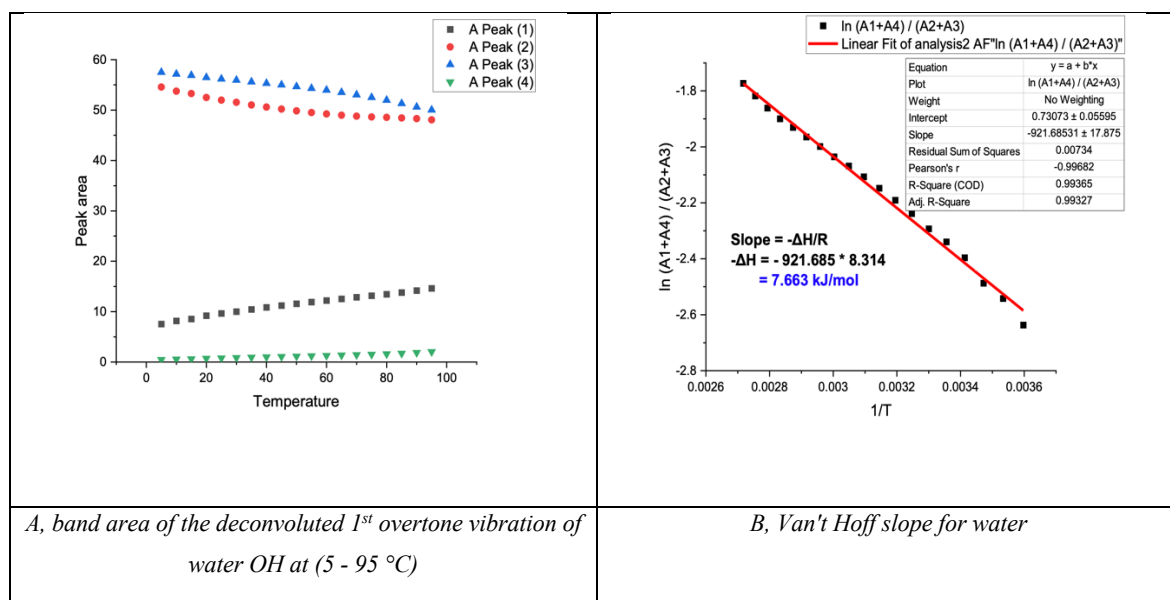


Figure 5.4 Deconvoluted 1<sup>st</sup> overtone band of water OH at (5 & 95 °C)



A, band area of the deconvoluted 1<sup>st</sup> overtone vibration of water OH at (5 - 95 °C)

B, Van't Hoff slope for water

Figure 5.5 Band area of water OH at (5 - 95 °C)

Figure 5.4 illustrates deconvoluted bands of the water at 5 °C and 95 °C. The rest of the water deconvoluted bands at the temperatures between 95 °C and 5 °C were also tested, but the actual spectra for the rest of the temperatures are not displayed. The accuracy of fitting the bands was calculated as ( $R^2 = 0.99975 \pm 0.0002$ ). The band area of all temperatures is displayed in Figure 5.5 A which shows the areas of bands 1 and 4 increase while 2 and 3 decrease with temperature. The best deconvolution was done by splitting the OH band into 4 bands, which corroborates other studies on different groups such as Monosmith and Walrafen<sup>119</sup> and Choppin.<sup>114</sup> Bands number 1 and 4 are more prominent in the 95 °C

spectrum than the same bands in 5 °C spectrum. On the other hand, the bands 2 and 3 which are smaller in the 95 °C spectrum than those in the 5 °C spectrum. The results were interpreted, suggesting that bands 2 and 3 are hydrogen bonding species and bands 1 and 4 are free OH species of the water molecule. This finding is consistent with the two aforementioned groups in Monosmith and Walrafen<sup>119</sup> and Coppin.<sup>114</sup> For more details, the area under each band was plotted against temperature when the latter ranges from 5 °C to 95 °C. In this case, it is possible to use the constant of equilibrium K to calculate the Van't Hoff equation.

$$K = \frac{[Peak\ 1 + Peak\ 4]}{[Peak\ 2 + Peak\ 3]}$$

However, the Van't Hoff equation can be calculated by using the slope of  $\ln K$  against  $1/T$  where T is the temperature in Kelvin.

$$\ln = \frac{[Peak\ 1 + Peak\ 4]}{[Peak\ 2 + Peak\ 3]}$$

Figure 5.5 (B) illustrates the calculated slope which equals (921.685). In turn,  $\Delta H$  can be obtained from the following equation

$$\text{slope} = - \frac{\Delta H}{R}$$

Where R is the gas constant (8.314).

The calculated  $\Delta H$  for the water is **7.663 KJ mol<sup>-1</sup>**, which corresponds to the energy absorbed by the system when breaking down the hydrogen bonding and forming free OH. Hence, any added materials to the system may affect the  $\Delta H$ . By then, any difference in the  $\Delta H$  value can be calculated when a substance is added to the water, affecting the hydrogen

bonding. The next step consists of adding LGO to the water, and the change of  $\Delta H$  will be calculated and discussed in detail.

### 5.2.2 LGO

As mentioned earlier, adding any chemical to the water may change the hydrogen bonding, affecting the  $\Delta H$  value of the system. In this section, LGO is added to the water to see how it affects hydrogen bonding. It is worth mentioning that LGO creates triol when interacting with water. However, the number of new hydroxyl groups formed was negligible. More details on the LGO water interaction are discussed later.

LGO was diluted with water in different concentrations: 0.04, 0.08, 0.4 and 0.8 m. Each diluted sample was tested at various temperatures, as done previously with the water system. This experiment aims to investigate the effect of LGO on the water OH vibration.

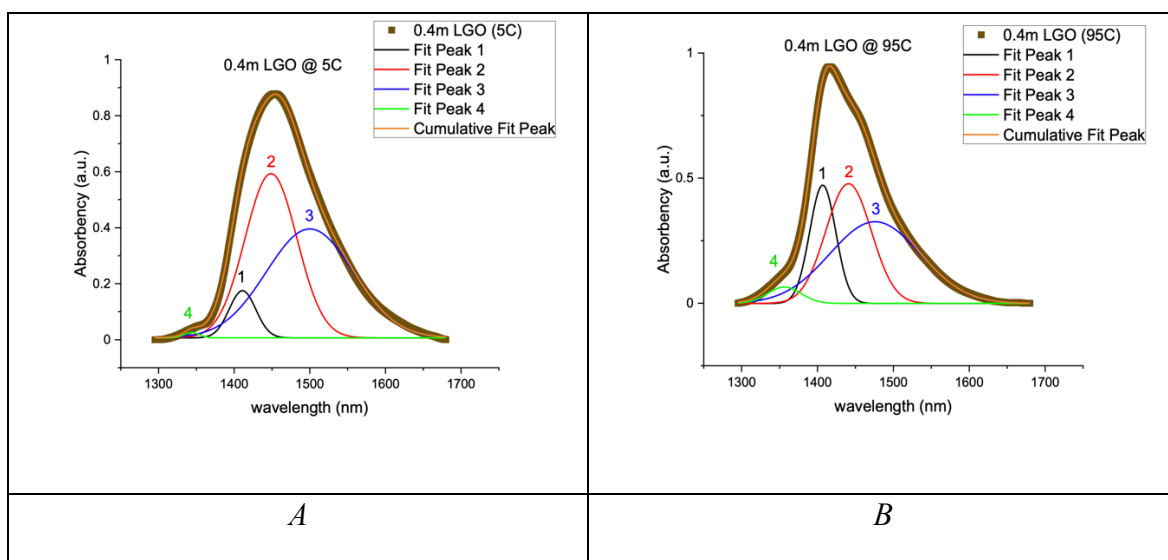


Figure 5.6 Deconvoluted 1<sup>st</sup> overtone band of 0.4 m LGO at (5 & 95 °C)

Figure 5.6 illustrates the change in the bands associated with hydrogen bonding and free OH in two temperatures, 95 °C and 5 °C. By comparing Figure 5.6 with the water system in Figure 5.4, more transformation from hydrogen bonding to free OH were observed in the diluted LGO sample than in the water system. This indicates an apparent effect of LGO on the water. Nevertheless, Figure 5.6 demonstrates a more significant change in the band area than the water system shown in Figure 5.4. In addition to the gradual increase/decrease in

the band area for the free-OH / H-bonded species, there is a critical change at about 60 °C for the LGO sample compared to the pure water, as illustrated in Figure 5.7. Another analytical method can be used to confirm this critical change that occurred at 60 °C.

It is worth mentioning that this effect of the LGO on water has been tested several times using different conditions. First, the sample was tested in temperatures starting from 5 °C heating up to the 95 °C and vice versa, using another sample from 5 °C to 95 °C showing the same result. On the other hand, a similar sample using D<sub>2</sub>O was tested to detect the change in the ketone vibration band during an equal heating time. For more details, this experiment is presented later in this chapter. Figure (A.4.3) indicates no significant difference in converting the ketone to the geminal diol.

Additionally, this experiment was done using two samples. The first is a freshly mixed LGO with water (no hydroxyl groups were present in the LGO). The second is a six-week-old solution. All results gave the same effect at 60 °C as mentioned earlier. The sample illustrated in this section was freshly mixed.

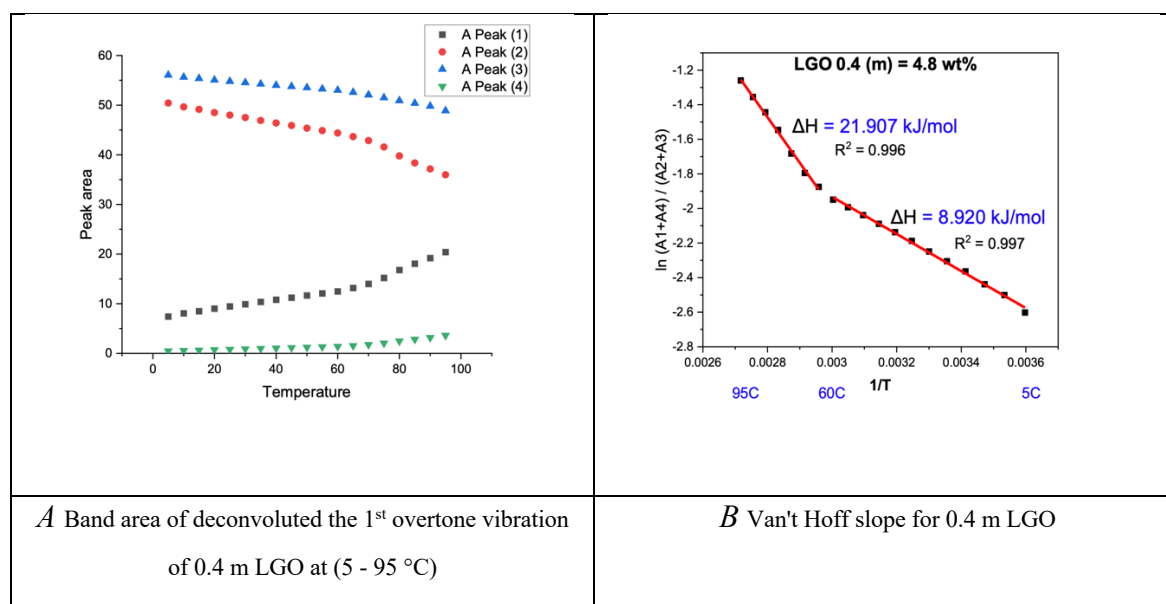


Figure 5.7 (A) Band area of deconvoluted OH band of 0.4 m LGO at (5 - 95 °C)

The STA was used for the same sample to support our findings. The results are consistent with those obtained from the NIR spectroscopy mentioned earlier. The STA supports this significant change found in NIRS, as seen in Figure 5.8. The figure documents a slight change in the heat flow at about 60 °C, as indicated by the first derivative. These results

suggest some change in the interaction within the solution at this temperature which corroborates the significant effect of LGO on the water at this specific temperature.

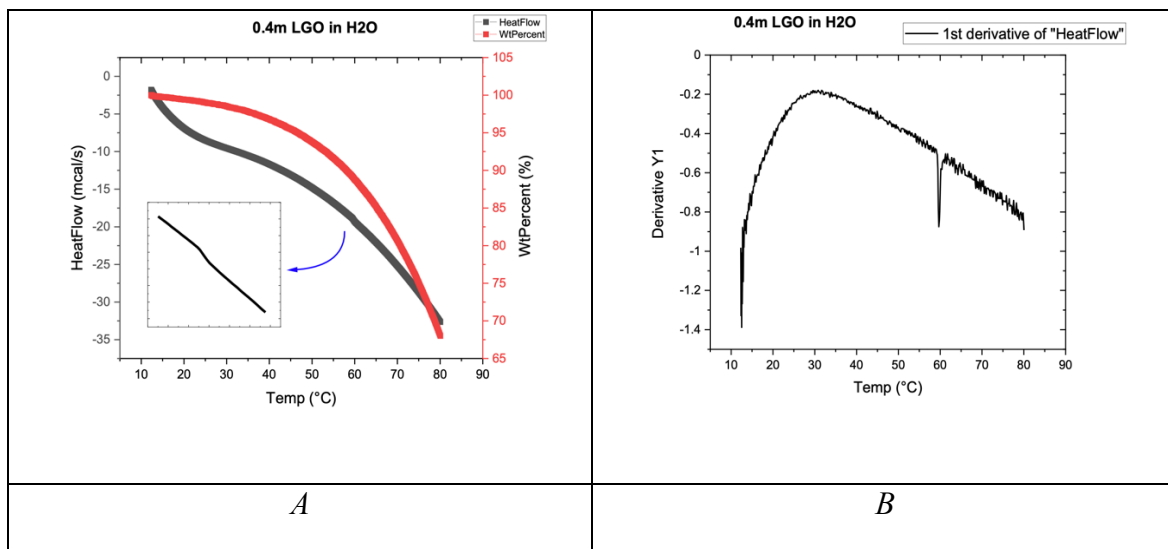


Figure 5.8 STA for (A) 0.4 m LGO in H<sub>2</sub>O and (B) its 1<sup>st</sup> derivative

Accordingly, the Van't Hoff equation which can be applied to two different parts of the system, below and above 60 °C. The  $\Delta H$  was calculated for the two parts of the system resulting in 8.920 kJ mol<sup>-1</sup> and 21.907 kJ mol<sup>-1</sup> for the temperatures below and above 60 °C respectively.

It has been found that LGO can significantly affect the  $\Delta H$  value for the water OH of hydrogen and non-hydrogen bonding. This result indicates that when LGO is present in the water, it helps break down H-bonding in the system at higher temperatures easier than in the pure water system. This phenomenon is significantly more effective above 60 °C. Additionally, when it is heated, LGO/diol self-associations break up, creating more potent monomers to bond with other species. The <sup>1</sup>H and <sup>13</sup>C NMR spectroscopy is carried out later in this chapter for more support for this finding.

Other concentrations of (0.04, 0.08, 0.8, 1.0 and 1.6 m) LGO in H<sub>2</sub>O were tested. The more concentrations are used, the wider vision is obtained. It is expected to observe some differences in the concentration of LGO towards this effect on the water. Generally, the different concentrations tested show similar behaviour to the earlier sample of 0.4 m LGO except the lowest concentration of 0.04 m LGO, where no change could be identified.

It is worth mentioning that a 0.8 molal sample is about 9 wt% LGO in water which is the maximum concentration that could be trusted. The maximum concentration of the LGO in

water, depending on the temperature, is around 10 wt%. Above that concentration, LGO is not appropriately dissolved in water, and therefore the results of deconvolution will not be accurate. Table (A.5.1) shows each sample of LGO in water in different concentrations, the results of the deconvoluted bands, the Van't Hoff equation and the  $\Delta H$ .

Table (A.5.1) presents two different behaviours of LGO in water. First, the low concentrations of 0.04 and 0.08 m show similar  $\Delta H$  to the water system. Although  $\Delta H$  is slightly higher than that of water, it does not show any significant change at specific temperature. The table also shows that even the very low concentrations of LGO can affect water behaviour. Second, the relatively higher concentrations of 0.4 and 0.8 m samples indicate significant change, with the water OH vibration reacting differently below and above 60° C. At lower temperatures, there is a slight increase of  $\Delta H$  values with concentrations compared to the water system. Nevertheless, above 60 °C, there is a dramatic increase in  $\Delta H$  with a more than double value. This suggests an increase in the ability of hydrogen bonding formation, probably caused by rearrangement of the chemical structure of the LGO at the specific temperature. That will affect the hydrogen bonding to be changed at high temperatures. If the LGO can affect water hydrogen bonding, one can wonder if the Cyrene behaves similarly. This question was investigated in the following experiment.

### 5.2.3 Cyrene

Cyrene was examined in a similar process/condition as LGO experiment regarding the deconvolution of the OH band and Van't Hoff equation. This work aims to differentiate between Cyrene, LGO and then MEK to establish how those different compounds affect the water. Diluted Cyrene in water represented by 0.04, 0.4, 0.8, 1.0 and 2.0 m was examined by NIR spectroscopy to investigate the 1<sup>st</sup> overtone of water OH.

Cyrene behaved similarly to LGO in terms of rising  $\Delta H$  of water hydrogen bonding, as demonstrated in Table (A.5.2). Cyrene shows an increase in  $\Delta H$  in correlation with its concentration. Based on our results,  $\Delta H$  values are 8.3, 10.4, 11.7, 11.5 and 16 KJmol<sup>-1</sup> respectively for the concentrations of 0.04, 0.4, 0.8, 1.0 and 2.0 m. However, Cyrene does not show a significant change in  $\Delta H$  at a specific temperature as observed with the LGO at 60 °C. An exception of 0.4 molal Cyrene sample can be considered. If it is considered a change, it shows a slightly different behaviour above 75 °C. However, this will be neglected as it is not found in other concentrations.

Cyrene is dissolved in water in very high concentrations above (90%)<sup>124</sup>, and adding more Cyrene to water affects the total hydroxyl group vibration. Hence, our water system is no longer ideal for measuring the hydrogen bonding effect due to the increase in the hydroxyl groups formed by the geminal diol-Cyrene.

Based on our results displayed in Table (A.5.2), Cyrene has influenced the hydrogen bonding of water molecules. This effect increased with the concentration of Cyrene. Unlike LGO, Cyrene has a significant change in a specific temperature within the same sample (same concentration in various temperatures). That provides the LGO with a different ability of affecting the water H-bonds. So far, it remains unclear to understand why this is happening with the LGO, in particular. One more sample containing the ketone group, MEK, was examined to verify if it affects the water.

#### **5.2.4 Methyl Ethyl Ketone MEK**

Methyl ethyl ketone (2-butanone) behaves with water similar to Cyrene. MEK in water affects  $\Delta H$  of hydrogen bonding by increasing the value of  $\Delta H$  for the water as in the case of Cyrene and LGO.  $\Delta H$  increase was observed with concentration, but  $\Delta H$  remains unaffected by any specific temperature, as displayed in *Table (A.5.3)*. As could be concluded that MEK behaves like Cyrene but less effectively as an interpretation of these results. It does not have such a significant change in a specific temperature within the same sample (same concentration in various temperatures).

These results further show that the LGO has a significantly different effect on water vibration of OH 1<sup>st</sup> overtone that affects the hydrogen bonding. This strongly suggests that LGO experiences some changes in its chemical structure when interacting with water. This structure modification also changes with temperature. In the next section, additional investigations of LGO and water interaction are conducted using NMR spectroscopy to reveal more information about this interaction.

### 5.2.5 NMR spectroscopy for LGO in water (temperature-dependent)

This section examines how the temperature affects the reaction equilibrium between LGO and diol, triol LGO in water. The sample was prepared two months before testing to get to the best equilibrium state and subsequently scanned using 500 MHz NMR spectroscopy.

As shown in Figure 5.9, <sup>13</sup>C NMR stacked spectra of 4 wt% LGO in D<sub>2</sub>O in variable temperatures, the CH<sub>2</sub> of C3 of the triol at about 37ppm reduced slightly with the rise of temperature until it reached 96 °C where it dramatically reduced, showing less triol forms of LGO. Moreover, the other end of the spectrum contained the alkene HC=CH for C4,3 and the ketone C=O of C2 at around 127, 153, 193ppm, which stayed constant throughout the whole temperature range until at 96 °C, when it increased considerably. Although <sup>13</sup>C NMR spectroscopy is not a quantitative method, the peak intensity provides a helpful guide to abundance.<sup>125</sup> In order to estimate the change quantitatively, <sup>1</sup>H NMR spectroscopy using peaks integration was carried out and presented in the next section.

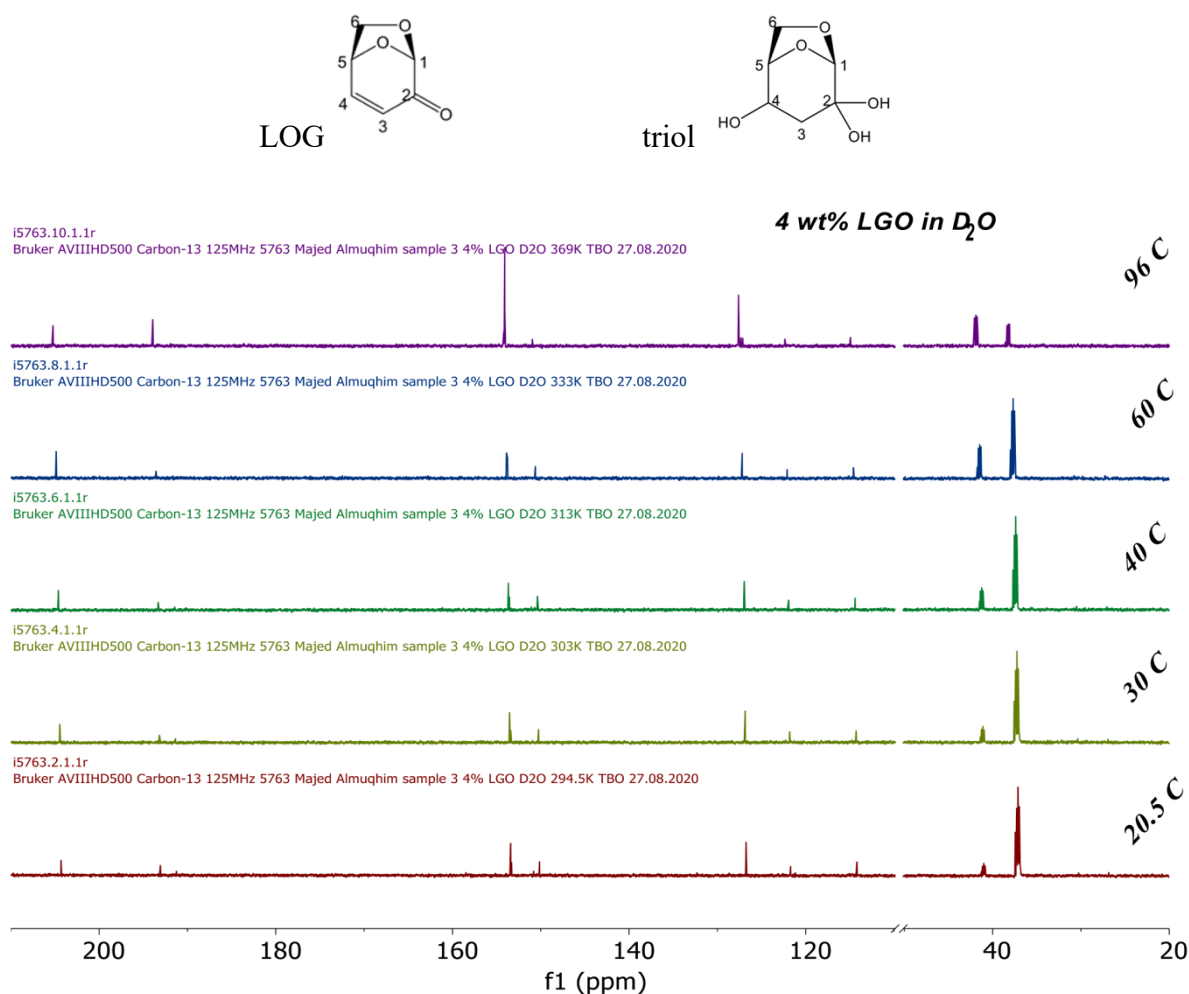


Figure 5.9 <sup>13</sup>C NMR stacked spectra of 4 wt% LGO in D<sub>2</sub>O in variable temperatures



In Figure (A.5.1), <sup>1</sup>H NMR stacked spectra of the same sample, the CH<sub>2</sub> at about 1.8 – 1.9 ppm presents a similar pattern where it first reduced slightly with the rise of temperatures until it reached 96 °C, where it dramatically reduced, showing fewer triol forms of LGO. The opposite occurred with the alkene. The protons of HC=CH carbon 4 and 3 respectively at about 7.4 and 6 ppm remain constant for the whole range of temperatures except 96 °C, which is noticeably increased. The results of the peak integration at 1.9 and 7.4 ppm suggest that the LGO was in the lowest stage even during the heating process until 96 °C, where the reaction reverted towards the product allowing the LGO to form back.

By comparing Figure 5.9 and Figure (A.5.1) of the <sup>13</sup>C and <sup>1</sup>H NMR respectively stacked spectra of 4 wt% LGO in D<sub>2</sub>O (0.33 m) in varying temperatures, one can assume that the solution at a temperature of 96 °C behaved differently. It shows that the triol forms converted back to the LGO. That pushes the equilibrium in the opposite direction when the temperature reaches 96 °C.

As will be discussed later in this chapter, heating the water solution of LGO at about 70 °C speeds up the interaction between the two components forming the triol form of LGO. This result is shown in Figure 5.11 using MIR spectroscopy. It is also clear that the same conversion of LGO to triol-LGO occurred using <sup>13</sup>C and <sup>1</sup>H NMR spectroscopy every day for 7 days as illustrated in Figure 5.18 and *Figure (A.5.12)*, respectively. By heating the sample using 500 Hz NMR spectroscopy up to 96 °C it showed changing for the reaction equilibrium reversibly towards forming the LGO as shown in both Figure 5.9 and Figure (A.5.1) of the <sup>13</sup>C and <sup>1</sup>H NMR spectroscopy, respectively. Integrations of peaks at 6 ppm and 1.7 ppm reveals the conversion of triol-LGO to LGO, as shown in Figure 5.10.

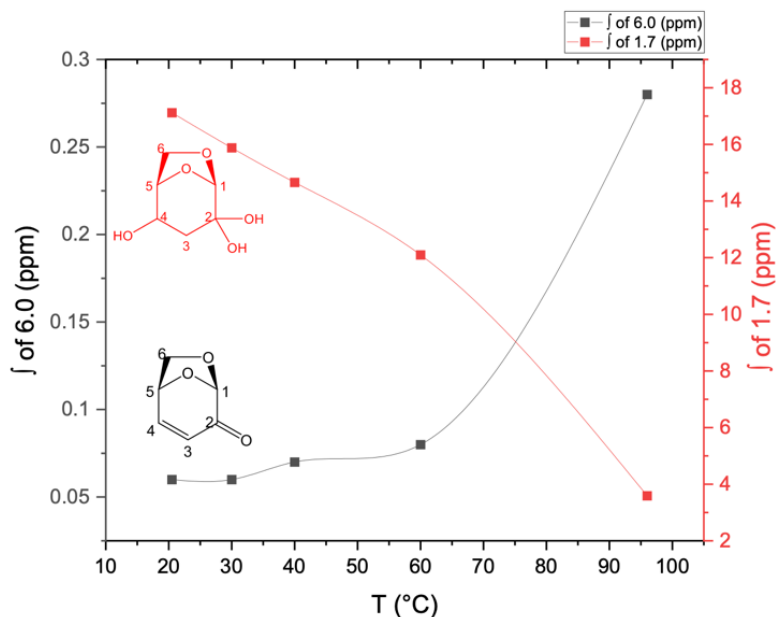


Figure 5.10 <sup>1</sup>H NMR spectroscopy integration results for LGO conversion by temperature change

Apart from the 4 wt% (0.33 m) LGO sample discussed earlier for the varying temperatures using <sup>13</sup>C and <sup>1</sup>H NMR spectroscopy, other concentrations of 1, 2, 10 and 25 wt% or (0.08, 0.16, 0.88 and 2.65 m) for the same sample were tested using the same method. All concentrations show an identical behaviour, and there is no clear evidence that this behaviour favoured any specific concentration. Hence, the sample of 4 wt% (0.33 m) was the only one presented in this chapter. Note that the sample of 25 wt% was saturated, and not all LGO was dissolved. Therefore, this sample is not as much as 25 wt% as it is written, but it may get to the maximum amount of LGO dissolved in water, which is slightly above 10% as mentioned earlier in this chapter.

### 5.3 H<sub>2</sub>O/LGO interaction (time-dependent)

It was mentioned earlier that the LGO interaction with water takes a relatively long time for the H<sub>2</sub>O to attack the ketone C=O and the alkene HC=CH of the LGO, forming a geminal diol on C2 and a hydroxyl group on C4, respectively. In order to investigate this reaction, multiple spectroscopic techniques have been applied. IR (mid and near – IR), UV-Vis and NMR spectroscopy were used to monitor the daily interaction between LGO and water. Cyrene was also tested through these techniques to compare it with the LGO.

#### 5.3.1 IR spectroscopy – fundamental vibration

The ketone double bond in the LGO located at about 1700 cm<sup>-1</sup> in the IR spectrum was investigated. As the diluted LGO will be dissolved in water, some bands may interfere with the LGO. The water H<sub>2</sub>O spectrum generally shows two main bands in the MIR region, one at 1650 cm<sup>-1</sup> and the other at 3400 cm<sup>-1</sup> for OH bending and stretching vibration respectively.<sup>78</sup> The ketone band for the LGO, on the other hand, rises a band at about the same region as the water OH bending vibration. Consequently, the two bands will present overlapped peaks which may prevent investigating the ketone band, especially with lower concentrations. So, deuterium oxide or heavy water (D<sub>2</sub>O) was used with the LGO instead of (H<sub>2</sub>O).

Deuterium oxide produces bands at about 1200 cm<sup>-1</sup> and 2500 cm<sup>-1</sup> for OD bending and stretching vibration respectively.<sup>126-128</sup> See Figure (A.4.3). Therefore, the ketone vibration will not be interfered. A mixture of (H<sub>2</sub>O and D<sub>2</sub>O) can also be used to enhance the spectrum and confirm the difference between the two species of water. With some relatively high concentrations of LGO, water can be used with extra care and deconvolution of the overlapped band can be applied.

The LGO was dissolved in water to examine its solubility limit. Samples of 9 – 13 wt% with 1 wt% step of LGO in water were tested. In Figure (A.5.2), the experiment reveals that the highest concentration can the LGO be dissolved in water is 11 wt%. Although samples were shaken very well by hands and tubes shaker, both samples 12 and 13 wt% contain some drops of LGO that could not be dissolved.

Based on an assessment done by Krishna *et al.*<sup>129</sup>, the LGO interact with water molecules forming triol LGO. The interaction breaks down the ketone double bonds of C2 and forms a



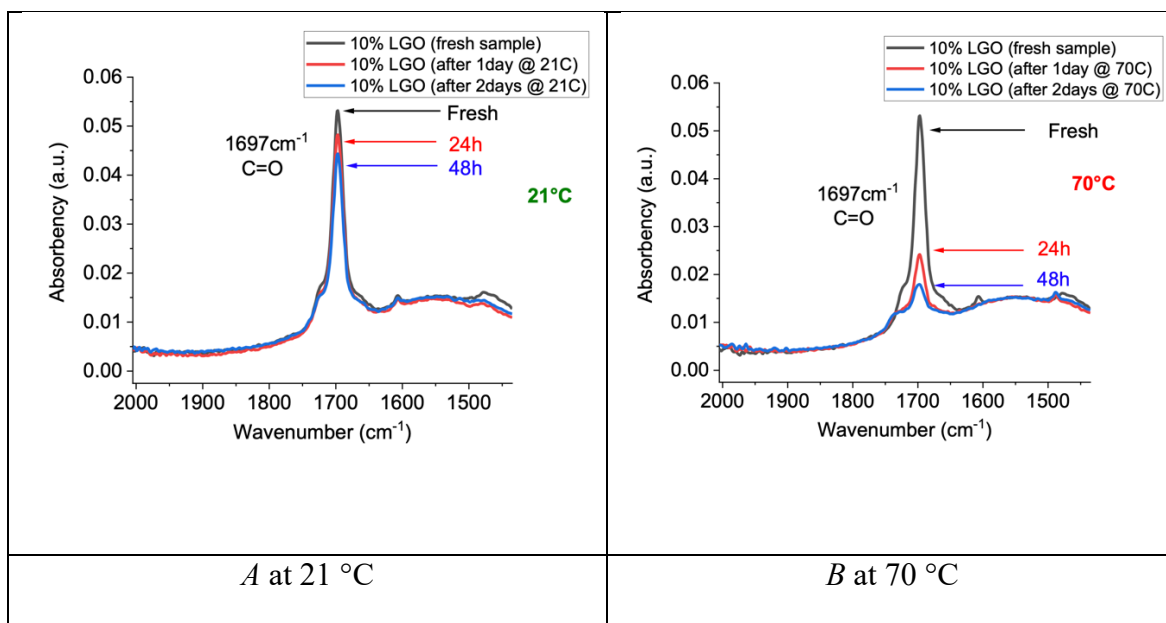


Figure 5.11 MIR spectra of 10 wt% LGO in H<sub>2</sub>O

Further IR assessment for the diluted LGO reveals more evidence of its reaction with water. Figure (A.5.4) (A) shows a small band at 1488cm<sup>-1</sup>, but grows with time for the diluted LGO. This band represents the bending (scissoring) vibration band for C3 (CH<sub>2</sub>). In contrast, a similar but smaller and at a relatively lower frequency band at 1475 cm<sup>-1</sup> appears in the pure LGO sample for the C6 (CH<sub>2</sub>). This confirms the breaking up of the C=C double bond between C3 and C4. In addition, a band at 970 cm<sup>-1</sup> appears as CH (trans) out-of-plane bending for the C=C for the pure LGO sample. Figure (A.5.4) (B), shows that this band is smaller and weaker in the diluted sample, especially after a longer time and/or higher temperature. That means that the double bond of C3=C4 was broken down. One more evidence for breaking down the C=C with diluted LGO is the pair of bands at 1605 cm<sup>-1</sup> and 1475 cm<sup>-1</sup>, which appears with the C=C stretching for (ring) compounds in the pure LGO as illustrated in Figure (A.5.5). This pair of bands disappear with the diluted LGO. See Figure (A.5.4) (A).

**The C-H stretching absorbance** lies between 2700 – 3300 cm<sup>-1</sup> of the IR spectroscopic range, depending on the type of carbon group.<sup>78</sup> With the pure LGO, most CH vibration comes from the single H-bonded to a carbon C-H, which usually appears around 2890 cm<sup>-1</sup>. As displayed in the pure LGO spectrum in Figure (A.5.6) (B), there are three bands located at 2900, 2969 and 3060 cm<sup>-1</sup>, which correspond to -CH<sub>2</sub>, -CH and =CH, respectively. The

band at 3060 cm<sup>-1</sup> indicates the vibration of =CH where the carbon double bonded with another carbon (sp<sup>2</sup>), moving the vibration slightly at a higher wavenumber. Methylene (>CH<sub>2</sub>) rises a pair of bands at about 2970 and 2900 cm<sup>-1</sup>. This absorbance indicates that the two hydrogens are connected to the C6. However, these two bands shift slightly to lower wavenumbers at 2920 and 2960 cm<sup>-1</sup> with the diluted LGO, revealing a new type of CH<sub>2</sub> at C3 and breaking down the double bond for (C3=C4) as illustrated in Figure (A.5.6) (A). The new bands are growing with time, indicating the slow interaction between the water and the LGO.

Our IR spectroscopy finding suggests that the reaction took over a week to reach an equilibrium state or get a better yield of the triol. Nevertheless, evidence is required to confirm this last result. Hence, NIRS was used as an alternative approach for monitoring the LGO conversion to triol as presented in the following subsection.

### 5.3.2 Near-infrared spectroscopy (NIRS) – 1<sup>st</sup> overtone vibration

NIRS also monitored the LGO interaction with water. The 1<sup>st</sup> overtone of the different types of CH stretching vibration agreed with the fundamental bands. This time, LGO was dissolved in H<sub>2</sub>O – not in D<sub>2</sub>O. In the last experiment, LGO was dissolved in D<sub>2</sub>O when using fundamental vibrations (IR) due to the interference between the two-component bands of the water binding and the ketone stretching vibration. The limitation of this experiment is that relatively small bands characterise the CH 1<sup>st</sup> overtone band in this region and are lying between the two big bands of combination and 1<sup>st</sup> overtone vibration for the water OH. This results in a slightly harder possibility to separate the CH bands for the investigation. See Figure 5.3 for the two large bands of the water.

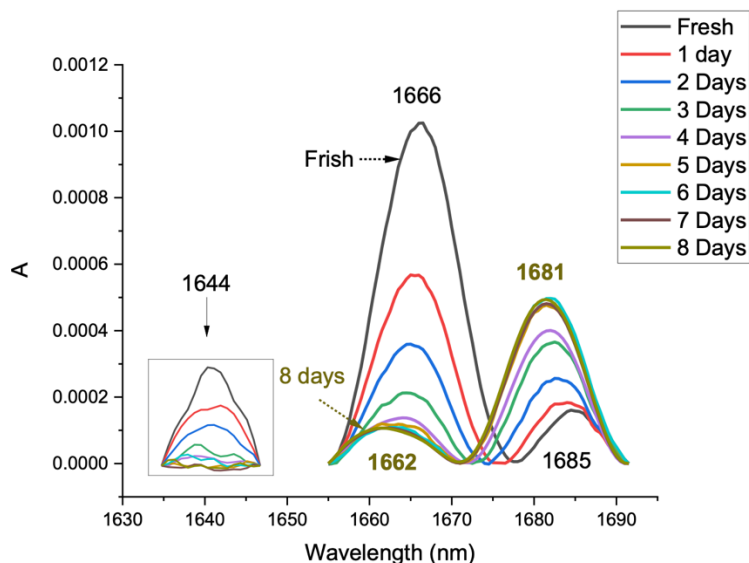


Figure 5.12 NIR spectra of diluted LGO (10 wt%) in H<sub>2</sub>O in different days

The 1<sup>st</sup> overtone bands of CH stretching are illustrated in Figure 5.12. In this figure, the aqueous solution of LGO was scanned every day since it is freshly mixed up for 8 days. These spectra were modified using the 2<sup>nd</sup> derivative to eliminate the effect of the two neighbouring OH bands of the water and recalculated negatively to get (peaks) instead of (minima). The band at 1666 nm (6002 cm<sup>-1</sup>) decreases with time, transforming to a band at 1681 nm (5949 cm<sup>-1</sup>). This indicates the breaking down of the double bond of the alkene C=C in the LGO. The growing band at 1681 nm confirms the born of a new CH<sub>2</sub> for the C3 when interfered with water. Lastly, the decrease of the band at 1644 nm (6083 cm<sup>-1</sup>) corresponds to the 1<sup>st</sup> overtone of =CH stretching for C3 and C4, where the carbon double bonded with another carbon (sp<sup>2</sup>). The decrease of this band indicates the breaking down of the alkene again. The size of this band area was expanded to fit into the same graph, but it has a lower intensity scale than it appears. The low intensity of this vibration band is consistent with its fundamental band in the MIR region at 3060 cm<sup>-1</sup> as shown in Figure (A.5.6) (A and B). The disappearance of this band with time indicates the breaking down of the double bond between the two carbon atoms at C3 and C4.

NIRS results for the LGO/H<sub>2</sub>O interaction shows an apparent transformation. One of the advantages of using the NIRS is monitoring this reaction in real-time. Additionally, it is a

quantitative technique, and therefore, it has the potential to be suitable for monitoring the production of LGO/Cyrene in a biorefinery.

In the next section, UV-Vis spectroscopy is used for the same experiment where the LGO/water interaction was daily analysed. It is expected to find significant results in the UV-Vis spectroscopy by investigating the ketone, alkene and the conjugated system for the LGO conversion.



### 5.3.3 UV-Vis for LGO

Based on our experiment, the pure LGO shows a very high absorbency in the UV range. Even when the sample is diluted as low as 2 wt% in water, it still produces an abnormally high (a.u.) value caused by the high path length cell used (1 cm). However, the samples were diluted to even lower concentrations until it was found that the concentration of 0.1 wt% and 0.001 wt% of LGO in water were the best choices. The reason is that there are two main absorbencies in different regions which have significantly different intensity values. Firstly, the concentration of 0.1 wt% was the best choice in the region 250-500 nm where two bands appear at 276 and 345 nm. Yet, this concentration is not appropriate for the region below 250 nm as the absorbency is relatively high.

Meanwhile, the concentration of 0.001 wt% was the best choice to detect an ideal band at 224 nm. Figure 5.13 presents the interaction between LGO and H<sub>2</sub>O with varying time measures. Generally, the spectra indicate primary and secondary absorption bands at 224 and 345 nm respectively. The primary band at 224 nm is due to the  $\pi \rightarrow \pi^*$  transition for the ketone which is responsible for the significant band with the highest intensity (note that the sample was 100 times diluted compared to the one in the secondary band). This band decreases with time which indicates the breaking down of C=O. The secondary band at 345 nm is more likely to be associated with the *ketone's*  $n \rightarrow \pi^*$  transition, which gives a low intensity. This band behaves similarly to the primary band with the breaking down of C=O.

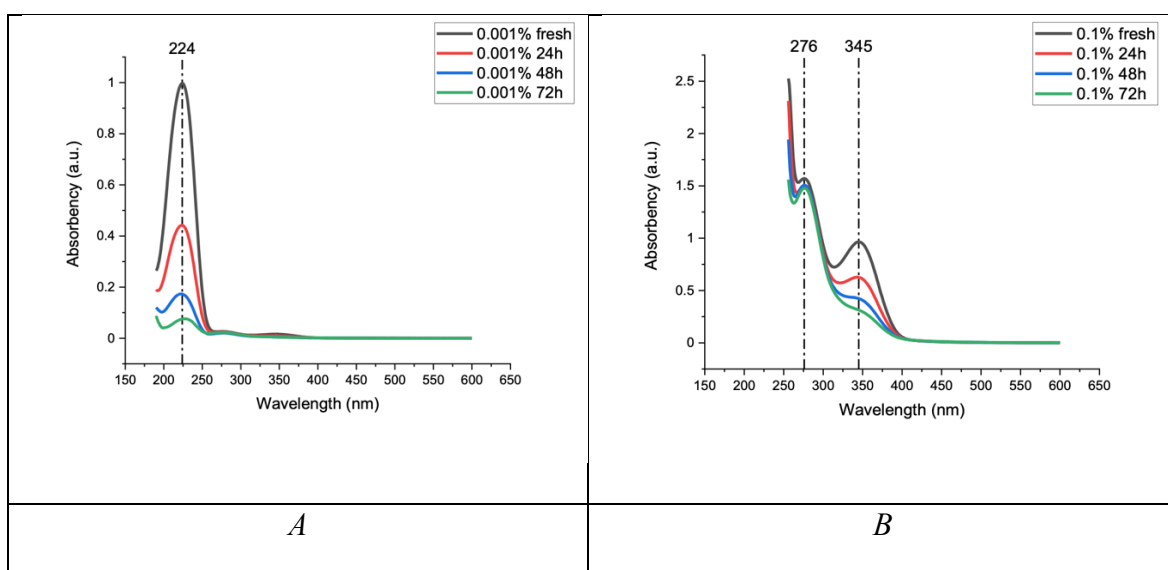
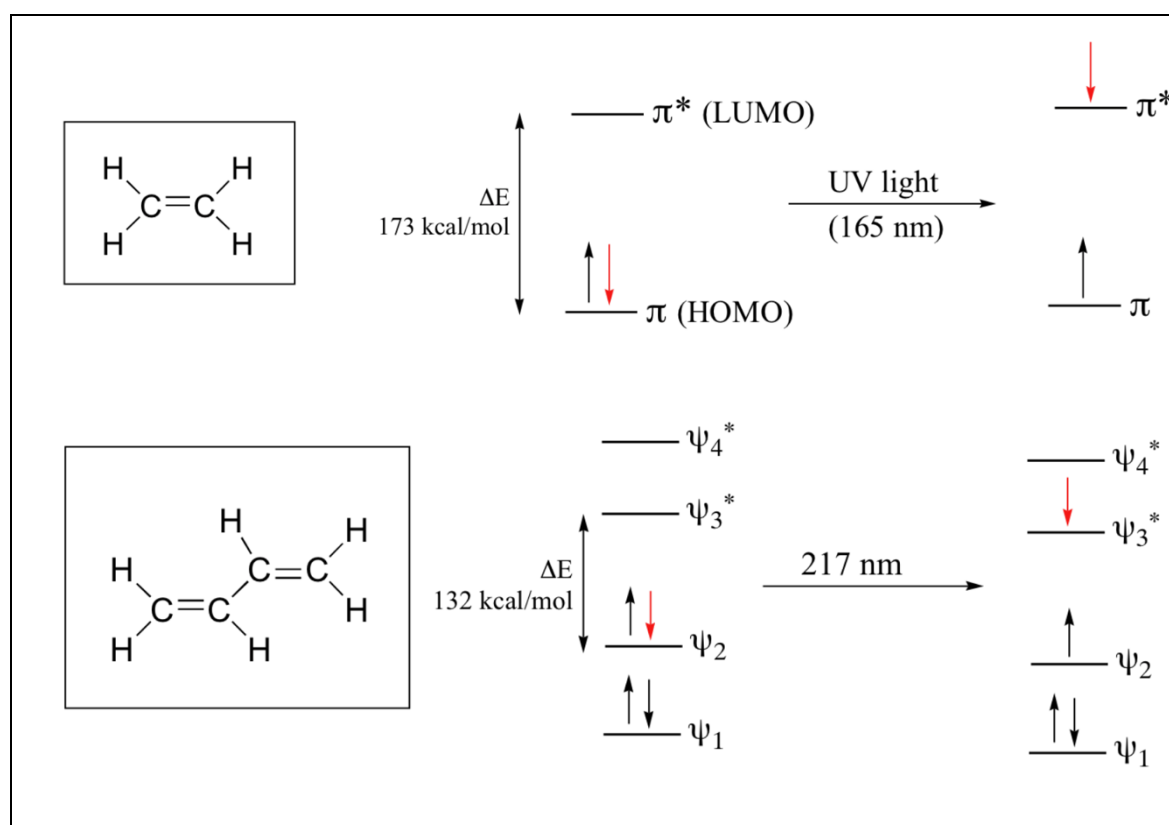


Figure 5.13 UV-Vis spectra of (A) 0.001 % and (B) 0.1 % LGO in H<sub>2</sub>O in different days

Within the UV-Vis region, the conjugation can shift the absorption band. As the compound becomes more conjugated, at a higher wavelength, the band appears<sup>80</sup>. For example, the conjugation in ethene and butadiene absorbs at 185 and 215 nm, respectively, as demonstrated in Scheme 5.2. Therefore, the absorbance at 276 nm in Figure 5.13 B is due to the conjugation system in LGO. This band does not show a significant change in intensity compared to the C=O bands. This result was interpreted as evidence of the presence of the LGO in an equilibrium state with the triol in the aqueous solution.



Scheme 5.2 the effect of conjugation

This scheme was used from chem.libretexts<sup>130</sup>

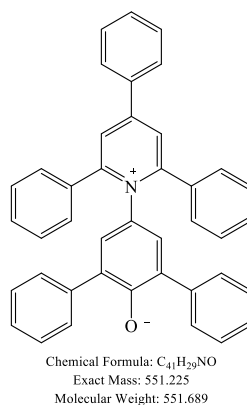
This experiment shows that the UV-Vis spectroscopy can be an adequate tool to detect sensible variation in the reaction process. It successfully indicated the LGO and the triol transaction in the very low concentrations of either 0.1 and even 0.001 wt%. That is a very sensitive analysis.

An alternative approach to monitoring this kind of transaction is by measuring the medium where the reaction occurs. As the LGO turns to triol in the aqueous solution, the polarity of

the solution increases when more hydroxyl groups are created in the triol. Reichardt's dye is a suitable method to be used in this case. Therefore, our next step is to examine Reichardt's dye absorbency in UV-Vis spectroscopy to monitor the LGO/water interaction change.

### 5.3.4 Reichardt's dye

Solvatochromism is an effective method used for determining the polarity of the solvent.<sup>131, 132</sup> It shows a significant band shift in UV-Vis spectroscopy when the dye is dissolved in different solvents. Reichardt's dye known as betaine  $E_T$  (30) is the most popular example of this phenomenon. Its IUPAC name is 2,6-diphenyl-4-(2,4,6-triphenyl-1-pyridinio)-1-phenoxide. It has been applied for analysing the polarity of different media quantitatively. This phenomenon enables to help reveal the chemical interaction between the solvent and the solute in terms of electron-pair donor/acceptor or hydrogen bonding interaction between the solute and the solvent. Different intermolecular forces induce the interaction between solvent and solute. One of these forces is hydrogen bonding donor HBD or hydrogen bonding acceptor HBA.<sup>132</sup> Zhenova *et al.*<sup>133</sup> used Reichardt's dye when investigating oxymethylene dimethyl ethers as a bio-derived solvent.



*Scheme 5.3 the Reichardt's dye structure*

First, a simple experiment was conducted to examine how the dye behaves differently when interacting with solvents depending on their polarity. This method was developed by Reichardt C.<sup>131, 132</sup> The solvents used were H<sub>2</sub>O, Cyrene, ethanol, 2-propanol, acetone, ethyl acetate (EtOAc), cyclohexane, and Reichardt's dye was added to each solvent. Figure (A.5.7) (A) demonstrates the effect of the solvent on the dye colour. The very poor solubility in water and cyclohexane samples is the main reason behind the colourless solution. Cyrene,

ethanol, 2-propanol, acetone and EtOAc indicate brown, purple, blue, green-blue and green colour as shown in the spectra in Figure (A.5.7) (B).

The colour changed depending on the solvent medium. Figure (A.5.7) (B) shows that the band gradually shifts from higher to lower wavelength as polarity increases. Both water and cyclohexane do not show any absorbency in the visible region as they are located at the two extreme ends of the polar-nonpolar scale. This work proved to be an adequate method for studying the medium.

As in the previous experiment of the time-dependent LGO:H<sub>2</sub>O interaction using UV-Vis spectroscopy, Reichardt's dye was used to analyse the change in the medium over time. A diluted LGO of 1 wt% in H<sub>2</sub>O was prepared. This experiment aims to examine the medium change over time. The double bonds of LGO ketone and the alkene functional groups break down and form triol when interacting with water. 20.8 and 19.8 mg of Reichardt's dye were added to the water and the 1 wt% LGO samples respectively and shaken well before filtered using a 0.45  $\mu\text{m}$  filter paper. The sample was then submitted to the UV-Vis spectroscopy daily for a few days. The same sample was used as a blank for the UV-Vis spectrometer with no dye. Therefore, the absorbance measured in the spectrum is the dye. Both water and LGO samples show no visual difference that can be detected by the naked eye to discriminate between before and after adding the dye. The two colours can be seen in Figure (A.5.8).

UV-Vis spectroscopy can reveal this change as illustrated in Figure 5.14. The figure indicates the medium change when the interaction between LGO and water occurs by detecting the change in the band position of the dye every day. Reichardt's dye shows a band at 305 nm when dissolved in water. This can answer why Reichardt's dye did not change the colour of the water. It is out of vis range. When adding the dye to the freshly mixed 1 wt% LGO in water, the band shifted dramatically to 386 nm lowering the solution's polarity. As time passes, the  $\lambda_{\text{max}}$  shifts gradually to lower wavelengths from 386 nm to 362 nm respectively for freshly mixed LGO in water to the fifth day. This can be interpreted as a sign that the polarity of the solution increased with time as demonstrated in Figure 5.15.

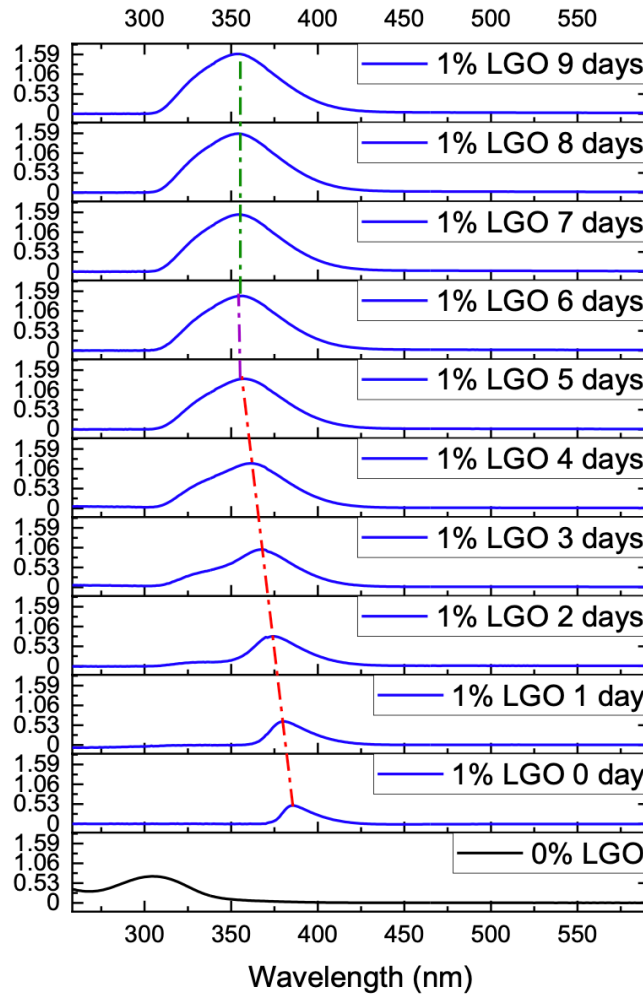


Figure 5.14 Reichardt's dye dissolved in 1 % LGO in different days

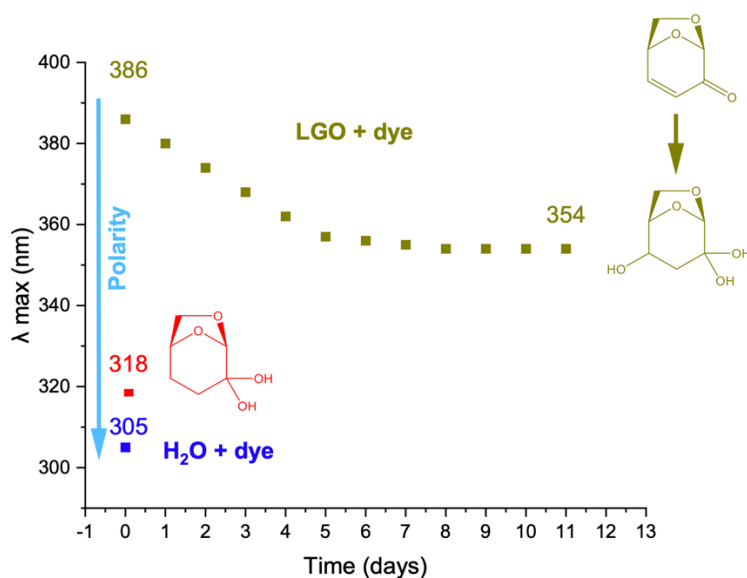


Figure 5.15  $\lambda_{\max}$  of the Reichardt's dye dissolved in 1% LGO in different days, 1% Cyrene and water

This work using Reichardt's dye is to detect the conversion of the LGO to the triol which supports the previous method of IR spectroscopy. Figure (A.5.9) shows a constant change demonstrated by the linear relationship between the shift of  $\lambda_{\max}$  and the time (days) with  $R^2$  of 1.00, which that Reichardt's dye method was able to detect changes with high precision. From day 6 onwards, the  $\lambda_{\max}$  gradually decreased until no more change was observed after the ninth day.

The observed shift of  $\lambda_{\max}$  can be interpreted as evidence that the LGO took about nine days to fully complete the interaction with water to reach the equilibrium state. The polarity was decreased when the LGO was added to the water showing a change in  $\lambda_{\max}$  from 305nm for the water to 386 nm for the 1% LGO. By then, the polarity has gradually increased, creating the triol and breaking down the alkene and ketone double bonds of the LGO.

In addition to  $\lambda_{\max}$  shifting observed every day, the intensity of the band also changed as illustrated in Figure (A.5.9) (B). It is suggested that the equilibrium state will be reached after 9 days of mixing LGO in water when both the intensity of the band and its shifting remain unchanged. This experiment is consistent with the UV-Vis, MIR and NIRS results as shown in Figure 5.13, Figure (A.5.6) and Figure 5.12 respectively. NMR spectroscopy for the LGO water interaction time-dependent experiment will be shown later in this chapter.

Based on the lab experiments and data analysis, one could conclude that LGO:water solution take at least 5-9 days to get to the equilibrium state (at room temperature and with no catalyst

added). This work has not been presented in the literature to the best of our knowledge. Krishna *et al.*<sup>129</sup> stated that the triol form of LGO was observed by HPLC and NMR spectroscopy but not quantitatively measured. They have allowed the diluted LGO for 100 hours to occur at room temperature to form the new product of triol forms of LGO.

On the other hand, Cyrene interacts with the water immediately after mixing them, changing the ketone to a geminal diol. This reaction was monitored for four days, and no noticeable difference in spectra was detected, as seen in Figure (A.5.10). The constant  $\lambda_{\max}$  value of all spectra indicates that the solution was well reacted immediately when they were mixed. The only difference found is at the 240 nm band, which increases with time. However, the main focus of this experiment is the  $\lambda_{\max}$  at 318 nm, which is the dye absorbency. This finding strongly suggests that the Cyrene reacts with the water immediately and gets to the equilibrium state.

As a result, Reichardt's dye effectively detected the change in the medium depending on the polarity. In terms of LGO polarity, Figure 5.14 and Figure 5.15 demonstrate that a concentration of 1% LGO has dramatically changed the water's polarity by shifting the band from 305 to 386 nm. Undoubtedly, the change from LGO to triol increases the polarity of the solution. Cyrene:water solution, on the other hand, is more polar than LGO: water solution in the same concentration as shown in Figure 5.15. Cyrene : water is closer to water in polarity than LGO : water.

### 5.3.5 NMR spectroscopy for LGO

To investigate the slow interaction between LGO and water, <sup>1</sup>H and <sup>13</sup>C NMR spectroscopy has been used to detect the change in the alkene and ketone groups. The first thing to analyse was the pure sample of LGO 99.11%. The LGO was dissolved in CDCl<sub>3</sub> (10 % LGO) and scanned using 300 MHz NMR spectroscopy. The <sup>1</sup>H NMR spectroscopy analysis, presented in Figure 5.16, spotted six main bands corresponding to the six associated protons of the LGO. The bands centred at ~ 6 and 7.2 ppm represent the two protons bonded with the two alkene carbons in positions 3 and 4, respectively. The two methine group protons at positions 1 and 5 are associated with bands centred at ~ 5.26 and 4.96 ppm, respectively. The two protons bonded to the carbon at position 6 are associated with the two groups of bands (exo- and endo-isomers) in the range of 3.88 – 3.64 ppm respectively.

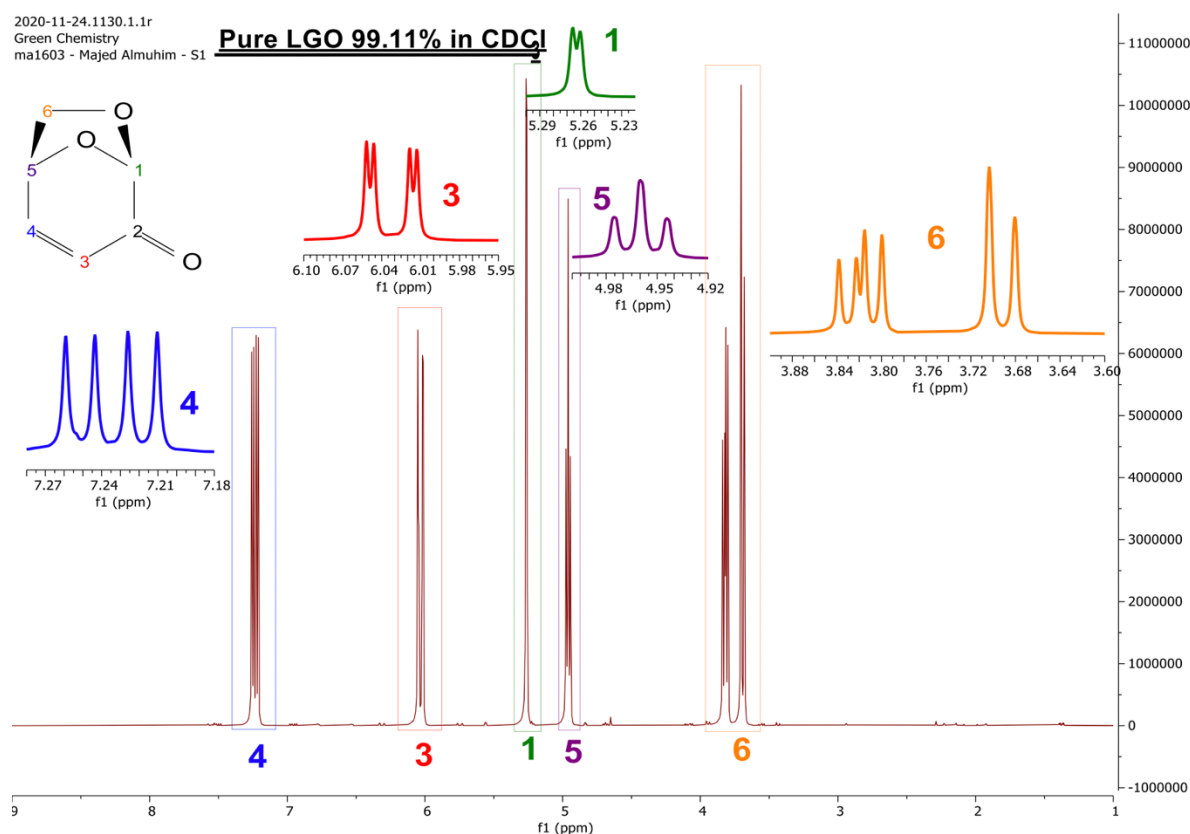


Figure 5.16 <sup>1</sup>H NMR spectrum for LGO 99.11% dissolved in CDCl<sub>3</sub>



Table 5.1 <sup>1</sup>H NMR spectroscopy assessment of LGO in CDCl<sub>3</sub>

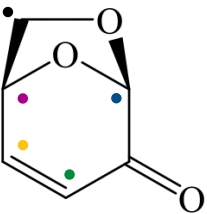
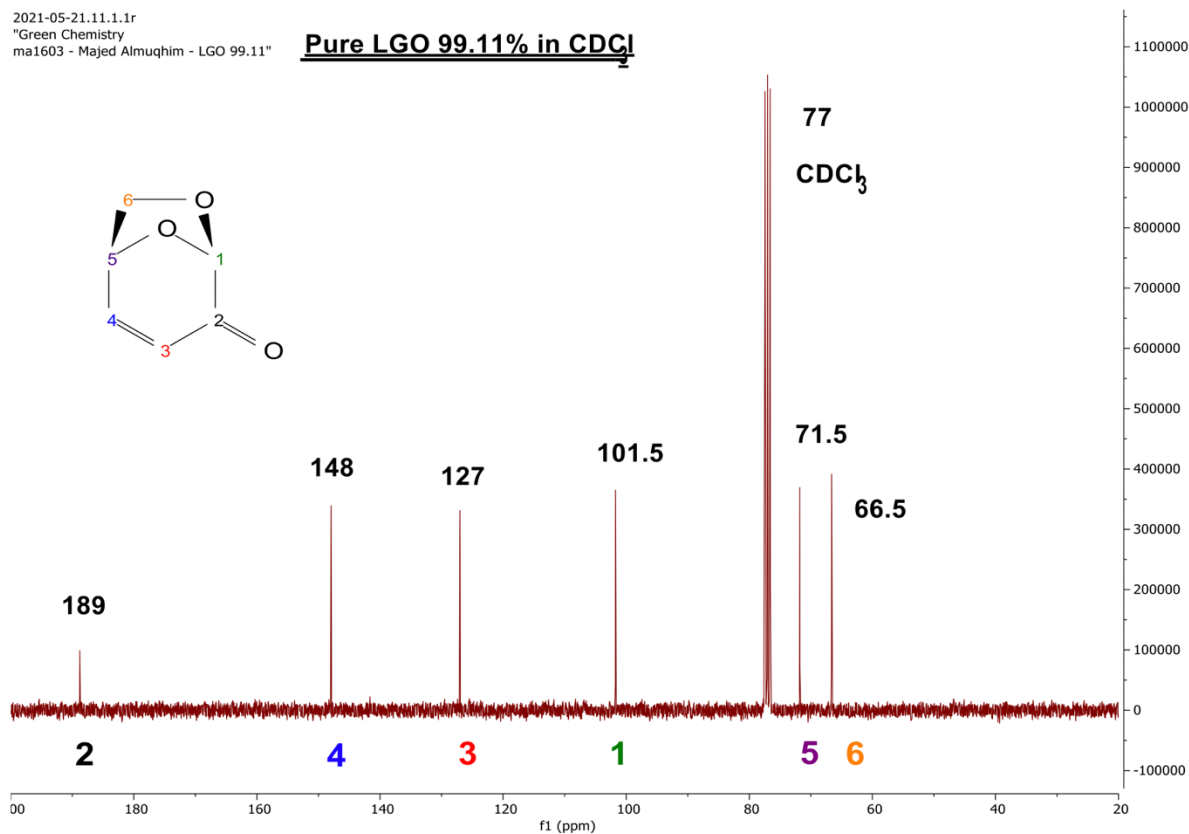
Shift (ppm)	Targeted proton	Molecule
3.6 , 3.8 •	O – CH <sub>2</sub> – C	
4.9 •	– CH < C, O	
5.2 •	– CH < 2O	
6.4 •	= CH – C	
7.2 •	– CH = C	

Figure 5.17 illustrates <sup>13</sup>C NMR spectrum of pure LGO dissolved in CDCl<sub>3</sub>. In addition to the peak at 77 ppm which corresponds to the solvent (chloroform-d), six prominent single peaks of the six carbon atoms appeared for LGO. Peaks at 189, 148, 127, 101.5, 71.5 and 66.5 ppm are associated with carbons number 2, 4, 3, 1, 5 and 6 respectively. This spectrum shows additional information that cannot be shown in <sup>1</sup>H NMR spectroscopy of the same sample such as the ketone carbon at position 2.

Based on this assessment, the difference between LGO and the triol (in water) can be seen and compared to the results obtained from the IR spectroscopy presented earlier in this chapter.

Table 5.2 <sup>13</sup>C NMR spectroscopy assessment of LGO in CDCl<sub>3</sub>

Shift (ppm)	Targeted C	Molecule
66.5 •	O – CH <sub>2</sub> – C	
71.5 •	– C < C, O	
101 •	– C < 2O	
127 •	= C – C	
148 •	– C = C	
189 •	> C = O	

### 5.3.6 LGO:water interaction time-dependent using NMR spectroscopy

As previously discussed, the interaction between LGO and water takes a long time. This process was monitored by NMR spectroscopy and displayed in this section. The comparison between LGO in water (freshly mixed) and (after 7 days) is illustrated in Figure 5.18 of <sup>13</sup>C NMR spectroscopy. After a few days of mixing LGO in water, new carbon bands appeared, allowing the reaction to produce more triol. This experiment reveals the relatively slow interaction between LGO and water as discussed earlier in this chapter, using mid and NIRS. Figure 5.18 (A) demonstrates a freshly mixed LGO in water (D<sub>2</sub>O) with only 6 carbon bands. This is similar to Figure 5.17. On the other hand, 6 additional carbon species appeared in the spectrum as presented in Figure 5.18 (B) along with the previous bands, indicating a reaction product. Other minor species also appeared in the spectrum in the same figure, which will be discussed later in this chapter.

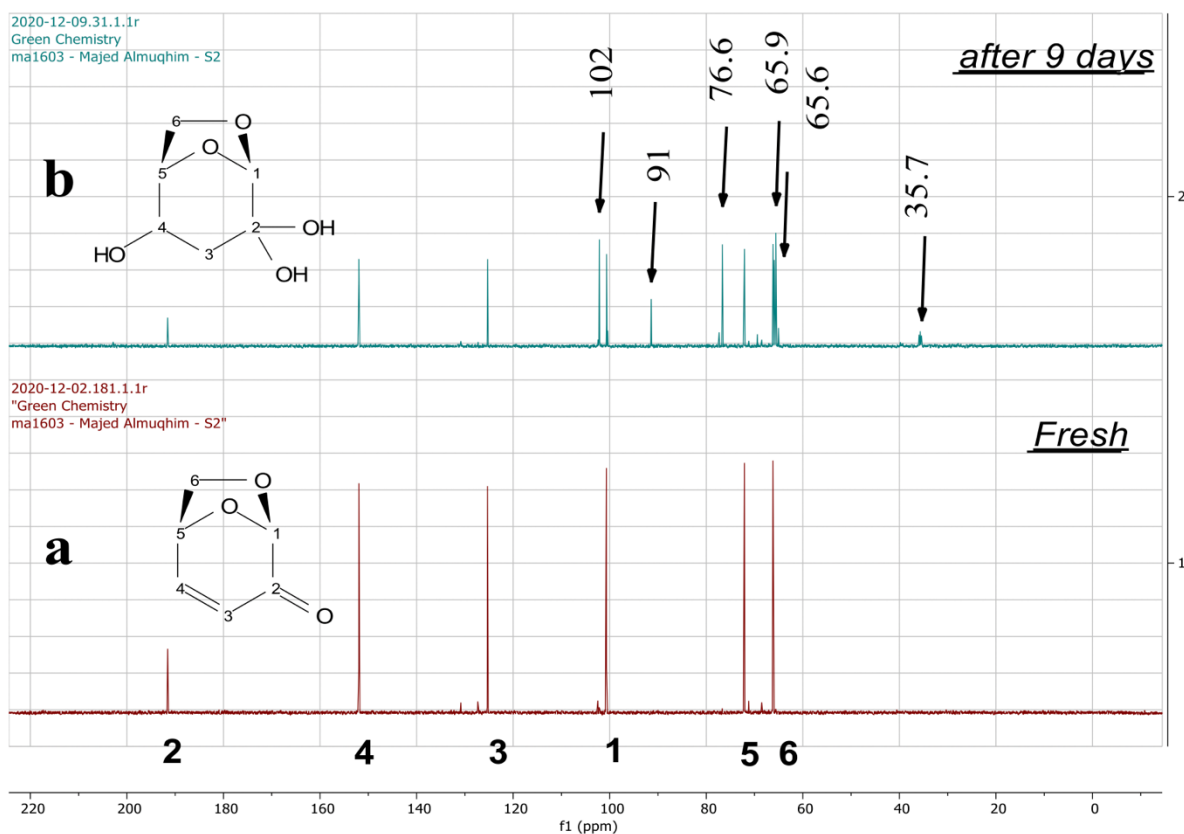


Figure 5.18 <sup>13</sup>C NMR spectrum for LGO dissolved in D<sub>2</sub>O a. freshly mixed and b. after few days

Cyrene, in comparison, reacts very quickly with water after mixing the two components with no apparent change in time, as can be seen in *Figure (A.5.11)*. This result is consistent with Reichardt's dye experiment for Cyrene : water interaction as discussed earlier in this chapter and presented in *Figure (A.5.10)*. The slow reaction between LGO and water is caused by the presence of the alkene functional group. This group is absent in the case of Cyrene.

*Figure (A.5.12)* presents the results of the <sup>1</sup>H NMR stacked spectra of LGO in D<sub>2</sub>O tested daily for seven days to monitor the conversion of LGO to triol to reflect the <sup>13</sup>C NMR spectroscopy results shown previously. The sample changed slowly with the growing appearance of new protons. Green arrows indicate the position (ppm) of the new proton species detected. The peak at around 2 ppm indicates more than one newborn proton. Overlapped peaks at 3.8ppm seem more complicated over time as additional new species appear. Peaks at 4.6 and 5.1 ppm gradually increased over time with also new protons formed. As shown by the peaks at 7.6 and 6.2 ppm, other species decreased and increased in the LGO and the triol, respectively, until they reached the equilibrium state. Cyrene, in comparison, reached the equilibrium rapidly after mixing the solution, and no change was detected by time, as indicated by both <sup>1</sup>H and <sup>13</sup>C NMR spectra illustrated in *Figure (A.5.12)* and *Figure 5.18*, respectively.

After monitoring the change in LGO to triol, more assessment for the triol is taking place. <sup>1</sup>H and <sup>13</sup>C NMR spectroscopy as well as 2D spectra for the triol was done to give more detailed characterisation of the product.

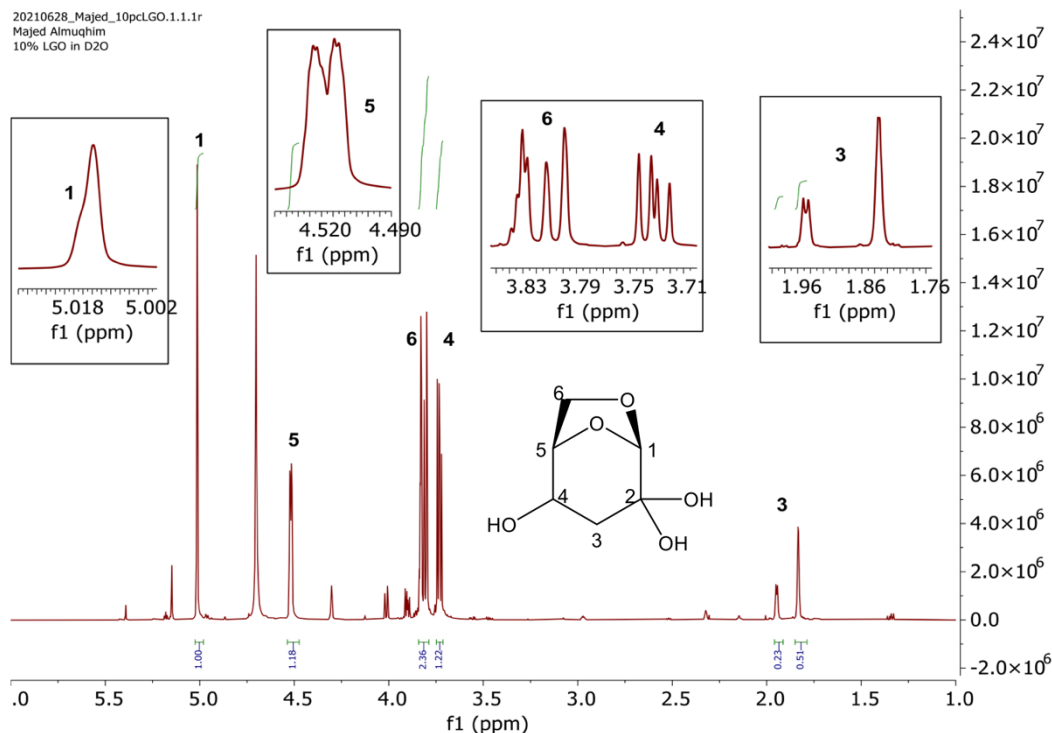


Figure 5.19 <sup>1</sup>H NMR spectrum of LGO in D<sub>2</sub>O when it is fully reacted with water forming triol

The two bands around 1.8 – 2.0 ppm represent two positions of two protons in C3 after the alkene group was broken down adding one more H in this carbon. Those two protons represent two different isomers which will be discussed later in more detail. The presence of D<sub>2</sub>O caused the low integration number for those protons as the sample was dissolved in D<sub>2</sub>O. This will also be discussed in the next chapter when investigating the MHC.

Table 5.3 <sup>1</sup>H NMR spectroscopy assessment of triol in D<sub>2</sub>O

Shift (ppm)	Targeted proton	Molecule
5.1 ●	–CH< 2O	
3.7 ●	>CH–OH	
4.5 ●	–CH< C,O	
3.8 ●	O–CH <sub>2</sub> –C	
2.8 2.4 ●	C–CH <sub>2</sub> –C	

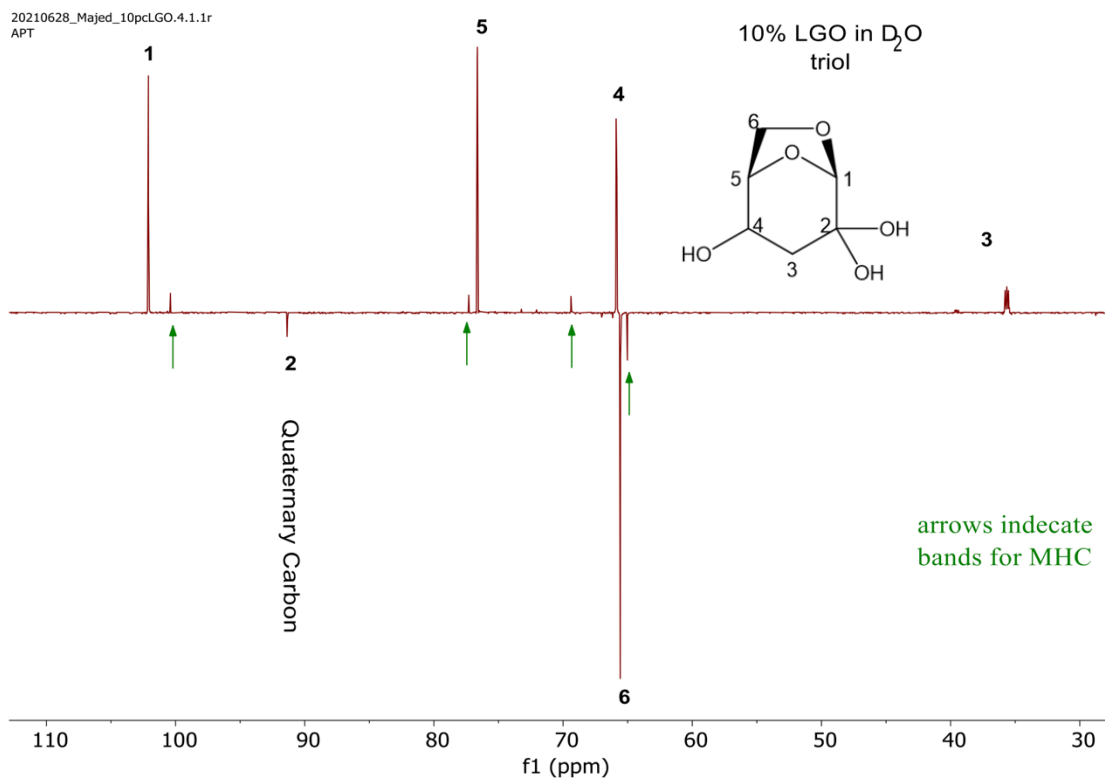


Figure 5.20 <sup>13</sup>C NMR (APT) spectrum of LGO in D<sub>2</sub>O when it is fully reacted with water forming triol showing CH bands “up” and CH<sub>2</sub> bands “down”. A small amount of MHC is present in the solution as indicated by the green arrows

Note that C6 bonded to H<sub>2</sub> showing negative band while C3 bonded to D<sub>2</sub> as it was dissolved in D<sub>2</sub>O.

Table 5.4 <sup>13</sup>C NMR spectroscopy assessment of triol in D<sub>2</sub>O

Shift (ppm)	Targeted C	Molecule
102 ●	– C < 2O	
65.8 ●	> C – OH	
76.6 ●	– C < C, O	
65 ●	O – CH <sub>2</sub> – C	
36 ●	C – CD <sub>2</sub> – C	
91 ●	> C – (2)OH	

Carbon number 6, which contains CH<sub>2</sub> of (exo and endo) position was changed over time. *Figure (A.5.19)* and *Figure (A.5.20)* show that the exo proton coupling remained the same with different intensities between freshly mixed and after 7 days while the endo position was not detected after mixing the LGO with water. This coupling is changed when producing triol LGO compared to the original LGO.

After 4 months of mixing the mixture of 10 wt% LGO in water, it is clear that almost all of LGO was converted to diol, triol forms of LGO as shown in Figure 5.21. This figure illustrates that the sample's antiphase (DEPT-135) spectrum shows positive and negative bands. The negative bands represent the protons of CH<sub>2</sub>, while the positive bands illustrate CH and CH<sub>3</sub>. As a result, bands at 65.6 and 65 ppm correspond to CH<sub>2</sub> of the carbon number 6 each with a different stereoisomer. The 2D spectra indicate that both bands are associated with the same overlapped region of proton in carbon 6. The slight negative band at 65 ppm connects with the proton that appeared at (3.9 and 4.00 – 4.05 ppm) as shown in H-H HSQC *Figure (A.5.15)*. Both carbon and proton respectively at 65 and 4.00 ppm are not very abundant suggesting that it is one of the different stereoisomers. Note that (DEPT-135) does not show quaternary carbons. So, no ketone carbon is shown in Figure 5.21. All our NMR spectroscopy assessments for the triol LGO are consistent with Crishna *et al.*<sup>129</sup>

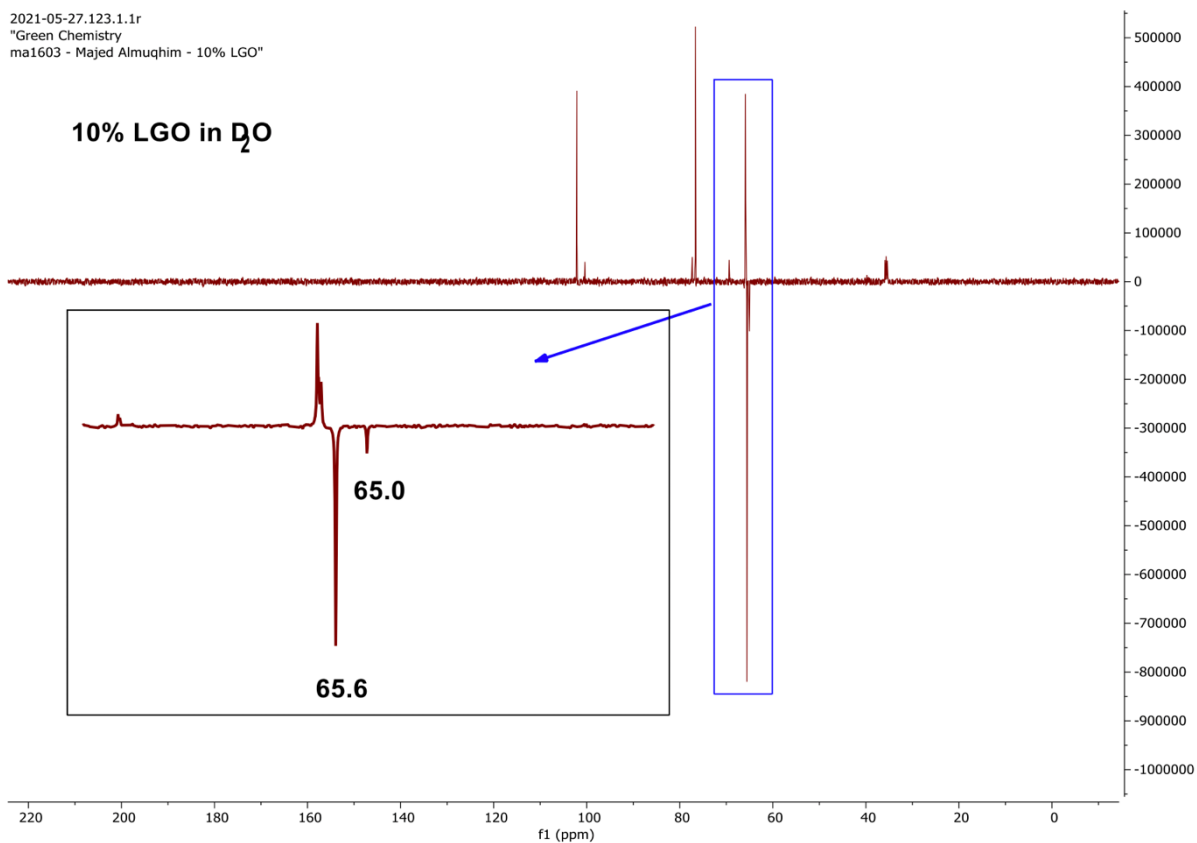


Figure 5.21 <sup>13</sup>C NMR antiphase spectra (DEPT-135) for LGO in D<sub>2</sub>O after 4 months. Negative bands show the CH<sub>2</sub> species

Figure 5.22 displays the conversion of LGO to triol-LGO by time. It shows that the conversion happened faster in the first few days up to the fifth day and then continued to grow at a more a slower rate for the next following days.



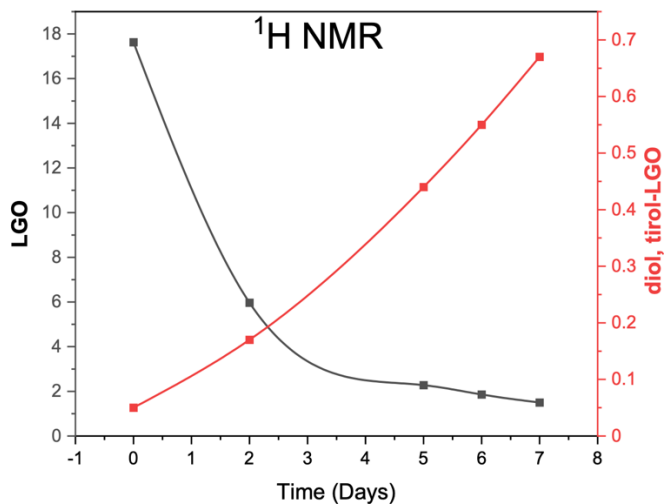


Figure 5.22 The conversion of LGO to triol-LGO by time

This is a complex system to be studied especially using NMR spectroscopy. More details and clearer images will be discussed and shown in the next chapter when this solution is heated and the triol is isolated and no more water is in the system. However, the diol on the C2 will no longer exist in the compound once the water is evaporated. The carbonyl group will be formed back as it will be discussed in more detail in chapter 6. A detailed interpretation of the triol and the MHC will be provided.

## The expected monohydroxy Cyrene

It is expected to form triol-LGO when the solution takes a few days to replace the ketone with a geminal diol on C2 and the alkene double bond with a hydroxyl group on C4. When the aqueous solution of the triol is heated to concentrate the triol, it is expected to form the ketone back. But the alkene will not be likely to form back after hydration. Hydration of the alkene occurs readily due to activation of the alkene through conjugation with ketone while dehydration to go from secondary alcohol to alkene requires an acid catalyst. It was not sure if the hydroxyl group at the C4 would remain. Figure 5.23 shows the difference in the ketone band intensity when the solution is freshly prepared and after seven days. The majority of the ketone group was replaced/exchanged by geminal diol. Note that this sample was dissolved in D<sub>2</sub>O to avoid overlapped bands of the bending OH vibration of the H<sub>2</sub>O with the carbonyl stretching. However, when the solution is heated in an open vessel, without exceeding 70 °C, the water molecules are eventually evaporated, and a yellow liquid is left behind which is expected to be pure MHC. In other words, when the LGO is hydrogenated, it becomes cyrene. The presence of some ketone might also be observed, but not dominant, as the solution is in an equilibrium state. MIR spectra in Figure 5.23 illustrated a very dominant ketone in the sample. This corresponds to a different type of ketone detected in the product which does not match the pure LGO.

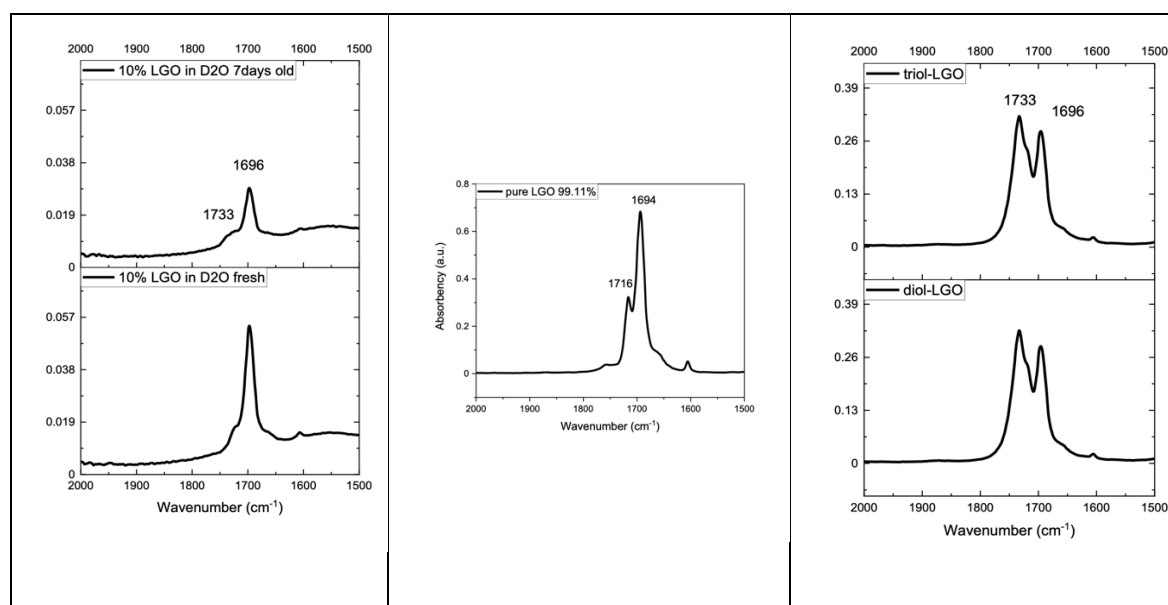


Figure 5.23 The MIR spectra of ketone absorbance of (from left) 10 wt% LGO in D<sub>2</sub>O freshly mixed and after 7 days, pure LGO and diol, triol-LGO

Specifically, the sample was separated into two beakers to be heated at different temperatures: 45 °C and 65 °C to form triol and diol-LGO. This is done to detect if there is

any different type of LGO (diol, triol) that could form at a particular temperature. In terms of ketone, it is shown that the LGO was changed and a different type of LGO was formed. There is about 37 cm<sup>-1</sup> difference between the two ketones. This finding suggests that the geminal diol converted to ketone but no more conjugated system in the compound. In other words, no alkene existed, and a hydroxyl group was formed. The alkene is expected to be different from the two samples. However, the expected diol, triol-LGO shows less alkene in MIR spectroscopy as demonstrated in Figure 5.24. The band at 3060 cm<sup>-1</sup> is clearly identified in pure LGO as it contains alkene. The other forms of LGO show dramatically decrease in the alkene band. Additionally, the bands 1605 and 1475 cm<sup>-1</sup> represent the carbon-carbon stretching of alkene decreased for the diol, triol-LGO, while pure LGO contains a higher peak intensity. This result suggests that the triol-LGO was formed.

The two different heating temperatures show similar (identical) MIR spectra suggesting that no separation of diol and triol LGO can be detected at any particular temperature. It is also expected that the two forms were produced, but no one is more dominant at any specific temperature. However, this experiment is demonstrated in more detail in the next chapter, where a higher range of temperatures is investigated.

Note that the solution of this sample took only seven days when the LGO was mixed with the water and then evaporated to isolate the new product of MHC. Therefore, some amount of LGO is still not converted yet, but it is evident that the ketone at 1696 cm<sup>-1</sup> represents the LGO. In the next chapter, the solution was prepared and left for a longer time to allow the conversion.

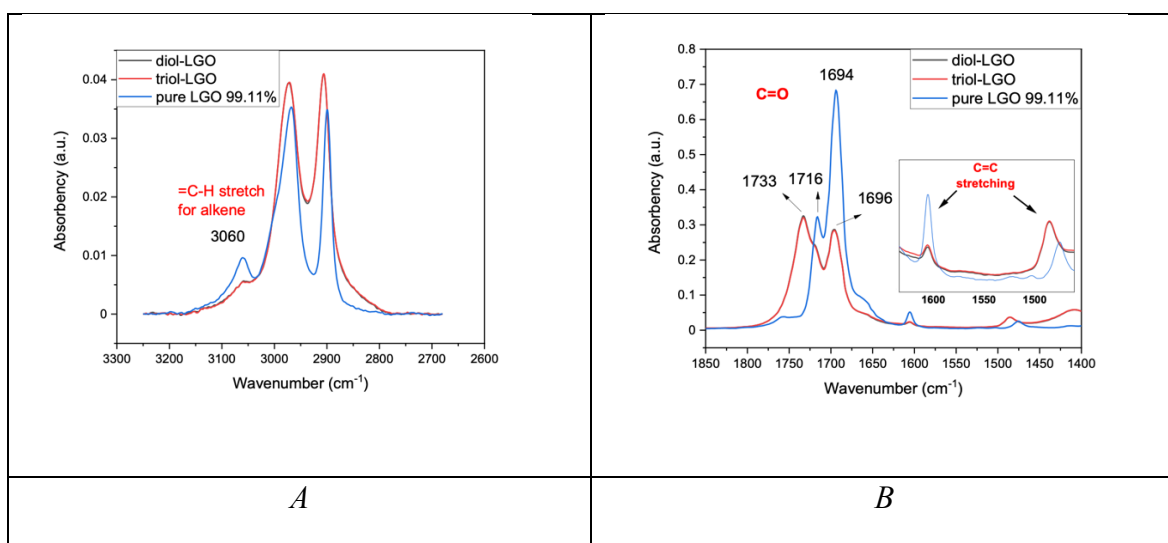


Figure 5.24 The MIR spectra of CH stretching of pure LGO and the expected two forms (diol, triol-LGO) in the range (from left) 3300 – 2600 cm<sup>-1</sup> and 1850 – 1400 cm<sup>-1</sup>

## 5.4 Conclusion

Above all, NIRS results for the water in variable temperatures provides very useful system to detect any change in the OH vibration. Adding LGO to water was an adequate example. The LGO : water interaction demonstrates a unique behaviour, especially when applying varying temperatures. A couple of different analytical techniques were applied to prove this phenomenon, including NMR spectroscopy, STA showing consistent results. All of what has been learnt from studying this model can be applied to different compounds interaction with water.

Additionally, LGO in an aqueous solution is converted to triol, taking a long time. The results from LGO time-dependent with different techniques provide a more precise image of the timescale of triol to be formed at room temperature with no catalyst added. This was studied in detail using varying instruments and methods including <sup>1</sup>H and <sup>13</sup>C NMR, N and M-IR, UV-Vis spectroscopic techniques. On top of that, Reichardt's dye has successfully enhanced the UV-Vis results by calculating the shift of the  $\lambda_{\max}$  depending on the change of the medium polarity. The LGO interaction with water provides access to a potentially helpful product, hydroxy Cyrene, which will be studied in the next chapter.

## Chapter 6: The production of Monohydroxy Cyrene (MHC)

### 6.1 Introduction

With the real need for bio-based chemicals as an alternative to those derived from fossil fuel,<sup>7, 8, 13, 108, 134</sup> hydroxy Cyrene has the potential success of being one of the bio-based building block chemicals. MHC is a potential platform molecule obtained in two steps from biomass. The single hydroxyl group in this compound allows for additional functionalisation. Producing diol by reducing the carbonyl group would lead to a monomer for polyester formation, making an ester or ether with a fatty acid/alcohol to give a surfactant and many other applications including, oxidation, substitution, sulphonation and so on. It could act as secondary alcohol and opens up a range of potential compounds derived from biomass. It has potential chirality which enhances its relevance active pharmaceutical ingredients (APIs).

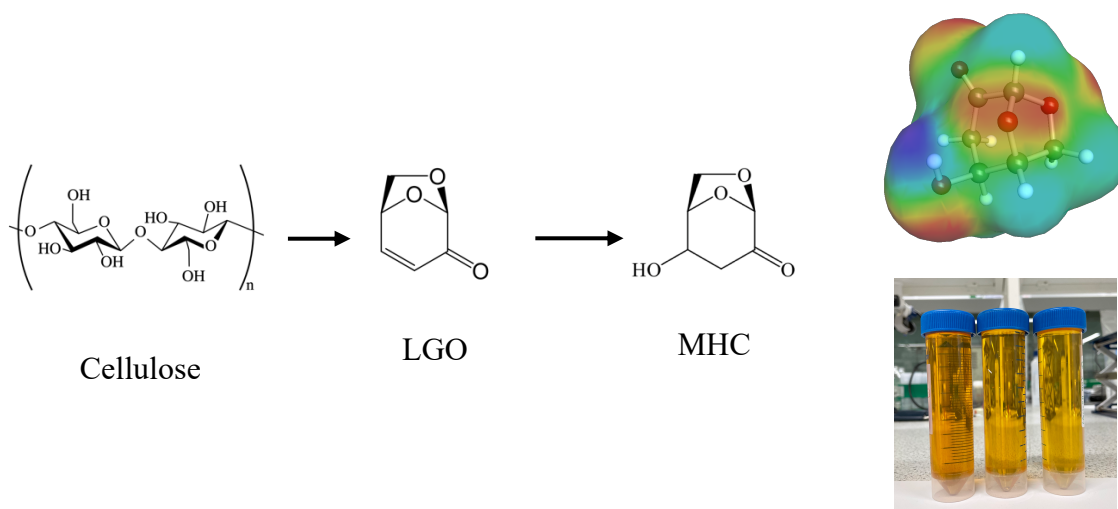
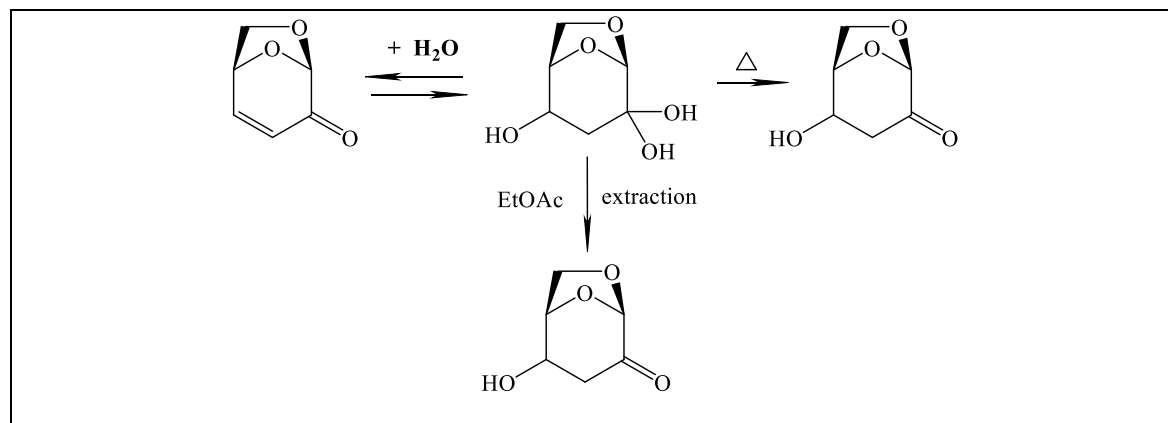


Figure 6.1 MHC. Two steps from biomass

MHC is a bio-based liquid obtained by hydrating LGO in a specific process. It has a chemical formula of (C<sub>6</sub> H<sub>8</sub> O<sub>4</sub>). It was dealt with as a by-product when producing Cyrene from LGO.<sup>135</sup> The MHC was produced and reported in some articles.<sup>135-139</sup> In this work, MHC was produced in high yield using different methods. It was analysed with many techniques such as NMR, IR, UV-Vis spectroscopy as well as CHN, MS and thermal analysis STA and

DSC. Some of its properties have been investigated indicating potential success for its future as a platform molecule.



Scheme 6.1 The production of MHC in two different methods

In the beginning, it was expected to form one hydroxyl group breaking the alkene double bond of the LGO in addition to the geminal diol which is formed at the ketone. That is a total of three hydroxyl groups or a triol Cyrene. This is what Krishna *et al.*<sup>129</sup> demonstrate as they formed the triol (a geminal diol on the ketone side and a hydroxyl group on the alkene side) by dissolving LGO in water for 3 days as shown in the first step of the reaction illustrated in Scheme 6.1.

## 6.2 MHC production methods

The next step of the reaction is to produce the MHC from the triol Cyrene in an aqueous solution. To ensure that the product is the right one, it was suggested by our group that two methods can be applied. The first method is concentrating the triol in the aqueous solution to dryness to form the ketone with one hydroxyl group. The second method is to use an organic layer of EtOAc to extract the MHC from the solution. In the end, the properties / characteristics of the product were analysed.

### 6.2.1 First method of extraction

This sample was prepared from LGO (90.67%) dissolved in deuterium oxide (D<sub>2</sub>O). The concentration was 10 wt% (error ± 0.14%). Another sample was dissolved in (H<sub>2</sub>O) at the

same concentration. When the solution of the triol was evaporated, it was expected to form the carbonyl group back. The sample then was evaporated at variable temperatures; 45, 65 and 95 °C. The ketone was formed when the water was evaporated. The product was observed to have a higher viscosity than LGO. Section 6.3 describes all findings.

### 6.2.2 Second method of extraction

An organic solvent such as EtOAc can be added to the triol in an aqueous solution to form two layers. The triol is expected to form the ketone in the organic phase keeping its hydroxyl group in place.

10% LGO in water was prepared. The sample was kept for two weeks to obtain the desired results. About 200 ml of the solution was put in a separating funnel (1 L) and 200 mL of EtOAc was added. The funnel was closed and shaken well. A quantity of magnesium sulphate  $MgSO_4$  was added to the organic liquid to dry any remaining water. The solution was filtered and then rotary evaporated to remove the solvent and finally put in a strong vacuum overnight. The compound is more viscos than LGO. Its colour is a bit darker than the original starting materials of LGO used in this process.

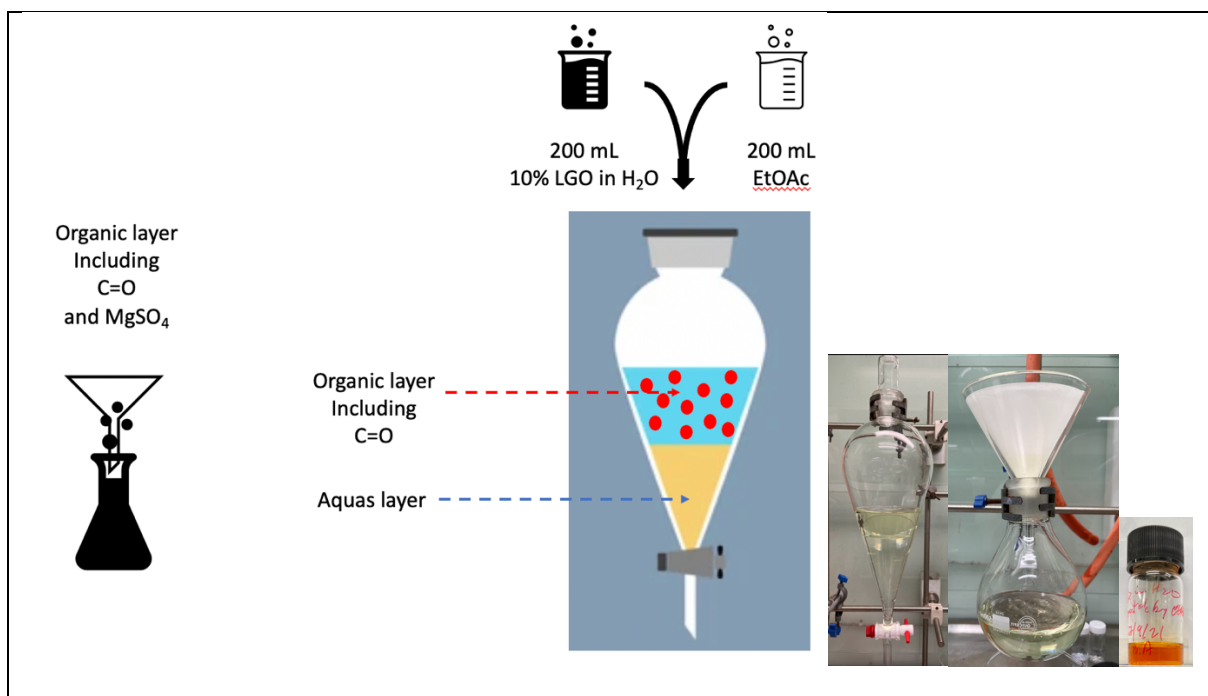


Figure 6.2 EtOAc extraction method

Based on the earlier GC and NMR spectroscopy results, the new product does not seem pure. Thin-layer chromatography (TLC) was used to analyse the purity of the product. With EtOAc as the mobile phase. This was followed by column chromatography to purify the product. The pure product then was collected, and the solvent was evaporated using a rotary evaporator. Some residues of EtOAc were in the compound so it was put under high vacuum overnight to evaporate the rest of the solvent. The sample was then submitted for IR and NMR spectroscopy.

According to both NMR and IR spectroscopic methods, the new product includes no alkene and shows a non-conjugated ketone. In addition, a hydroxyl group is evident. Both methods produced MHC but the first method gave a better yield of 88% MHC while the extraction method produced only a 45% yield based on GC analysis. The purification of the product using column chromatography enhanced the yield to 98 and 72% respectively for the first and the second method.  $^{13}\text{C}$  NMR spectroscopic analysis shows the difference between MHC produced from the organic layer extraction before and after purification.



## 6.3 Analytical techniques used for the MHC

### 6.3.1 NMR spectroscopy

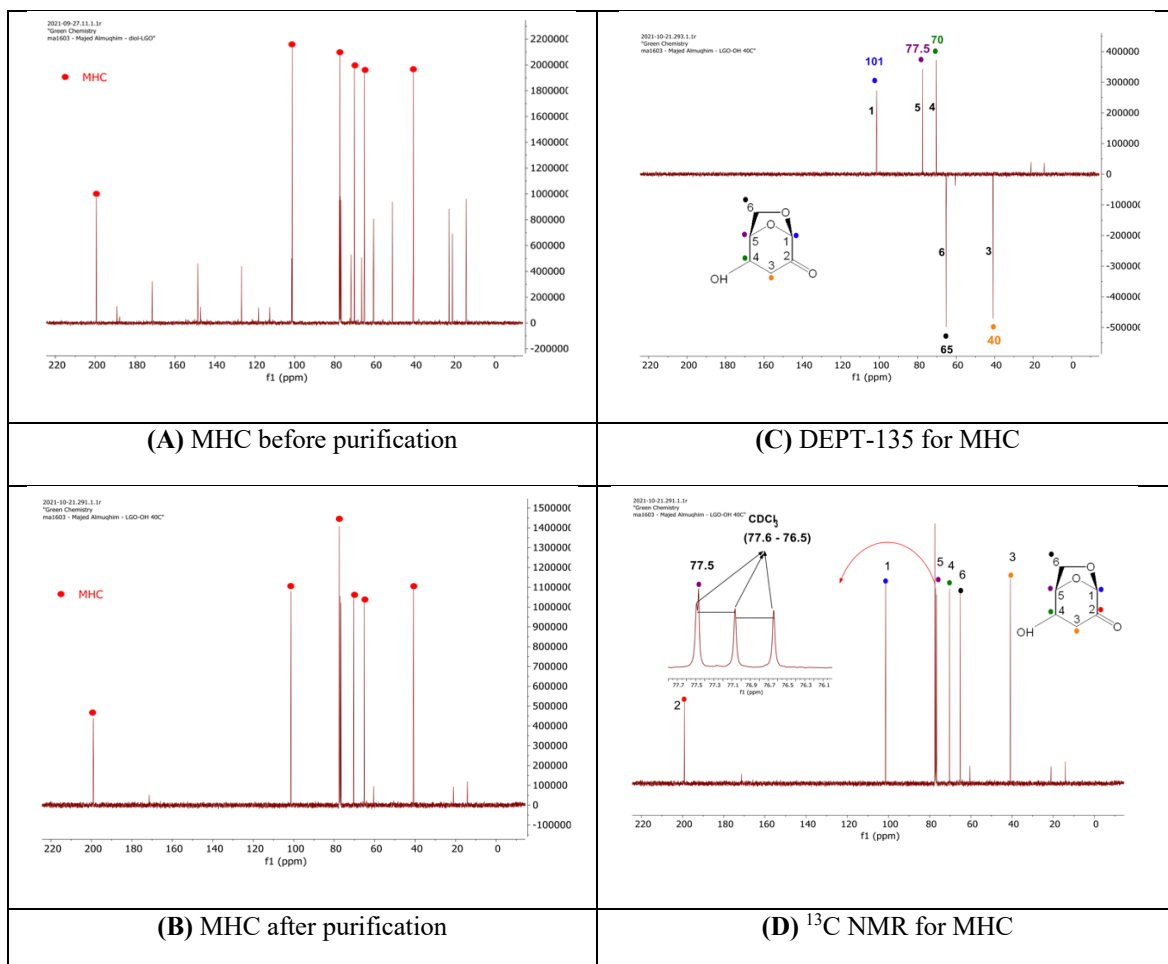
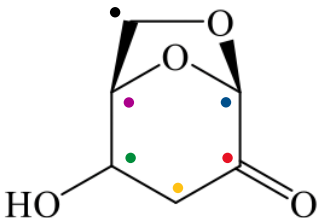


Figure 6.3  $^{13}\text{C}$  NMR spectra of MHC

The  $^{13}\text{C}$  NMR spectrum for the new product MHC indicates that there are six main peaks corresponding to the six carbons in this compound. Note that all results shown here are after purification as will be discussed later. Although the product was treated carefully to evaporate the solvent EtOAc used in the separation process, it seems that there are some residues apparent in the spectrum. They are very small and will be neglected. The singlet peak at 77.5 ppm corresponds to C5 and interferes with the solvent  $\text{CDCl}_3$  triplet peaks. That will be easier to distinguish between the two bands when using DEPT-135 as the latter does not show the quaternary carbon therefore is no band for  $\text{CDCl}_3$ . See Figure 6.3 (C) for DEPT-135. Additionally, no alkene bands were observed in the new product. The conjugated system in LGO makes the ketone band appear in a lower shift than MHC rising peaks at 189

ppm and 198 ppm respectively. This result is consistent with the IR results presented in Figure 6.5 as discussed in the next section. Table 6.1 demonstrates the  $C^{13}$  NMR spectroscopy assessment for MHC.

Table 6.1  $^{13}C$  NMR spectroscopy assessment of MHC in  $CDCl_3$

Shift (ppm)	Targeted C	Molecule
101	$-C < 2O$	
70	$>C - OH$	
77.5	$-C < C, O$	
65	$O - CH_2 - C$	
40	$C - CH_2 - C$	
198	$>C=O$	

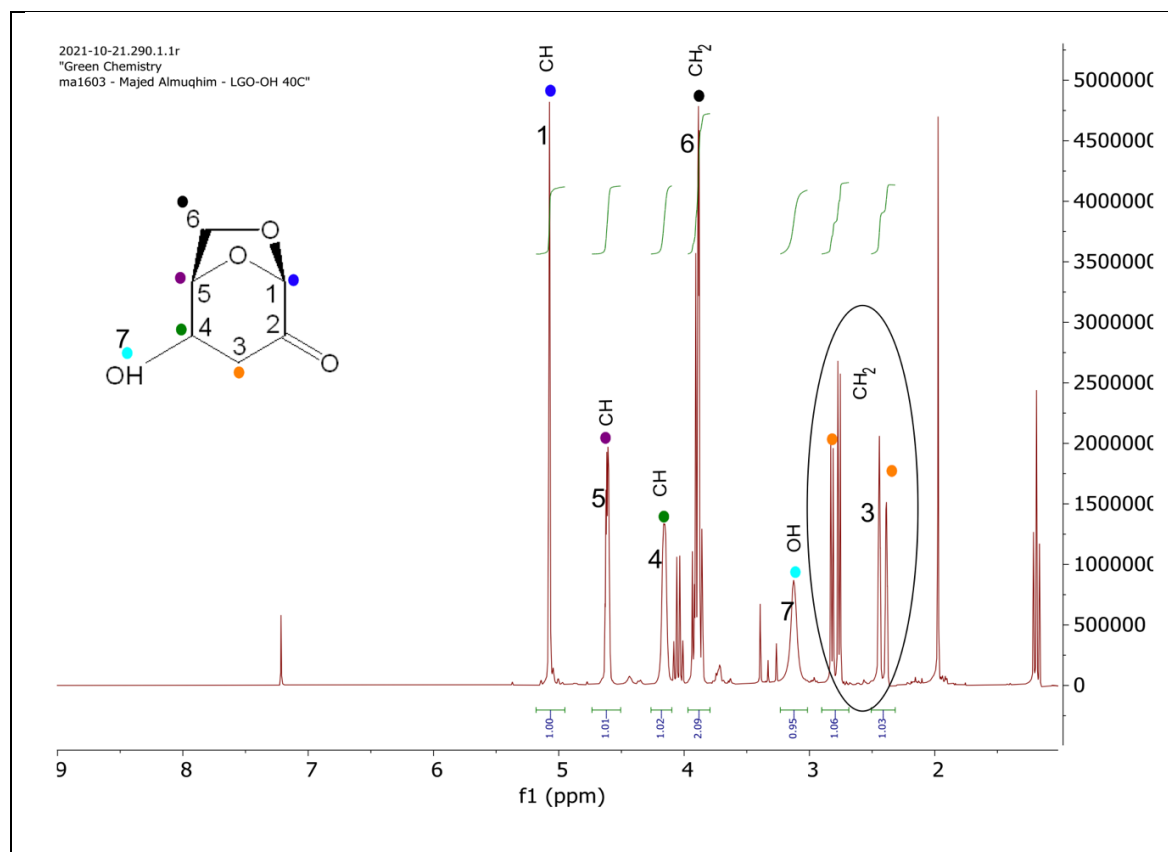


Figure 6.4  $^1H$  NMR spectroscopy for MHC

Table 6.2  $^1\text{H}$  NMR spectroscopy assessment of MHC

Shift (ppm)	Targeted proton	Molecule
5.1 ●	$-\text{CH} < 2\text{O}$	
4.2 ●	$> \text{CH} - \text{OH}$	
4.7 ●	$-\text{CH} < \text{C}, \text{O}$	
3.8 ●	$\text{O} - \text{CH}_2 - \text{C}$	
2.8 2.4 ●	$\text{C} - \text{CH}_2 - \text{C}$	

The integration results on Figure 6.4, show 8 protons. Table 6.2 illustrates that there is only one proton bonded to each of C1, C4 and C5 while C3 and C6 are bonded to two protons each. The broad band at 3.1 ppm corresponds to the proton of the hydroxyl group connected to C4. The spectrum indicates that the two protons on C3 are in different environments. In addition, the compound shows three different coupling constants of the two protons on the C3 in the range 2.4 – 2.8 ppm. This is discussed in more detail later in this chapter.

HSQC NMR spectroscopy illustrates proton-carbon single bond correlations. Therefore, it helps to display the correct position of each proton connected to a specific carbon. That makes it easier to confirm the assessment of the new compound MHC. In comparison with the spectrum of the starting material LGO, it is very clear that the new two protons at (2.4 – 2.8 ppm) on C3 are coupled with the new band of C3 at 40 ppm on  $^{13}\text{C}$  NMR spectroscopy as shown in figure (A.6.1). Also, illustrated in the figure that the protons appear at 3.8, 4.2, 4.7 and 5.1 in the  $^1\text{H}$  NMR spectrum correspond to carbon bands at 65, 70, 77.5 and 101 ppm in the  $^{13}\text{C}$  NMR spectrum.

The dots in COSY NMR spectroscopy are located between protons that are coupled. They indicate which neighbouring protons are coupled with. Figure (A.6.2) illustrates  $^1\text{H}$  COSY NMR spectrum for MHC in  $\text{CDCl}_3$ . This fits with the MHC assessment done earlier. Table 6.3 demonstrates the protons coupling.

Table 6.3 <sup>1</sup>H COSY NMR spectroscopy assessment of MHC. It shows protons coupling

Protons location	Shift (ppm)		Protons location	Shift (ppm)
C3	2.4	Coupled with	C3	2.8
C3	2.8		C4	4.2
C6	3.8		C5	4.7

MHC was obtained in the best yield compared to the literature.<sup>140-144</sup> Table 6.4 shows the comparison between the works.

Table 6.4 MHC production from the literature

group	method	additives	MHC after purification (%)
Sharipov <i>et al.</i> <sup>137</sup>	water	Et <sub>3</sub> N	39
Ma <i>et al.</i> <sup>136</sup>	water	Et <sub>3</sub> N	72
Shafizadeh <i>et al.</i> <sup>143</sup>	Organic extraction	-	77
Shafizadeh <i>et al.</i> <sup>141</sup>	water	Et <sub>3</sub> N	NA
Matsumoto <i>et al.</i> <sup>140</sup>	Organic extraction	-	80.6
Rennecke <i>et al.</i> <sup>144</sup>	-	-	82
Diot-Neant <i>et al.</i> <sup>142</sup>	water	K <sub>3</sub> PO <sub>4</sub>	82
<b>Our experiment</b>	<b>Water</b>	<b>No additives</b>	<b>98</b>
<b>Our experiment</b>	<b>EtOAc extraction</b>	<b>No additives</b>	<b>72</b>

When the temperature exceeds 60 °C it was expected that the geminal diol would stay. This idea is based on our finding in the NMR spectroscopy for the LGO/water interaction at different temperatures where at a temperature of 90 °C the triol formed LGO.

### 6.3.2 IR spectroscopy

The IR spectrum showed a ketone group at  $\sim 1700\text{ cm}^{-1}$  with a significant change between the pure LGO and the new product of MHC. Pure LGO shows the ketone band at  $1693\text{ cm}^{-1}$  while the new product gives a band at  $1732\text{ cm}^{-1}$  corresponding to a 40 wavenumbers shift. This finding suggests that the new product has no conjugated system as is the case with the LGO. Also, it seems that the product, despite the different temperatures used, has lost the alkene group between C3 and C4. Pure LGO has a band at  $1605\text{ cm}^{-1}$  which is a unique signature for the alkene C=C in IR spectroscopy. The other three spectra of the MHC have lost the band at  $1605\text{ cm}^{-1}$  forming a new band at  $1470\text{ cm}^{-1}$  for  $\text{CH}_2$  (asymmetrical deformation) which is clear evidence of loss of the alkene group. Figure 6.5 shows the difference between LGO and the other three products in the range  $1300 - 1800\text{ cm}^{-1}$ . Additionally, LGO shows bending of =C-H bond for the alkene at  $1380\text{ cm}^{-1}$  which is not the case in the other three products supporting the loss of the alkene. All these interpretations were supported by using NMR spectroscopy.

The stretching vibration of the =C-H group for an alkene is revealed by a small band above  $3000\text{ cm}^{-1}$  which is the case with pure LGO ( $3060\text{ cm}^{-1}$ ). Clearly the MHC does not show any band in that region even at the three different temperatures.

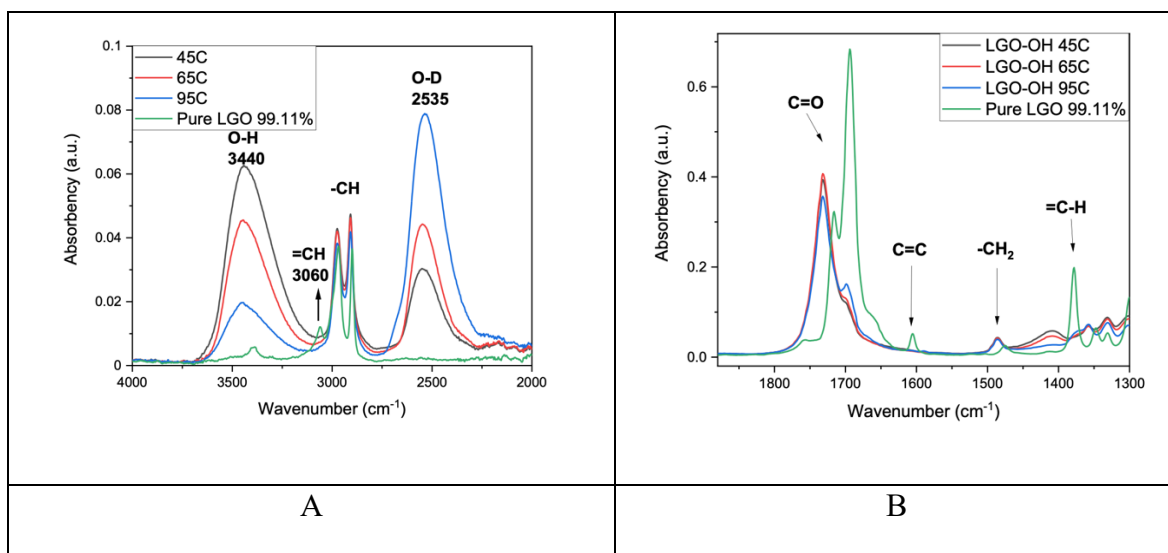


Figure 6.5 IR spectra of LGO and MHC

The products show clear evidence of the presence of the hydroxyl groups (O-H and O-D) at  $3440$  and  $2535\text{ cm}^{-1}$  respectively while pure LGO does not show any vibration activities in

these regions. The reason that both OH and OD are present is that the sample of LGO was dissolved in D<sub>2</sub>O. The hydrogen in the hydroxyl group exchanges rapidly as indicated in Figure 6.5. The higher the temperature the more OD groups are created in comparison with OH groups. It seems that the OH exchanges quicker in lower temperatures while the O-D is more stable at higher temperatures. However, the temperature range used here seems to have no significant effect on the production of MHC. Only a very small negligible difference was observed by NMR spectroscopy at the highest temperature of 95 °C. This is discussed in more detail later in this chapter.

### 6.3.3 Gas Chromatography (GC)

Gas chromatography could present additional support for our hypothesis. The new oil was analysed using the method with EtOAc as a solvent. The concentration was not calculated as the sample was very small and this experiment aimed to analyse the purity (%) and the retention time for the new compound and subsequently compare it with the LGO and the Cyrene. Three samples were submitted for analysis: the pure and non-pure new compound and the impurity.

The results showed that the separated new “pure” compound actually has a purity of 98%. About half of the impurity components are caused by one compound which appeared at 11.2 minutes very close to where LGO occurs at 11.3 minutes. Note that Cyrene gives a peak at 10.5 minutes.

Table 6.5 GC results of the new compound, LGO and Cyrene using the first method

Sample name	Main compound		Secondary compound	
	R.T. (minutes)	Amount (%)	R.T. (minutes)	Amount (%)
The new compound	13.511	98.08	11.24	1.13
	13.512	97.80	11.24	0.94
	13.511	98.06	11.24	0.93
	<u>Average</u>	<b>13.511</b>	<b>97.98</b>	<b>11.24</b>
Impurity	11.240	92.57	There is no specific compound was found. Most of them less than 1.5 % and beyond 13.00 minutes.	
	11.241	89.00		
	11.242	87.99		
	<u>Average</u>	<b>11.241</b>	<b>89.85</b>	
LGO	<b>11.3</b>	-	-	-
Cyrene	<b>10.4</b>	-	-	-

The main concern about method 1 is that the peak is fronting. So, the method was modified to method 2 trying to avoid this issue. See chapter 2 for more details.

Table 6.6 GC results of the new compound, LGO and Cyrene using the modified method

Sample name	R.T. (minutes)	Sample name	R.T. (minutes)
<b>LGO</b>	13.329	<b>Comp (1)</b>	23.508
	13.345		23.488
	13.331		23.517
	<u>Average</u> <b>13.335</b>		<u>Average</u> <b>23.504</b>
<b>Cyrene</b>	11.000	<b>Comp (2)</b>	13.505
	10.998		13.507
	10.999		13.511
	<u>Average</u> <b>10.999</b>		<u>Average</u> <b>13.508</b>
<b>The new compound</b>	23.224		
	23.251		
	23.249		
	<u>Average</u> <b>23.241</b>		

A noticeable result is that the product prepared from D<sub>2</sub>O (named LGO-OD) and MHC prepared from H<sub>2</sub>O (named comp 1) have similar retention times. By analysing each peak and stacking them together to identify the starting time when the compound hits the detector, the two compounds appear to have similar matching times when the peak started. Therefore, it can be deduced that the two compounds are the same and exclude the possibility that one of them is DHC. Thereafter, the impurity (named comp 2) matches the LGO in retention time. Hence, it can be confirmed that there is some LGO in an equilibrium with MHC. Note that each sample was analysed three times and all gave the same results.

#### 6.3.4 CHN analysis

The CHN analysis reinforces our confidence in the previous findings. Cyrene and LGO give results matching the theoretically calculated percentage. Our product MHC results show that they match the MHC theoretical calculations. The results are shown in table (A.6.1).



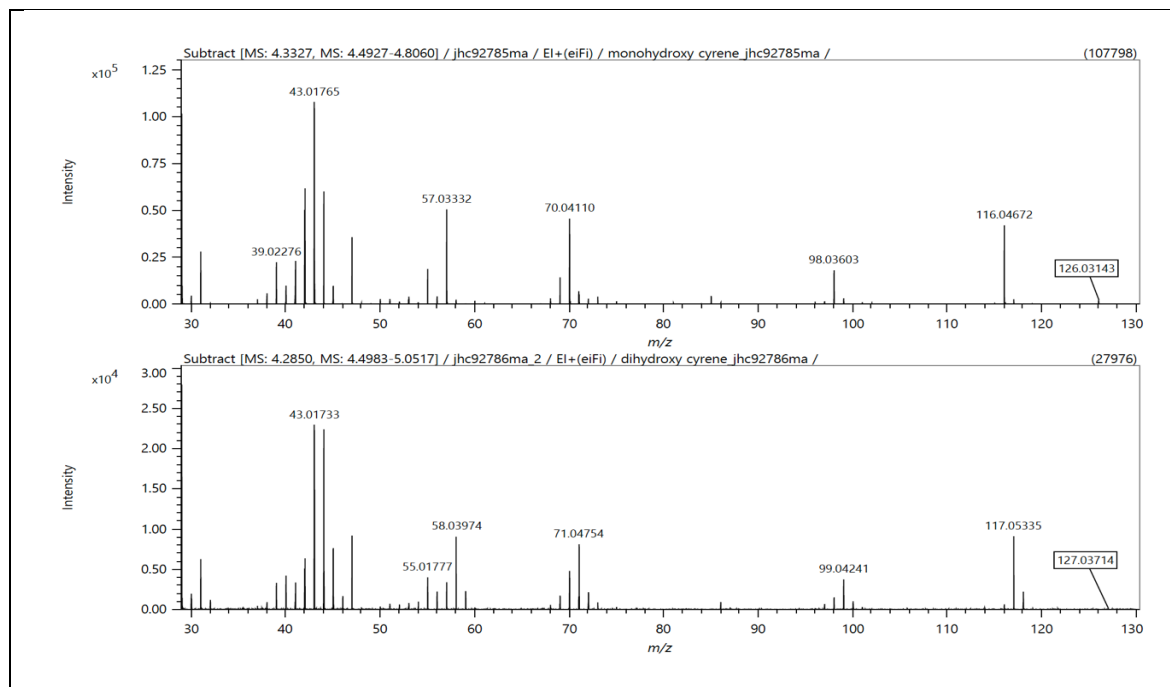
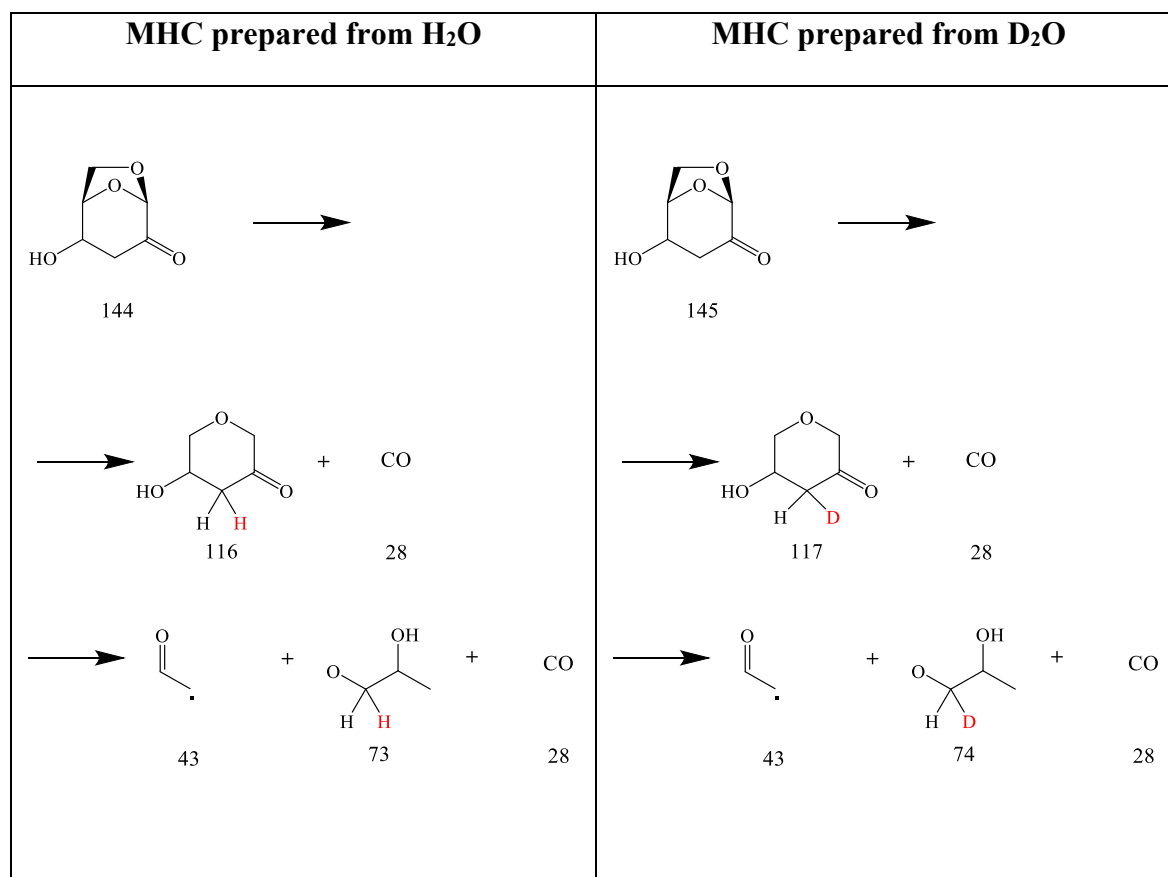
6.3.5 MS spectrometry and the difference between MHC prepared from H<sub>2</sub>O and D<sub>2</sub>O

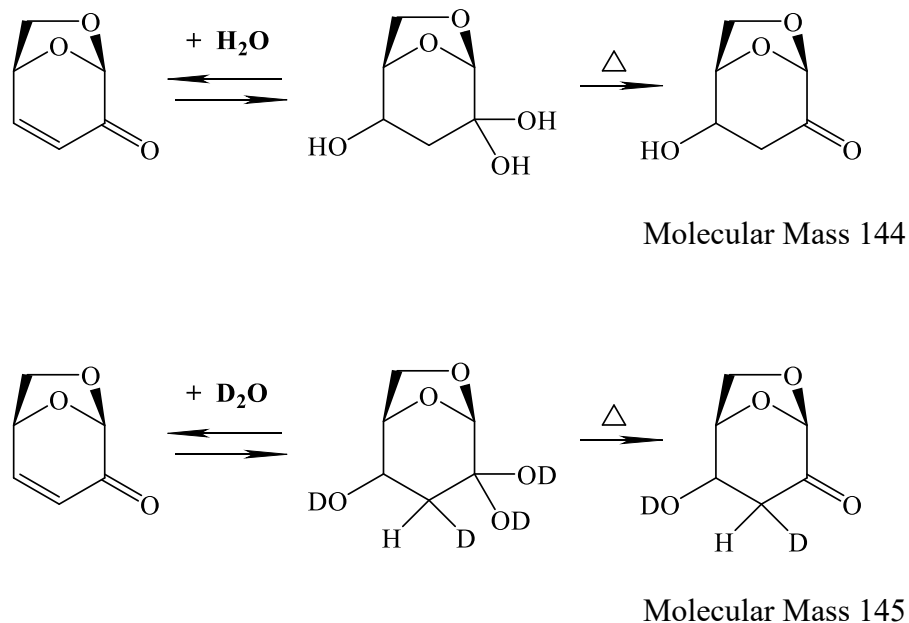
Figure 6.6 MS fragments of MHC

The MS analysis, Figure 6.6, confirms the differences between the two compounds but with only one m/z unit. The first obvious fragmentation for MHC prepared from H<sub>2</sub>O is a molecular mass of 116 which is CO (144 – 116 = 28 CO). The second fragment is a molecular mass of 98 which is CO<sub>2</sub> (144 – 98 = 46). The other sample is the MHC prepared from D<sub>2</sub>O. They have the same fragmentation pattern with one m/z unit extra for the bottom MS spectrum presented in Figure 6.6. Table 6.7 illustrates the fragments of the MHC. There is one m/z unit more in the MS when using deuterium oxide caused by substitution of H with D.

Table 6.7 MS fragments for MHC



The main idea behind the one number difference between the two MS spectra in Figure 6.6 comes from hydrogen atoms bonded to C3 of MHC. There is one hydrogen atom on C3 of LGO (alkene). When it is reacted with water H<sub>2</sub>O (or D<sub>2</sub>O) and hydrated, it is expected that the C3 will bond with another H atom or D atom respectively. As illustrated in Scheme 6.2, one more mass number is added to the MHC when prepared from D<sub>2</sub>O.



*Scheme 6.2 LGO interaction with H<sub>2</sub>O and D<sub>2</sub>O*

Infrared spectra of MHC were obtained to further characterise the product. As DEPT-135 C NMR spectroscopy and MS spectrometry identified the differences in the products which were prepared from H<sub>2</sub>O or D<sub>2</sub>O, IR spectroscopy, in contrast, supports this hypothesis that the difference in the spectra of the MHC was caused by the different water types used (H<sub>2</sub>O and D<sub>2</sub>O). The fingerprint region in Figure 6.7 (D) demonstrates very clear differences between the samples. As mentioned earlier when the reason behind this difference was not clear, it was thought that the impurity in the starting materials or even the methods used in the process may cause this difference. Open-air evaporation for the LGO in an aqueous solution was thought to produce a dimer of MHC while the rotary evaporator produces a monomer of MHC. The purity of LGO also was expected to change the product. All of these possibilities were studied.

This experiment aims to confirm the difference between using H<sub>2</sub>O and D<sub>2</sub>O to produce MHC. To simplify the experiment, three samples with different LGO purity, production methods and light and heavy water sources (D<sub>2</sub>O and H<sub>2</sub>O) were used. Table 6.8 presents the samples and the description of how they were prepared and proceeded.

Table 6.8 Samples of MHC

sample	Purity of LGO	method	Water used
MHC from 94% LGO r.e.	94%	heating in a rotary evaporator	H <sub>2</sub> O
MHC from 90% LGO atm	90%	heating in an open beaker	D <sub>2</sub> O
MHC from 94% LGO r.e.	94%	heating in a rotary evaporator	H <sub>2</sub> O

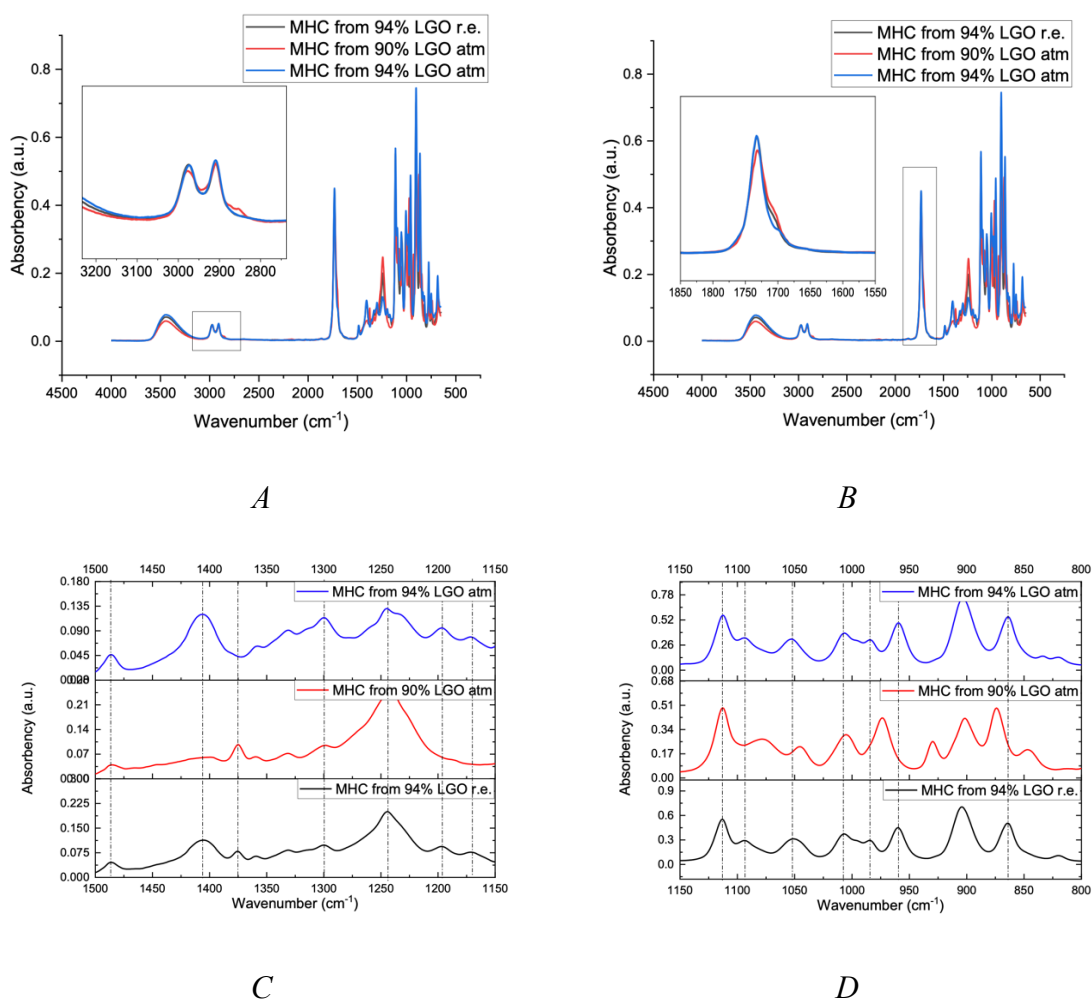


Figure 6.7 Spectra of MHC in different water sources and production methods

To prove that there is no dimer produced from this reaction, there are two negative bands due to  $\text{CH}_2$  that resulted from the  $^{13}\text{C}$  NMR DEPT-135 as well as proton integrations for the  $^1\text{H}$  NMR. The two protons bonded to C3 rule out the possibility of a dimer of MHC.

#### 6.4 The effect of the temperature on the MHC production

As mentioned earlier in this chapter, the MHC was prepared at the first using the evaporation method. Therefore, heating at different temperatures was investigated. When the water was evaporated, the analysis of the remaining product showed the effect of the temperature on the product. The product from the different temperature preparations was examined using IR and NMR spectroscopic techniques.

Two samples of 10 wt% LGO in  $\text{D}_2\text{O}$  were prepared, 50 mL each. the samples were kept at 21 °C in a dark cupboard for 6 weeks to allow the reaction to be fully completed.

Then the samples were divided into three vials, and each was heated to allow the water to evaporate at three different temperatures, 45, 65 and 95 °C taking 6, 1 and ½ an hour respectively. The remaining liquids were all thick brown oily liquid.

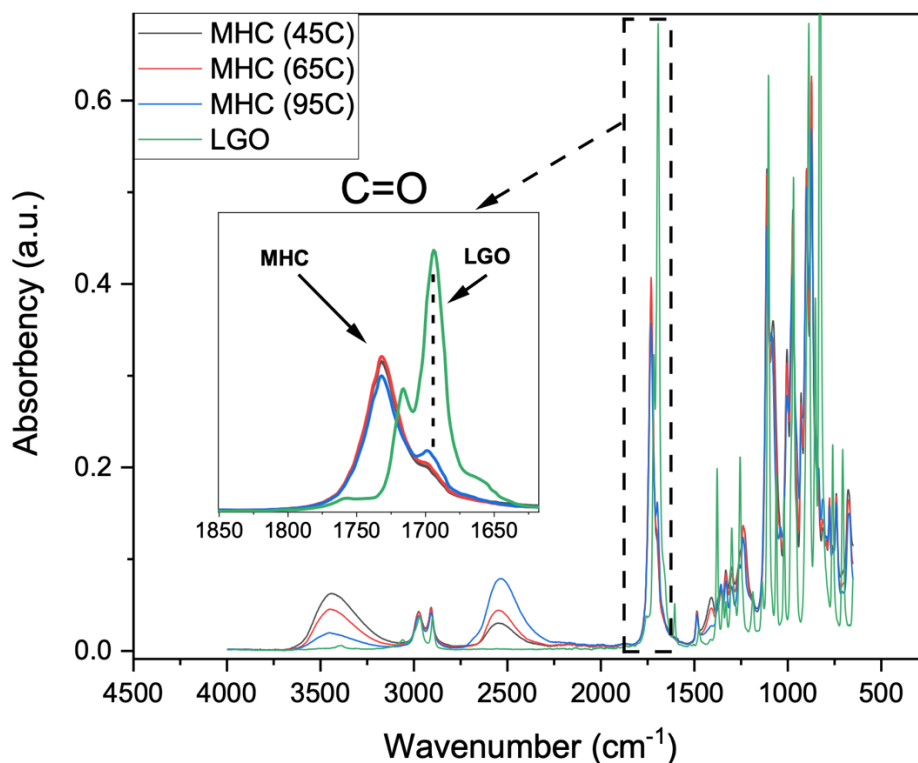
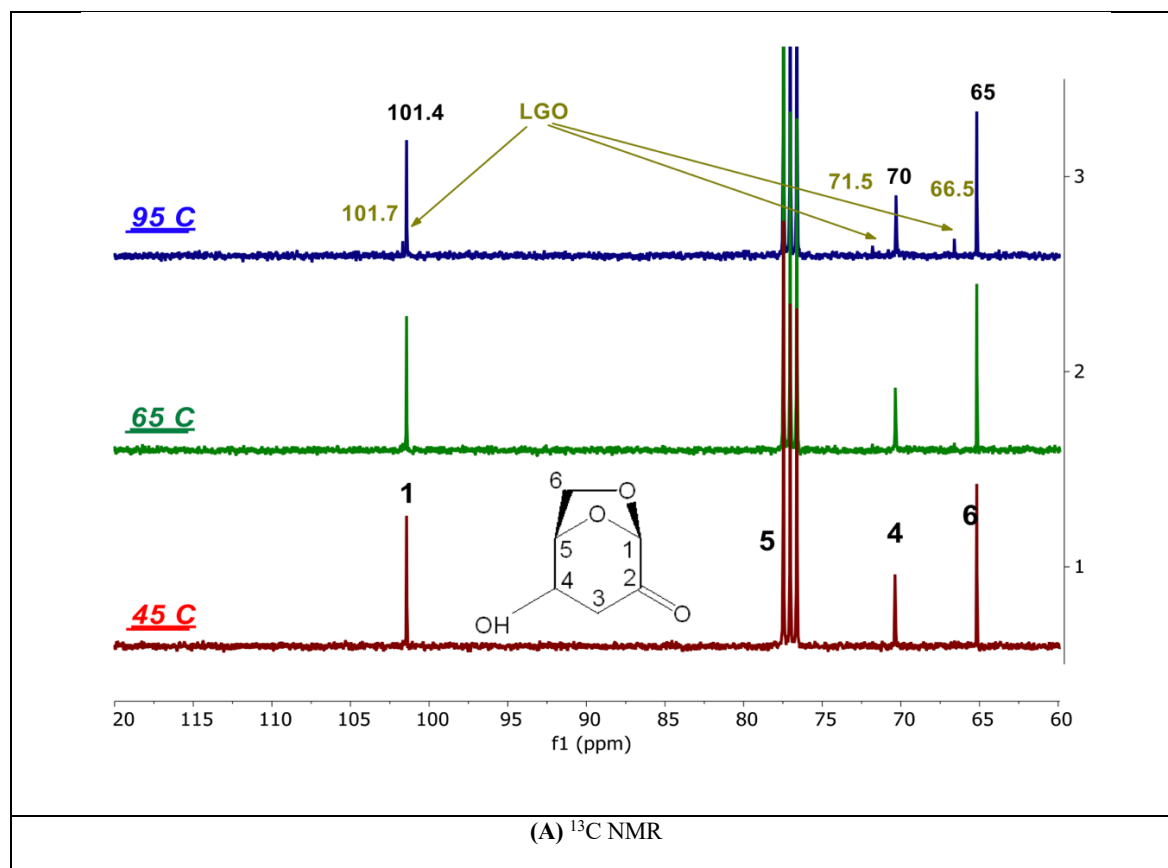


Figure 6.8 IR spectra for MHC prepared in different temperatures

Figure 6.8 shows IR spectra of LGO and three samples of MHC prepared at different temperatures of 45, 65 and 95 °C. The figure indicates that the ketone vibration of MHC prepared at 95 °C shows a higher frequency shoulder at ( $1732\text{ cm}^{-1}$ ) compared to other temperatures. Similarly, the intensity of the major band at  $1693\text{ cm}^{-1}$  is slightly lower than the band observed from the lower temperatures, indicating a smaller amount of MHC at this temperature. It seems that the amount of LGO in MHC increases for the sample prepared at 95 °C in comparison with the other samples. It can be concluded that this compound is not stable at high temperatures in the presence of water.

IR bands due to hydroxyl groups show very pronounced changes. Bands at  $3440$  and  $2535\text{ cm}^{-1}$  represent OH and OD stretching vibrations respectively. As discussed earlier, the hydrogen in the hydroxyl group exchange rapidly with  $\text{D}_2\text{O}$ . This exchange became clearer as the OD exchanges with OH. Since the IR bands of the OH and OD appear in different positions, it is easy to see this dramatic change. On top of that, it seems that the MHC tends to form more OD than OH at higher temperatures and vice versa as illustrated in Figure 6.8. Also see Figure 6.5 as an expansion for this region.



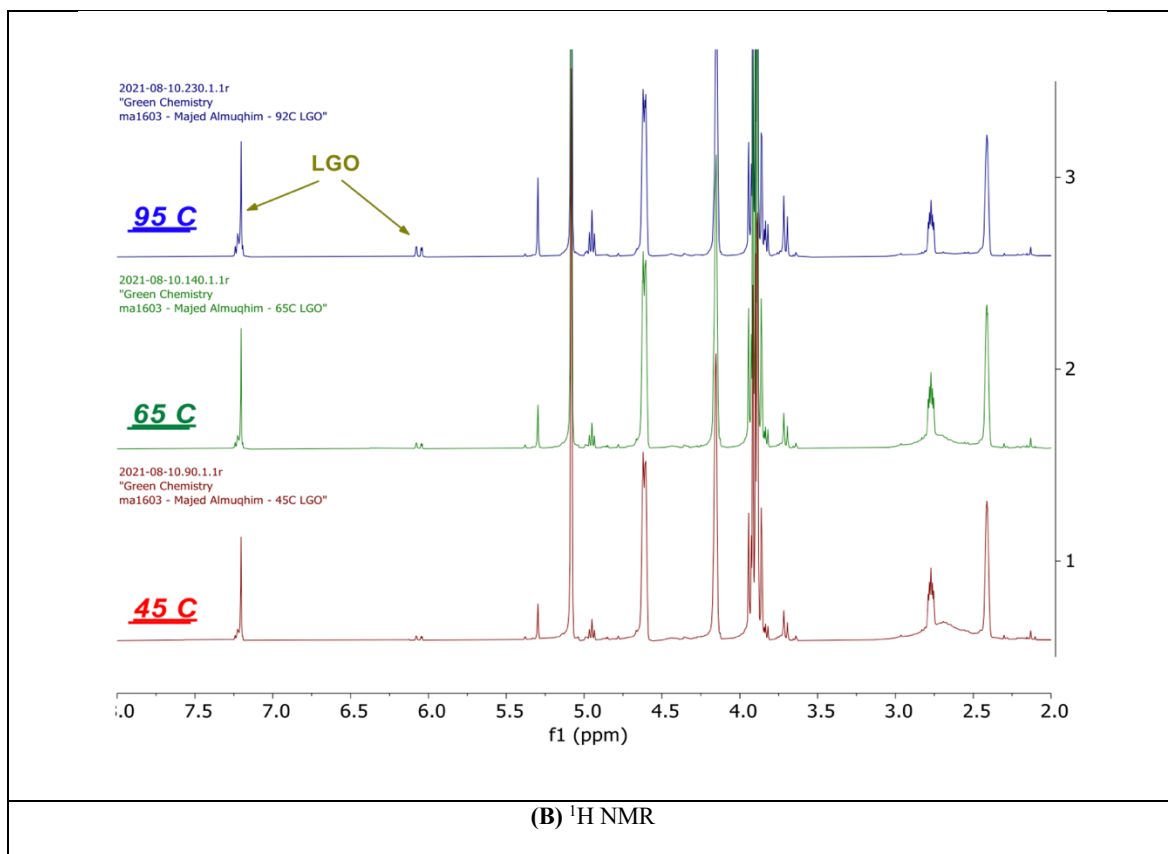


Figure 6.9 NMR spectra of MHC production in different temperatures

The same samples were submitted for  $^{13}\text{C}$  and  $^1\text{H}$  NMR spectroscopy. The results are consistent with those from IR spectroscopy.  $^{13}\text{C}$  and  $^1\text{H}$  NMR spectroscopy revealed that the MHC prepared at 95 °C tended to form a very small amount of LGO more than the 65 and 45 °C samples.

The integration of the MHC peaks in the  $^1\text{H}$  NMR spectra shows that the amount of LGO increased with the sample prepared at 95 °C. The integration results emphasise that the protons bonded to C4 and C3 of LGO have higher integration values in the MHC prepared at 95 °C in comparison with the lower temperature samples. Table 6.9 displays the integration of the protons bonded to C4 and C3 of LGO at 148 and 127 ppm respectively.

Table 6.9 the calculated integration for LGO in the new product MHC

The temperature used when preparing MHC	Protons for LGO bonded to carbon number:	
	C4	C3
45	0.14	0.02
65	0.14	0.02
95	0.22	0.04

Although the amount of LGO present in MHC is very small based on the integration in Table 6.9, there is a noticeable difference with the MHC prepared at 95 °C. Thereafter, temperatures of 45 and 65 °C are better options for the MHC production using the hating method. At lower temperatures it takes longer for the water to evaporate from the aqueous solution.

### 6.5 Protons on C3 of MHC

As discussed earlier that the MHC was prepared from H<sub>2</sub>O and from D<sub>2</sub>O, it is worth knowing the position of each one. This can be done by examining the protons on carbon 3 of the MHC. As this carbon was (alkene) with the starting materials (LGO) having only one H bonded to it, D<sub>2</sub>O as a solvent gave D to this carbon to be bonded to one hydrogen and one deuterium – C (H,D) –. Since the deuterium did not appear in NMR spectroscopy, only H was able to appear. Hence, stacking the two spectra of MHC prepared in two different water types may help to clarify the coupling of each one. In this case, using the MHC which was prepared from D<sub>2</sub>O can reveal the difference. Figure 6.10 shows only two bands corresponding to the one H atom on C3 while the other atom is D, which does not show any band in the NMR spectroscopy. By stacking the two spectra, the two atoms can be identified. Table 6.10 and Table 6.11 demonstrate the integration of the two protons showing the difference between using D<sub>2</sub>O and H<sub>2</sub>O for the production of MHC.



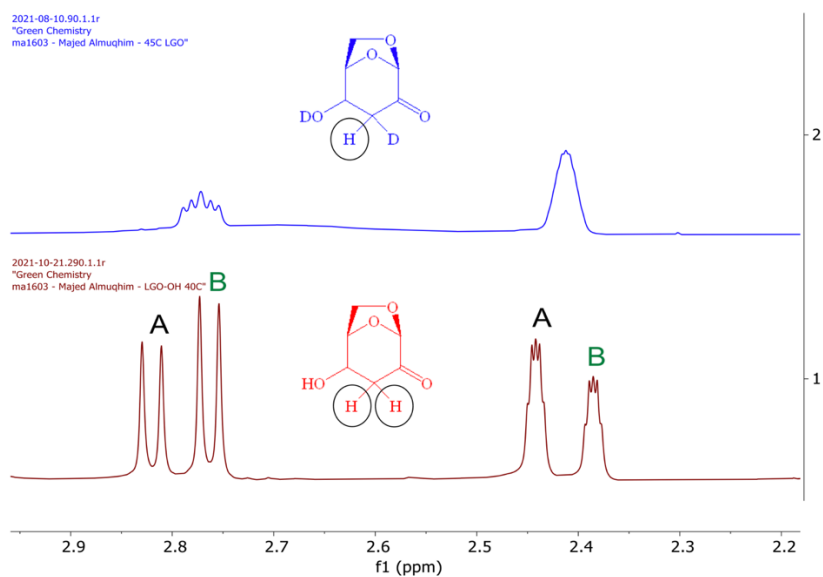


Figure 6.10 The difference between  $^1\text{H}$  NMR spectra of MHC prepared from  $\text{H}_2\text{O}$  and  $\text{D}_2\text{O}$

Table 6.10 The integration of each peak for Figure 6.10 of MHC prepared from  $\text{H}_2\text{O}$

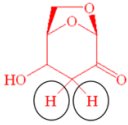
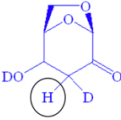
	Isomer A				Isomer B			
	ppm	∫	ppm	∫	ppm	∫	ppm	∫
<b>Protons on C3 of MHC</b>								
<b>H</b>	2.82	0.45	2.44	0.59	2.76	0.57	2.38	0.41
<b>H in each isomer</b>	1.04				0.98			
<b>Total H</b>	2.02							

Table 6.11 The integration of each peak for figure (5.30) of MHC prepared from D<sub>2</sub>O

	Isomer A				Isomer B			
	ppm	J	ppm	J	ppm	J	ppm	J
<i>H</i>	2.77	0.56	--	--	2.41	0.65	--	--
<i>H in each isomer</i>	0.39				0.58			
<i>Total H</i>	0.97							

Using water and deuterium oxide improves our ability to identify the position of each proton in the molecule, and in particular the hydrogen atoms connected to C3 in MHC. As shown in Figure 6.10 a spectrum of MHC prepared from H<sub>2</sub>O shows four different bands corresponding to 2 hydrogen atoms bonded to C3. The molecule may have different coupling with the neighbouring protons. That can be calculated by the coupling constant. As illustrated in Figure 6.11 that the molecule has three different coupling constants which means that the proton on C3 is coupled with 3 different neighbouring protons.

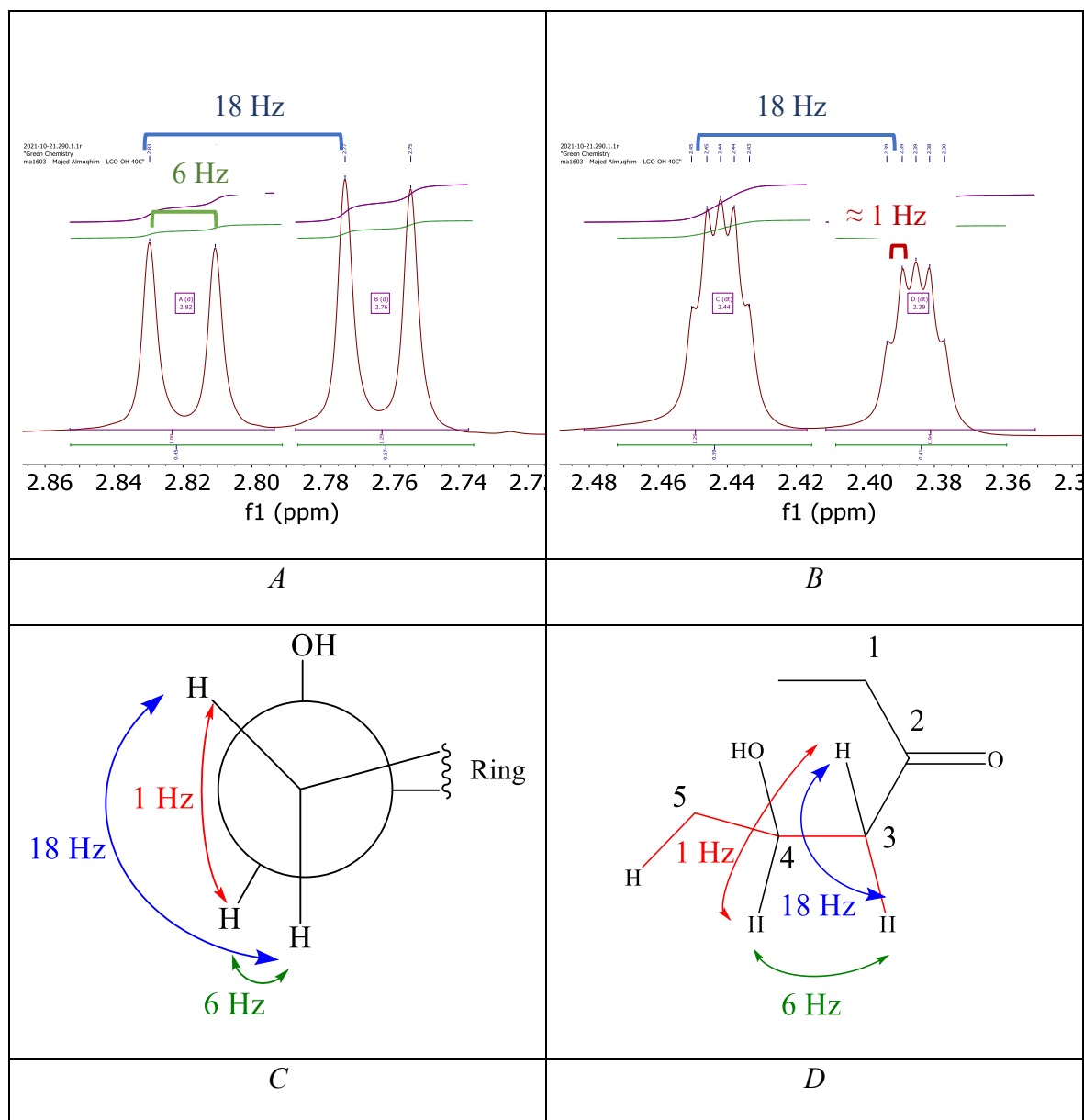


Figure 6.11 Protons coupling on C3

### Calculating the protons positions for the C3

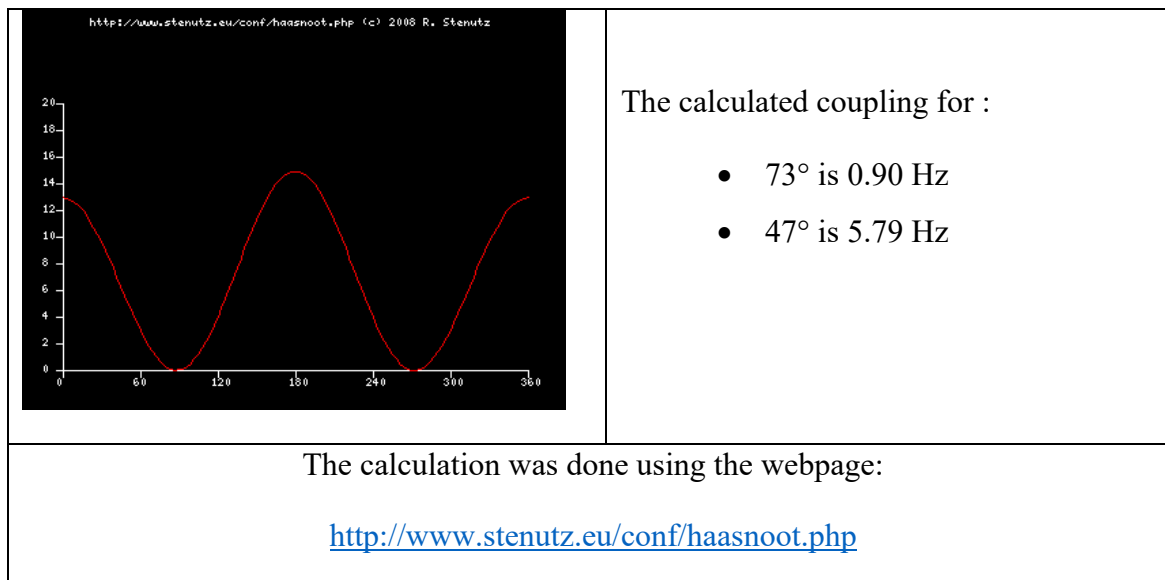
NMR field = 300 M Hz

$\therefore 1 \text{ ppm} = 300 \text{ Hz}$

$J$  value =

1.  $2.83 - 2.77 = 0.06$  ppm  $\times 300 = 18$  Hz
2.  $2.83 - 2.81 = 0.02$  ppm  $\times 300 = 6$  Hz
3.  $2.39 - 2.386 = 0.0034$  ppm  $\times 300 \approx 1$  Hz
4.  $2.39 - 2.38 = 0.001$  ppm  $\times 300 = 3$  Hz (total multiplet)

Additionally, one of the two protons on C3 (at  $\sim 2.4$  ppm) is coupled with the proton on C5 as seen in Figure 6.11 by  $^1\text{H}$  COSY NMR spectroscopy by the W conformation.<sup>145</sup> It is highlighted by the red bonds illustrated in Figure 6.11 (D). To help identify the position of each proton, the following graph was used and calculated the degree of each bond.



## 6.6 LGO - H<sub>2</sub>O interaction using microwave/raman spectroscopy

As discussed earlier in this chapter the heating of LGO in an aqueous solution speeds up the reaction producing the triol, it seems worthwhile to try MW heating. MW has been successfully used in many biomass hydrolysis/pyrolysis experiments.<sup>146</sup>

Raman spectroscopy with its ability to detect the polarizability of a molecule and using a probe with real-time analysis was chosen to monitor the change in the LGO interaction with water under MW conditions. The polarizability occurs when a molecule is affected by an external electrical field which may acquire its dipole moment.<sup>147</sup> In the case of water, the electrons are very attracted to the oxygen atom. Thus, water molecules have very low polarizabilities which makes Raman spectroscopy an ideal method for aqueous solutions as illustrated in Figure 6.12

A sample of 10 wt% of LGO in water was prepared and submitted to the MW which was designed with a Raman probe connected to the reaction vessel for real-time monitoring. A small amount of the sample was taken, before and after this experiment, to be scanned using IR to support the results. The sample was subjected to MW under 70 °C for 24 hours. During the reaction, Raman spectroscopy was used to analyse the samples every 5 minutes. A total of about 288 spectra were collected. The MW showed 127 W of power was consumed during the first 25 second to warm up the sample to the desired temperature. For the rest of the experiment, 3 – 10 W was used to maintain the temperature.

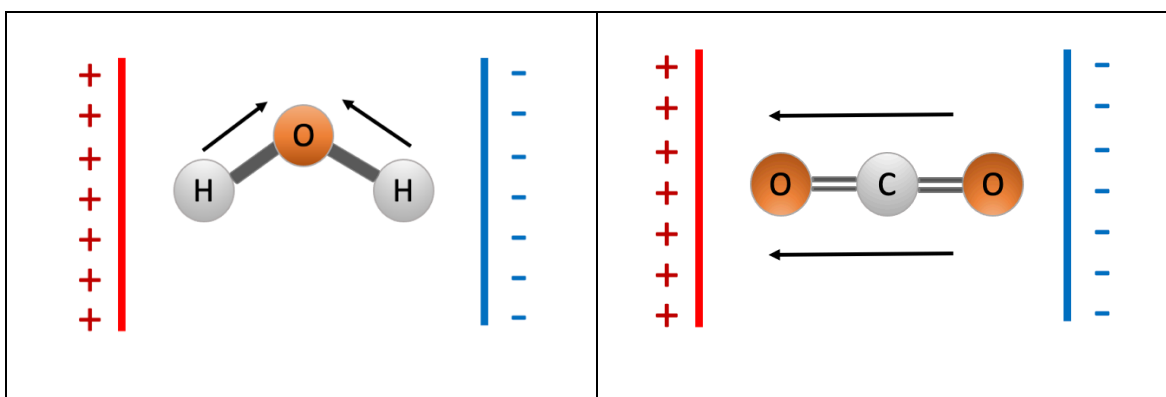


Figure 6.12 The polarizability effect on H<sub>2</sub>O and CO<sub>2</sub> molecules

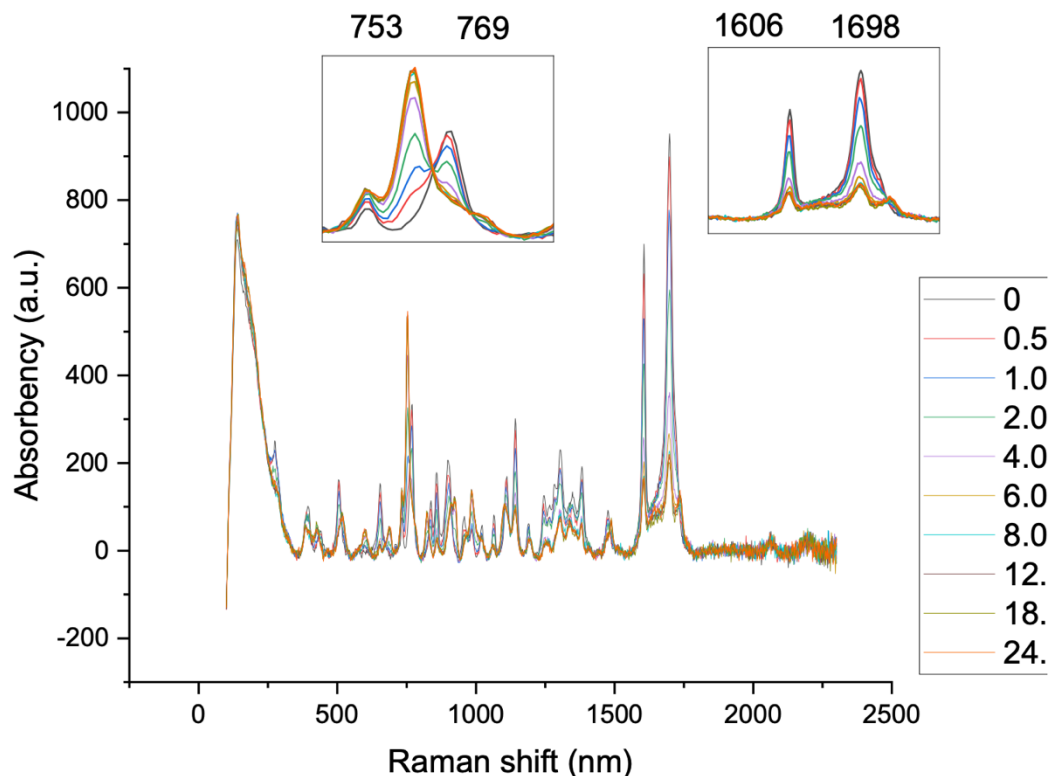
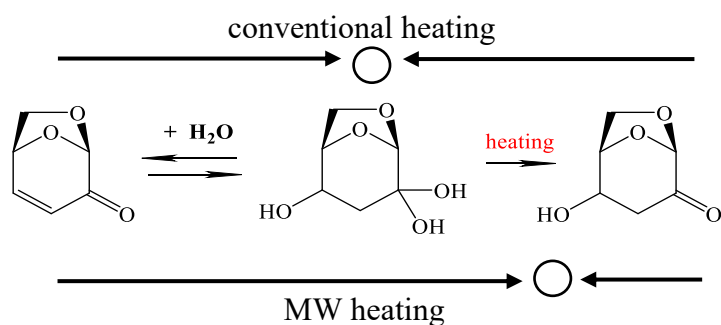


Figure 6.13 Raman spectra of LGO in water under MW heating from freshly mixed (0 to 24) hours

Based on our results illustrated in Figure 6.13, using a MW to produce MHC helps the reaction go even faster than conventional heating. It takes only a few hours to complete the process, leading to the best yield of the triol. Bands at 1606 and 1698  $\text{cm}^{-1}$  correspond to C=C and C=O respectively for the LGO. It is noticeable that the LGO converted very quickly taking 4 – 6 hours for the full conversion to the triol. The speed of this reaction using MW at room temperature with conventional heating is shown in Figure 5.11 in chapter 5. Under normal conditions when the LGO is mixed with the water along time is required (depending on the temperature), for the equilibrium to push to the triol with a neglectable amount of MHC present in the solution. Then if this solution is heated to evaporate the water, MHC is produced.

Interestingly, the equilibrium under MW heating was different. During MW heating, MHC is noticeably produced with the triol. It seems that MW pushes the reaction equilibrium towards the products (MHC) but shortly after the MW stops the equilibrium goes back to the pre-MW state. This interesting phenomenon was only apparent in a MW environment.



*Scheme 6.3 The difference between conventional and MW heating on the equilibrium*

Figure 6.14 demonstrates how the MHC was dominant during the MW heating process. As shown in the spectra Figure 6.14 (A), difference between the pure LGO and MHC ketones absorbency range is substantial. Then during the normal conversion of LGO to MHC at 21 °C, no significant amount of MHC were produced as illustrated in Figure 6.14 (C). Similarly, no MHC was evident in Figure 6.14 (B) when the sample was scanned before and after using the MW. Raman spectroscopy with its ability to be used inside the MW vessel, spotted a noticeable amount of MHC appearing during the MW heating process as shown in Figure 6.14 (D). Straight after the end of the MW programme, the same sample was scanned again with Raman but no MHC was detected.

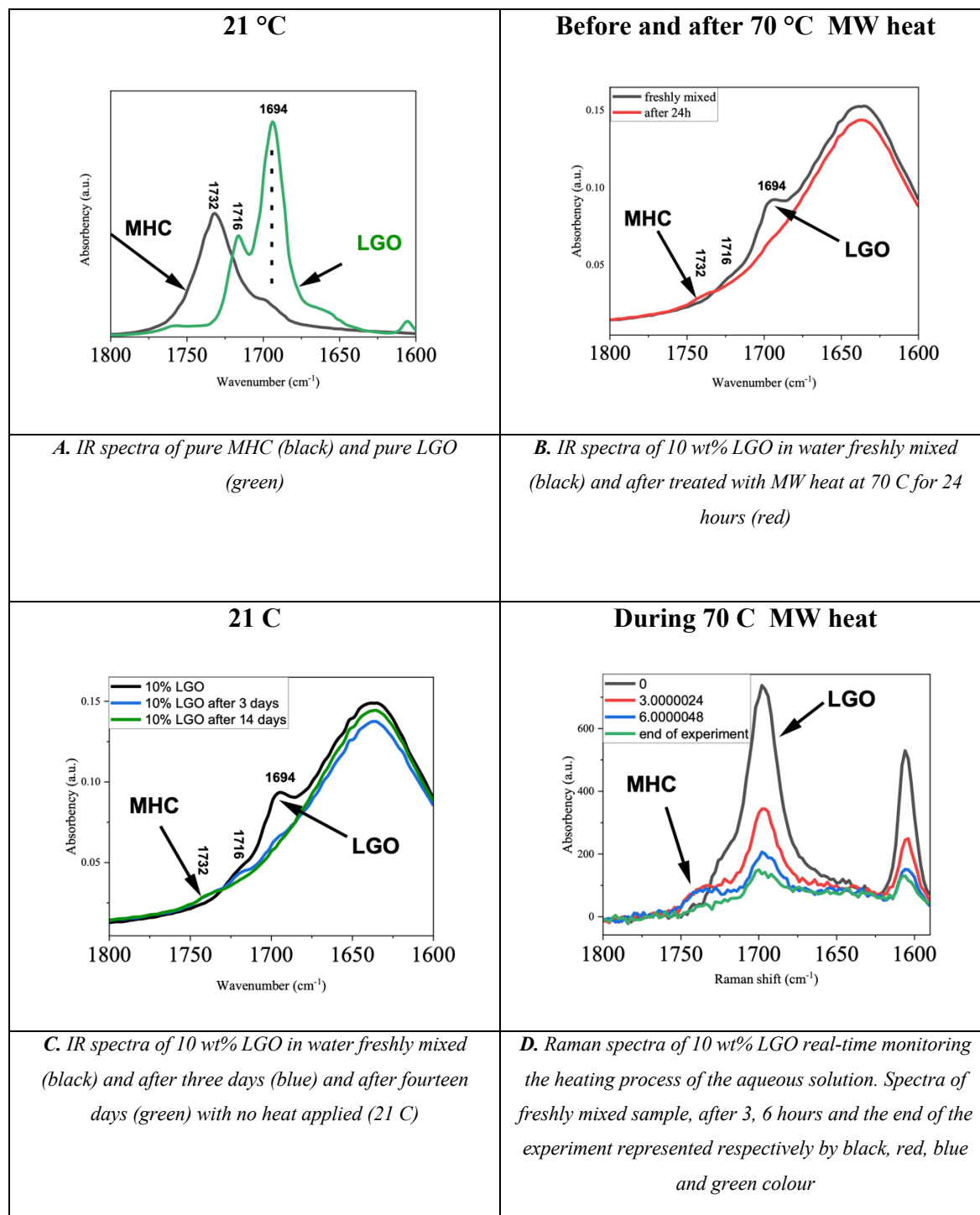


Figure 6.14 IR and Raman spectra of the LGO in different process



## 6.7 Monohydroxy Cyrene properties

MHC has a light yellow colour like Cyrene and LGO. When the MHC is purified, its colour becomes lighter as displayed in Figure 6.15. This compound has a higher viscosity than both Cyrene and LGO probably due to the hydroxyl group. It is important to study the basic properties of MHC such as polarity and solubility including the measurement of, BP, MP and thermal analysis.



*Figure 6.15 (Left). MHC produced in different temperatures 90, 60 and 40 °C and (right). MHC 40 °C after purification*

### 6.7.1 The polarity of MHC

As discussed earlier in chapter (5) Reichardt's dye is used to measure polarity in solutions. 1% of MHC was dissolved in 20 mL of water. 10 mL of the solution was used as a background for UV-Vis spectroscopy. Reichardt's dye (20.1 mg) was added to the other 10 mL of the solution. Then it was shaken well and filtered using a 45 micron syringe filter. As shown in Figure 6.16 the MHC displays a similar spectrum to Cyrene. Reichardt's dye absorbency is affected by the medium in which it is dissolved. The lower the wavelength of  $\lambda_{\text{max}}$ , the more polar is the medium. It can be concluded that MHC has a similar polarity to Cyrene and water but it is different to LGO. See Figure 5.15 in chapter (5).

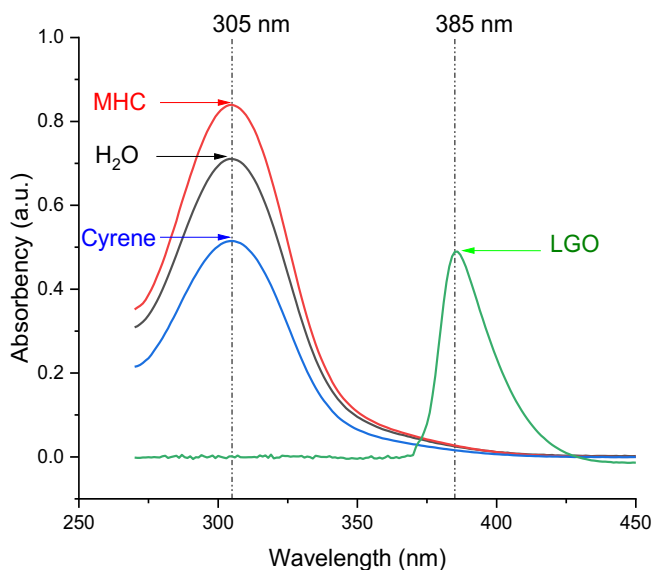


Figure 6.16 UV-Vis spectra of 1% aqueous solutions of: LGO (green), Cyrene (blue), MHC (red) and H<sub>2</sub>O (black). All samples showing the effect of the solution on Reichardt's dye

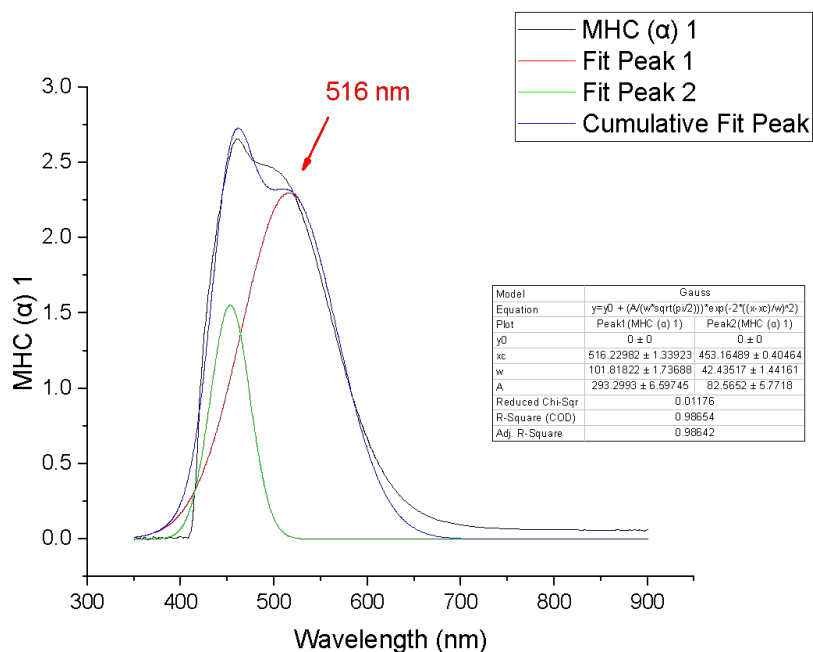


Figure 6.17 UV-Vis spectrum of pure MHC with Reichardt's dye (deconvoluted bands)

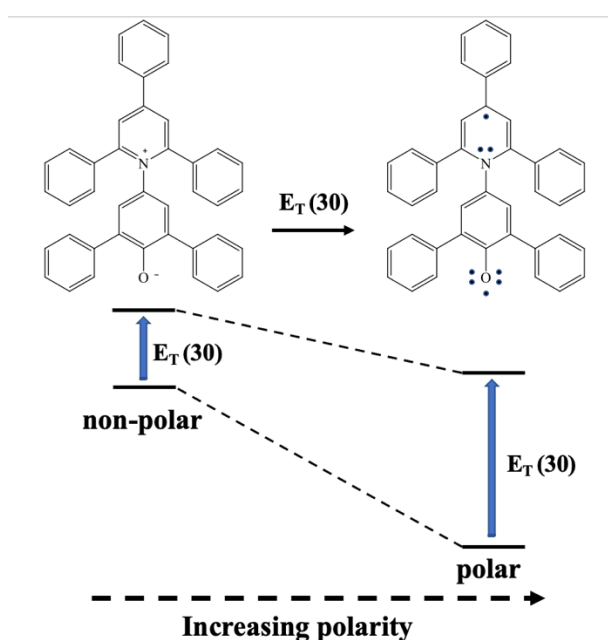
Reichardt's dye was dissolved in pure MHC to test its polarity. The sample was scanned using UV-Vis spectroscopy. Figure 6.17 illustrates the dye absorbency at 516 nm which corresponds to the intramolecular charge-transfer  $\pi \rightarrow \pi^*$  of the dye.

$$E_T(30) \text{ (kcal mol}^{-1}\text{)} = 28591 / \lambda_{\text{max}} \text{ nm}$$

$$= 55.4$$

$$E^{N_T} = E_T(\text{solvent}) - 30.7 / 32.4$$

$$= 0.763$$



*Scheme 6.4 Solvent effect on Reichardt's dye absorbency*

The  $E_T$  value of the MHC is 55.4 which is high and similar to methanol.<sup>132</sup> The  $E^{N_T}$  scale ranges from 1.00 to 0.00 for the most polar solvent (water) and tetramethyl silane TMS for the least polar solvent respectively. MHC has a value of 0.763 which suggests a polar solvent on this scale.

### 6.7.2 Solubility

MHC with its polar property can be dissolved in many solvents except non-polar ones. It dissolves in a range of solvents from the most polar (water) to toluene where it stops

dissolving. Cyrene, in comparison, gives similar properties and it dissolves in toluene although it is not soluble in heptane.

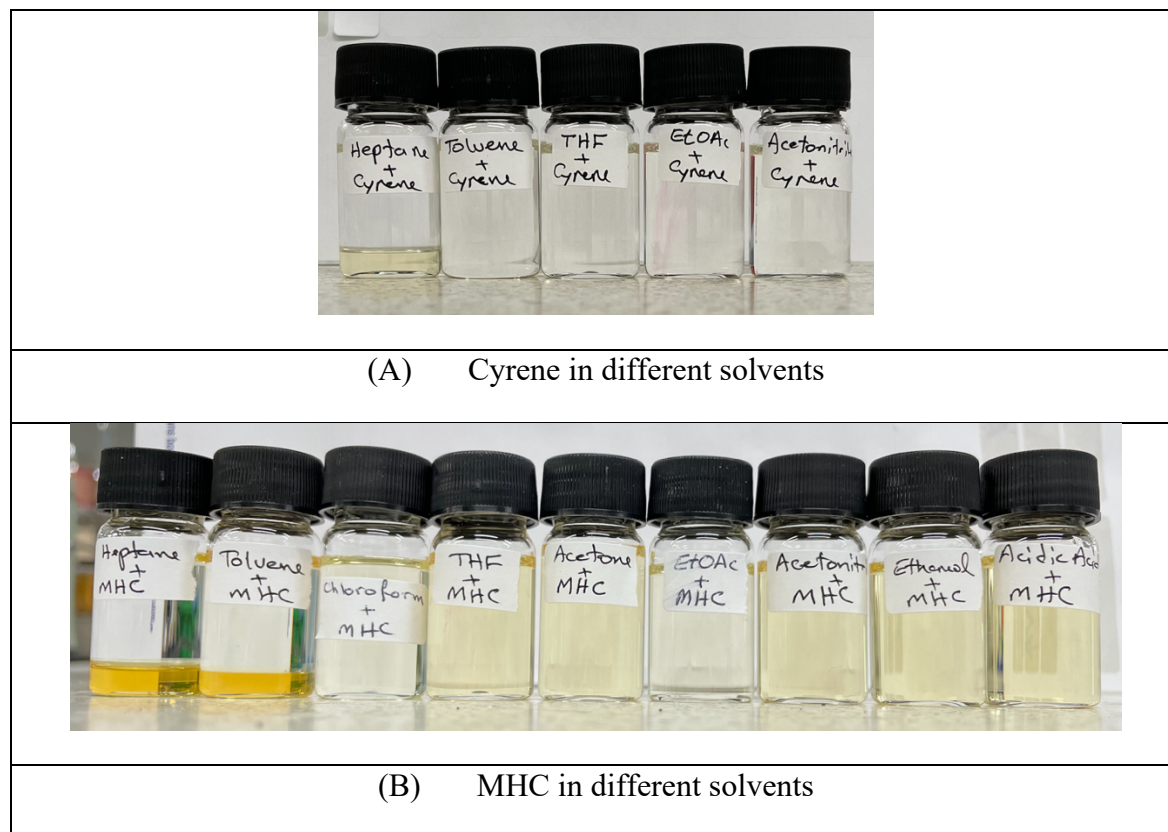
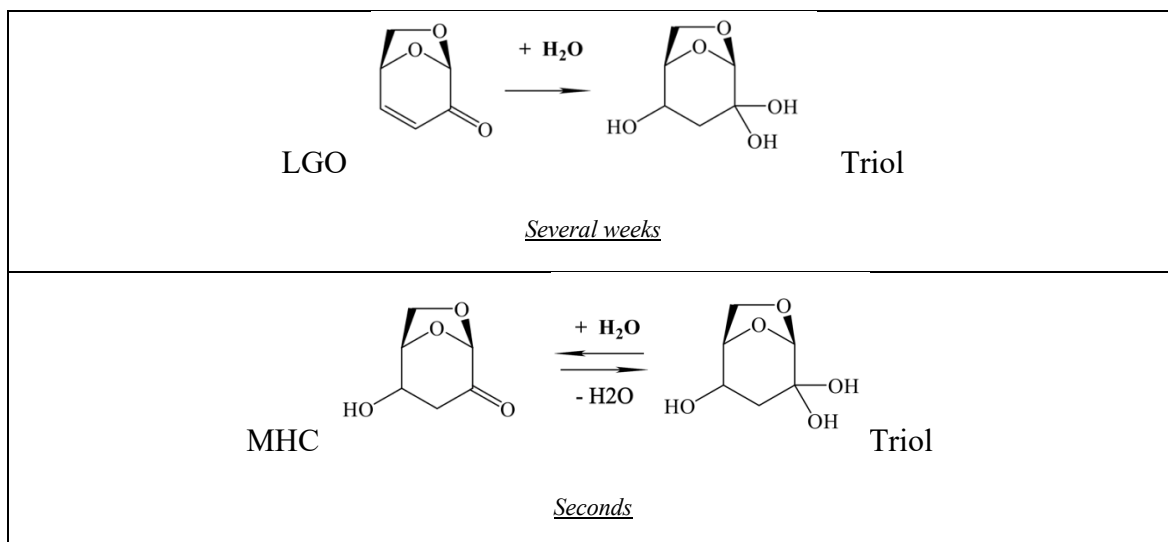


Figure 6.18 Solubility of (A) Cyrene and (B) MHC in different solvents

### 6.7.3 Dissolving MHC in water

It is worth examining the new product of the heated LGO oil to see how it behaves. A sample of 10% MHC, which was prepared at 45 °C, was dissolved in D<sub>2</sub>O and studied using IR spectroscopy. This experiment aimed to detect how rapidly MHC dissolves and react in water. Despite its viscosity, the product easily dissolved by shaking the vial for a few seconds. The solution was then examined by IR spectroscopy. The results on Figure 6.19 illustrate that the new compound has converted its carbonyl group into geminal diol very rapidly in comparison with the starting material (LGO). The latter may takes days to several weeks to be fully converted into the triol in an aqueous solution. The new compound is similar to Cyrene in this behaviour.



*Scheme 6.5 The difference between LGO and MHC in water*

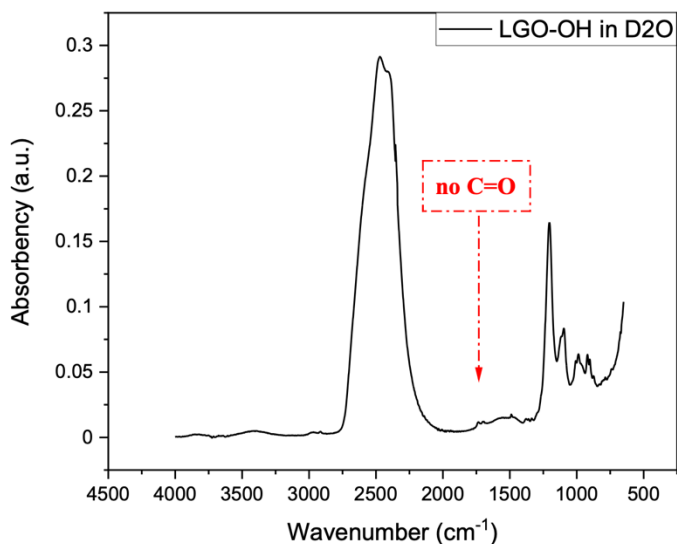
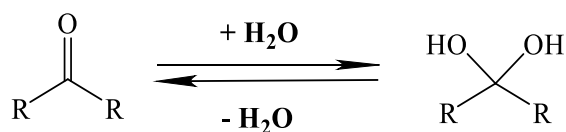


*Figure 6.19 IR spectrum of 10% MHC in D<sub>2</sub>O shows no vibration band for the ketone*

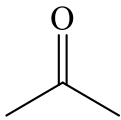
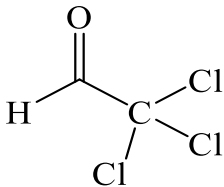
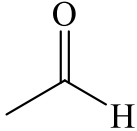
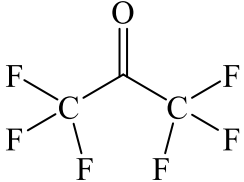
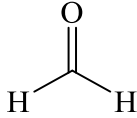
It is well known, in organic chemistry, that water attacks the double bond of aldehydes and ketones forming now products.<sup>80, 148, 149</sup>



*Scheme 6.6 The reaction of ketone in water forming geminal diol*

The reaction usually needs an acidic catalyst for proton production. The equilibrium constant  $K$  in Table 6.12 indicates how the compound favours being hydrated when mixed with water.<sup>80</sup> Acetone, acetaldehyde and formaldehyde respectively give  $K$  of 0.001, 1.06 and 2280.

Table 6.12 Equilibrium constant for some compounds containing ketone when interacting with water forming geminal diol\*

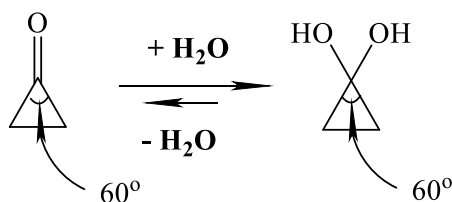
Compound	equilibrium constant $K$	Compound	equilibrium constant $K$
 Acetone	0.001	 Chloral	2000
 Acetaldehyde	1.06	 Hexafluoroacetone	$1.2 \times 10^6$
 Formaldehyde	2280		

\* stated by Clayden *et al.*<sup>80</sup>

Consequently, formaldehyde has more chance to form the geminal diol form the carbonyl group. Adding halogenic substituents increases hydration due to their electronic effect. Trichloroacetaldehyde (chloral  $\text{Cl}_3\text{CCHO}$ ) is a good example of an aldehyde that react with water to first form a hydrate. “Chloral hydrate” has no carbonyl group and is invisible in the  $1600 - 1700 \text{ cm}^{-1}$  region of the FTIR spectroscopy but does show OH absorption at  $3400$

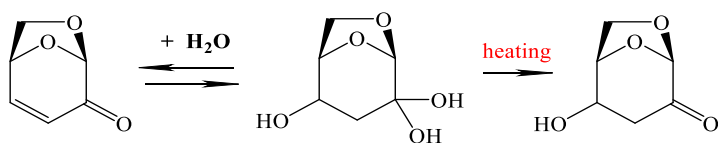
$\text{cm}^{-1}$ . When heating “chloral hydrate”, the resulting materials show very high absorbances in the  $\text{C}=\text{O}$  region at about  $1770 \text{ cm}^{-1}$  while the  $\text{O}-\text{H}$  band no longer exists. This means that water attacks the carbonyl group and creates a hydroxyl group (geminal diol in this example) but when heated, the compound prefers to form the carbonyl group instead of the hydroxyl group.<sup>80</sup>

Small rings molecules such as cyclopropanone prefer to be in the hydrated form as the later allows a smaller bond angle as a result of moving from  $\text{sp}^2$  to  $\text{sp}^3$  with an angle of  $120^\circ$  to  $109^\circ$  respectively.<sup>80</sup> So, in this case, the hydrated cyclopropanone is preferable in the equilibrium.



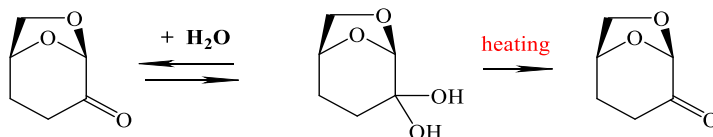
*Scheme 6.7 the ketone angle affects the equilibrium*

In our experiment, it seems that LGO slowly creates the geminal diol at the carbonyl carbon as seen before in our studies. When the aqueous LGO is heated, it produces an oil which has lost the geminal diol and formed a carbonyl compound instead. A hydroxyl group appears in the IR spectra of the resulting oils of MHC meaning that the compound still contains an  $\text{OH}$  group even after heating. Removing the alkene from the IR and NMR spectra and no  $\text{CH}_2$  (other than  $\text{C}_6$ ) appears in the DEPT-135  $^{13}\text{C}$  NMR spectrum of the product. This suggests the possibility of creating an  $\text{OH}$  instead of an alkene on  $\text{C}_4$  and  $\text{H}$  in  $\text{C}_3$ . This is also supported by the shift of the ketone bands of both IR and NMR spectroscopy towards higher wavenumber and ppm respectively.



*Scheme 6.8 the interaction between LGO and water producing geminal diol then MHC*

Cyrene behaves differently. When Cyrene is dissolved in water, the product is hydrated very quickly forming a geminal diol on the carbonyl group. But when this solution is heated to different temperatures, 45 – 100 C, it loses the hydroxyl and forms the carbonyl group which brings the solution to the original compound as Cyrene.



*Scheme 6.9 the interaction between Cyrene and water producing geminal diol then Cyrene*

In this experiment, which is similar to what was done with LGO, 10 wt% Cyrene in D<sub>2</sub>O was prepared and left for 24 hours to allow any reaction to be fully completed. Then the sample was separated into three vials and each was heated to allow the water to evaporate at three different temperatures, 45, 65 and 95 °C taking 9, 3 and 1 hours respectively. The remaining liquids for the three samples were similar to the Cyrene, except for the one heated at 95 °C which became slightly darker in colour. This was done to collect the remaining oil and examine it to see if the Cyrene is in different forms at different temperatures when interacting with water. The three samples were examined using IR spectroscopy.



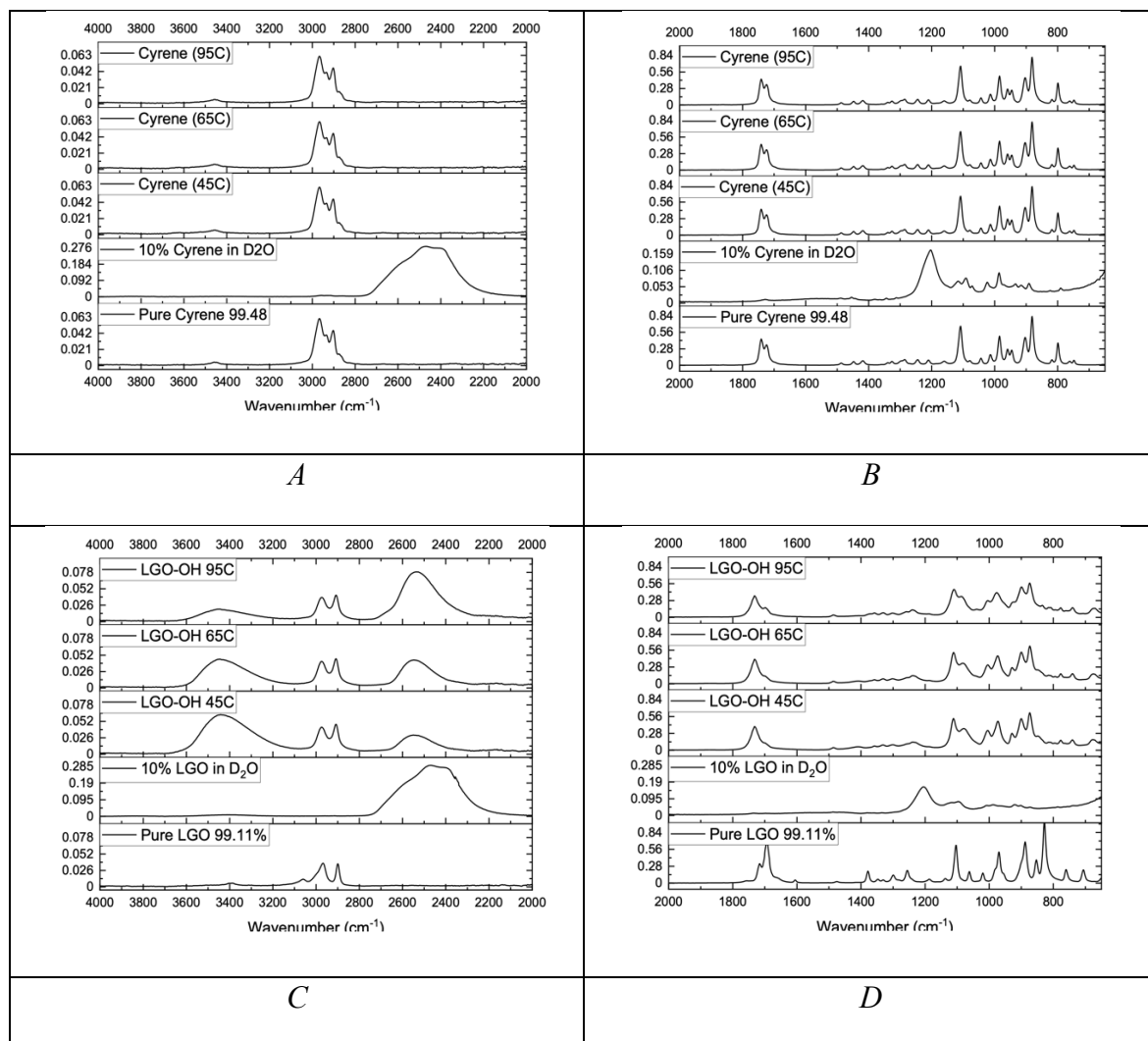
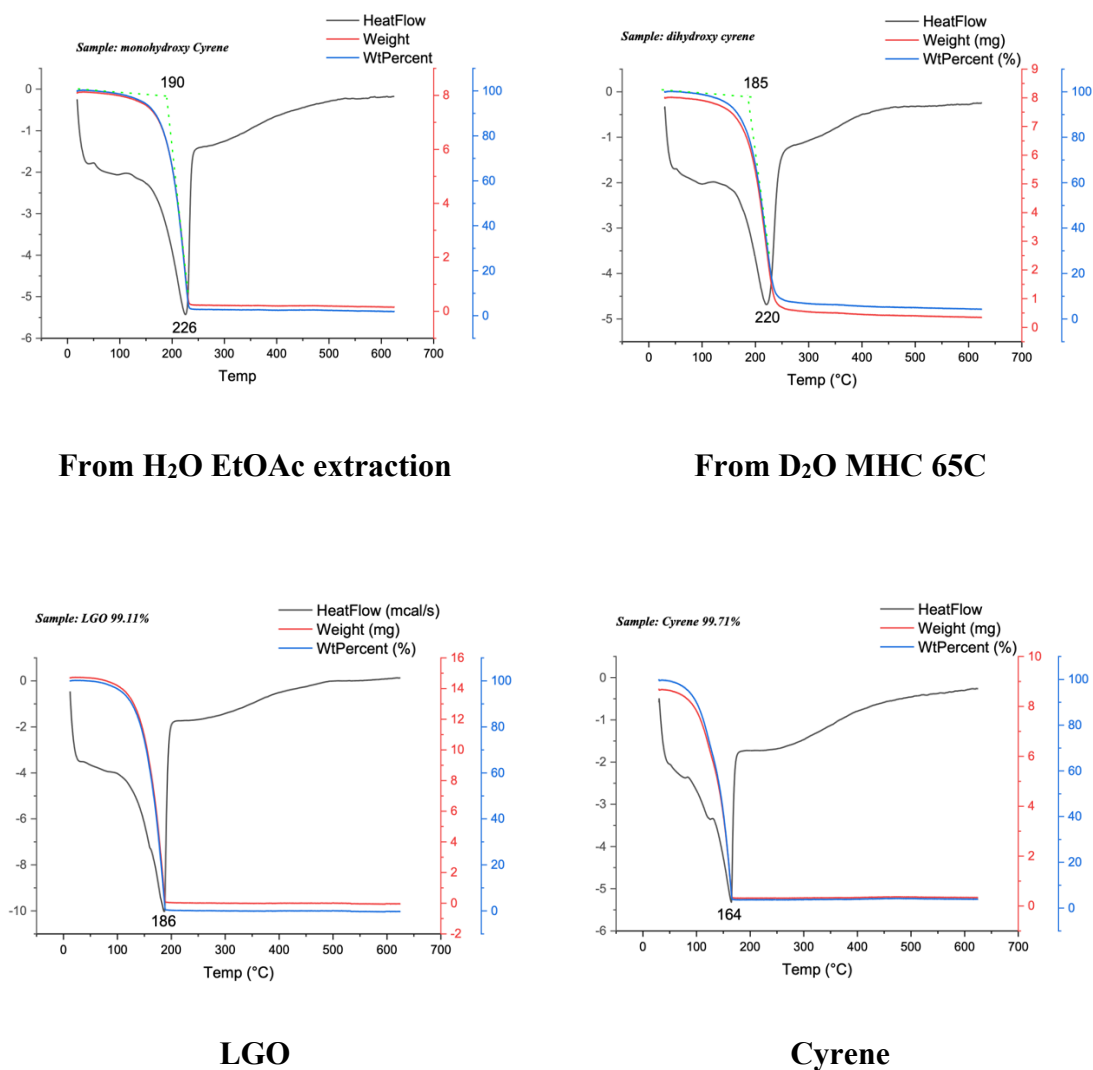


Figure 6.20 shows no difference between the produced oils in comparison with the original Cyrene sample

As demonstrated in Figure 6.20, the Cyrene has the same carbonyl band before adding water and after heating the aqueous solution of Cyrene in water ( $D_2O$ ). In addition, the hydroxyl group no longer exists in the product as is clear from the IR spectra which indicates that the Cyrene has lost the water and got back to the starting material Cyrene.

LGO, on the other hand, behaves differently as discussed earlier. It forms the hydroxyl group after dissolving in water and it does not lose it when the solution is heated. The conjugation with the alkene is presumably stabilising the carbonyl, resisting attack from water

## 6.7.4 Thermal analysis

From H<sub>2</sub>O EtOAc extractionFrom D<sub>2</sub>O MHC 65C

LGO

Cyrene

Figure 6.21 shows that the MHC has higher boiling point than both Cyrene and LGO

Both samples of MHC show similar thermal properties as illustrated in Figure 6.21. The new compound has greater thermal stability than LGO or Cyrene. As expected, the likely strong intermolecular association in MHC means that it has a higher boiling point than LGO and Cyrene. The melting point is below  $-60\text{ }^{\circ}\text{C}$  which is the minimum temperature that could be reached by the instrument. Figure 6.22 illustrates how the compound shows no change in the DSC.

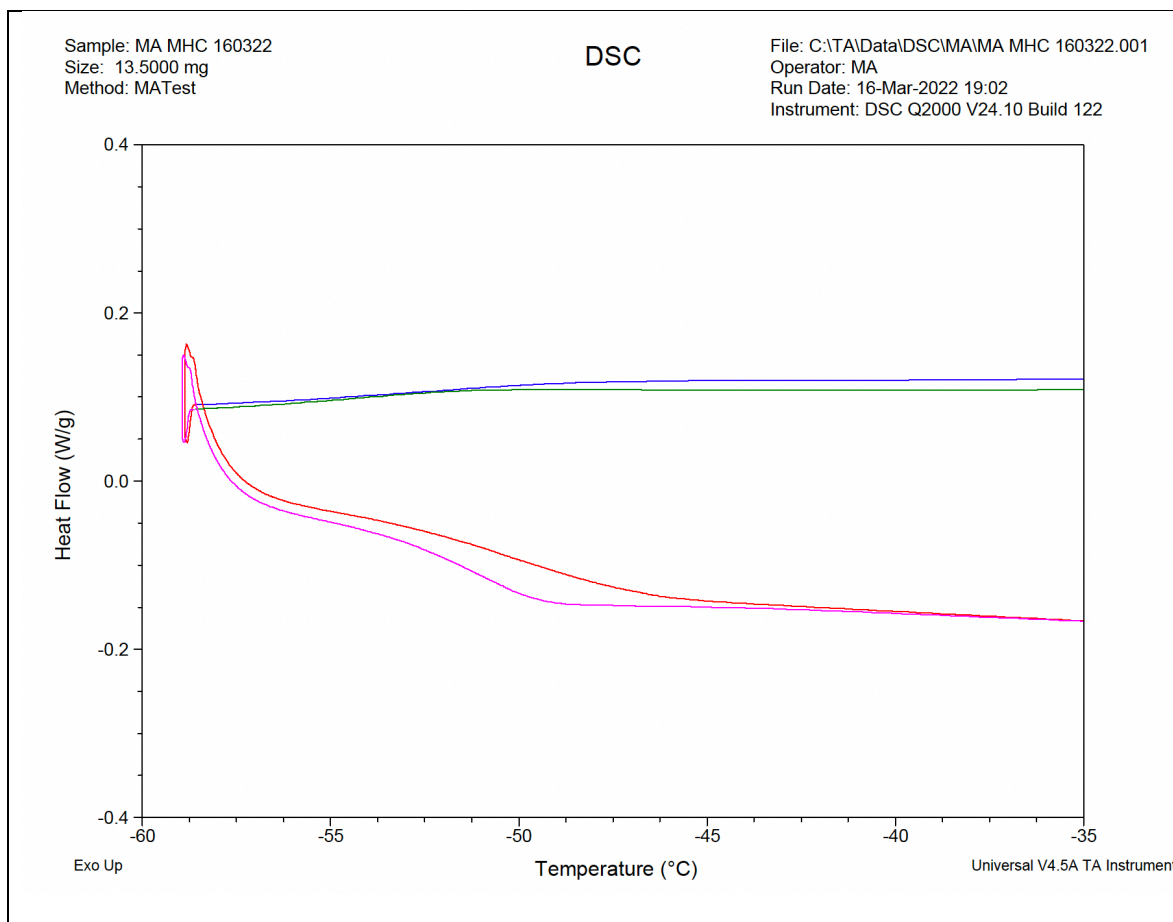


Figure 6.22 DSC for MHC

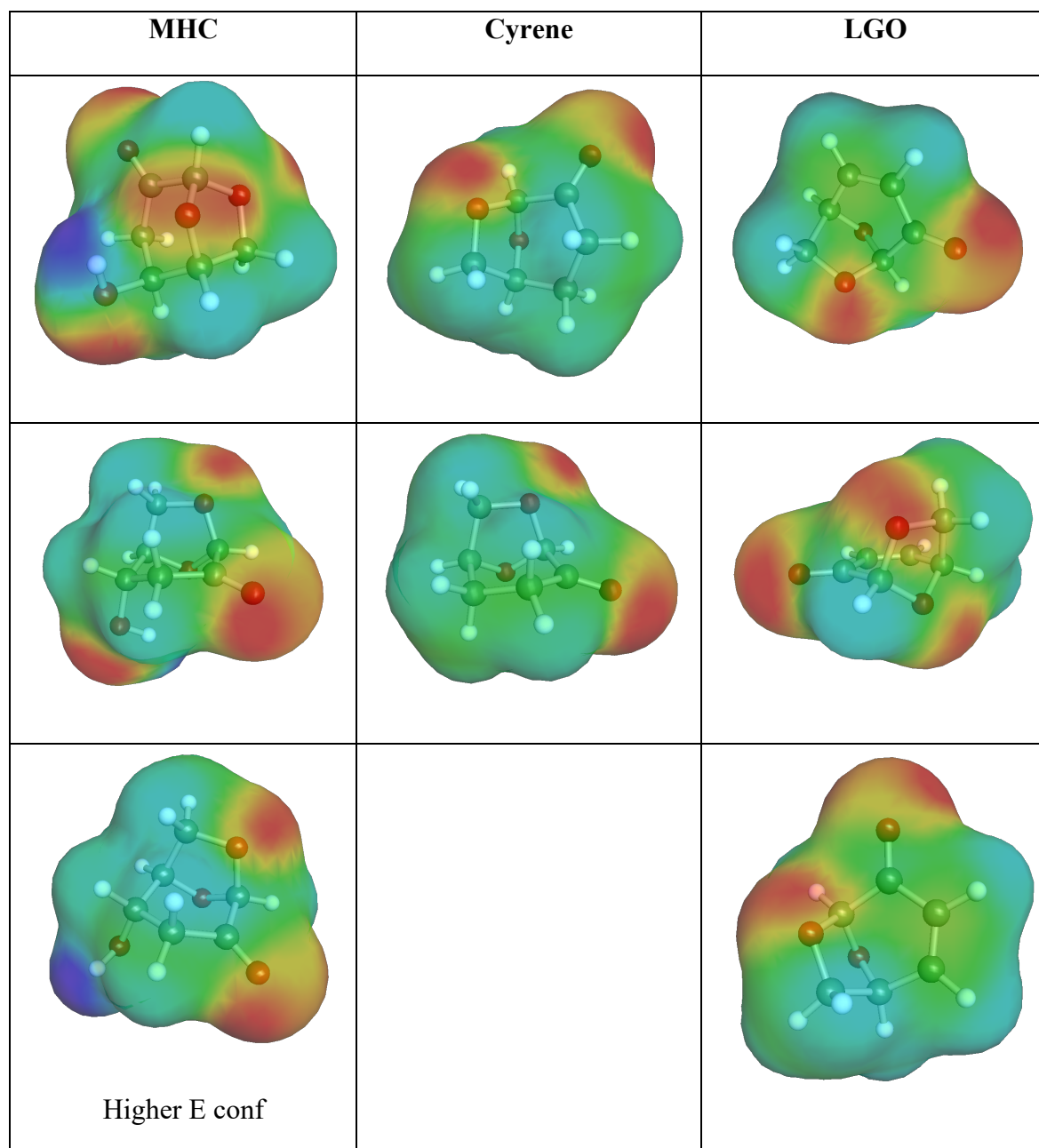


Figure 6.23 shows 3D modelling using COSMO to identify the intramolecular H-bonding for MHC, Cyrene and LGO in different electronic configurations

## 6.8 Conclusion

To sum up, LGO was successfully converted to MHC using only water and no catalyst was needed. MHC was produced in a high yield (98 %) at room temperature. This method was sufficient in comparison with the EtOAc extraction method. The only issue found is the time which took few weeks for the solution to be fully converted from LGO to the triol. To enhance the procedure, a MW was used to heat the solution for faster conversion. In the end, LGO was converted to triol in about 4 – 6 hours.

The MHC was characterised using different analytical techniques. The results of those instruments fit together for the MHC assignment. Some properties of the product were recorded such as polarity, solubility in different solvents, the behaviour with the water and some thermal analysis including STA and DSC.



## **Chapter 7: Conclusion and future work**

### **7.1 Conclusion**

By applying the NIRS method, some green chemistry principles might be attained, achieving a more environmentally friendly analytical approach. In terms of cost, waste, time consumption, simplicity and sustainability, NIRS is a powerful tool compared to other analytical methods. To our knowledge, the use of such a technique has not previously been applied using a fibre-optic probe in a biomass MW refinery. This technique is expected to open up an entirely new approach to control chemical reactions in industrial and research labs and to open up numerous novel device applications in different areas of analytical chemistry.

The fibre-optic probe connected to NIRS proved to address specific challenges, such as the high absorbency of the water in IR. Water's vibration bands are intense and temperature-dependent. The variable temperature experiment of water reveals potential discrimination of the different OH species. Quantitative measurements for some sugars and their derivatives in aqueous solutions using NIR spectroscopy were applied accurately compared to HPLC. NIRS also proved its ability to track the conversion of LGO to Cyrene in real-time.

NIRS was used to track the interaction of LGO with water to form the triol. The 1st overtone of CH vibration was investigated to track the change from alkene CH to alkane CH. The second derivative was applied to the spectra in order to enhance the results. The results were consistent with MIR, NMR, UV-Vis spectroscopy and Reichardt's dye experiment.

NIRS examined the hydrogen bonding in sucrose, glucose, and lactose monohydrate with success. NIRS is extremely moisture-sensitive. Monitoring the lactose monohydrate sample's evaporation revealed that time and temperature significantly impacted the evaporation process. It was successfully used for monitoring the sawdust moisture level when gaining moisture from the surrounding environment, finding that the sawdust sample contains different types of hydrogen bonding. It is a quick method to detect biomass moisture contents when stored, used, or transported.

LGO was successfully converted to MHC using only water and no catalyst was added, resulting in a high yield (98 %) at room temperature. This approach was more effective than

the EtOAc extraction method. To convert LGO to triol, time was an issue in the first step. With MW to heat the solution at 70 °C, this conversion was completed in four to six hours. The product was characterised using different techniques, including IR, STA, DSC and Reichardt's dye. The single hydroxyl group in the MHC allows for additional functionalisation. Producing diol by reducing the carbonyl group for a monomer, making an ester or ether with a fatty acid/alcohol to make a surfactant and many other applications, including oxidation, substitution and sulphonation. It could act as a secondary alcohol and open a range of potential compounds derived from biomass. It has a chirality property which means a possibility of including active pharmaceutical ingredients (SPIs).

## 7.2 Future work

One of the limitations of using (Bruker Equinox55) Near-infrared spectroscopy with DRIFT technique is that it cannot cover the whole range of NIR 8000 – 12000  $\text{cm}^{-1}$ . In order to apply the correct range, MIR detector was used to collect 4000 – 5000  $\text{cm}^{-1}$  and NIR detector to collect the range 5000 – 8000  $\text{cm}^{-1}$ . So, each sample must be scanned twice. Note that changing the set-up takes time. Another limitation of the fibre-optic probe of Bruker NIRS is the fixed path length cell of 2 mm. As a result, it shows a high intensity of the water's 1<sup>st</sup> overtone band, reaching 3 (a.u.).

The high absorbency of the water vibration in the NIRS causes a challenge to investigate the CH vibration in aqueous solutions. The CH 1<sup>st</sup> overtone band is located between the two giant bands of the combination and 1<sup>st</sup> overtone of the water. For this reason, it is necessary to use some data analysis. Cutting the desired band and correcting the baseline may enhance the spectrum. The second derivative also eliminates this error.

It is essential to collect more data for different samples of sugars to identify the differences between the species for the solid samples in chapter 4. Additionally, more sawdust samples are needed, different biomass species, sizes and environments. This will help to complete a library of NIR spectra of biomass. Once the data are completed with logical interpretations of the spectra, using appropriate chemometric analysis is recommended. This approach showed a potential successful technique in replacing the current standard oven-drying method.

Due to the available NIRS instrument, the temperature-dependent experiment in chapter 5, was studied for the water self-association at ambient pressure. It is worth investigating the



effect of the different pressure on the hydrogen bonding of this solution. This work would also hopefully identify the reason behind this dramatic change in the water self-association, which was detected for the LGO in water. Furthermore, it is worth investigating the 2<sup>nd</sup> overtone OH of the water. Using the same method as the temperature-dependent, compare the results with those in chapter 5. Adjusting the probe to different path lengths allows for more opportunities to detect different higher-order overtones. Using a built-in temperature controller is also recommend rather than a hot plate with a separate thermometer. The temperature controller may help reduce the measurement error.

In chapter 6, the production of the MHC was carried out using the interaction between the LGO and water at room temperature for a few weeks to form the triol. The triol was then concentrated to dryness to form the MHC converting the diol by the carbonyl group. Speeding up this process is suggested by using the MW to form the triol at 70 °C, which takes a shorter time and concentrating the solution to dryness to form the MHC. The MW, however, was used for the aqueous solution of LGO for four hours to form the triol. Therefore, concentrating the solution to dryness is highly recommended to form the MHC. Additionally, determining the direction of the hydroxyl group bonded to the C4 of the MHC is suggested. Finally, measuring the BP of the MHC is also recommend.



# Appendix

## Appendix of Chapter 1

Table (A.1.1) Discrimination between methods

<i>method</i>	<i>Speed</i>	<i>Green</i>	<i>Possibilities to be online</i>	<i>Quantitative / qualitative</i>
<b><i>NIR</i></b>	Fast	Yes	Yes	More quantitative
<b><i>MIR</i></b>	Fast	Yes	Yes	More qualitative
<b><i>HPLC</i></b>	Slow	No	No	Both
<b><i>GC</i></b>	Slow	No	No	Both
<b><i>NMR</i></b>	Slow	No	No	Both

Table (A.1.2) NIRS used for biomass and chemometric analysis applied

<i>Author</i>	<i>Range (nm)</i>	<i>Range (cm<sup>-1</sup>)</i>	<i>Materials analysed</i>	<i>Aim of work</i>	<i>Chemometric methods</i>
<i>Buning-Pfaue</i> <sup>59</sup>	1100 – 2500	4000 – 9100	Food (potato, meet, cheese)	Check the water contents	1 <sup>st</sup> and 2 <sup>nd</sup> derivatives and PCA
<i>Yano et al</i> <sup>61</sup>	800 – 2500	4000 – 12500	Glucose and citric acid	Glucose and citric acid in the aqueous solution of the blood	2 <sup>nd</sup> derivative
<i>Maleki et al.</i> <sup>62</sup>	305 – 1710	5848 – 32787	Soil	Materials properties of soil constituents	Unscrambler

<i>Liu et al.</i> <sup>63</sup>		4000 – 10000	Biomass (corn stover and switchgrass )	Chemical composition	PCA
<i>Felipe Bachion de Santana et al.</i> <sup>65</sup>	432 – 2448	4085 – 23148	Soil	Soil Organic Matter (SOM)	PCA
<i>Osborne</i> <sup>150</sup>	1100 – 2500	9090 – 4000	Flour, moisture and protein	Comparison of different techniques for linearisation and scatter correction	Multiple linear regression MLD, multiplicati ve scattering correction MSC
<i>Osborne and Fearn</i> <sup>151</sup>	1200 – 2400	8333 – 4166	Tea	Discrimination of commercial black tea	2 <sup>nd</sup> derivative
<i>Hazen et al.</i> <sup>152</sup>	1538 – 1818	6500 – 5500	Glucose concentrati on	To build a model of determining concentration	PLS Partial least square
<i>Wolfrum and Sluiter</i> <sup>60</sup>	400 – 2500	4000 – 25000	Corn stover	biomass composition prediction	PLS
<i>Yano et al.</i> <sup>61</sup>	800 – 2500	4000 – 12500	blood anticoagula nt and glucose powder.	predictions of the concentrations of glucose and citric acid in the aqueous	2 <sup>nd</sup> derivative

				solution of the blood anticoagulant	
<i>Maleki et al.</i> <sup>62</sup>	401 – 1638	6105 – 24937	Soil	material properties	MSC Using Unscrambler
<i>Saiga et al.</i> <sup>153</sup>	900 – 1700	5882 – 11111	Glucose in aqueous solution	Studying the effect of Ultrasonic Cavitation on the glucose spectrum	PCR, PLS
<i>Liu et al.</i> <sup>63</sup>	4000 – 10000	1000 – 2500	Biomass of Switchgrasses	Determination of biomass chemical composition	PLS
<i>Manley</i> <sup>154</sup>	4000 – 12500	800 – 2500	Moisture, protein and olive oil	Determination of moisture, protein and olive oil	PCA, PLS, PCR
<i>Li et al.</i> <sup>155</sup>	4000 – 9090	1100 – 2500	Orange juice	determination of glucose, fructose, sucrose, and citric and malic acids	Derivatives and MSC. Stepwise multiple linear regression (SMLR) and PLSR
<i>Nascimento et al.</i> <sup>156</sup>	4000 – 10000	1000 – 2500	Biomass	real-time monitoring of fermentations using (NIRS) probe	Derivatives and PCA

<i>Delwiche et al.</i> <sup>157</sup>	4000 – 10000	1000 – 2500	Starch and Cellulose	Moisture contents and water activities	Original spectra
<i>Li et al.</i> <sup>158</sup>	4000 – 10000	1000 – 2500	Biomass hydrolysates	Detection of acetic acid, furfural and HMF contents	PLS
<i>Arshadi et al.</i> <sup>70</sup>	4003 – 25000	400 – 2498	Pine and Spruce sawdust	The change in chemical and physical properties of sawdust during large-scale outdoor storage	PCA and PLS
<i>Sun et al.</i> <sup>67</sup>	15385, 12739 and 12077	650, 785 and 828	Lactose monohydrate	Determination of mean particle size of pharmaceutical powders	The frequency domain photon migration (FDPM) technique
<i>Higgins et al.</i> <sup>93</sup>	4000 – 25000	400 – 2500	Drugs	Nano particle size determination of milling process	PLS
<i>Chicoma et al.</i> <sup>92</sup>	9500 – 13000	769 – 1052	Vinyl acetate-butyl acrylate	Evaluation of particle size by monitoring the evolution of the average size of the polymer	PLS

				particles during emulsion polymerisation reactions.	
<i>Collins</i> <sup>118</sup>	4762 – 14286	700 – 2100	H <sub>2</sub> O	The behaviour of the 1 <sup>st</sup> overtone of water in various temperatures	Pure spectra
<i>Wojtkow and Czarnecki</i> <sup>159</sup>	5000 – 7500	1333 – 2000	tert-Butyl Alcohol/Water Mixture	the effect of temperature and concentration on the structure of TBA/water mixtures	PCA
<i>Sasic et al.</i> <sup>120</sup>	7692 – 6250	1300 – 1600	H <sub>2</sub> O	The behaviour of the 1 <sup>st</sup> overtone of water in various temperatures	Van't Hoff plot
<i>Jin and Ikawa</i> <sup>115</sup>	7800 – 6200	1282 – 1613	H <sub>2</sub> O	The behaviour of the 1 <sup>st</sup> overtone of water in various temperatures and pressures	Van't Hoff plot

<i>Buijs and Choppin</i> <sup>160</sup>	9090 – 7700	1100 – 1299	H <sub>2</sub> O	A study of different vibration band in water spectra in various temperatures	Pure spectra
<i>Choppin and Buijs</i> <sup>161</sup>	9090 – 7700	1100 – 1299	H <sub>2</sub> O, HCl, HBr, HNO <sub>3</sub> , HClO <sub>4</sub> , H <sub>2</sub> O <sub>2</sub> , NaOH, KOH, NaNO <sub>3</sub> , and NaClO <sub>4</sub>	Studying the effects of ionic solutes on the structure of liquid water	Pure spectra
<i>Choppin and Violante</i> <sup>114</sup>	6000 – 7700	1666 – 1299	H <sub>2</sub> O, water-acetone and water-dioxane mixtures	Calculating the hydrogen atoms involved in hydrogen bonding	Pure spectra and deconvolution of spectra
<i>Monosmith and Walrafen</i> <sup>119</sup>	5500 – 8000	1818 – 1250	H <sub>2</sub> O	The behaviour of the 1 <sup>st</sup> overtone of water in various temperatures	Pure spectra and Van't Hoff plot
<i>Paquette and Jolicoeur</i> <sup>162</sup>	1800 – 920	10870 – 5555	H <sub>2</sub> O and some electrolytes	Study of the hydration of various ions and	Van't Hoff plot



				nonelectrolytes	
<i>Palombo et al.</i> <sup>163</sup>	1000 – 3333	10000 – 3000	H <sub>2</sub> O & 1-Octanol	Association of Water in Wet 1-Octanol	Pure spectra
<i>Maeda and Ozaki et al.</i> <sup>116</sup>	1818 – 1111	9000 – 5500	H <sub>2</sub> O	Relationship between spectral changes and hydrogen bonds	PCR and PLS
<i>Christy</i> <sup>101</sup>	2500 – 1000	10000 – 4000	H <sub>2</sub> O & silica gel	water adsorption on silica gel surface	Second derivative
<i>Libnau et al.</i> <sup>104</sup>	2381 – 1111	9000 – 4200	H <sub>2</sub> O	Water behaviour in N and M-IR region	Pure spectra and Van't Hoff plot
<i>Giangiacomo</i> <sup>106</sup>	2400 – 1100	9091 – 4167	H <sub>2</sub> O, Glucose, fructose, and sucrose	investigate the spectroscopic response of solutions of glucose, fructose, and sucrose	Pure spectra
<i>Christy</i> <sup>100</sup>	2500 – 1000	10000 – 4000	amylose amylopectin, cellulose and starch	Studying the surface OH groups in carbohydrate polymers	Second and fourth derivative

<i>Simeone et al.</i> <sup>164</sup>	2500 – 1000	10000 – 4000	sucrose, glucose and fructose	Determination of some sugars in sweet sorghum juice	First derivative and PLS
<i>Omar et al.</i> <sup>165</sup>	1100 – 700	9091 – 14286	Mixture of water and sugars (sucrose, glucose and fructose)	Determining fruit's intrinsic quality	First derivative and PLS
<i>Noda et al.</i> <sup>166</sup>	1667 – 870	11500 – 6000	Oleyl alcohol	Analysing the complex NIR spectra for alcohol in various temperature	2D correlation approach
<i>Noda et al.</i> <sup>166</sup>	1667 – 976	10250 – 6000	N-methylacetamide (NMA)	Disassociation of H-bond	2D correlation approach
<i>Norris</i> <sup>167</sup>	2500 – 1100	9091 – 4000	Milk and pharmaceutical tablets	Understanding and correcting the factors which affect diffuse transmittance spectra	MULR programme for regression
<i>Norris</i> <sup>168</sup>	2500 – 400	4000 – 25000	Wheat	To develop a method for understanding the spectra change overtime	MLR regression and second derivative

Appendix

<i>Dahm et al.</i> <sup>169</sup>	1900 – 1000	5263 – 10000	Milk	Studying the baseline shift on spectra during coagulation of milk	Pure spectra
<i>Amerov et al.</i> <sup>170</sup>	1691 – 1111	5400 – 9000	Blood samples	Determination of glucose in whole blood	Net analyte signal NAS, PLS and PCA

Table (A.1.3) The green chemistry principles achieved when applying this project










green chemistry principles	No	Picture	By applying
1. Waste prevent		<p><b>1. WASTE PREVENTION</b></p>  <p>Prioritize the prevention of waste, rather than cleaning up and treating waste after it has been created. Plan ahead to minimize waste at every step.</p>	NIRS
3. Less hazardous chemical syntheses		<p><b>3. LESS HAZARDOUS CHEMICAL SYNTHESIS</b></p>  <p>Design chemical reactions and synthetic routes to be as safe as possible. Consider the hazards of all substances handled during the reaction, including waste.</p>	
5. Safer solvents and auxiliaries		<p><b>5. SAFER SOLVENTS &amp; AUXILIARIES</b></p>  <p>Choose the safest solvent available for any given step. Minimize the total amount of solvents and auxiliary substances used, as these make up a large percentage of the total waste created.</p>	
6. Design for energy efficiency		<p><b>6. DESIGN FOR ENERGY EFFICIENCY</b></p>  <p>Choose the least energy-intensive chemical route. Avoid heating and cooling, as well as pressurized and vacuum conditions (i.e. ambient temperature &amp; pressure are optimal).</p>	MW
7. Use of renewable feedstocks		<p><b>7. USE OF RENEWABLE FEEDSTOCKS</b></p>  <p>Use chemicals which are made from renewable (i.e. plant-based) sources, rather than other, equivalent chemicals originating from petrochemical sources.</p>	NIRS & MW
8. Reduce derivatives		<p><b>8. REDUCE DERIVATIVES</b></p>  <p>Minimize the use of temporary derivatives such as protecting groups. Avoid derivatives to reduce reaction steps, resources required, and waste created.</p>	MW
11. Real time pollution prevention		<p><b>11. REAL-TIME POLLUTION PREVENTION</b></p>  <p>Monitor chemical reactions in real-time as they occur to prevent the formation and release of any potentially hazardous and polluting substances.</p>	NIRS
12. Safer chemistry for accident preventing		<p><b>12. SAFER CHEMISTRY FOR ACCIDENT PREVENTION</b></p>  <p>Choose and develop chemical procedures that are safer and inherently minimize the risk of accidents. Know the possible risks and assess them beforehand.</p>	MW
 <p>© COMPOUND INTEREST 2015; WWW.COMPOUNDCHEM.COM Shared under a CC Attribution-NonCommercial-NoDerivatives licence.</p>			

Table (3) green chemistry principal

## Appendix of Chapter 4

NIR spectra of LGA in variable temperature

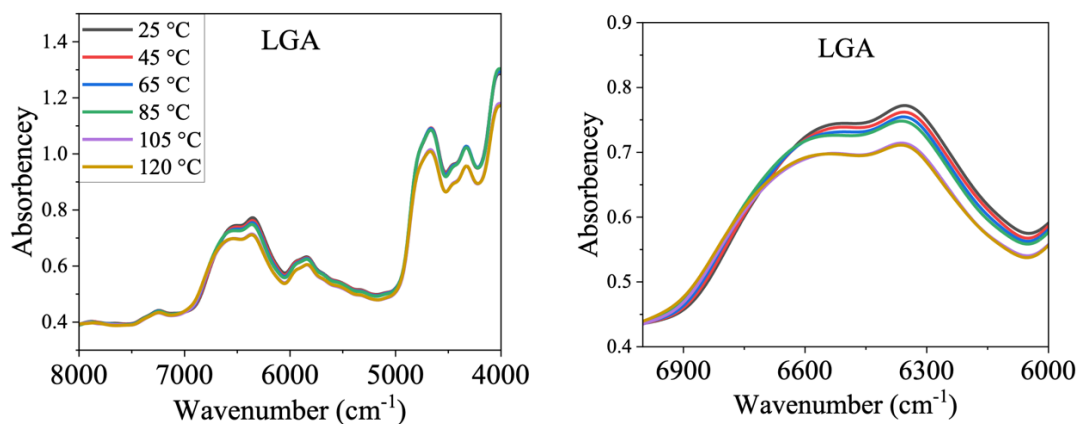


Figure (A.4.1) NIR spectra of LGA in variable temperature

STA analysis of LGA

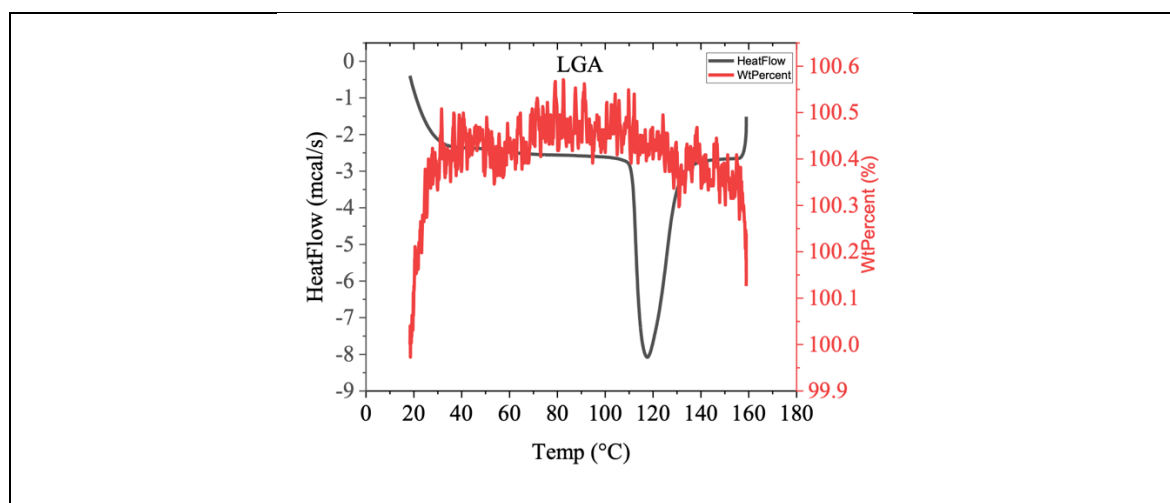
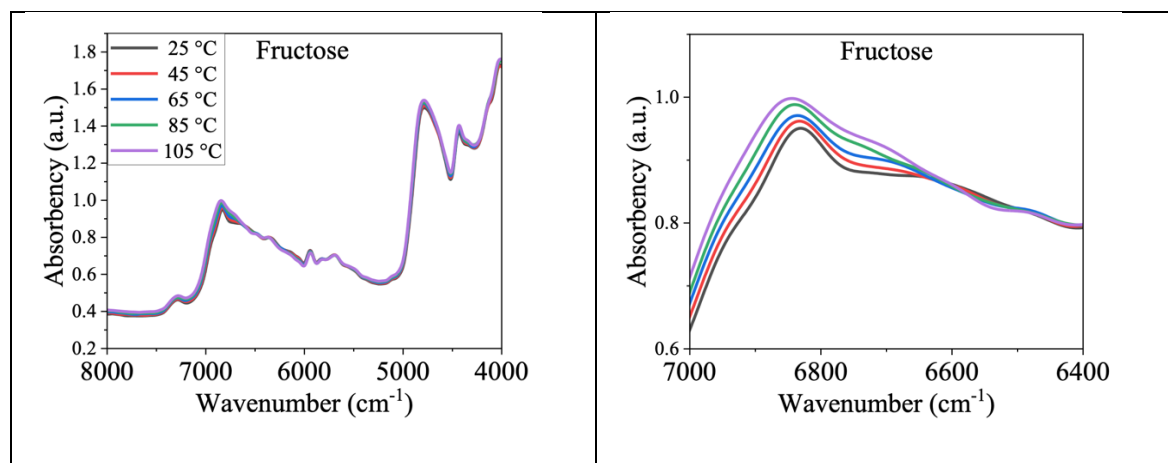


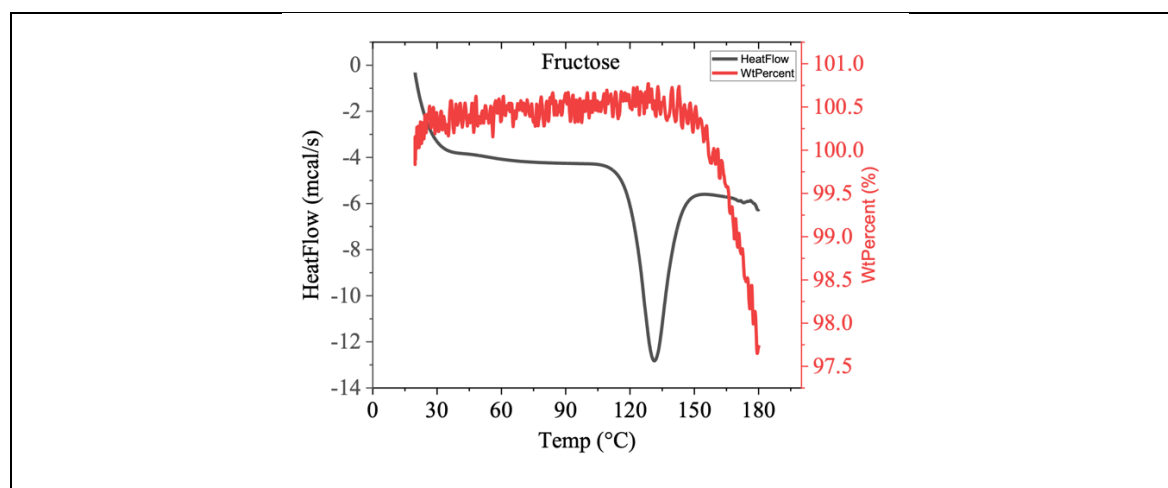
Figure (A.4.2) STA analysis of LGA

Although STA result shows heat flow change at above 120 °C which indicates the lose of moisture, weight did not show any change. It suggests that the LGA sample contain no moisture or very niglihtable amount of moisture which did not affect the hydrogen bonding activities in the NIRS

## NIR spectra of fructose in variable temperature

*Figure (A.4.3) STA analysis of LGA*

## STA analysis of fructose

*Figure (A.4.4) STA analysis of fructose*

Similarly, STA result for fructose sample shows heat flow change at above 120 °C which indicates the lose of moisture, 2.5% weight loss was detected. It suggests that the LGA sample contain some moisture which may affect the hydrogen bonding activities in the NIRS.

## Appendix of Chapter 5

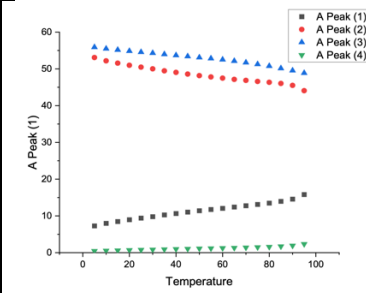
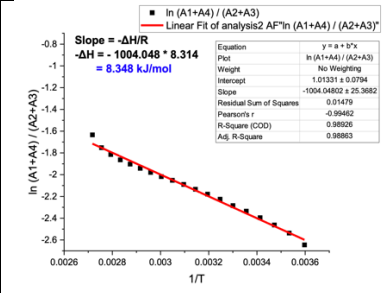
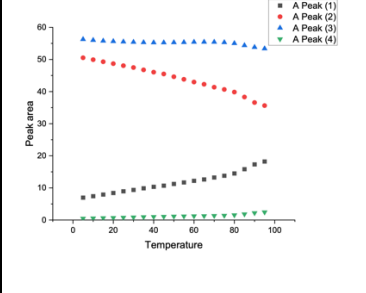
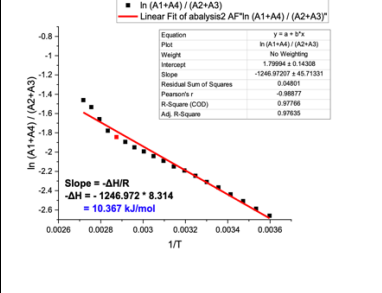
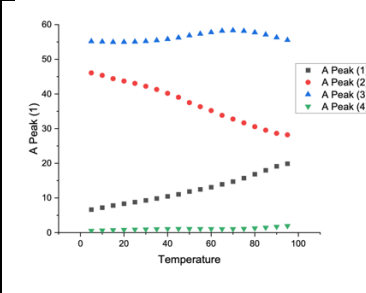
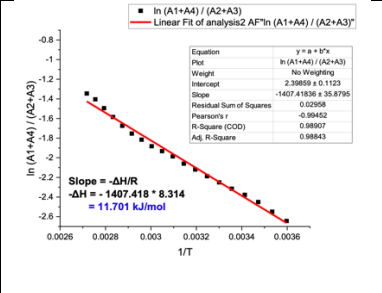
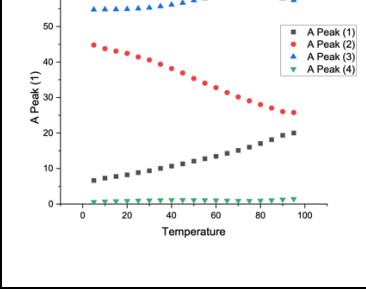
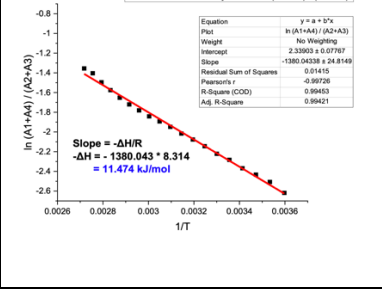
### LGO in water

Table (A.5.1)  $\Delta H$  for the different concentrations of LGO calculate by Van't Hoff equation based on the deconvoluted bands of OH 1<sup>st</sup> overtone

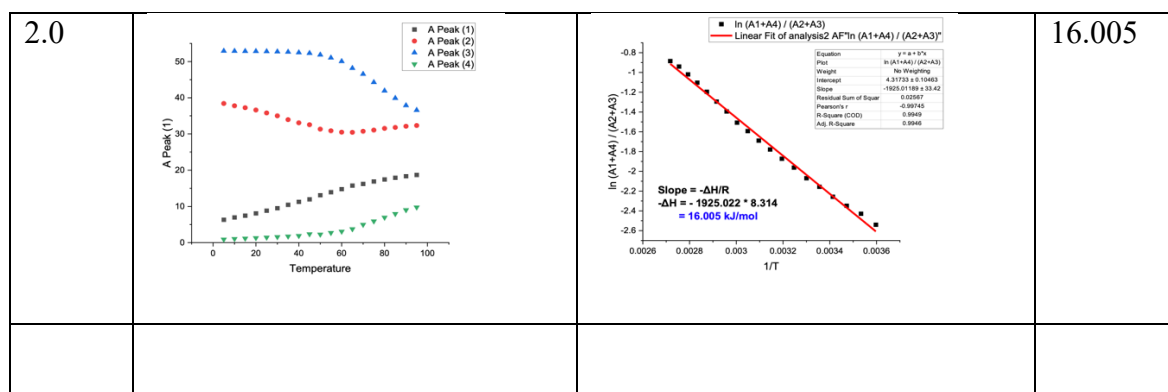
Conce (molal)	Bands deconvolution	Van't Hoff equation	$\Delta H$ (KJ/mol)
0.04			8.568
0.08			8.239
0.4			8.920, 21.907
0.8			10.152, 21.393

## Cyrene in water

Table (A.5.2)  $\Delta H$  for the different concentrations of Cyrene calculate by Van't Hoff equation based on the deconvoluted bands of OH 1<sup>st</sup> overtone

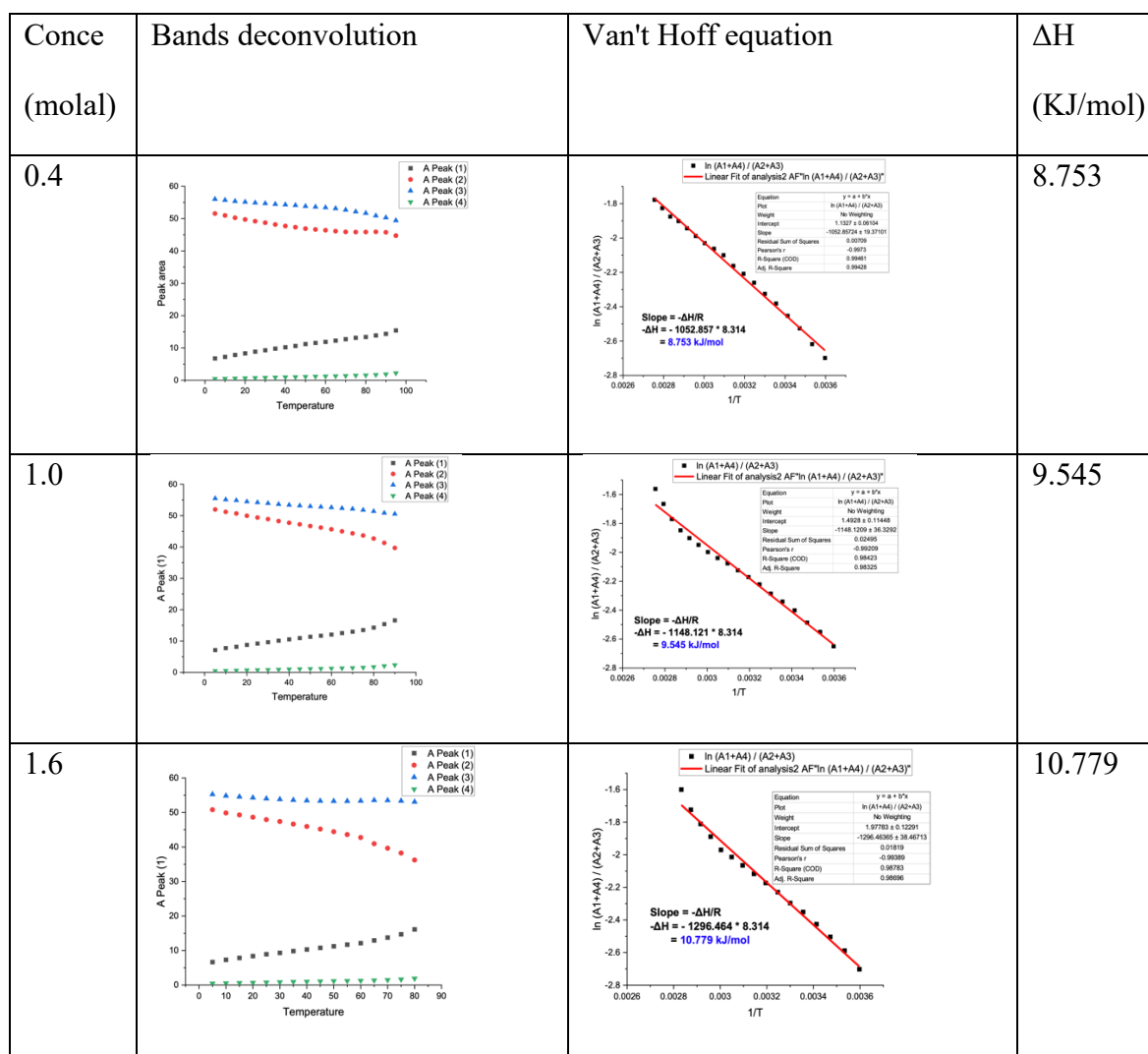
Conce (molal)	Bands deconvolution	Van't Hoff equation	$\Delta H$ (KJ/mol)
0.04			8.348
0.4			10.367 or 9.211 below 80C
0.8			11.701
1.0			11.474

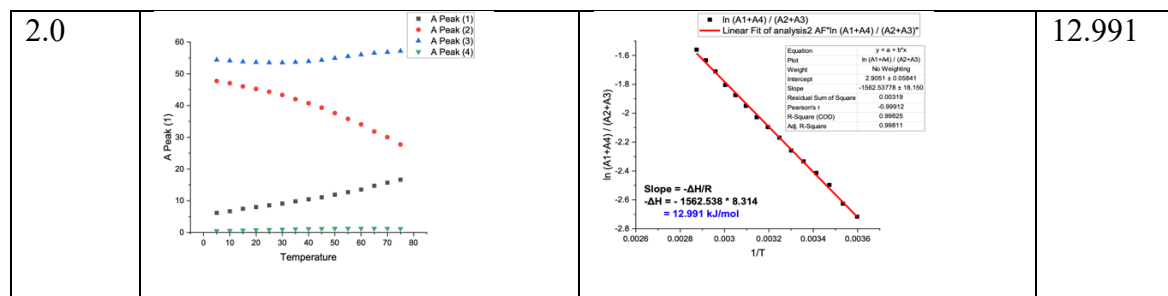




MEK in water

Table (A.5.3)  $\Delta H$  for the different concentrations of MEK calculate by Van't Hoff equation based on the deconvoluted bands of OH 1<sup>st</sup> overtone





NMR spectroscopy for LGO : water interaction at variable temperatures

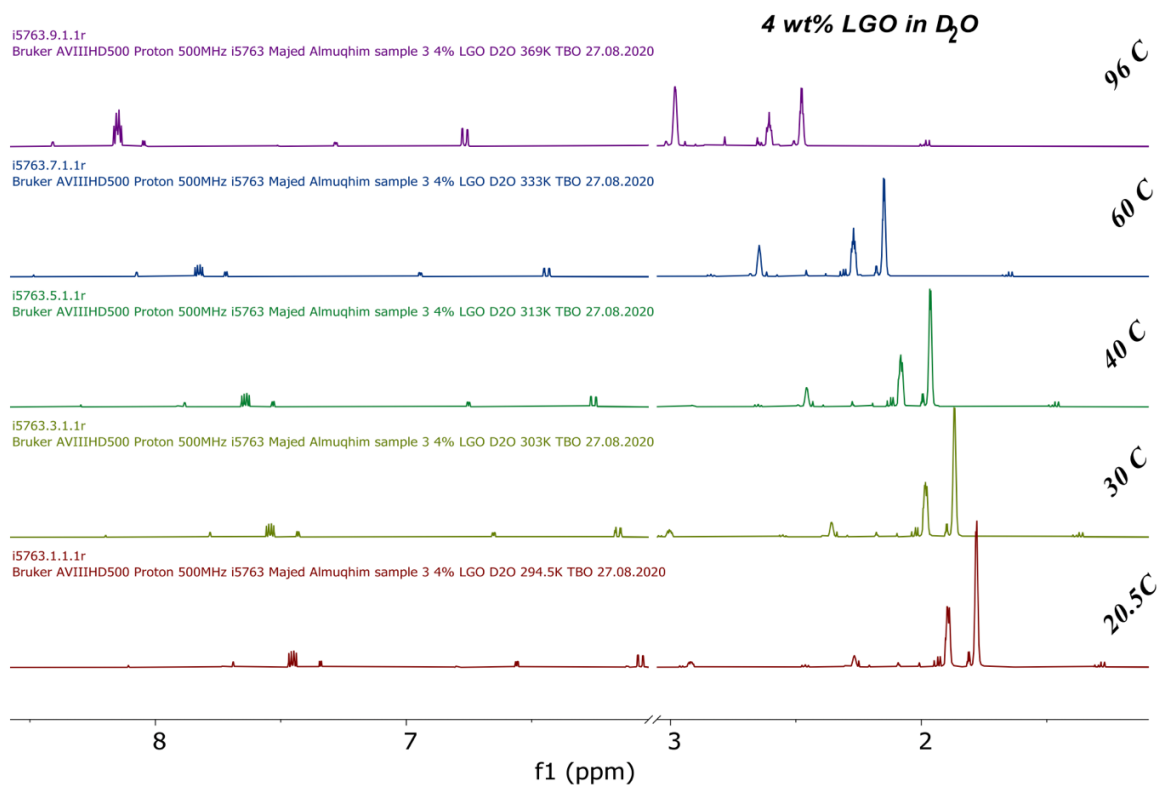


Figure (A.5.1) <sup>1</sup>H NMR stacked spectra of 4 wt% LGO in D<sub>2</sub>O in variable temperatures

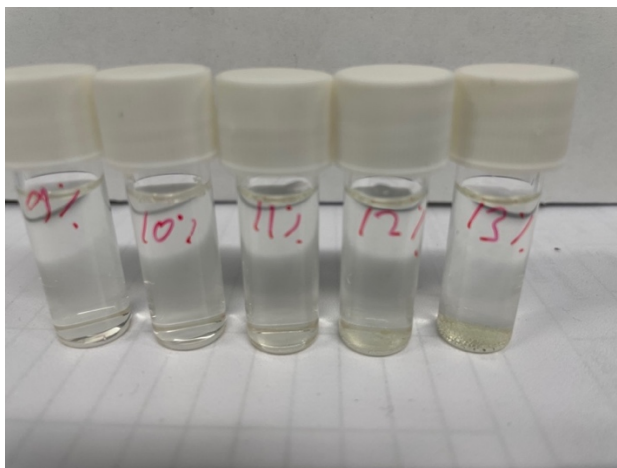


Figure (A.5.2) wt% LGO in water is the maximum concentration

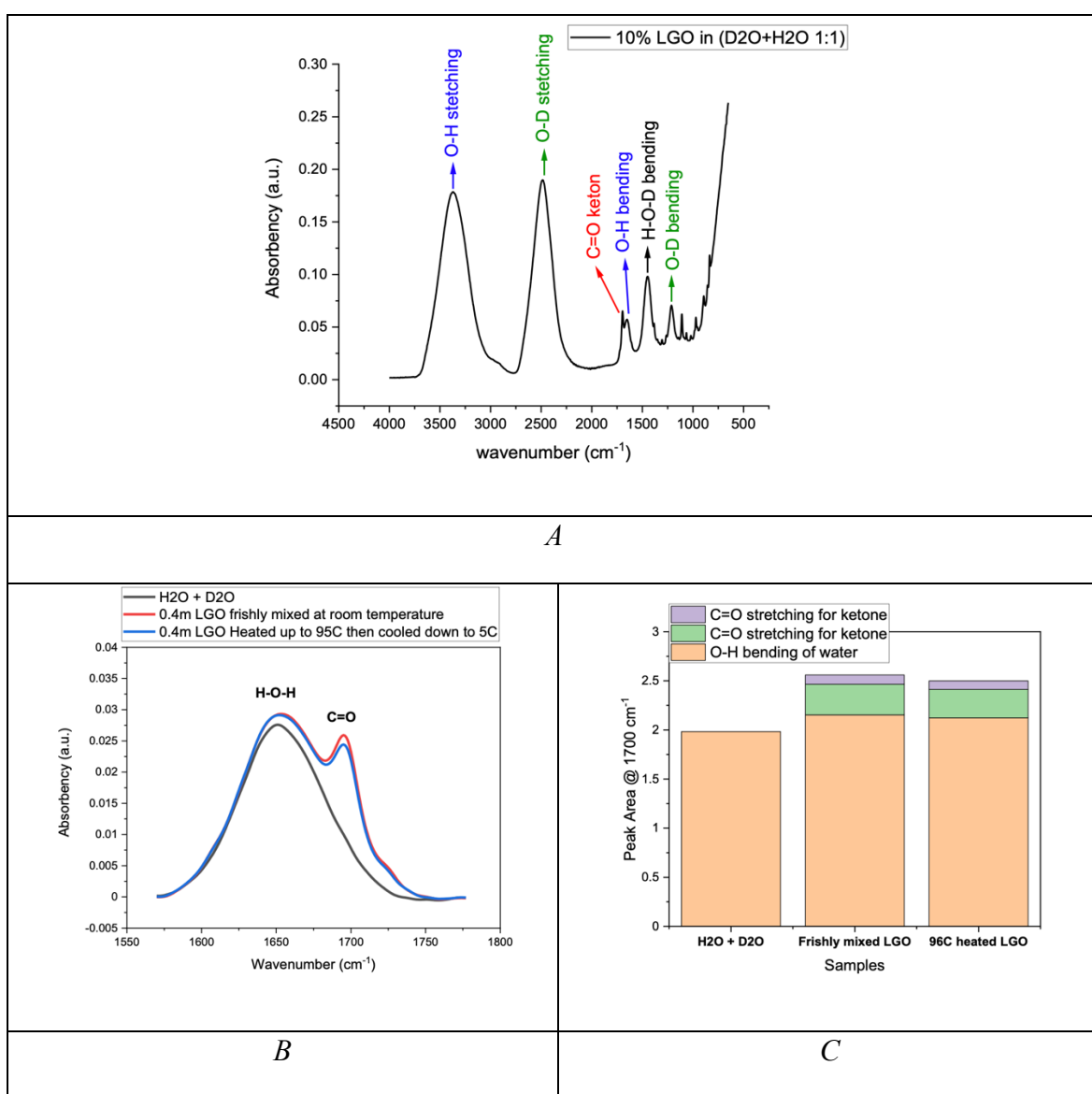


Figure (A.5.3) MIRS for (A) 10 wt% LGO in 1:1 ratio D<sub>2</sub>O and H<sub>2</sub>O (B) and (C) the band area of the deconvoluted bands

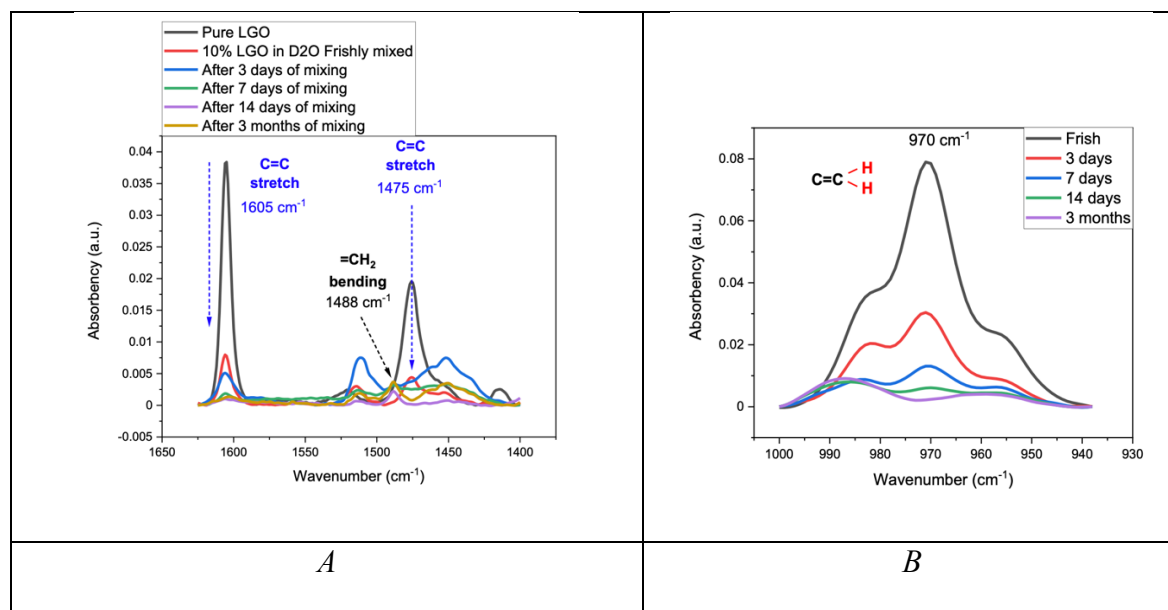


Figure (A.5.4) MIR spectra of 10 wt% LGO in D<sub>2</sub>O in different days

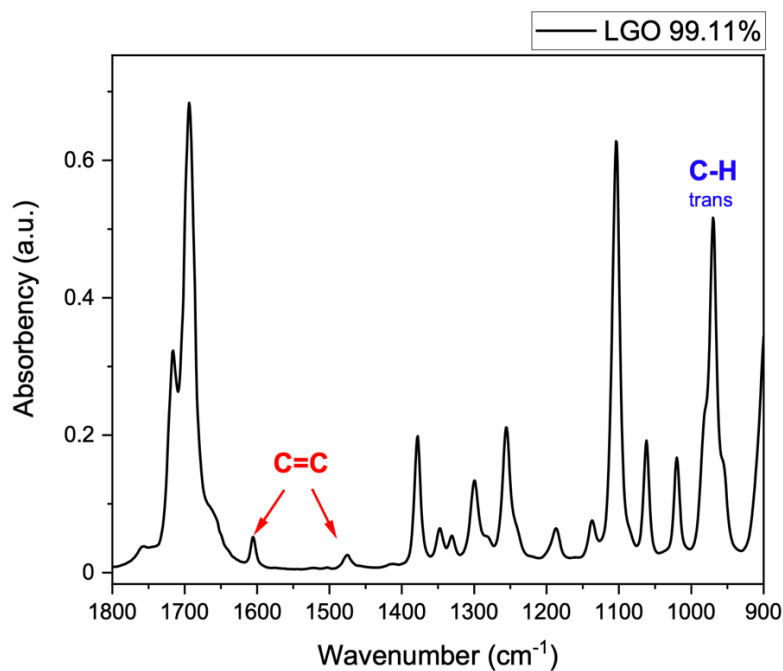


Figure (A.5.5) MIR spectrum of pure LGO

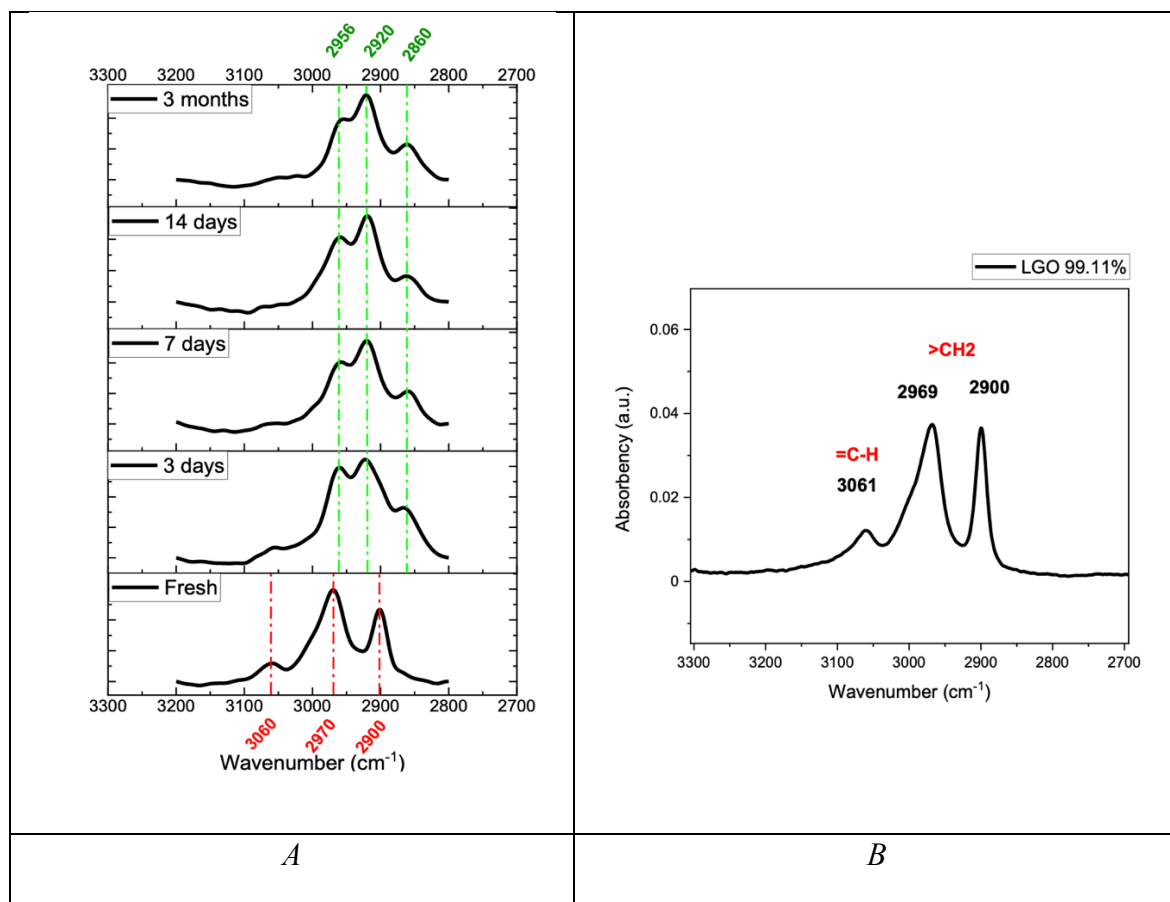


Figure (A.5.6) MIR spectra of (A) diluted LGO (10 wt%) in water in different days and (B) pure LGO

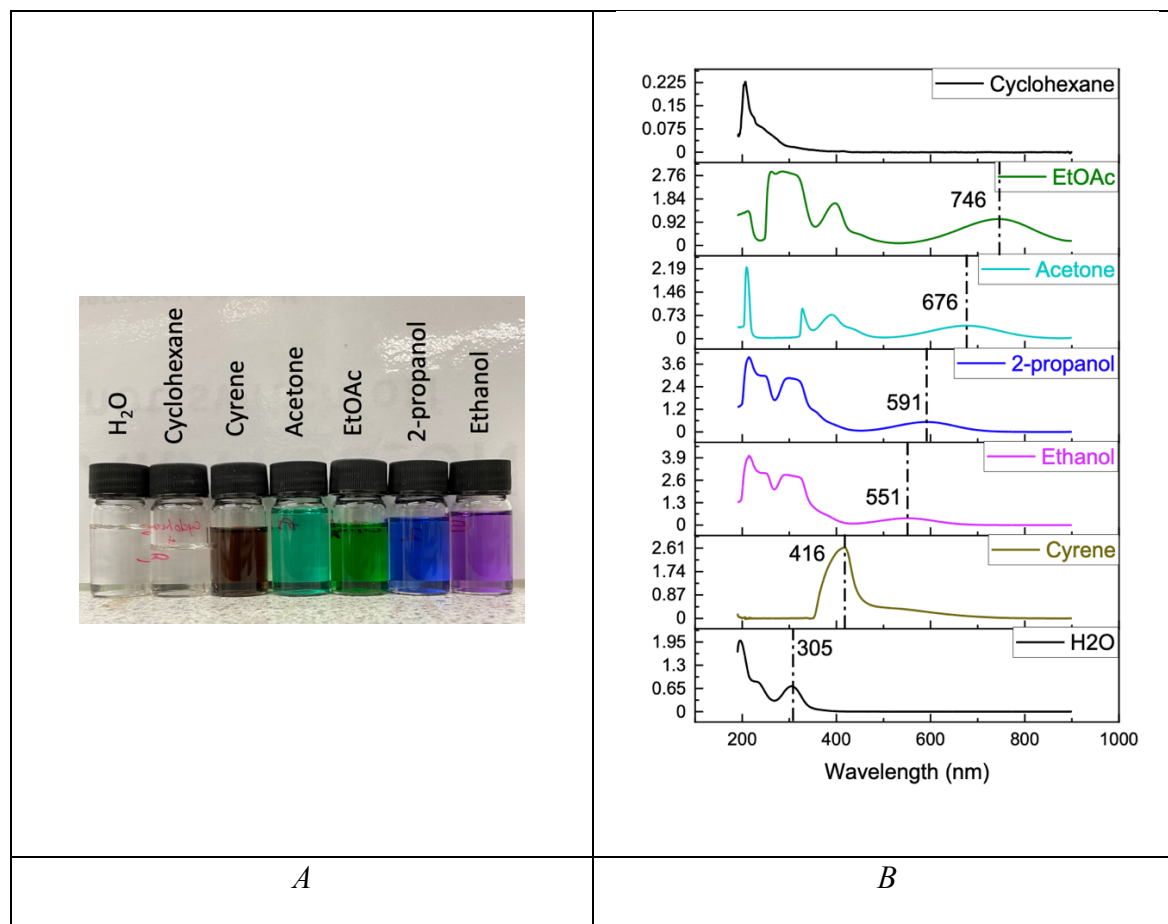


Figure (A.5.7) Reichardt's dye dissolved in different solvents showing (A) different colours and (B) different UV-Vis spectra

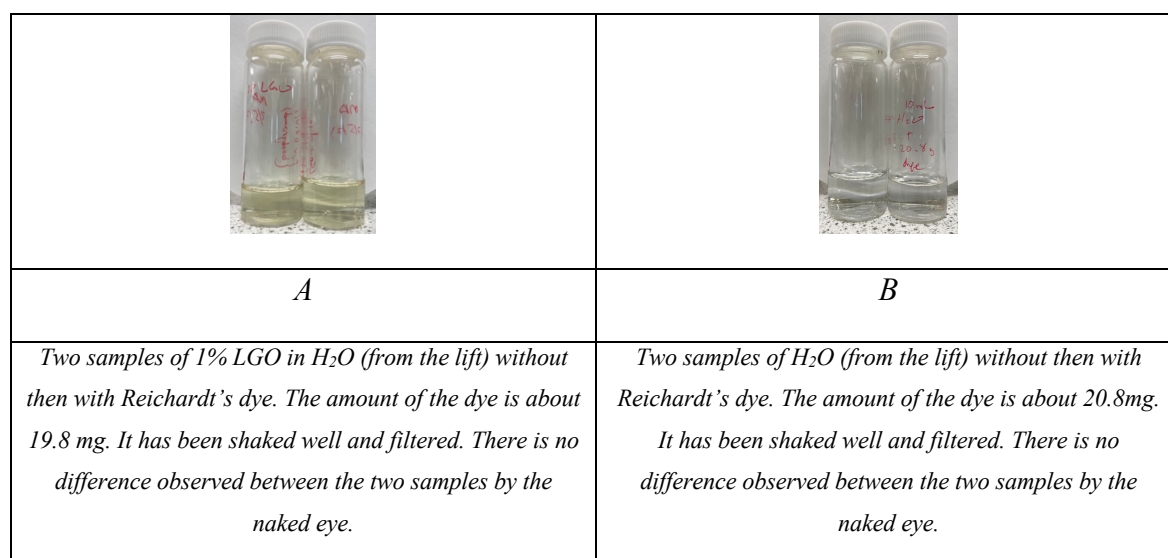


Figure (A.5.8) Reichardt's dye added to the sample before and after of (A) 1% LGO and (B) water

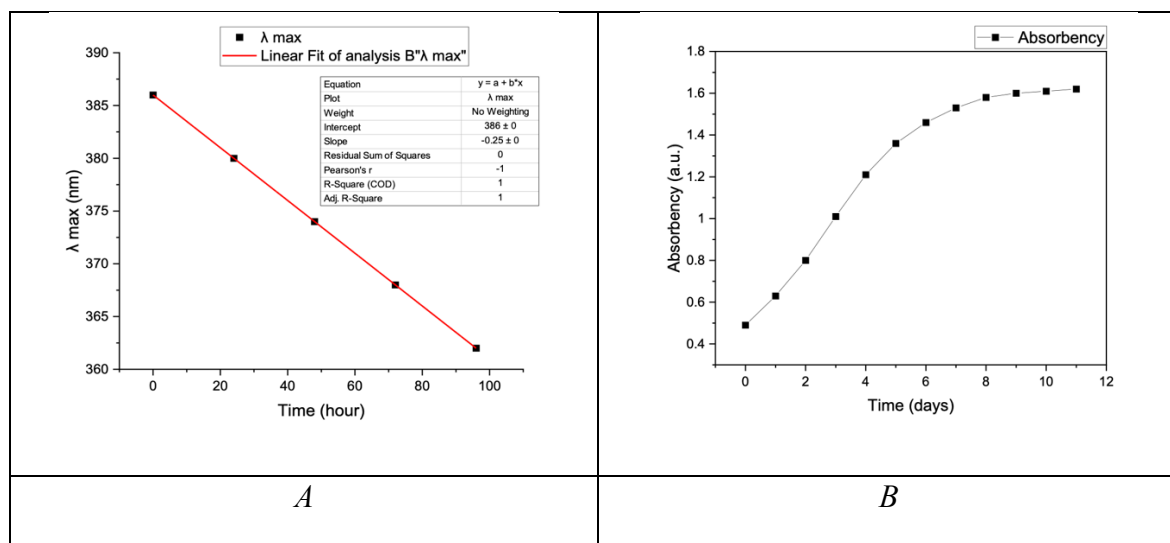


Figure (A.5.9) (A)  $\lambda_{max}$  shift of the Reichardt's dye dissolved in 1% LGO in the first four days which shows  $R^2$  of 1.00 and (B) the intensity of the band which grows with time in addition to the shifting

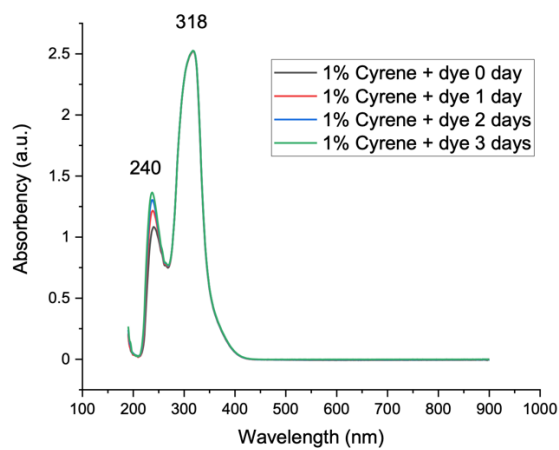


Figure (A.5.10) Reichardt's dye dissolved in 1% Cyrene in different days

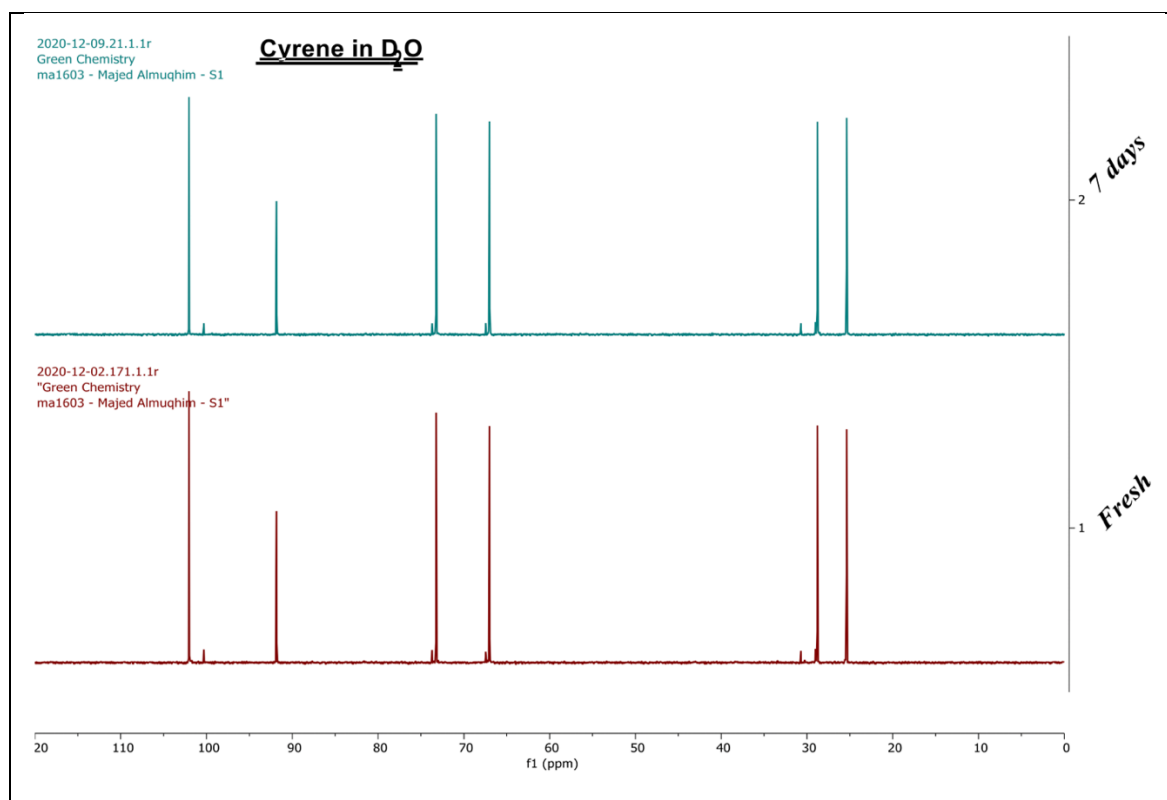


Figure (A.5.11)  $^{13}\text{C}$  NMR spectra overtime of Cyrene in  $\text{D}_2\text{O}$



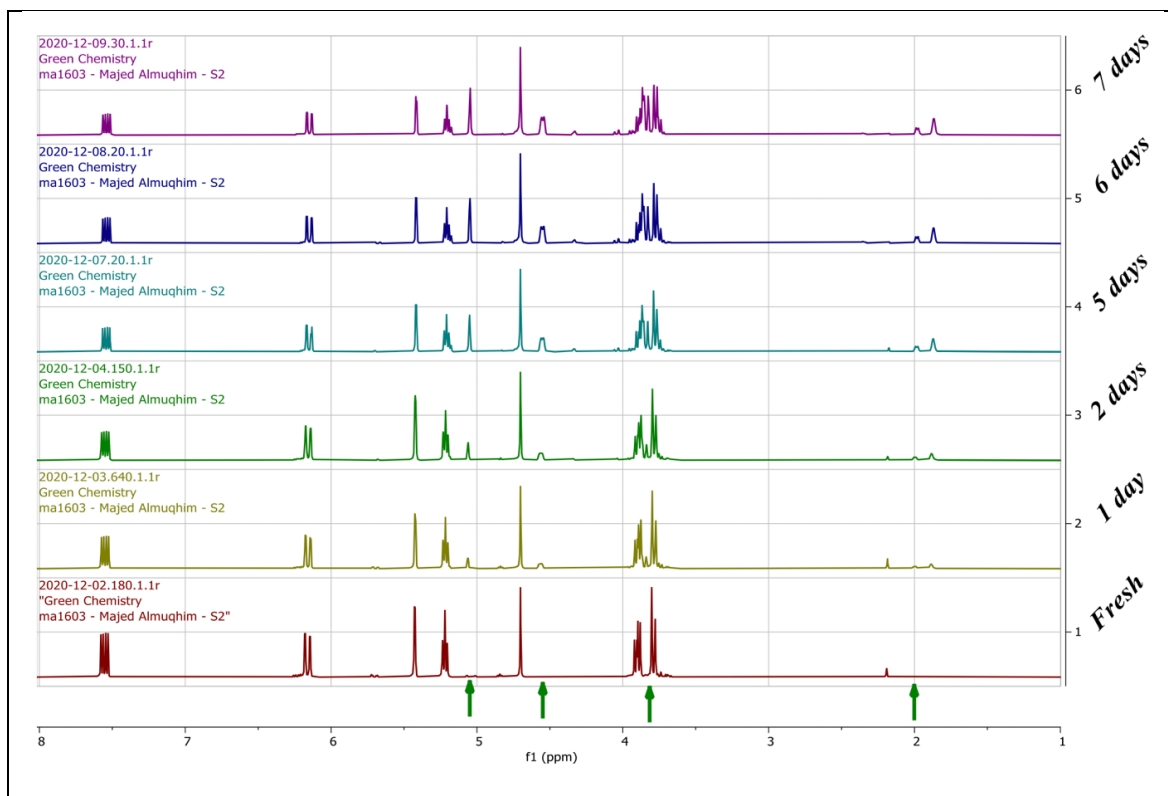


Figure (A.5.12)  $^1\text{H}$  NMR stacked spectra of LGO in  $\text{D}_2\text{O}$  by time

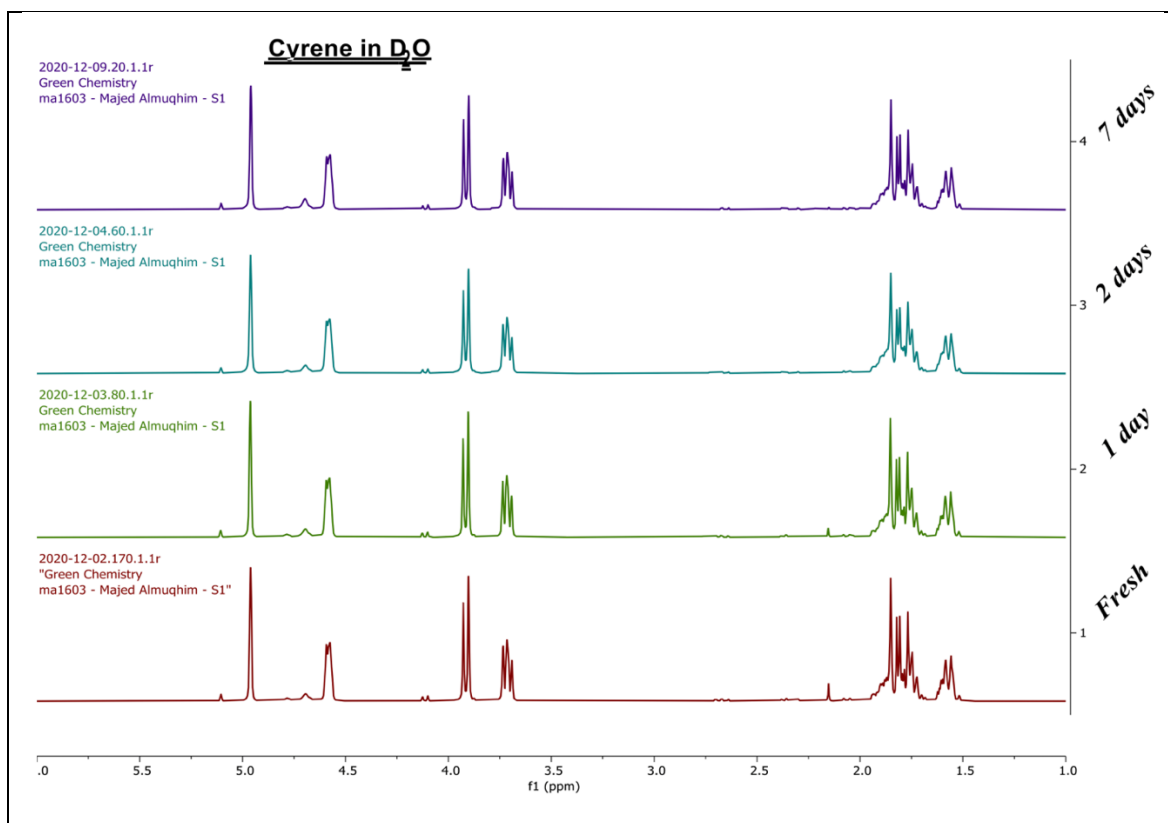


Figure (A.5.13)  $^1\text{H}$  NMR spectra overtime of LGO in  $\text{D}_2\text{O}$

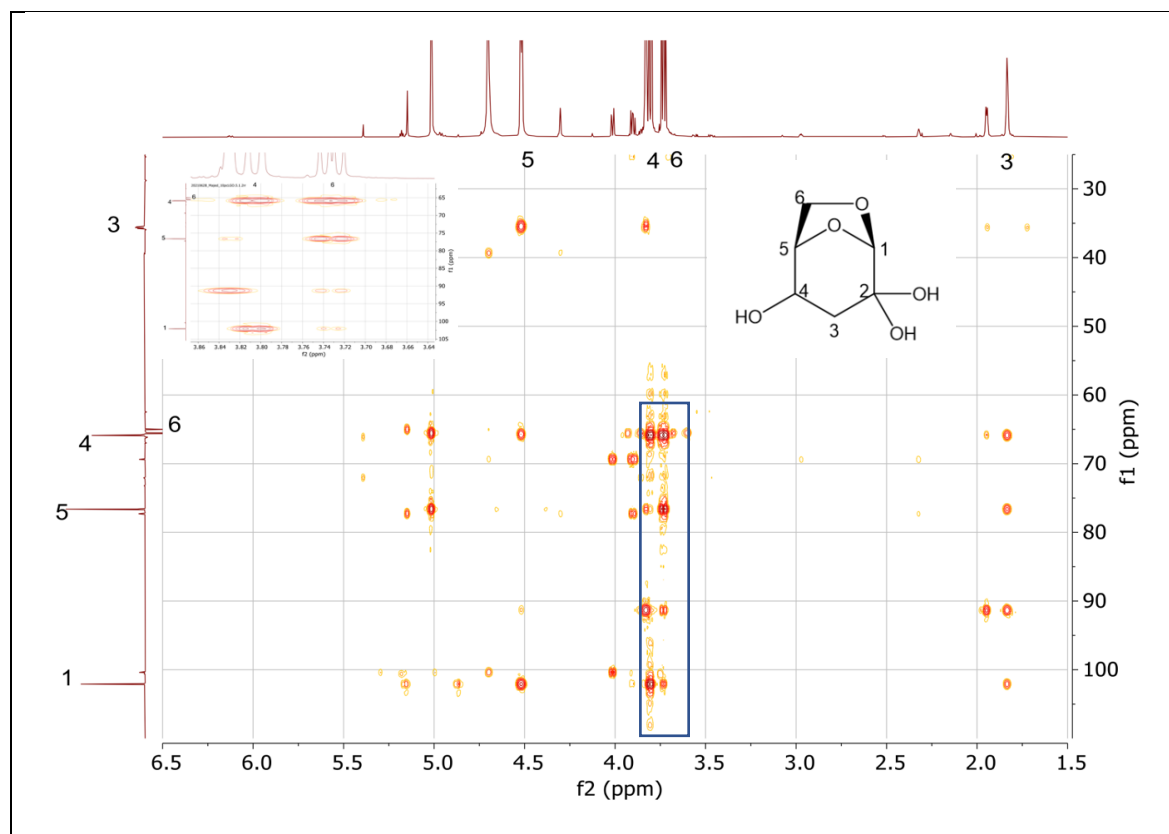


Figure (A.5.14) H-C HSQC spectrum of LGO in D<sub>2</sub>O. Sample was prepared 13/04/2021, analysed at 27/04/2021. 14 days old

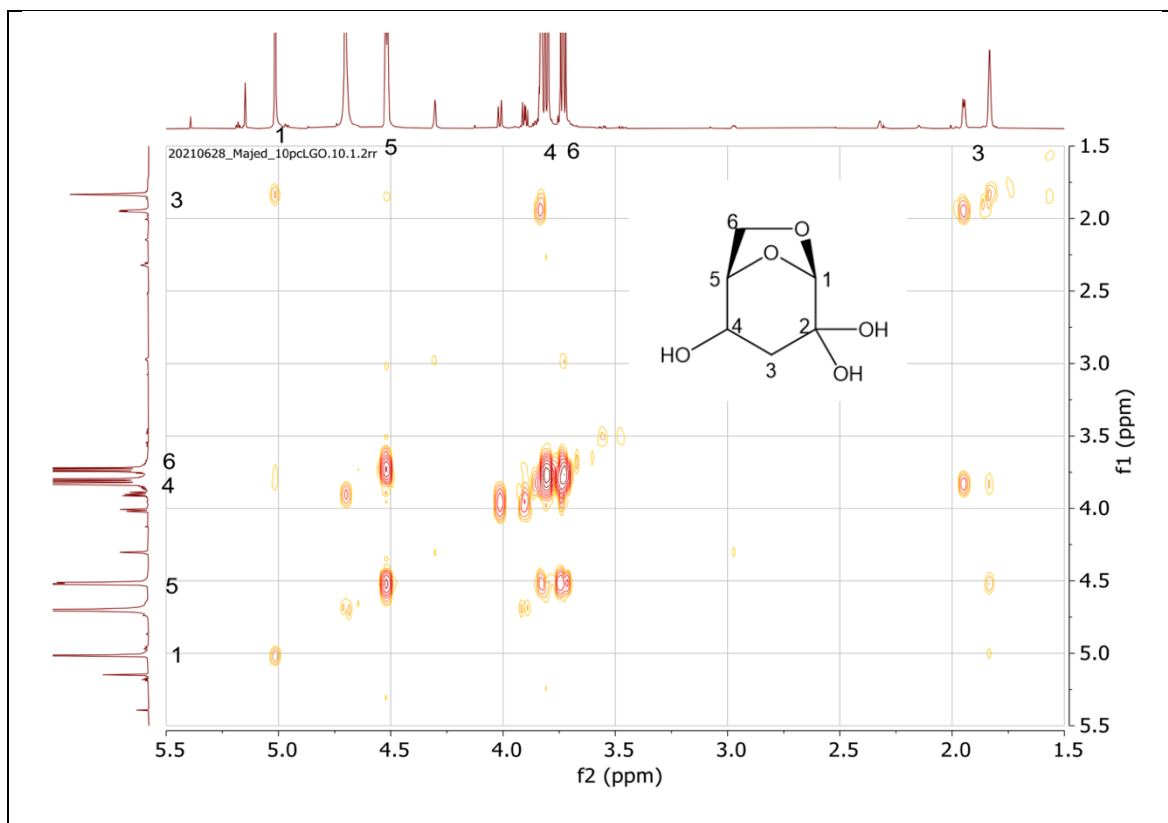


Figure (A.5.15) H-H HSQC spectrum of LGO in D<sub>2</sub>O (triol)

Figure (A.5.14) of H-C HSQC spectrum of LGO in D<sub>2</sub>O helps identify which proton corresponds to which carbon, and ultimately detect the new species formed.

A closer look at <sup>1</sup>H NMR spectroscopy in the range of 4.1 – 3.6 ppm in Figure (A.5.16) indicates that a new proton appeared at 3.85 ppm, which is associated with the proton of carbon 4 when a hydroxyl group attached to it after a few days of mixing the solution. It overlapped with the proton of carbon 6. Before breaking the alkene bond between carbon 3 and 4, peaks at 7.2 and 6.2 ppm only appeared for these carbon positions. In addition, other overlapped peaks with the two protons of carbon 6 can be identified, as previously discussed in chapter 5 about (exo- and endo-isomers). The overlapped peaks are caused by a new product of LGO affecting the position of these protons as well as a possibility of diastereomer species of LGO, diol and triol LGO. This group of bands becomes complicated with time, making the data analysis about integration or coupling of this region more challenging. An investigation of the variable temperature of the same sample may help interpret some overlapped bands in this region, as discussed in chapter 5 and 6. Note that all bands in this region tended to shift slightly towards lower numbers as time increased.

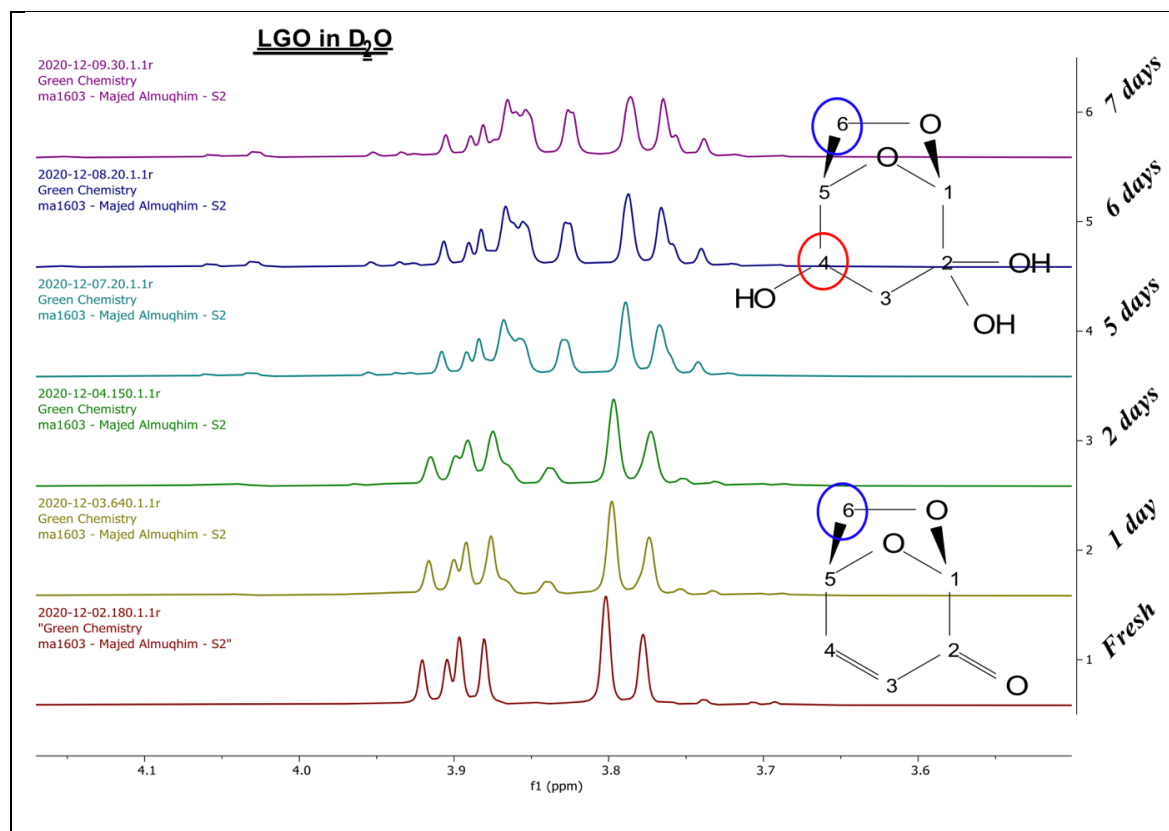


Figure (A.5.16)  $^1\text{H}$  NMR stacked spectra of LGO in  $\text{D}_2\text{O}$  during time at range of 4.1 – 3.6 ppm

Peaks at 1.9 and 2.0 ppm are due to the new born of another proton at carbon 3. See *Figure (A.5.17)*. The carbon at this position was an alkene and its proton appears only at  $\sim 6$  ppm. When the compound undergoes a conjugated system due to interaction with water, the alkene double bond is broken and the carbon at this position is linked to two protons.

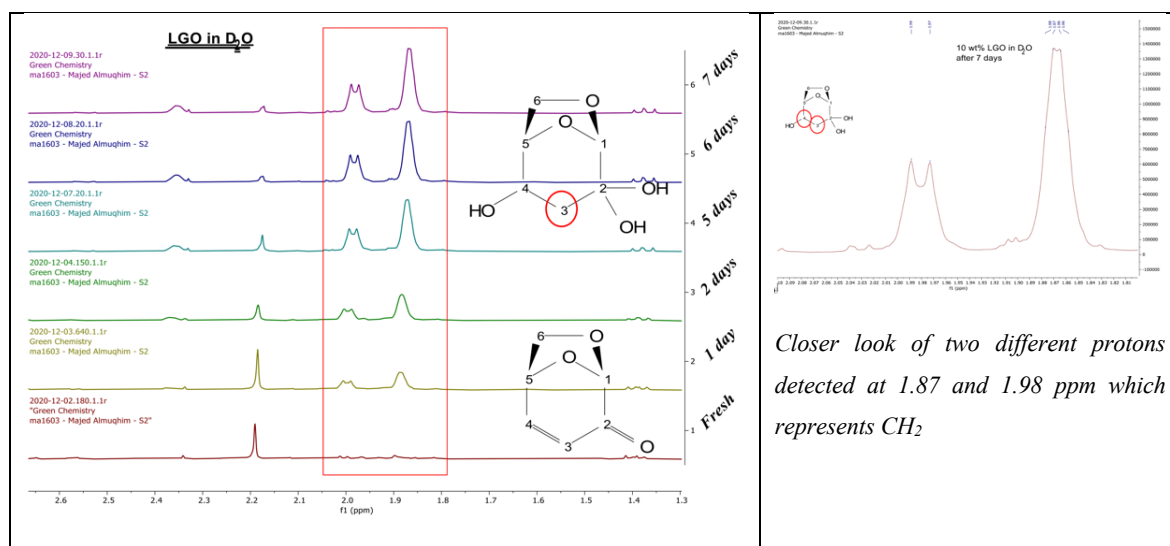


Figure (A.5.17)  $^1\text{H}$  NMR stacked spectra of LGO in  $\text{D}_2\text{O}$  during time at range of 2.6 – 1.3 ppm

Figure (A.5.17) shows  $^1\text{H}$  NMR spectra for LGO in water after 7 days of preparing the mixture. Two different protons were detected at 1.87 and 1.98 ppm, representing  $\text{CH}_2$  protons on C3. Figure (A.5.18) illustrates the difference between the  $^1\text{H}$  NMR spectrum of 10 wt% LGO in water freshly mixed and after 7 days. It shows new protons ( $\text{CH}_2$ ) of C3, as discussed in chapter 5. There is also another new peak at 5.05 ppm representing another proton ( $\text{CH}$ ) of C5. These findings support the assumption that LGO converted to triol. Furthermore, the peaks at 1.78 and 1.98 ppm of protons bonded to carbon 3 as shown in Figure (A.5.17), are coupled with the new peak that appeared after 7 days at 35.7 ppm of  $^{13}\text{C}$  NMR spectroscopy in Figure 5.18. The evidence of this coupling can be shown in Figure (A.5.14) of H-C HSQC spectrum.

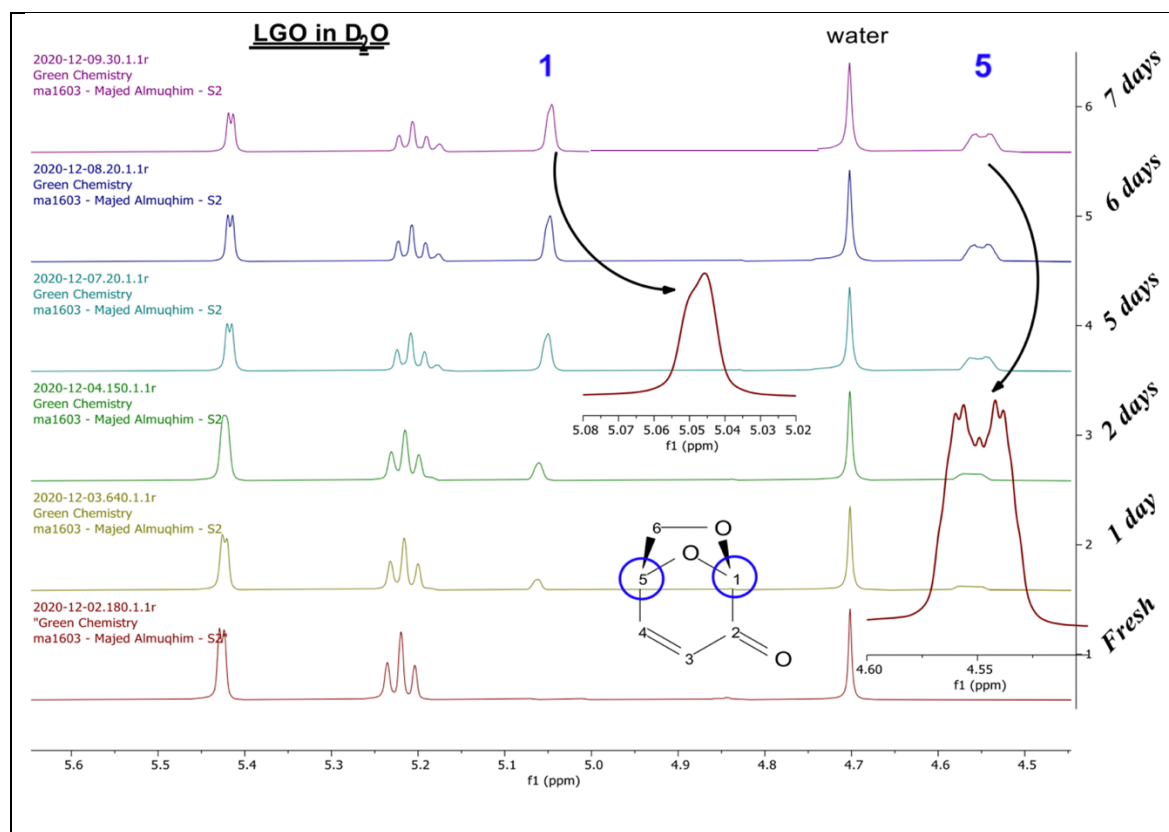


Figure (A.5.18)  $^1\text{H}$  NMR stacked spectra of LGO in  $\text{D}_2\text{O}$  during time at range of 5.6 – 4.5 ppm

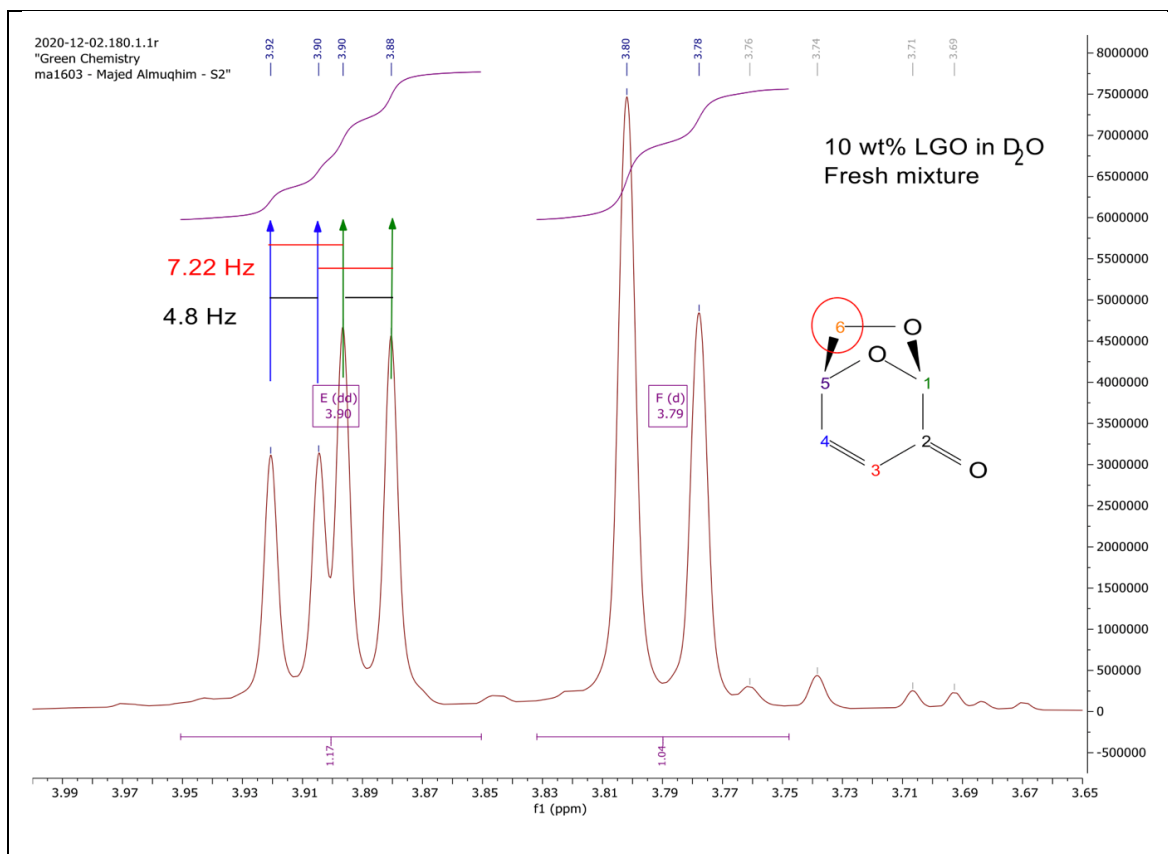


Figure (A.5.19)  $^1\text{H}$  NMR spectra for LGO in water of fresh mixture. Two groups of peaks respectively centred at 3.9 and 3.8 ppm of (exo, endo) protons of carbon number 6 were detected, and coupling was calculated

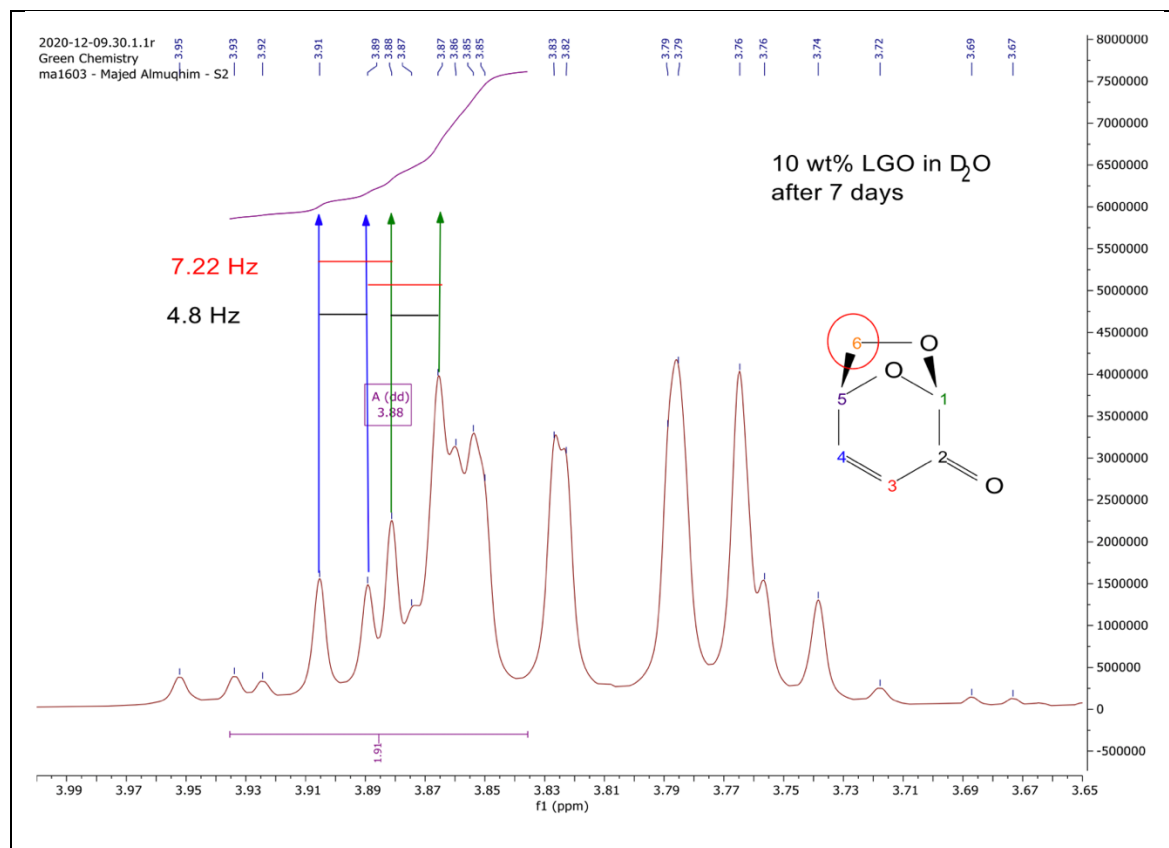


Figure (A.5.20)  $^1\text{H}$  NMR spectra for LGO in water after 7 days of preparing the mixture. New species, and some of original ones, were detected in the spectrum at the range 3.7 – 4 ppm. The spectrum overlapped with new species. The (dd) peak at 3.88 matched the coupling of exo proton of previous spectrum. Coupling of peak 3.79 was not matched



## Appendix of Chapter 6

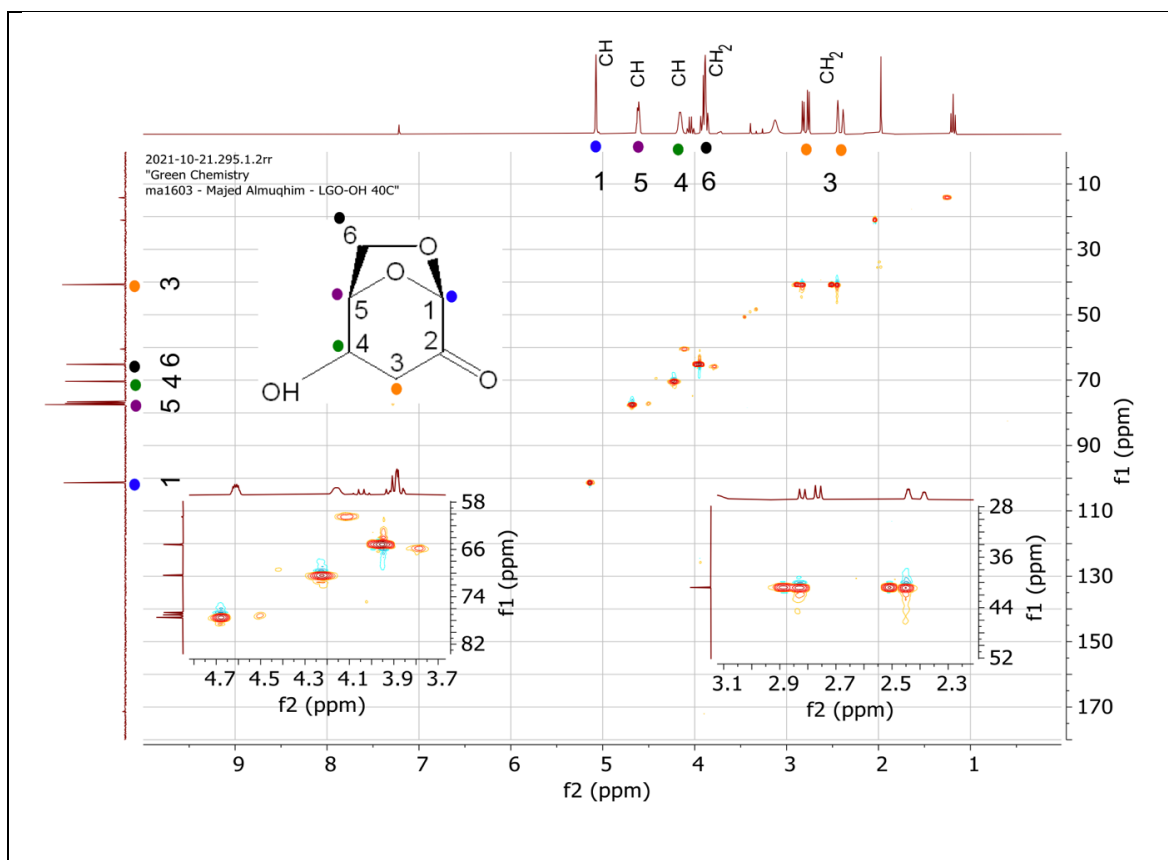


Figure (A.6.1) 2D  $^1\text{H}+^{13}\text{C}$  HSQC NMR spectrum for MHC in  $\text{CDCl}_3$ . The MHC was produced from LGO dissolved in  $\text{H}_2\text{O}$

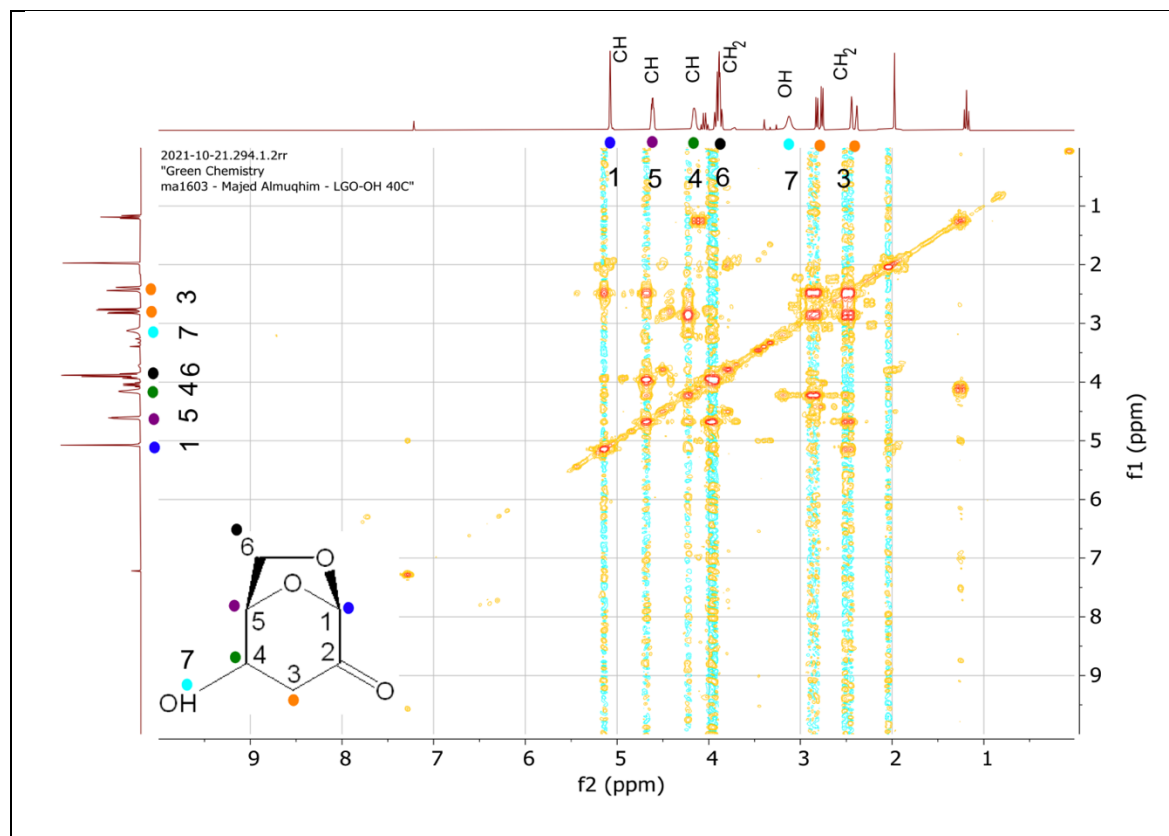


Figure (A.6.2)  $^1\text{H}$  COSY NMR spectrum for MHC in  $\text{CDCl}_3$ . The MHC was produced from LGO dissolved in  $\text{H}_2\text{O}$


Table (A.6.1) CHN analysis

sample	Calculated (%) for			MW	Formula
	<i>C</i>	<i>H</i>	<i>others</i>		
<b>Cyrene</b>					
(test 1)	55.8	6.23	37.97		
(test 2)	55.56	6.11	38.33		
(calculated)	56.25	6.25	37.5	128	C <sub>6</sub> H <sub>8</sub> O <sub>3</sub>
<b>LGO</b>					
(test 1)	56.21	5.12	38.67		
(test 2)	56.01	4.99	39.00		
(calculated)	57.14	4.76	38.09	126	C <sub>6</sub> H <sub>6</sub> O <sub>3</sub>
<b>LGO-OH 45</b>					
(test 1)	49.12	5.22	45.57		
(test 2)	48.62	5.62	45.76		
(calculated)	45.00	5.00	50.00	160	C <sub>6</sub> H <sub>8</sub> O <sub>5</sub>
(calculated)	50.00	5.56	44.44	144	C <sub>6</sub> H <sub>8</sub> O <sub>4</sub>
<b>Comp (1)</b>					
(test 1)	48.71	5.81	45.48		
(test 2)	48.55	5.26	46.19		
(calculated)	45.00	5.00	50.00	160	C <sub>6</sub> H <sub>8</sub> O <sub>5</sub>
(calculated)	50.00	5.56	44.44	144	C <sub>6</sub> H <sub>8</sub> O <sub>4</sub>
<b>Comp (2)</b>					
(test 1)	48.71	5.81	45.48		
(test 2)	48.55	5.26	46.19		
(calculated)	57.14	4.76	38.09	126	C <sub>6</sub> H <sub>6</sub> O <sub>3</sub>




## Posters

### Poster presented for the university of York:




**Green Chemistry**  
Centre of Excellence

# NIR Spectroscopy as a Greener Tool to Control Microwave Hydrolysis




UNIVERSITY of York



**Maied Almughim**, Dr. Vitaliy Budarin, Dr. Alice Fan and Professor James Clark

### Introduction



**BIOMASS MICROWAVE HYDROLYSIS**

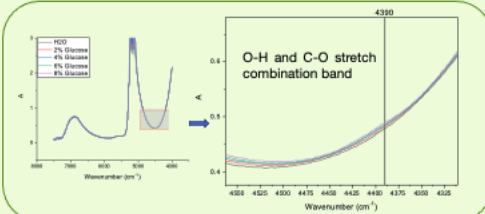
The aim of this work is to provide a framework of better process analysis for biomass conversion. The conversion of bio-resources including food supply chain wastes and other forms of biomass to achieve better selectivity to the desired product(s), higher carbon efficiencies and less waste is highly desirable from green chemistry prospective.

### Results

There are some promising results as shown below:

• **Glucose:**

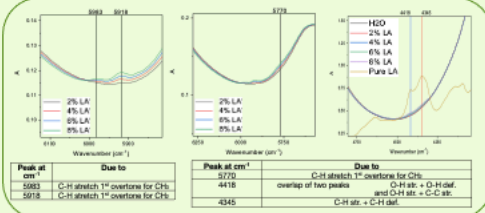
C1=CC=C(C=C1)O



O-H and C-O stretch combination band

• **Levulinic Acid (LA):**

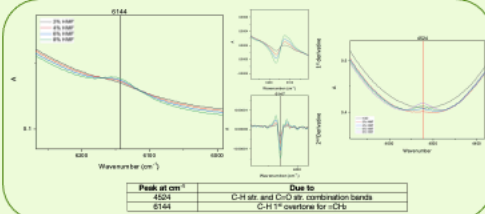
CC(=O)C(O)C(=O)O



Peak at cm <sup>-1</sup>	Due to	Peak at cm <sup>-1</sup>	Due to
5083	C-H stretch 1 <sup>st</sup> overtone for CH <sub>3</sub>	3170	C-H stretch 1 <sup>st</sup> overtone for CH <sub>2</sub>
5918	C-H stretch 1 <sup>st</sup> overtone for CH <sub>2</sub>	4416	overlap of two peaks: C-H str. + O-H def. and C-H str. + C-C str.
		4345	C-H str. + C-H def.

• **5-Hydroxymethyl-furfural (HMF):**

O=C1C=CC(=O)O1




Peak at cm <sup>-1</sup>	Due to
4504	C-H str. and C=O str. combination bands
8144	C-H 1 <sup>st</sup> overtone for -CH <sub>2</sub>

### Methodology

**Microwave hydrolysis**


- Microwave is clean and efficient method for biomass conversion.
- Budarin *et al* and his group have achieved novelty using low temperature pyrolysis of wheat straw.<sup>2</sup>
- They produced bio-oil with desired properties such as lower acidity, Sulphur level and lower contents of alkali metal in addition to energy efficient.
- They produced different chemicals and obtained mixtures in simpler contents by using low temperature pyrolysis on microwave which is considered as an improvement in biomass conversion field.

Conventional heating



Furnace

Microwave volumetric heating

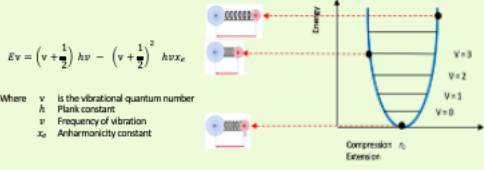


Microwave source

V. Budarin, P. Shuttleworth, M. De Bruin, T. Farnes, M. Cooper, H. Bland, G. Macquarrie, J. Clark

### Near-Infrared spectroscopy

- NIR spectroscopy is a simple, nondestructive and rapid method of analysis.<sup>3</sup>
- No sample preparation, no reagents, no solvents needed subsequently no waste.



Where  $v$  is the vibrational quantum number  
 $h$  Plank constant  
 $\nu$  Frequency of vibration  
 $x_e$  Anharmonicity constant

$$E_v = \left(v + \frac{1}{2}\right) h\nu - \left(v + \frac{1}{2}\right)^2 h\nu x_e$$

Where  $h$  Plank constant  
 $\nu$  Frequency of vibration  
 $c$  is speed of light


### Conclusion

- Using NIR showed promising results with this approach.
- Clearly the use of NIR spectroscopy with real time probe to control biomass conversion in quantitative analysis should be an ideal technique.
- This method represents a new approach in microwave hydrolysis.
- In terms of cost, waste, time saving, simplicity, green and sustainability, NIRS is a powerful method among other chemical methods.
- It merits further investigation the use of NIRS with low temperature microwave for biomass hydrolysis monitoring.

### References

- J. D. Sachs and K. Ben. *The Age of Sustainable Development*. Columbia University Press, 2015.
- V. Budarin, J. Clark, B. Langran, P. Shuttleworth, S. Breeden, A. Wilson, D. Macquarrie, K. Mikowski, J. Jones, T. Bridgeman and A. Ross. *Bioresource Technology*, 2009, **100**, 6064-6080.
- M. Lancaster. *Green Chemistry 3rd Edition: An Introductory Text*, Royal Society of Chemistry, 2016.
- C. E. Housecroft and E. C. Constable. *Chemistry: An Introduction to Organic, Inorganic and Physical Chemistry*. Prentice Hall, 2010.
- B. OSBORNE. *Analyst*, 1986, **113**, 263-267.


# Poster 2 presented in the 5th European Green and Sustainable Chemistry Conference EuGSC




**Green Chemistry**  
Centre of Excellence

## Near-Infrared Spectroscopy as an Analytical Tool for The Biorefinery

Majed Almuqhim, Dr. Alice Fan and Professor James Clark



UNIVERSITY  
of York



**Objective**

To optimise a greener analytical method for biomass conversion to chemicals by NIR real time monitoring of the process.

**Results**

**Qualitative & Quantitative**

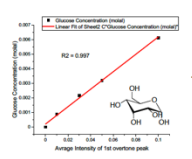


Figure 1(a). A linear regression of different concentrations of glucose with  $R^2$  of 0.997 using NIR

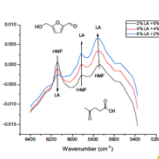


Figure 1(b). Clear differentiation between HMF and LA in different ratios using NIR

**Moisture Contents**

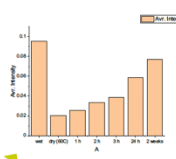


Figure 2(a). Sawdust sample when it is Heated and exposed to air

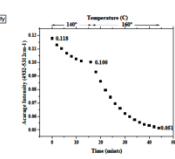


Figure 2(b). Water contents of a sugar when heated at different temperatures.

**Introduction**

Near infrared is an important tool among other instruments with its ability to be used as a real time technique. Transmittance, reflection and transflection probes can be connected for variable measurements. Data can be transferred by fibre-optic cables allowing for an in-line monitoring processes. Different parameters can be investigated instantly as well as chemical change during a reaction process. The probe can be built inside the reactor vessel to monitor the process in real time.

**Methodology**

**Near-infrared spectroscopy**  
NIR spectroscopy is a simple, nondestructive and rapid method of analysis.<sup>1</sup> No sample preparation, no reagents, no solvents needed subsequently no waste.

The principal of IR spectroscopy underlies the interaction between electromagnetic radiation and matter.<sup>2</sup> The vibration in bonds between atoms caused by IR radiation is stretching/compression. It is called **oscillation** of the bond. By subjecting the molecule to an energy (IR), a transition to **higher vibrational level** may occur. Tan et al studied the OH 1<sup>st</sup> overtone band of water and found how the sensitivity of this bond can give detailed information<sup>3</sup> which we can then use it to monitor the change in this bond when the water interacts with another molecule.

**Chemical Conversion**

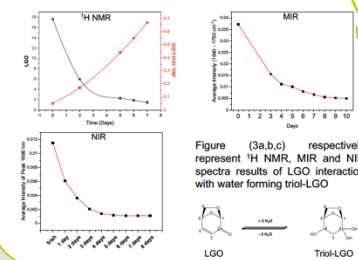


Figure (3a,b,c) respectively represent <sup>1</sup>H NMR, MIR and NIR spectra results of LGO interaction with water forming triol-LGO

**Temperature Change**

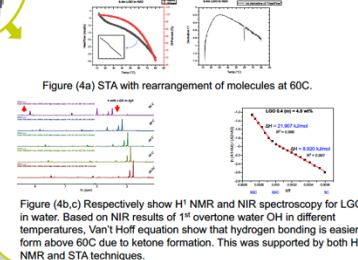


Figure (4a) STA with rearrangement of molecules at 60C.

Figure (4b,c) Respectively show <sup>1</sup>H NMR and NIR spectroscopy for LGO in water. Based on NIR results of 1<sup>st</sup> overtone water OH in different temperatures, Van't Hoff equation show that hydrogen bonding is easier to form above 60C due to ketone formation. This was supported by both <sup>1</sup>H NMR and STA techniques.

**Conclusion**

NIR is a multitask instrument and successfully used for real-time monitoring for variable parameters simultaneously saving time, money, chemicals and labour as well as it is eco friendly. By applying NIR it is possible to achieve several Green Chemistry Principles such as waste prevention, less hazardous chemical synthesis, safer solvents and auxiliaries, use of renewable feedstocks and real time pollution prevention.

**Acknowledgement**

The authors acknowledge FC Five Pty Ltd, BBI ReSolute and Circa Group for the support as well as Saudi Cultural Bureau for the scholarship fund.

**References**

1. M. Lascaris, *Green Chemistry 3rd Edition: An Introductory Text*, Royal Society of Chemistry, 2016
2. C. E. Sroog and E. C. Corns, *Chemistry: An Introduction to Organic, Inorganic and Physical Chemistry*, Prentice Hall, 2010
3. J. Tan, Y. Sun, L. Ma, H. Peng, Y. Guo, W. Gu and X. Shao, *Chemometrics and Intelligent Laboratory Systems*, 2020, 206, 104150



# Presentation in Renewable Resources Biorefinery 2022

(Presented by Professor James Clark)

## The Levoglucosenone (LGO) biorefinery: The interactions and reactions of LGO and Cyrene with water

Majed Almuqhim, A. Fan and J. Clark  
Green Chemistry Centre of Excellence, University of York, United Kingdom  
[ma1603@york.ac.uk](mailto:ma1603@york.ac.uk)

Levoglucosenone (LGO) and Cyrene are bio-based compounds derived from biomass in 1 or 2 steps<sup>1</sup>. Cyrene has rapidly become recognized as a green and safe polar aprotic solvent able to replace toxic amide solvents in many applications. The LGO-Cyrene biorefinery is now being scaled up and the first 1000+ MT production facility is under construction in France<sup>2</sup>. As with all biorefineries water will be ubiquitous and given the hydrogen bonding abilities of LGO and Cyrene, it is important that we understand the relevant interactions and possible reactions between these compounds. Indeed, the reversible reaction of Cyrene with water has been reported and the potential value of Cyrene-water mixtures as solvent systems has been described<sup>3</sup>. Here we report our fundamental and detailed spectroscopic studies on Cyrene-water and LGO-water. These studies reveal multiple species including those with unusually strong hydrogen bonding (Figures 1 and 2). For example, in the range 5-60 °C, LGO has a small effect on the water self-association increasing the enthalpy change  $\Delta H$  from 7.663 kJ/mol to 8.920 kJ/mol whereas, at temperatures between 60 and 95 °C, LGO has a much more dramatic effect on the water H-bonding with  $\Delta H$  increasing to 21.907 kJ/mol.

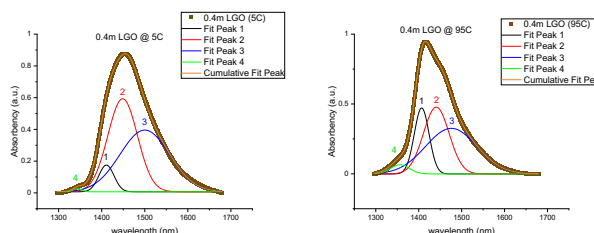


Figure 1. Deconvolution of NIR spectrum of 0.4 m LGO at 95 °C and 5 °C. Peaks 1,4 represent non-hydrogen bonding species. Peaks 2,3 represent hydrogen bonding species.

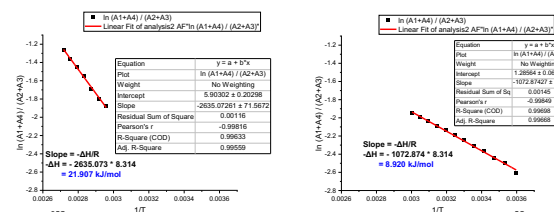


Figure 2. Van't Hoff slope of 0.4 m LGO the range of temperatures 95-5 °C. a. High enthalpy value from 60 °C and above. b. Lower enthalpy value but higher than pure water.

For LGO-water systems we have been able to confirm the production of 5-hydroxycyrene, and have been able to isolate this compound in reasonable yields making this a potential new platform chemical within the LGO biorefinery.

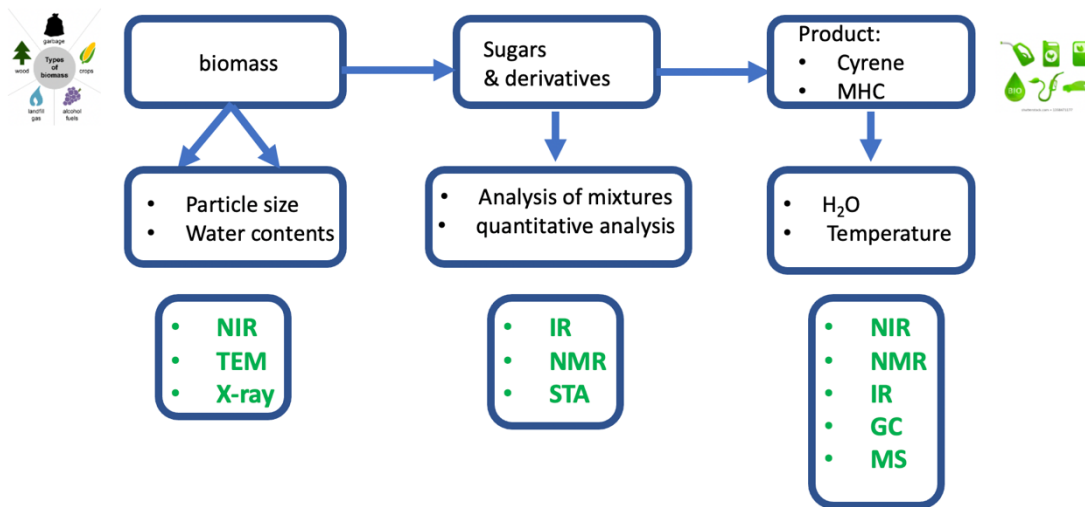
### Acknowledgements

This project has received funding from the Bio-Based Industries Joint Undertaking (BBI-JU) under grant agreement No 887674. The JU receives support from the European Union's Horizon 2020 Research and Innovation Programme and the Bio-Based Industries Consortium. We also acknowledge the Saudi Cultural Bureau for the scholarship fund.

### References

1. J. Sherwood, A. Constantinou, L. Moity, C. R. McElroy, T. J. Farmer, T. Duncan, W. Raverty, A. J. Hunt and J. H. Clark, *Chemical Communications*, 2014, **50**, 9650-9652.
2. Resolute Project, <https://www.resolute-project.eu/>, (accessed Jan 14, 2022)
3. R. A. Milescu, M. L. Segatto, A. Stahl, C. R. McElroy, T. J. Farmer, J. H. Clark and V. G. Zuin, *ACS Sustainable Chemistry & Engineering*, 2020, **8**, 18245-18257.

## Thesis structure:





## Abbreviations and symbols

$\Delta H$	Enthalpy change
CHN	It is an Elemental Analysis (Carbon, Hydrogen and Nitrogen)
DAVINCI+	Deep Atmosphere of Venus Investigation of Noble Gases, Chemistry, and Imaging, Plus
DFF	2,5-diformylfuran
DI	Deionised water
DMSO	Dimethyl sulfoxide
DRIFT	Diffuse Reflectance Fourier Transform
DSC	Differential Scanning Calorimetry
GC	Gas Chromatography
GC/MS	Gas Chromatography/ Mass Spectrometry
H-bonding	Hydrogen-bonding
HBA	hydrogen bonding acceptor
HBD	hydrogen bonding donor
HCl	Hydrogen chloride or hydrochloric acid
HMF	5-Hydroxymethyle-furfural
HPLC	High-Performance Liquid Chromatography
IR	Infrared region of the spectrum
LA	Levulinic Acid
LGA	Levoglucozan
LGO	Levoglucozenone
LHV	Lower Heating Value
m	Molality
M	Molarity

MEK	Methyl ethyl ketone or butanone
MHC	Monohydroxy Cyrene
mm	Millimeter
MS	Mass Spectrometry
MW	Microwave
NASA	the National Aeronautics and Space Administration
NIRS	Near-Infrared spectroscopy
NMR	Nuclear Magnetic Resonance
PCA	Principle Component Analysis
PLS-DA	Partial Least Squares for Discriminant Analysis
PLSR	Partial Least Squares Regression
PVC	Polyvinyl chloride
REACH	Registration, Evaluation, Authorisation and restriction of Chemicals
STA	Simultaneous Thermal Analysis
SWE	Subcritical Water Extraction
UV-Vis	Ultraviolet and visible region of the spectrum
Vis/NIR	visible / Near-Infrared spectroscopy

## References

1. J. Clark, *Green Chemistry*, 2019, **21**, 1168-1170.
2. J. D. Sachs and K. Ban, *The Age of Sustainable Development*, Columbia University Press, 2015.
3. J. Sherwood, *Bioresource Technology*, 2020, **300**, 122755.
4. J. Sherwood, 2021.
5. M. W. Ryberg, T. K. Bjerre, P. H. Nielsen and M. Hauschild, *Journal of Industrial Ecology*, 2021, **25**, 765-777.
6. E. a. I. S. Department for Business, *Journal*, 2019, 46.
7. S. Jin, F. P. Byrne, J. H. Clark, C. R. McElroy, A. Quinn, J. Sherwood and A. J. Hunt, *RSC advances*, 2021, **11**, 39412-39419.
8. Y. Gu and F. Jerome, *Chemical Society Reviews*, 2013, **42**, 9550-9570.
9. P. T. Anastas, L. G. Heine and T. C. Williamson, ACS Publications, 2000.
10. P. T. Anastas and M. M. Kirchhoff, *Accounts of chemical research*, 2002, **35**, 686-694.
11. Y. Gu and F. Jérôme, *Green Chemistry*, 2010, **12**, 1127-1138.
12. F. Chemat, M. A. Vian and G. Cravotto, *International journal of molecular sciences*, 2012, **13**, 8615-8627.
13. M. Bandres, *CR Chim*, 2011, **14**, 636-646.
14. T. M. Mak, X. Xiong, D. C. Tsang, K. Iris and C. S. Poon, *Bioresource technology*, 2020, **297**, 122497.
15. V. L. Budarin, P. S. Shuttleworth, J. R. Dodson, A. J. Hunt, B. Lanigan, R. Marriott, K. J. Milkowski, A. J. Wilson, S. W. Breeden and J. Fan, *Energy & Environmental Science*, 2011, **4**, 471-479.
16. P. E. Marriott, L. D. Gómez and S. J. McQueen-Mason, *New phytologist*, 2016, **209**, 1366-1381.
17. V. Budarin, J. Clark, B. Lanigan, P. Shuttleworth, S. Breeden, A. Wilson, D. Macquarrie, K. Milkowski, J. Jones, T. Bridgeman and A. Ross, *Bioresource Technology*, 2009, **100**, 6064-6068.
18. V. K. Thakur, M. K. Thakur, P. Raghavan and M. R. Kessler, *ACS Sustainable Chemistry & Engineering*, 2014, **2**, 1072-1092.
19. M. Lancaster, *Green Chemistry 3rd Edition: An Introductory Text*, Royal Society of Chemistry, 2016.
20. L. O. Garciano II, N. H. Tran, G. K. Kannangara, A. S. Milev, M. A. Wilson and H. Volk, *Chemical engineering science*, 2014, **107**, 302-310.
21. V. G. Zuin, *Pure and Applied Chemistry*, 2016, **88**, 29-36.
22. S. Van den Bosch, W. Schutyser, R. Vanholme, T. Driessen, S.-F. Koelewijn, T. Renders, B. De Meester, W. Huijgen, W. Dehaen and C. Cortin, *Energy & environmental science*, 2015, **8**, 1748-1763.
23. V. Budarin, P. Shuttleworth, M. De Bruyn, T. Farmer, M. Gronnow, L. Pfaltzgraff, D. Macquarrie and J. Clark, *Catalysis Today*, 2015, **239**, 80-89.
24. M. De Bruyn, J. Fan, V. Budarin, D. Macquarrie, L. Gomez, R. Simister, T. Farmer, W. Raverty, S. McQueen-Mason and J. Clark, *Energy & Environmental Science*, 2016, **9**, 2571-2574.

25. C. J. Chuck and J. Donnelly, *Applied energy*, 2014, **118**, 83-91.
26. C. J. Chuck, F. Santomauro, L. A. Sargeant, F. Whiffin, T. Chantasuban, N. R. A. Ghaffar, J. L. Wagner and R. J. Scott, *Biofuels*, 2014, **5**, 293-311.
27. J. Massaya, K. H. Chan, B. Mills-Lamprey and C. J. Chuck, *Biomass Conversion and Biorefinery*, 2021, 1-17.
28. Y. Huang, P. Chiueh and S. Lo, *Sustainable Environment Research*, 2016, **26**, 103-109.
29. S. Toor, L. Rosendahl and A. Rudolf, *Energy*, 2011, **36**, 2328-2342.
30. M. North and P. Styring, *Fundamentals*, De Gruyter, 2019.
31. M. North and P. Styring, *Transformations*, De Gruyter, 2019.
32. C. Oggi, *Chemistry Today*, 2018, **36(4)**, 64.
33. T. D. Foust, A. Aden, A. Dutta and S. Phillips, *Cellulose*, 2009, **16**, 547-565.
34. D. Mohan, C. U. Pittman Jr and P. H. Steele, *Energy & fuels*, 2006, **20**, 848-889.
35. M. Miura, H. Kaga, T. Yoshida and K. Ando, *Journal of Wood Science*, 2001, **47**, 502-506.
36. D. E. Clark and W. H. Sutton, *Annual Review of Materials Science*, 1996, **26**, 299-331.
37. A. Dominguez, J. Menéndez, Y. Fernandez, J. Pis, J. V. Nabais, P. Carrott and M. R. Carrott, *Journal of analytical and applied pyrolysis*, 2007, **79**, 128-135.
38. J. Fan, F. Santomauro, V. Budarin, F. Whiffin, F. Abeln, T. Chantasuban, D. Gore-Lloyd, D. Henk, R. Scott, J. Clark and C. Chuck, *Journal of Cleaner Production*, 2018, **198**, 776-784.
39. J. Fan, M. De Bruyn, V. Budarin, M. Gronnow, P. Shuttleworth, S. Breeden, D. Macquarrie and J. Clark, *Journal of the American Chemical Society*, 2013, **135**, 11728-11731.
40. J. Fan, M. De Bruyn, Z. Zhu, V. Budarin, M. Gronnow, L. Gomez, D. Macquarrie and J. Clark, *Chemical Engineering and Processing-Process Intensification*, 2013, **71**, 37-42.
41. C. E. Housecroft and E. C. Constable, *Chemistry: An Introduction to Organic, Inorganic and Physical Chemistry*, Prentice Hall, 2010.
42. R. Schwan, C. Qu, D. Mani, N. Pal, G. Schwaab, J. M. Bowman, G. S. Tschumper and M. Havenith, *Angewandte Chemie*, 2020, **132**, 11496-11504.
43. N. J. Tro, *Chemistry: A Molecular Approach, Loose-Leaf Edition*, Pearson Education, 2019.
44. J. G. Anderson, *University Chemistry: Frontiers and Foundations from a Global and Molecular Perspective*, MIT Press, 2022.
45. H. A. Ruiz, M. Galbe, G. Garrote, D. M. Ramirez-Gutierrez, E. Ximenes, S.-N. Sun, D. Lachos-Perez, R. M. Rodríguez-Jasso, R.-C. Sun and B. Yang, *Bioresource Technology*, 2021, **342**, 125961.
46. W.-H. Chen, S. Nižetić, R. Sirohi, Z. Huang, R. Luque, A. M. Papadopoulos, R. Sakthivel, X. P. Nguyen and A. T. Hoang, *Bioresource technology*, 2022, **344**, 126207.
47. T. R. Sarker, F. Pattnaik, S. Nanda, A. K. Dalai, V. Meda and S. Naik, *Chemosphere*, 2021, **284**, 131372.
48. J. H. Clark and F. Deswarte, *Introduction to Chemicals from Biomass*, Wiley, 2014.
49. X. Huang, S. Kudo, S. Asano and J.-i. Hayashi, *Fuel Processing Technology*, 2021, **212**, 106625.

50. A. Burrows, J. Holman, A. Parsons, G. Pilling and G. Price, *Chemistry3: Introducing Inorganic, Organic and Physical Chemistry*, Oxford University Press, 2017.
51. B. G. Osborne and T. Fearn, *Near infrared spectroscopy in food analysis*, Longman Scientific & Technical, 1986.
52. L. M. Harwood and T. D. W. Claridge, *Introduction to Organic Spectroscopy*, Oxford University Press, 1997.
53. S. B. Duckett and B. C. Gilbert, *Foundations of Spectroscopy*, Oxford University Press, Incorporated, 2000.
54. C. Pasquini, *Journal of the Brazilian Chemical Society*, 2003, **14**, 198-219.
55. W. F. McClure, *Analytical chemistry*, 1994, **66**, 42A-53A.
56. T. Davies, *Analisis*, 1998, **26**, 17-19.
57. D. A. Burns and E. W. Ciurczak, *Handbook of Near-Infrared Analysis*, CRC Press, 2007.
58. B. G. Osborne, *Encyclopedia of analytical chemistry: applications, theory and instrumentation*, 2006.
59. H. Buning-Pfaue, *Food Chemistry*, 2003, **82**, 107-115.
60. E. J. Wolfrum and A. D. Sluiter, *Cellulose*, 2009, **16**, 567-576.
61. T. Yano, H. Matsushige, K. Suehara and Y. Nakano, *Journal of Bioscience and Bioengineering*, 2000, **90**, 540-544.
62. M. Maleki, A. Mouazen, H. Ramon and J. De Baerdemaeker, *Biosystems Engineering*, 2007, **96**, 427-433.
63. L. Liu, X. Ye, A. Womac and S. Sokhansanj, *Carbohydrate Polymers*, 2010, **81**, 820-829.
64. M. Sanderson, F. Agblevor, M. Collins and D. Johnson, *Biomass & Bioenergy*, 1996, **11**, 365-370.
65. S. K. O. Felipe Bachion de Santana, Andre Marcelo de Souza and Tonei Jesus Pappi, *Spectroscopy Europe*, 2019, **31**, 4.
66. P. Williams, *Cereal Chem*, 1979, **56**, 169-172.
67. Z. Sun, S. Torrance, F. K. McNeil-Watson and E. M. Sevick-Muraca, *Analytical chemistry*, 2003, **75**, 1720-1725.
68. A. Phuphaphud, K. Saengprachatanarug, J. Posom, K. Maraphum and E. Taira, *Biosystems Engineering*, 2020, **197**, 76-90.
69. A. Phuphaphud, K. Saengprachatanarug, J. Posom, K. Maraphum and E. Taira, *Vibrational Spectroscopy*, 2019, **101**, 71-80.
70. M. Arshadi, D. Nilsson and P. Geladi, *Journal of Near Infrared Spectroscopy*, 2007, **15**, 379-386.
71. A. Alamia, A. Larsson, C. Breitholtz and H. Thunman, *International Journal of Energy Research*, 2017, **41**, 2001-2019.
72. Lemonick and Sam, *Journal*, 2021, **99**, 2.
73. J. Workman and L. Weyer, *Practical Guide and Spectral Atlas for Interpretive Near-Infrared Spectroscopy*, CRC Press, 2012.
74. B. Zelent and J. Vanderkooi, *Analytical biochemistry*, 2009, **390**, 215-217.
75. A. Herburger, M. Ončák, C. K. Siu, E. G. Demissie, J. Heller, W. K. Tang and M. K. Beyer, *Chemistry—A European Journal*, 2019.
76. S. LEMONICK, *Journal*, 2021, **99**, 3.
77. S. Duckett, B. Gilbert and M. Cockett, *Foundations of molecular structure determination*, Oxford University Press, USA, 2015.

78. D. L. Pavia and G. M. Lampman, *Spectroscopy*, Brooks/Cole, Cengage Learning, 2009.
79. B. De Freitas Homen De Faria, P. Santana Barbosa, J. Valente Roque, A. De Cassia Oliveira Carneiro, P. Rousset, K. Candelier and R. F. Teófilo, 2022.
80. J. Clayden, N. Greeves and S. Warren, *Organic Chemistry*, OUP Oxford, 2012.
81. B. Caballero, P. Finglas and F. Toldra, *Encyclopedia of Food and Health*, Elsevier Science, 2015.
82. V. R. Preedy, *Dietary Sugars: Chemistry, Analysis, Function and Effects*, Royal Society of Chemistry, 2012.
83. J. M. deMan, J. W. Finley, W. J. Hurst and C. Y. Lee, *Principles of Food Chemistry*, Springer International Publishing, 2018.
84. F. Pileidis and M. Titirici, *Chemsuschem*, 2016, **9**, 652-655.
85. A. Mukherjee, M. Dumont and V. Raghauan, *Biomass & Bioenergy*, 2015, **72**, 143-183.
86. X. Zhuang, H. Zhang, J. Yang and H. Qi, *Bioresource Technology*, 2001, **79**, 63-66.
87. A. P. Pereira, T. J. Woodman and C. J. Chuck, *Sustainable Energy & Fuels*, 2021, **5**, 6189-6196.
88. J. J. Seyer, P. E. Luner and M. S. Kemper, *Journal of pharmaceutical sciences*, 2000, **89**, 1305-1316.
89. J. Workman and L. Weyer, *Practical Guide to Interpretive Near-Infrared Spectroscopy*, CRC Press, 2007.
90. A. B. Brizuela, L. C. Bichara, E. Romano, A. Yurquina, S. Locatelli and S. A. Brandán, *Carbohydrate research*, 2012, **361**, 212-218.
91. M. Blanco and A. Peguero, *Talanta*, 2008, **77**, 647-651.
92. D. L. Chicoma, C. Sayer and R. Giudici, *Macromolecular Reaction Engineering*, 2011, **5**, 150-162.
93. J. P. Higgins, S. M. Arrivo, G. Thureau, R. L. Green, W. Bowen, A. Lange, A. C. Templeton, D. L. Thomas and R. A. Reed, *Analytical chemistry*, 2003, **75**, 1777-1785.
94. L. Fridh, S. Volpé and L. Eliasson, *International Journal of Forest Engineering*, 2014, **25**, 222-228.
95. L. Fridh, S. Volpé and L. Eliasson, *International Journal of Forest Engineering*, 2017, **28**, 42-46.
96. L. Fridh, *Skogforsk, Uppsala. Arbetsrapport*, 2012.
97. S. Volpé, *FPIInnovations. Advantage Report*, 2013, **14**, 17.
98. M. R. Ladisch and K. Dyck, *Science*, 1979, **205**, 898-900.
99. V. Rebar, E. Fischbach, D. Apostolopoulos and J. Kokini, *Biotechnology and bioengineering*, 1984, **26**, 513-517.
100. A. A. Christy, *Industrial & Engineering Chemistry Research*, 2013, **52**, 4510-4516.
101. A. A. Christy, *Vibrational Spectroscopy*, 2010, **54**, 42-49.
102. J. Giermańska and M. Szostak, *Journal of Raman spectroscopy*, 1991, **22**, 107-109.
103. K.-i. Izutsu, Y. Hiyama, C. Yomota and T. Kawanishi, *AAPS PharmSciTech*, 2009, **10**, 524-529.
104. F. O. Libnau, O. M. Kvalheim, A. A. Christy and J. Toft, *Vibrational spectroscopy*, 1994, **7**, 243-254.
105. Y. Ozaki, W. F. McClure and A. A. Christy, *Near-Infrared Spectroscopy in Food Science and Technology*, Wiley, 2006.

106. R. Giangiaco, *Food Chemistry*, 2006, **96**, 371-379.
107. M. B. Comba, Y. h. Tsai, A. M. Sarotti, M. I. Mangione, A. G. Suárez and R. A. Spanevello, *European Journal of Organic Chemistry*, 2018, **2018**, 590-604.
108. J. Sherwood, A. Constantinou, L. Moity, C. R. McElroy, T. J. Farmer, T. Duncan, W. Raverty, A. J. Hunt and J. H. Clark, *Chemical Communications*, 2014, **50**, 9650-9652.
109. V. Corne, M. C. Botta, E. D. Giordano, G. F. Giri, D. F. Llompert, H. D. Biava, A. M. Sarotti, M. I. Mangione, E. G. Mata and A. G. Suárez, *Pure and Applied Chemistry*, 2013, **85**, 1683-1692.
110. S. Kudo, N. Goto, J. Sperry, K. Norinaga and J.-i. Hayashi, *ACS Sustainable Chemistry & Engineering*, 2017, **5**, 1132-1140.
111. D. E. Richardson and W. D. Raverty, *Predicted environmental effects from liquid emissions in the manufacture of levoglucosenone and Cyrene*, Appita, 2016.
112. X. Chen and X. Bai, *Waste Management*, 2022, **144**, 376-386.
113. A. M. Sarotti, R. A. Spanevello and A. G. Suárez, *Green Chemistry*, 2007, **9**, 1137-1140.
114. G. Choppin and M. Violante, *The Journal of Chemical Physics*, 1972, **56**, 5890-5898.
115. Y. Jin and S.-i. Ikawa, *The Journal of chemical physics*, 2003, **119**, 12432-12438.
116. H. Maeda, Y. Ozaki, M. Tanaka, N. Hayashi and T. Kojima, *Journal of Near Infrared Spectroscopy*, 1995, **3**, 191-201.
117. R. C. Dougherty, *The Journal of chemical physics*, 1998, **109**, 7372-7378.
118. J. Collins, *Physical Review*, 1925, **26**, 771.
119. W. Monosmith and G. Walrafen, *The Journal of chemical physics*, 1984, **81**, 669-674.
120. S. Šašić, V. Segtnan and Y. Ozaki, *The Journal of Physical Chemistry A*, 2002, **106**, 760-766.
121. V. S. Langford, A. J. McKinley and T. I. Quickenden, *The Journal of Physical Chemistry A*, 2001, **105**, 8916-8921.
122. J. Tan, Y. Sun, L. Ma, H. Feng, Y. Guo, W. Cai and X. Shao, *Chemometrics and Intelligent Laboratory Systems*, 2020, **206**, 104150.
123. H. W. Siesler, Y. Ozaki, S. Kawata and H. M. Heise, *Near-Infrared Spectroscopy: Principles, Instruments, Applications*, Wiley, 2008.
124. M. De Bruyn, V. L. Budarin, A. Misefari, S. Shimizu, H. Fish, M. Cockett, A. J. Hunt, H. Hofstetter, B. M. Weckhuysen and J. H. Clark, *ACS sustainable chemistry & engineering*, 2019, **7**, 7878-7883.
125. J. B. Lambert, E. P. Mazzola and C. D. Ridge, *Nuclear Magnetic Resonance Spectroscopy: An Introduction to Principles, Applications, and Experimental Methods*, Wiley, 2019.
126. S. W. Krauss, R. Schweins, A. Magerl and M. Zobel, *Journal of applied crystallography*, 2019, **52**, 284-288.
127. K. Park, Y. Kim and K. J. Lee, *Journal of Radioanalytical and Nuclear Chemistry*, 2019, **322**, 487-493.
128. H. Belhadj, A. Hakki, P. K. Robertson and D. W. Bahnemann, *Physical Chemistry Chemical Physics*, 2015, **17**, 22940-22946.
129. S. H. Krishna, T. W. Walker, J. A. Dumesic and G. W. Huber, *ChemSusChem*, 2016, **10**.

130. Chem.Libretxts.org, The effect of conjugation, [https://chem.libretxts.org/Bookshelves/Organic\\_Chemistry/Map%3A\\_Organic\\_Chemistry\\_\(Bruice\)/13%3A\\_Mass\\_Spectrometry\\_Infrared\\_Spectroscopy\\_and\\_Ultraviolet\\_Visible\\_Spectroscopy/13.19%3A\\_The\\_Effect\\_of\\_Conjugation\\_on\\_max](https://chem.libretxts.org/Bookshelves/Organic_Chemistry/Map%3A_Organic_Chemistry_(Bruice)/13%3A_Mass_Spectrometry_Infrared_Spectroscopy_and_Ultraviolet_Visible_Spectroscopy/13.19%3A_The_Effect_of_Conjugation_on_max), (accessed 03 April, 2022).
131. C. Reichardt, *Chemical Society Reviews*, 1992, **21**, 147-153.
132. C. Reichardt, *Chemical reviews*, 1994, **94**, 2319-2358.
133. A. Zhenova, A. Pellis, R. A. Milesco, C. R. McElroy, R. J. White and J. H. Clark, *ACS Sustainable Chemistry & Engineering*, 2019, **7**, 14834-14840.
134. P. G. Jessop, *Green Chemistry*, 2011, **13**, 1391-1398.
135. L. M. Mouterde, F. Allais and J. D. Stewart, *Green Chemistry*, 2018, **20**, 5528-5532.
136. X. Ma, X. Liu, P. Yates, W. Raverty, M. G. Banwell, C. Ma, A. C. Willis and P. D. Carr, *Tetrahedron*, 2018, **74**, 5000-5011.
137. B. T. Sharipov, A. N. Davydova, L. K. Faizullina and F. A. Valeev, *Mendeleev Communications*, 2019, **29**, 200-202.
138. Z. J. Witczak, P. Kaplon and M. Kolodziej, in *Timely Research Perspectives in Carbohydrate Chemistry*, Springer, 2002, pp. 171-180.
139. B. T. Sharipov, A. N. Davidova, A. S. Ryabova, N. F. Galimzyanova and F. A. Valeev, *Chemistry of Heterocyclic Compounds*, 2019, **55**, 31-37.
140. K. Matsumoto, T. Ebata, K. Koseki, K. Okano, H. Kawakami and H. Matsushita, *Journal*, 1995.
141. F. Shafizadeh, R. H. Furneaux, D. Pang and T. T. Stevenson, *Carbohydrate Research*, 1982, **100**, 303-313.
142. F. Diot-Néant, L. Mouterde, J. Couvreur, F. Brunois, S. Miller and F. Allais, *European Polymer Journal*, 2021, **159**, 110745.
143. F. Shafizadeh, R. H. Furneaux and T. T. Stevenson, *Carbohydrate Research*, 1979, **71**, 169-191.
144. R. W. Rennecke, K. Eberstein and P. Köll, *Chemische Berichte*, 1975, **108**, 3652-3655.
145. M. Balci, *Basic 1H- and 13C-NMR Spectroscopy*, Elsevier Science, 2005.
146. I. K. Yu, H. Chen, F. Abeln, H. Auta, J. Fan, V. L. Budarin, J. H. Clark, S. Parsons, C. J. Chuck and S. Zhang, *Critical Reviews in Environmental Science and Technology*, 2021, **51**, 1479-1532.
147. B. Schrader, *Infrared and Raman Spectroscopy: Methods and Applications*, Wiley, 2008.
148. M. B. Smith, *A Q&A Approach to Organic Chemistry*, CRC Press, 2020.
149. J. E. McMurry, *Organic Chemistry*, Cengage Learning, 2015.
150. B. OSBORNE, *Analyst*, 1988, **113**, 263-267.
151. B. Osborne and T. Fearn, *Food chemistry*, 1988, **29**, 233-238.
152. K. H. Hazen, M. A. Arnold and G. W. Small, *Applied Spectroscopy*, 1998, **52**, 1597-1605.
153. N. Saiga, C. Hamada and J. Ikeda, *Ultrasonics*, 2006, **44**, e101-e104.
154. M. Manley, *Chemical Society Reviews*, 2014, **43**, 8200-8214.
155. W. Li, P. Goovaerts and M. Meurens, *Journal of agricultural and food chemistry*, 1996, **44**, 2252-2259.
156. R. J. A. d. Nascimento, G. R. d. Macedo, E. S. d. Santos and J. A. d. Oliveira, *Brazilian Journal of Chemical Engineering*, 2017, **34**, 459-468.



157. S. R. DELWICHE, R. E. PITT and K. H. NORRIS, *Cereal Chem*, 1992, **69**, 107-109.
158. J. Li, M. Zhang, F. Dowell and D. Wang, *ACS omega*, 2018, **3**, 5355-5361.
159. D. Wojtków and M. A. Czarnecki, *The Journal of Physical Chemistry A*, 2005, **109**, 8218-8224.
160. K. Buijs and G. Choppin, *The Journal of Chemical Physics*, 1963, **39**, 2035-2041.
161. G. Choppin and K. Buijs, *The Journal of Chemical Physics*, 1963, **39**, 2042-2050.
162. J. Paquette and C. Jolicoeur, *Journal of Solution Chemistry*, 1977, **6**, 403-428.
163. F. Palombo, T. Tassaing, M. Paolantoni, P. Sassi and A. Morresi, *The Journal of Physical Chemistry B*, 2010, **114**, 9085-9093.
164. M. L. F. Simeone, R. A. Parrella, R. E. Schaffert, C. M. Damasceno, M. C. Leal and C. Pasquini, *Microchemical Journal*, 2017, **134**, 125-130.
165. A. F. Omar, H. Atan and M. Z. MatJafri, *Spectroscopy Letters*, 2012, **45**, 190-201.
166. I. Noda, Y. Liu, Y. Ozaki and M. A. Czarnecki, *The Journal of Physical Chemistry*, 1995, **99**, 3068-3073.
167. K. H. Norris, *NIR news*, 2001, **12**, 6-9.
168. K. Norris, *NIR news*, 2009, **20**, 11-15.
169. D. Dahm, C. Hansen, D. Hopkins and K. Norris, *NIR news*, 2010, **21**, 16-17.
170. A. K. Amerov, J. Chen, G. W. Small and M. A. Arnold, *Analytical chemistry*, 2005, **77**, 4587-4594.